Laser Induced Splicing of Photonic Crystal and Standard Single Mode Fibers

CHONG JOO HIN

School of Electrical & Electronic Engineering

A thesis submitted to the Nanyang Technological University

in fulfillment of the requirement for the degree of

Doctor of Philosophy

2005

Statement of Originality

I hereby certify that the content of this thesis is the result of work done by me and has not been submitted for a higher degree to any other University or Institution.

31 May 2005
Date

CHONG JOO HIN

SUMMARY

Optical fiber is the medium of choice to meet the ever-increasing demand for huge information transmission and presently there is no technology that can match the information transmission speed and capacity of optical fiber communications systems. Developments and improvements in optical communications technology have been occurring with tremendous rapidity in parallel with its increasingly wide scale deployment. Potential advantages of optical fiber technology as engineering and economic considerations have stimulated a growing activity in the development of relevant devices and processes to exploit the maximum benefits of this technology.

In the field of optical fiber communications, the importance of *fiber splicing* as a practical tool needs no emphasis. Current splicing methods (mechanical and arc fusion splicing techniques) often restrict the quality of the joint and that of the transmitted signal. This is even more pronounced when splicing fibers of different types, for example splicing of standard single mode fiber to Er-doped fiber. This thesis presents work on a unique technique for splicing of variety of optical fibers using lasers. Although lasers have been extensively used in many applications, their potential for splicing of optical fibers has not been explored to that extent. This may be partly due to the difficulty in determining the optimum parameters for laser splicing and partly because of the problems with the process implementation due to the small size of the fiber itself. Therefore published research work is very limited in this field and no commercial system is available at present. In this interdisciplinary project, extensive investigations have been performed to determine the characteristics

of laser splicing technique and for carrying out the process optimization. The splice joints thus formed have been studied comprehensively such as examination of splice structural details under high magnification microscopes, attenuation measurement etc. The advantages of laser splicing technique include delivery of intense energy over a small area, localized heating, uniformity, repeatability, precise control of process parameters, no contamination of fiber joints, possibility of performing epoxy and fusion splicing with one system, and avoidance of arc in potentially explosive environment.

The project also involves development of Computer Aided Laser Splicing System to automate the process of laser splicing and to provide optimum process parameters. Considerable time has been spent in designing the system so as to incorporate user-friendly features and obtain reliable splice joints. Using this system, similar fibers (such as SMF-to-SMF) as well as dissimilar fibers (for example SMF-to-PCF) have been spliced successfully. Additionally, good results have been obtained in the splicing of multi-fiber ribbon cables.

Design and development of a laser splicing system for joining a new class of photonic crystal fibers (PCF) to standard single mode optical fibers (SMF) is of paramount importance since the conventional electric arc fusion machine fails to perform this operation. Experimental results show that electric arc splicing method results in bubble formation around the fiber ends and subsequent collapse of the air-holes within the PCF fiber. The investigations performed in this project demonstrate that the laser splicing technique overcomes these problems and enhances the quality of the splice by reducing condensation trapped inside the air holes and keeping minimum collapse of the air holes. The achievement of good splice between various types of

PCF to SMF depends on several factors including laser power, laser beam exposure time, and fiber-overlapped stroke. In addition, good fiber preparation and handling skills must be employed to optimize the splice characteristics for two different kinds of optical fibers. The novel CO_2 laser splicing system developed for this purpose has yielded a splice loss of ≤1dB. It is an undeniable fact that the capillary effect in the PCF causes trapping of moisture or that of cleaning solution within the air holes. The air holes with a size of fraction of a micron trap the water particles. It is not easy to detect these microscopic water droplets and clean them completely during the splicing process. Theoretical models have been developed to support the experimental studies. In an attempt to understand the mechanism of laser splicing in PCF and condensed PCF, a model involving laser induced plasma effect has been developed. The modeling approach has been useful as the absorbed optical power by the fiber may be enhanced due to the generation of laser plasma. A unique phenomenon involving shifting of the molten region during the splicing process has been observed.

The work done under this project (the technique of laser splicing and the system developed) paves the way for more exciting developments in the field of optical communications. Indeed, we have demonstrated the versatility of this technique by successfully fabricating long period gratings and some optical filters.

ACKNOWLEDGEMENT

I would like to express my utmost appreciation and gratitude to my project supervisor, Associate Professor Mukkamala Kameshwar Rao, who has encouraged me to carry out the PhD program after working for almost 2 decades in the industry and educational institutions. With his patience, continual support and encouragement, I manage to overcome many obstacles over this period.

I also would like to thank Associate Professor Shum Ping, (Director for Network Technology Research Centre), our technicians, Mr. Poh Khoon Yong, Madam Wee-Chew Lee Foong, Mr. Chong Lui Tat and Ms. Thung Lina offering their help to support my PhD studies.

LIST OF FIGURES

Figure 2-1 High Index Photonic Crystal Fiber

Figure 2-2 Low Index Photonic Crystal Fiber

Figure 2-3 Periodic wave traveling on the silicon surface by CO_2 laser irradiation

Figure 3-1 Tensile strength of single mode fibers spliced by commercial electric arc splicing system

Figure 3-2 Tensile strength of single mode fibers spliced by laser fiber splicing system developed in the laboratory

Figure 3-3 Structure of silica – $Si(OH)_4$ tetrahedron

Figure 3-4 Overlap stuffing is introduced to balance the expansion force, inner surface force, and to compensate the unevenness of the fiber end-faces

Figure 3-5 Functional block diagram of the laser splicing system

Figure 3-6 Power Monitor Method for fiber Alignment

Figure 3-7 Marco-Bending Alignment Method

Figure 3-8 Core alignments by CCD camera, the core diameter is widened by light reflection at the core region

Figure 3-9 CO_2 laser redirected by the *palmScan* (picture at top right corner) to the fibers to be spliced

Figure 3-10 Complete Setup for Laser Splicing System

Figure 3-11 (a) Volume expansion when excess laser power is applied to the splice joint (b) Volume compression at slightly low laser power

Figure 4-1 Hole spacing or pitch = $\wedge$ and hole size = d_{hole} of PCF

Figure 4-2 LMA-PCF with d_{hole}=1μm, period= 3.2 μm, core diameter = 9.375μm

Figure 4-3 Direct Coupling Losses between SMF to LMA-PCF

Figure 4-4 Axial Misalignment Losses between SMF and PCF

Figure 4-5 Tilt Misalignment Losses between SMF and PCF

Figure 4-6 (a) Cross-section of NL-PCF with core diameter of 2.6μm. (b) Intensity distribution in the transversal plane

Figure 4-7 Direct Coupling Loss of SMF to NL-PCF

Figure 4-8 Axial Misalignment Losses between SMF and NL-PCF

Figure 4-9 Experimental setup for Marco-bending measurement

Figure 4-10 Marco-bending losses at wavelengths of 1300nm and 1550 nm

Figure 5-1 Laser beam positioned more towards the single mode fiber than the PCF during splicing. Three laser interaction layers are also shown.

Figure 5-2 Laser Intensity Profiles for CO_2 laser sources with average power levels of (a) 3.1W (b) 4.4W

Figure 5-3 (a) Thermal conductivity for silica (b) Thermal conductivity in air.

Figure 5-4 Refraction at the interface between atmosphere and fiber

Figure 5-5 Schematic of one-dimensional thermal transfer model

Figure 5-6 (a) Top view for laser beam falls on the fiber at x-z plane (b) side-view for cross-section of fiber

Figure 5-7 Temperature Distribution across the fiber from **z** = -200μm to 200 μm with laser power≅4.4W.

Figure 5-8 Higher laser power needs shorter laser exposure time for melting the fibers into semi-liquid state

Figure 5-9 Fiber temperature declines if the misalignment of laser δ increases

Figure 5-10 Temperature of Fibers vs laser exposure time

Figure 5-11 Overview of temperature distribution over time and width of fiber

Figure 5-12 Three-Dimensional Optical fiber comprising inner core of solid silica or air-hole and cladding layer

Figure 5-13 Thermal Energy Distribution in the SMF cross section

Figure 5-14 Thermal Energy Distribution in the cross section of hollow core fiber with hole-size of 5μm

Figure 5-15 Thermal Energy Distribution in the cross section of hollow core fiber with hole-size of 50μm

Figure 5-16 Temperature dependence of Ionization Probability

Figure 5-17 Dependence of electron density on irradiance for $Si(OH)_4$ Cascade ionization may not occur if I< 5.482 W/m^2

Figure 5-18 Dependence of electron density on irradiance for $Si(OH)_4$ with cascade ionization and diffusion loss

Figure 5-19 Electron density declines with time if the ionization rate is lower than the electron loss rate

Figure 5-20 The increase of electron density of condensed silica fiber is primarily contributed by the $Si(OH)_4$ content. The electron densities of SiO_2 and water decline with time.

Figure 6-1 (a) Type of PCF used for splicing (b) Bubble formation at the fiber ends in the electric arc splicing process

Figure 6-2 First successful splice obtained between non-standard diameter $LPCF_C$ and SMF by laser splicing system

Figure 6-3 High Speed Camera with recording time 1000fps is placed horizontally towards the spliced fibers

Figure 6-4 A complete Splicing Process for Splicing of $SPCF_T$ to SMF

Figure 6-5 (a) Top image illustrates the cross-section of $SPCF_T$ with an index profile of $d/\Lambda = 0.388$ and period $\Lambda = 8.5\mu m$. (b) Bottom image shows the $SPCF_T$ -to–SMF splice joint.

Figure 6-6 Configuration of Large mode areas PCF

Figure 6-7 Time resolved fiber splicing process under the 4.382W laser irradiation

Figure 6-8 Configuration of Highly Non-Linear PCF (NL-PCF)

Figure 6-9 Transmitted signal over the wavelength of 1200-1700nm is almost absorbed by methanol

Figure 6-10 Improvement in the Transmitted power due to Reduced Condensation

Figure 6-11 Real time imaging of laser splicing process for joining of Time resolved splicing process of SMF to NL-PCF

Figure 6-12 Air holes of NL-PCF are compressed and deformed far away from the center of the laser beam spot placed ~30μm away from the fiber joint at the SMF. The image shows the migration of the hottest spot by 115.7 μm away from the fiber joint.

Figure 6-13 (a) The interface between $LPCF_c$ and SMF is joined but it is weak. (b) Few more laser pulses cause the trapped water to expand faster than the silica capillaries, *bubble-Pockets* are formed within the PCF. (c) Water bubble is formed and gradually bursts out to the ambience (d) Water bubble disappears (e) Last two process repeat as more laser pulses apply, less water is trapped. (f) Water bubble is pushed into the lump after molten silica compressed.

Figure 6-14 Inner-surface (air-holes) deformation at active region due to failure of the air capillaries to sustain the pressure caused by the rapid change of temperature near the fiber surface closer to the impinging laser.

Figure 6-15 Laser plasma speeds up heat flow and results in the further azimuthal shift of air hole deformation away from the center of beam

Figure 6-16 Collapse of air holes far away from the peak of laser beam spot

Figure 6-17 (a)) High laser power at the splicing region squeezes a silica lump (b) Cross section of PCF near the spliced region. (c) Magnified view of periodic fringes seen moving towards the center of the PCF

Figure 7-1 CO_2 Laser Splicing Systems

Figure 7-2 Beam shaping may provide different laser intensities to different types of fibers

Figure 7-3 Beam scanning to obtain varying laser intensities across different fibers

Figure 7-4 Tapered-core fibers can be used as a buffer to match the different mode field diameters between SMF and NL-PCF

LIST OF CONTENT

SUMMARY I

ACKNOWLEDGEMENT IV

LIST OF FIGURES V

CHAPTER 1 INTRODUCTION 1

1.1 MOTIVATION 1

1.1 An Exciting New Development: The Photonic crystal fibers (PCFs) 3

1.2 Laser Splicing Technique 5

1.3 Project Objectives & Scope of Work 6

1.4 Major Contributions of the Thesis 8

1.5 Organization of the Thesis 10

CHAPTER 2 Theoretical Background and Literature Review 11

2.1 Introduction 11

2.1.1 The Emergence of Photonic Crystal Fibers 12

2.1.2 Splicing of Optical Fibers 17

2.1.3 Laser-Material Interaction 20

2.2 Theoretical Development and Modeling Review 30

Characteristics of Photonic Crystal Fibers 30

2.2.2 An Overview of Fiber Splicing Techniques 37

2.2.3 Laser Induced Thermal Energy 42

CHAPTER 3 SYSTEM & PROCESS DEVELOPMENT OF LASER SPLICING FOR OPTICAL FIBERS 48

3.1 Optical Fiber Splicing Technology 48

3.1.1 Advantages for Laser Fiber Splicing System 50

3.1.2 Process Optimization for Laser Splicing of Optical Fibers 55

3.1.3 CO_2 Laser Fusion Technology and Photonic Crystal Fiber 58

3.2 Design Considerations for Laser Splicing System 59

3.2.1 Fiber Alignment and Control 60

3.2.2 CO_2 laser Beam Control Subsystem 63
3.2.3 Imaging and Measurement Subsystem 64
3.3 Operational Parameters on Splicing of SMF-to-PCF 69
3.3.1 Laser Power and Control 70
3.3.2 Mode Field Discrepancy 71
3.3.3 Fiber End-face Overlapped Stroke and Laser Exposure Time 71

CHAPTER 4 STUDIES ON LOSSES IN PHOTONIC CRYSTAL FIBERS..73

4.1 Introduction 73
4.1.1 Properties of Photonic Crystal Fibers 75
4.1.2 Types of Photonic Crystal Fibers Used 77
4.2 Misalignment Losses and Simulation Results 81
4.2.1 Misalignment Losses between SMF and PCF 82
4.3 Marco-bending losses in PCF 90
4.3.1 Experimental Studies on PCF Marco-bending 90
4.4 OH^- ion Loss in PCF 92

CHAPTER 5 MODELING OF LASER-FIBER INTERACTION 93

5.1 Laser Interactions with Photonic Crystal Fibers 93
5.2 Thermal Energy Transfer in Optical Fibers 98
5.2.1 Electric-Arc Heating in PCF 98
5.2.2 Laser-Induced Thermal Energy and Temperature Distribution 100
5.2.3 Beam Offset Consideration 117
5.3 Thermal Transfer Mechanism and Scattering Loss in Single Hollow Core Photonic Crystal Fiber 118
5.4 CO_2 Laser Interaction with Silica 124
5.4.1 Photonic Thermal Effects 125
5.5 Computation of Laser Optical Breakdown 126
5.5.1 Rate Equation for Optical Breakdown 128
5.5.2 Optical Breakdown by CO_2 laser 135

CHAPTER 6 EXPERIMENTAL INVESTIGATIONS, RESULTS AND DISCUSSIONS 145

6.1 Introduction 145

6.1.1 Types of PCFs and their Specifications used in this project 147
6.2 PCF-to-SMF Splicing by Electric Arc Method 149
6.2.1 Technical Limitations on Electric Arc Splicing System 149
6.2.2 Experimental Results for Electric Arc Splicing of SMF-to-PCF 150
6.2.3 Discussion on Electric Arc Splicing of SMF-to-PCF 152
6.3 PCF-to-SMF Splicing Using Laser Fusion Technique 155
6.3.1 Experimental Results on Laser Splicing of $SPCF_T$/LMA-PCF to SMF 159
6.3.2 Experimental Results on Laser Splicing of NL-PCF-to-SMF 164
6.4 Discussions and Analysis 169
6.4.1 Splicing Results 170
6.4.2 Volume Expansion and Compression in PCF During the Splicing Process .. 173
6.4.3 Asymmetrical Air hole Deformation in PCF 177
6.4.4 Periodic Fringes Inside the Fiber Cross-section 183

CHAPTER 7 CONCLUSION AND RECOMMENDATIONS 185

7.1 Conclusion 185
7.2 Recommendations 189

BIBLIOGRAPHY 194

REFERENCES 195

Appendix A- 1- CO2 Laser Power Table 208
Appendix A- 2 Imaging System 209
Appendix A- 3: Thermal Parameters for Silica Fibre 213
Appendix A- 4: Three Dimensional Heat Transfer Model 215
Appendix A- 5: Axial Offset between LMA-PCF and SMF 230
Appendix A- 6: Tilt Offset between LMA-PCF and SMF 231

CHAPTER 1 INTRODUCTION

This chapter begins with a brief introduction of optical fiber technology outlining some of the important features of the emerging photonic crystal fibers and their potential for variety of applications. This is followed by a short description of the fiber splicing process and finally the scope of the work is presented. The project objectives and the organization of the report are discussed.

1.1 MOTIVATION

In this new millennium, with the exploding internet traffic volume and limitless business opportunities, high speed, high capacity communications systems have become imperative to meet the ever increasing demand for huge information transmission. Undoubtedly optical fiber is the medium of choice to achieve these objectives; presently there is no technology that can match the information transmission speed and capacity of optical fiber communications systems. The information explosion, ushered in by the Internet has led to a paradigm shift in the telecommunication industry from voice-based services to data optimized services. The massive increase in the availability of the high speed inexpensive personal computers has led to the deployment of large scale distributed computing networks to serve large number of users and enabling them to share software, database and other resources. Direct communication between computers is now a necessity in many working

environments, resulting in greatly expanded requirement for high-speed digital communication channels. Some applications requiring extreme high speed interconnections include rapid access to very large data bases (for example those in finance sector), high definition image transmission (such as medical images, HDTV, 3-D imaging for robotics), computer-computer communications, internal communications with super computers, information superhighway communications, and cable TV with massive number of channels. Such transmission capabilities are impossible in microwave and other types of communications systems. A typical optical fiber is made of silica (SiO_2) and consists of high refractive index central core layer surrounded by a low refractive index cladding layer. Silica fibers exhibit lowest attenuation at a wavelength of 1550 nm, a wavelength that is currently exploited by the industry. The bandwidth and data rate limitations of an optical fiber are due to various dispersion effects that can cause a pulse to spread. Fibers can be designed to be either single-mode or multimode. Single mode fiber (SMF) is the fiber of choice for applications combining long-distance and high data rate. The advantages of SMF in high data capacity and low attenuation have overcome the disadvantages of fabrication difficulty in tolerances and light coupling efficiency from the source. Another major disadvantage of SMF is its ability to operate efficiently only at certain wavelengths.

Developments and improvements in optical communications technology have been occurring with tremendous rapidity in parallel with its increasingly wide scale deployment. Potential advantages of optical fiber technology have stimulated a growing activity in the development of relevant devices and processes to exploit the maximum benefits of this technology. The recent activity on Photonic Crystal Fiber is one such a development that has attracted significant interest from many quarters. Its

unique characteristics show great promise for its potential applications in the area of optical fiber communications. One of the key benefits of PCF is its ability to operate over a wide range of wavelengths [1,2,3]. However, it is often imperative to use PCF together with SMF in order to realize its benefits and hence splicing of these two types of fibers is an important factor in the development of new applications. With commercial electric arc fusion system, severe problems are encountered in PCF-to-SMF splicing [4]. In this project, considerable efforts have been put to tackle these problems and a unique ***Laser Splicing technique*** has been developed. Good results have been obtained in the splicing of SMF-to-PCF as well as SMF-to-SMF by this technique. A brief introduction on the characteristics of photonic crystal fibers and features of laser splicing technique are discussed in the following sections.

1.1 An Exciting New Development: The Photonic crystal fibers (PCFs)

Photonic crystal fibers (PCF), a new class of optical fibers reported in 1996 [2], consists of an array of microscopic air-holes, which are in fact capillaries of air that run along the entire fiber length. These tiny capillaries strongly scatter the light, blocking its escape into the cladding. Although the idea was first conceived in 1991, the first working PCF was fabricated only in late 1995 by Professor Phillip Russell of the United Kingdom. Russell and coworkers demonstrated that photonic crystal fibers with a periodic array of air holes in the cladding region guide light by modified total internal reflection (MTIR). This was followed by many interesting developments which started yielding PCFs with remarkable properties and greatly enhanced capabilities. The spacing between the holes in PCF can be as small as a micrometer and the hole-size can be as small as 25 nanometers. Light is guided at defect which is

intentionally introduced in the PCF during its fabrication process. This has the effect of changing the characteristics of the guided modes. In conventional fibers, light confinement is achieved mainly by total internal reflection, whereas in PCF light is trapped by total internal reflection and another new physical effect known as *Photonic Band Gap (PBG)*, that relies on the coherent Bragg scattering of light into the core. Light incident at the core cladding interface is strongly scattered by the air-holes. For suitable wavelength and angle of incidence, this multiple scattering process results in constructive interference of all rays in the core. Thus photonic band gap enables transmission of only certain bands of wavelengths. Two main categories of PCFs are now available; they are high index guiding PCF and low index guiding PCF. In the *High Index Guiding PCF*, light propagates mainly by the modified total internal reflection (MTIR). On the other hand, photonic band gap effect is the dominant mechanism that confines light in the *Low Index Guiding* PCFs. A few variations of high index PCF are available including Large Mode Area PCF (LMA-PCF) and Highly Non Linear PCF (NL-PCF). The structural difference between these fibers is that former has small air holes and the latter contains large air holes. At the time of our investigations, low-index PCFs were not easily available in the market. Photonic crystal fiber can provide unique dispersion and nonlinear characteristics that have been used to demonstrate a number of novel effects, including the generation of a broadband super-continuum and a zero group-velocity dispersion (GVD) at low wavelengths (765 nm). Due to its extraordinary properties, new applications of PCF are being discovered continuously. Some example applications include dispersion compensation, white light sources, ultra-large mode area fiber, ultra low loss fiber, sensors etc. It is generally perceived that prospects for PCF are great if it is used together with the standard single mode optical fiber. However, proper splicing of two

different types of optical fibers poses a great challenge especially if the fibers contain air holes. For the initially procured PCF, the manufacturers advised us not to splice the PCF to a single mode fiber (SMF) by ourselves and highlighted the immense difficulties those might be encountered. However, we have demonstrated that successful and reliable splicing of SMF-to-PCF as well as SMF-to-SMF can be achieved by using a unique ***Laser Splicing Process***, which is discussed in the next section.

1.2 Laser Splicing Technique

In the field of optical fiber communications, the importance of *fiber splicing* as a practical tool needs no emphasis. Current splicing methods, including mechanical and arc fusion splicing techniques, often restrict the quality of the joint and that of the transmitted signal. This is even more pronounced when splicing fibers of different types, for example splicing of standard single mode fiber to an Er-doped fiber (EDF). We have devoted significant amount of time (and resources) to address this important issue and hence this project also deals with a unique technique for splicing of variety of optical fibers using lasers. *Laser splicing*, as the name implies, involves the use of controlled high power laser beam to provide simpler, economical and efficient solutions to splice formation and related activities. Although lasers have been extensively used in many applications, their potential for splicing of optical fibers has not been explored to that extent. This may be partly due to the difficulty in determining the optimum parameters for laser splicing and partly because of the problems with the process implementation due to the small size of the fiber itself. The situation is further complicated because the optical fiber made of silica is transparent

to light, its absorption of laser light in the fiber is generally very small at many wavelengths. Therefore published research work is very limited in this field and no commercial system is available at present. This thesis includes work on the development of Laser Splicing Technique highlighting its important benefits over the conventional splicing methods. The characteristics of splice joints of photonic crystal fibers formed by laser splicing process have been studied with particular emphasis on their usefulness in photonic device development. The advantages of laser splicing technique include delivery of intense energy over a small area, localized heating, uniformity, repeatability, precise control of process parameters, no contamination of fiber joints, possibility of performing epoxy and fusion splicing with one system, and avoidance of arc in potentially explosive environment.

1.3 Project Objectives & Scope of Work

This is an interdisciplinary project involving optical fiber and material processing technologies. Due to the limited availability of information on both photonic crystal fiber as well as laser splicing, the primary objective of this project is to perform extensive investigations on the characteristics of the laser splicing technique with special attention focused to study the splice joint formed between PCF and standard single mode fiber (SMF). The ultimate goal is to develop a comprehensive laser splicing system for forming low loss fiber joints for variety of optical fibers and for fabrication of specialty fiber devices. The dependence of splice characteristics has been studied with various laser parameters such as power, exposure time, and continuous/pulsed mode of operation. We have used CW laser for most of our investigations. The splice joints thus formed have been studied extensively by

examining their structural details under high magnification microscopes, and performing attenuation and other relevant measurements. The loss of the joints is estimated by using an optical loss test set. From these investigations and studies, as well as with theoretical modeling, optimum splice parameters are obtained. Theoretical models have been developed to support the experimental studies. The modeling approach has been useful as the absorbed optical power by the fiber may be enhanced by the generation of laser plasma.

The project also involves development of Computer Aided Laser Splicing System to automate the process of laser splicing. Considerable time has been spent in designing the system and to incorporate user-friendly features and to deliver optimum process parameters. Using this system, similar fibers (such as SMF-to-SMF) as well as dissimilar fibers (for example SMF-to-PCF) have been spliced successfully. Additionally, good results have been obtained in the splicing of multi-fiber ribbon cables. Both the technique of laser splicing and the system developed in this project pave the way for more exciting developments in the field of optical communications. Indeed, we have demonstrated the versatility of this technique by successfully fabricating long period fiber gratings and other optical filters .The main objectives of project are summarized below:

- Studies on the problems with the electric arc-fusion splicing system.
- Design and development of a laser splicing system for splicing of photonic crystal and single mode optical fibers.
- Parametric optimization for achieving a good splice
- Study on the laser-PCF interactions during the splicing process.
- Study on the plasma formation in a condensed PCF.

1.4 Major Contributions of the Thesis

Optical fiber splicing technology is unique to Photonic Crystal Fiber (PCF) which is staggered by bundle of air-filled silica capillaries to form its cladding. Design and development of a laser splicing system for joining a new class of photonic crystal fibers (PCF) to standard single mode optical fibers (SMF) is of paramount importance since the conventional electric arc fusion machine fails to perform this operation. Examples of problems that are observed in the splicing of PCF with the electric arc system include (i) Failure of the PCF to be recognized by the imaging system due to its special structure (ii) Bubble formation at the fiber ends due to condensation in the air holes (iii) Serious collapse of air-holes due to the non-localized heating from the arc fusion splicing system. The investigations performed in this project demonstrate that the laser splicing technique overcomes the above-mentioned problems and enhances the quality of the splice by reducing condensation trapped inside the air holes and keeping the collapse of air holes to minimum. The mechanism of energy transfer from laser into the fiber joint is very different than that from the electric arc system. The achievement of good splice between various types of PCF to SMF depends on several factors including laser power, laser beam exposure time, fiber-overlapped stroke and other parameters. In addition, good fiber preparation and handling skills must be employed to optimize the splice for two different kinds of optical fibers. Hence, a novel CO_2 laser splicing system has been developed, which has yielded a splice loss of ≤1dB. It is an undeniable fact that the capillary effect in the PCF causes trapping of moisture or cleaning solution within the air holes. The air holes with a size of fraction of a micron trap the water particles, it is not easy to detect and clean completely during the splicing process. To understand the mechanism of laser splicing in PCF, both large mode area PCF (LMA-PCF) and highly non-linear

PCF (NL-PCF) have been studied. Every PCF has a unique design of micro-structural cross section with specific features depending on factors such as air hole pattern, size of air holes, hole-to-hole spacing or strut-width and silica material composition. If any cross-section of the PCF along its length is deformed, the performance will be affected. A one dimensional thermal transfer model has been employed to determine optimum splice parameters by keeping collapse of air holes in PCF to minimum. Additionally, a three dimensional thermal model has been developed which provides the thermal energy distribution over the fiber cross-section. A generic rate equation describing the rate of change of electron density caused by inverse Bremsstrahlung mechanism is used to explain the optical breakdown phenomenon of the PCF.

The project also involves development of a computer aided laser splicing system, consisting of the following (i) Fiber alignment and control subsystem (ii) CO_2 laser beam controlled subsystem (iii) Imaging and measurement subsystem (iv) System control and interface subsystem. A user-friendly software program is developed for enhancing the performance of the system.

The personal computer is interfaced with the micro-positioning subsystem to allow precise fiber alignment and a laser gun assembly subsystem provides controlled power for proper splicing of fibers. The imaging subsystem captures the fiber image during the alignment and splicing process; and also provides an estimation of the splice loss. The quality of the splice is measured by the attenuation measurement subsystem consisting of a live fiber detector. The details of these subsystems will be presented in the chapter 4 in the thesis.

1.5 Organization of the Thesis

The thesis is divided into SEVEN chapters and arranged in the following manner:

Chapter 1 is the introductory chapter and covers motivation, objective, scope of work and major contribution to the thesis.

Chapter 2 reviews previous work as well as theory of photonic crystal fibers, splicing technologies and interaction of laser with dielectrics.

Chapter 3 looks into the existing electric arc splicing technologies and compares them with the laser fusion technology. It also presents important considerations for the design and development of a laser splicing system.

Chapter 4 describes the spectral characteristics of various types of PCF and gives a theoretical and experimental analysis on the bending characteristics of these fibers.

Chapter 5 presents a 1-Dimensional thermal transport model for SMF and PCF; and extends this model to 3-Dimensional thermal transport model based on EM wave analysis. A general rate equation to analyze the laser-PCF interaction models is discussed.

Chapter 6 presents a detailed description on the experimental results on splicing of SMF-to-PCFs and provides an analysis on splicing of various types of optical fibers.

Chapter 7 gives a conclusion on the results achieved and presents some recommendations for future development.

CHAPTER 2 Theoretical Background and Literature Review

This chapter begins with an introduction of the single mode fiber and a brief description on the development of emerging Photonic Crystal Fiber (PCF) is reported. A review on the fiber splicing mechanisms and theoretical studies is presented and an exhaustive literature survey of related areas of these interdisciplinary topics has been undertaken. Fiber splicing technology is complex especially to the PCF, therefore, an overview of laser induced thermal energy in the dielectrics and condensed matter is included.

2.1 Introduction

The continuous development of optical fiber technology has been supporting the high demand of high bit rate, high bandwidth and low transmission loss in the optical communication systems and networks over the last 2-3 decades. In 1970s, multi-mode optical fibers with transmission loss of 2dB/km were widely used together with the light source operating at a wavelength of 850nm [5], subsequently in the late 80s to early 90s, the telecommunications networks used multi-mode fibers [5,6,7] and 1330nm light source quite extensively. In mid of 90s, single mode fiber led an important role in telecommunications industry as the 1550nm laser source was greatly in use to improve the capacity of broadband communications. In late 90s, the wavelength division multiplexing (WDM) and frequency division multiplexing (FDM) were used to exploit the huge bandwidth of the optical fiber to transmit large

capacity of information. Research and development on optical dense wavelength divisional multiplexer (DWDM) networks have matured considerably over the past few years; the use of single mode optical fiber in the 1550nm window for the design of DWDM architectures and protocols might lead an individual to make unrealistic assumptions about the properties of fiber and optical components, and hence might result in an un-realizable or impractical design. One of the major problems with standard silica fiber is its limitation to operate only at certain specific wavelengths. If an optical fiber can be made to operate over wide range of wavelengths, it would not only be beneficial in increasing the channel capacity of a DWDM system, but it will also avoid unnecessary complications involved in the installation related problems with an existing optical fiber system. [8,9,10]. In 1996, a group of UK scientists from the Southampton University created a new kind of optical fiber made of pure silica, called photonic crystal fiber [4], that could operate in the spectrum range from 400 nm to 2000nm. This new technology was set to revolutionize the world of telecommunications and it could provide the solution to transmit vast quantities of data almost instantaneously around the globe.

2.1.1 The Emergence of Photonic Crystal Fibers

Photonic crystals are microstructures with 1D, 2D and 3D periodic variations of the refractive index with a period in the order of the wavelength. This new kind of fiber with a photonic crystal cladding has unique optical properties [11,12,13] and a defect introduced in a photonic crystal lattice can guide light for wavelengths within a photonic band-gap. The cladding in this fiber has the structure of two-dimensional photonic crystal and it consists of a 2D periodic or random array of closely packed

hollow glass fibers [14,15] The development of Microstructure Glass Technology (MSGT) has facilitated the growth of 1D and 2D microstructures made from glass and low melting temperature conductors with minimal size down to 0.2 micrometers. Structures are fabricated by stacking an array of rods or capillaries in hexagonal, triangular, square, rectangular or oval circular configuration and then two or three stages of preform reduction at a temperature of approximately 2000°C to produce fibers in a conventional fiber drawing tower [16]. The fiber is subsequently coated with polymer and wound on a bobbin for suitable handing.

The microstructure arrangement of capillary tubes in the photonic crystal fibers (PCFs) contains air holes throughout the length of the fiber. The core of PCF is a solid silica rod and its cladding is a two dimensional *photonic crystal* made of un-doped silica [1, 2]. The flexibility of microstructure arrangement in PCFs creates a wide range of spectral characteristics that single mode fibers cannot achieve. Hence their applications are not limited to transmission wave-guide only, but it is also possible to use them as opto-electronic tools for spectroscopy, metrology, biomedicine, imaging and transmission devices. As the geometry of PCF is periodic in the transverse dimension but uniform in the longitudinal direction, it can exhibit a two-dimensional band gap for a given longitudinal wave number and forbid a certain range of frequencies from propagating transversely in the fiber. If a defect is introduced in the fiber, frequencies in the band-gap can propagate only in the defect since they are forbidden from propagating in the lattice, and thus a wave-guide is formed.

The material is often un-doped silica in which the high index region is silica glass and the low index region is typically air-void. The PCF can perform as single-mode

operation from the UV to IR spectral regions [4], its large mode area with core diameters can be larger than 20μm, it exhibits highly non-linear characteristics with optimized dispersion properties, and its numerical aperture (NA) [17] values range arbitrarily from low to about 0.9. Two main categories of PCF are *high index guiding* fibers *and low index guiding* fibers.

(a) High Index Guiding Fibers

The high index guiding fibers are similar to the conventional fibers; light signal in a solid core is guided by the Modified Total Internal Reflection (M-TIR) principle. The total internal reflection is caused by the lower effective index in the micro-structured air-filled region. The high index guiding fiber consists of a high index core region made of pure silica, surrounded by a lower effective index provided by the micro-structured region as shown in Figure 2-1. In simple case, the effective index of such a fiber can be approximated by a standard step index fiber. The refractive index of the micro-structured cladding in PCF is wavelength dependent but not the core; therefore, it allows a design of endlessly-single-mode fiber, where only a single mode is supported regardless of optical wavelength. Furthermore, it is possible to alter the dispersion properties of the fibers, thereby making it possible to design fibers with an anomalous dispersion at visible wavelengths.

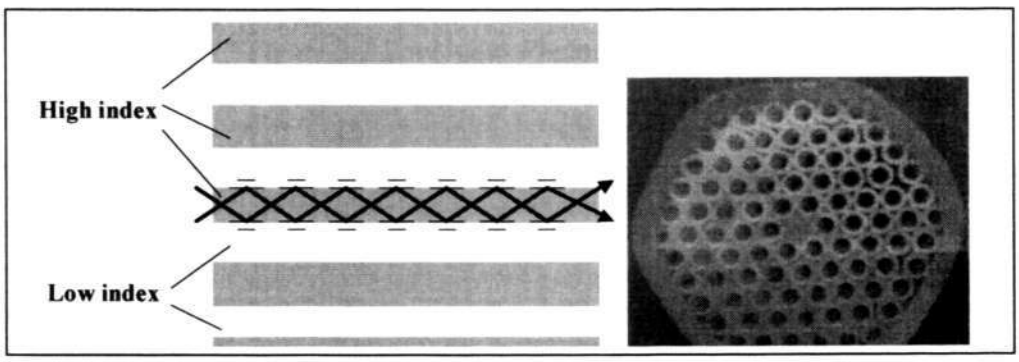

Figure 2-1 High Index Photonic Crystal Fiber

(b) Low Index Guiding Fibers

The low index guiding fibers guide light by the photonic band-gap (PBG) effect. The light is confined to the low index core as the PBG effect makes propagation in the micro-structured cladding region impossible as shown in Figure 2-2. The periodic microstructure in PBG fibers results in a so-called photonic band-gap, where light at certain wavelengths cannot propagate.

In a PBG fiber, the core is created by introducing a defect in the PBG structure and this defect is not a solid silica rod but an *extra* air hole, thereby creating an area where the light can propagate. As the light can only propagate at the defect region, a low index-guiding core has been created. Light is guided through air that is a completely different mechanism than that observed in standard fiber.

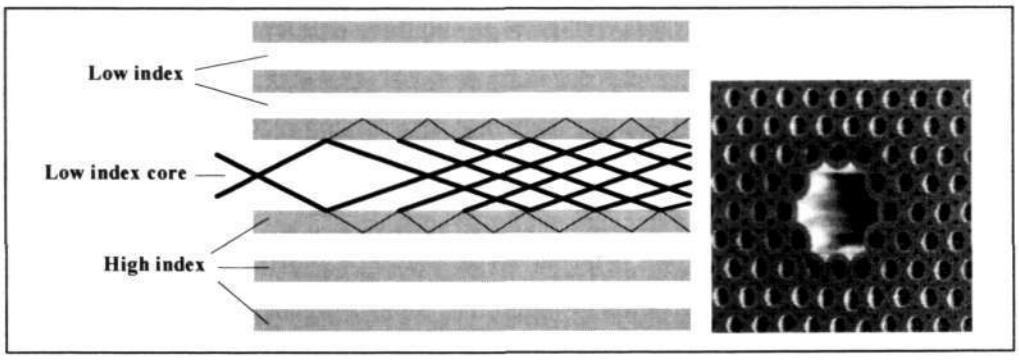

Figure 2-2 Low Index Photonic Crystal Fiber

The band-gap guiding crystal fibers offer a radically different wave-guiding medium compared to conventional fibers and thus provide a high degree of interest from a fundamental point of view. Moreover, the ability of isolating light at low index core

regions in these fibers opens a range of additional possibilities that are not achievable with conventional fibers, as well as index guiding crystal fibers [18,19].

Since the introduction of first photonic crystal fiber in 1996, a lot of attention has been focused by scientists to study and understand its optical characteristics such as single-mode operation [1], bending losses and dispersion property. Extensive theoretical work is in progress and many simulation models have been presented. However, practical applications of PCF are not sufficiently found in the literature.

Due to the complexity of fabrication, the low index PCF (i.e. hollow core PCF) is only made available recently. For the past 2-3 years, only high index PCF was available in the market, such as large mode area or endlessly (single mode) PCF, polarization PCF and non-linear PCF.

Photonic crystal fibers are also available in a wide range of specialized designs, each adding a unique function to the specialty fiber created. Some of these functions are insensitivity to fiber bending, reduced fiber loss, zero dispersion, polarization stability, and high-power delivery. With their benefits of single-mode function at wide range of operating wavelengths, there is a huge potential for practical applications of PCF, for example in (i) in the fabrication of long period grating filter [20,21], (ii) all-optical signal processing devices using liquid-crystal-filled photonic crystal fibers (LC-PCF) that guide light by the photonic band-gap effect and (iii) a tunable switch with an extinction ratio of 60 dB and an insertion loss of only 1 dB developed by a team from Denmark and Sweden [22]. With the current high cost of PCF, it is not economical to use PCF as a main transmission media in a communication link. Hence, PCF is widely used in the development of specialty optical devices; it has even greater potential in the areas of telecommunications, sensor technology, spectroscopy and

medicine if it is integrated with single mode fibers [23]. One of the main stumbling blocks in these applications is the problem encountered in the splicing of PCF to single mode fiber and this problem must be resolved for the effective use of PCF technology.

2.1.2 Splicing of Optical Fibers

In the early 70s, mechanical splices were considered the most convenient and simple tool to join two fiber ends. The mechanical splices employ some type of ferrule or tube in which the fibers are inserted [24,25]. A common method involves the use of an accurately produced rigid alignment tube into which the prepared fiber ends are permanently bonded by some kind of optical epoxy. For mechanical splice of multimode mode fibers, if it uses ceramic capillaries with an inner diameter just large enough to accept the diameter of fibers, the average insertion loss can be as low as 0.1dB. Mechanical splicing technique is still considered acceptable for splicing of multi-mode fibers. It is difficult to achieve low insertion loss in the splicing of single mode fiber with core diameter in the range of 5~9μm. Arc fusion splicing offers superior results for joining single mode fibers. The first arc fusion system for splicing of optical fibers emerged in the late 1970s [27], and even today, it is one of the very important tools in the optical laboratory.

Plastic optical fiber (POF), another type of multimode fiber with large core diameter (about 0.5-1mm), is low in cost and easy to handle. It is considered suitable for short-haul data transmission applications in computer links. However, the growth of POF has been prohibited by two major disadvantages, namely the relatively high loss of about 120-200 dB/km and its *low heat resistance.* In 1990, Hara et al [29] developed a device to splice plastic optical fiber (500 micrometers diameter, fluoro-polymer

cladding) by thermal fusion. The device heats the fibers inserted in a polymer PEEK tube [25, 29], which helps to align the fiber axes and protects the fused joint mechanically. This device is intended to produce splices with good light transmission and mechanical strength. The joint can withstand 1.2 kg-f of tensile force and the its bending radius is as small as 3 cm. The mechanical strength can be improved easily by adding epoxy [29]. Another way of joining this type of fiber is to use ultrasonic welding [30]; this method can bond the fibers with low loss without damaging the cladding layer except at the welding surface.

Splicing of *Erbium-doped optical fiber* (EDF) is considerably more difficult than other fiber types (of course before the invention of PCF). It is because EDF has small core (2-4μm) that makes core/clad concentricity critical. Furthermore, EDF splicing [32,33] is challenging because the core-dopant ions diffuse when fiber is heated, much more rapidly than the dopants in the fiber to which this fiber is normally spliced. Mode field diameter expansion in the dopant is the main contributions to the splice loss. In the splicing process, it uses Arc-on-Alignment (AOA) technique to correct the misalignment between fiber ends. Furthermore, using specific fusion time and fusion current are used to determine the mode-field diameter (MFD) of erbium-doped fiber to match with MFD of the dissimilar fiber [32, 33, 34].

Of course there are many other types of optical fibers available in the market such as twin-core optical fiber, polarization maintaining optical fiber (PMF) and others, the basic splicing techniques [35] described above should be applicable to these fibers as well. Some of the important factors involved in the splicing process, such as fiber-to-fiber alignment and splice losses measurement are described below.

(i) Fiber-to –fiber Alignment

Three possible misalignments that are encountered in splicing of fibers include axial, lateral and angular misalignments [36 37,38]. To obtain a good splice, fiber-to-fiber alignment must be very precise. This is especially critical for splicing of dissimilar fibers as the mismatch of the cohesive forces between their core and cladding may result in the failure of self-regulated alignment. The optical fibers are placed into the v-grooves, their axial and lateral alignments can be adjusted with reasonable precision by micro-controller stages. The angular misalignment can be minimized by cleaving the fiber ends properly. In terms of monitoring and controlling the fiber alignment, the active or passive alignment technique [37, 38, 39] is generally implemented in the splicing system. Some of the commercial electric arc splicing systems (such as that from Corning) employ imaging technique as well as the macro-bending method to perform active alignment, whereas others (e.g. Fujikura and Sumitomo) use only image profile alignment method [36].

In one study [40], it is reported that the possible buckling of the fibers in splicing system causes an appreciable change (fluctuation) in the refractive index of the fiber material, which in turn leads to some loss of the transmitted information. A fusion-spliced optical fiber is examined with a laser sheet of light. A CCD camera is used to record the transverse interference pattern from the fiber. The buckling on the fiber material in one direction of the spliced point is distinct inside the transverse interference pattern. Even though it is possible for this phenomenon to occur, it appears that end users have rarely faced this problem, and therefore we believe that this problem is not severe if the splicing is carefully performed.

(ii) Measurement of fiber losses

The measurement of splice loss is one of the important procedures in the splicing of optical fibers because it determines the quality of splice. The splice loss measurement can be in the active or passive mode depending on the system used. Active measurement involves launching of laser signal from one end of fiber and measuring the signal intensity at the end of spliced fiber. *Marco-bending* method is also a type of active measurement technique. In order to determine the splice loss, *cut back* technique is normally used in the laboratory. Optical time domain reflectometry (OTDR) is another active measurement method where only one fiber end is used for launching of light as well as for capturing of received signals. A drawback of the OTDR is the presence of a dead zone that is typically 3m. The passive measurement method involves comparison of 3D images of fiber ends to estimate the splice loss; it is widely used in the commercial electric arc splicing systems.

Laser splicing of optical fibers [41] is essentially an interaction of laser and silica material, therefore achieving of a good splice is not just limited to selecting the right type of laser, but it is also important to gain good understanding of the laser-silica interaction. This interaction is expected to be much more unique and complex for the PCF. The following section deals with an overview of lasers used in material processing applications.

2.1.3 Laser-Material Interaction

The fusion splicing process involves quick, clean, and uniform heating of fiber ends. CO_2 laser is a best candidate for melting of optical fibers due to high-energy

absorption in silica at its operating wavelength of 10.6μm. Optical absorption, scattering, and amplification are very much dependent on the material properties and the laser characteristics [42]. The historical development of transforming materials by laser beams has been strongly influenced by the growth of the laser systems [43]. The investigations of laser effects on materials began to appear soon after the first demonstration of ruby laser in 1960. Due to the poor reproducibility and poor control of laser beam, no appreciable for material processing work could be carried out. The ruby laser was soon challenged by the newly developed Nd:YAG laser, which is inherently more stable and capable of delivering beam of superior quality. Therefore, Nd:YAG laser has been very popular and offered many industrial applications. For many rugged industrial applications like welding and cutting [44, 45, 46], the CO_2 laser is an ideal choice because it is technologically simple, versatile, produces high continuous power and is energy-efficient [47]. Another promising candidate is excimer laser, which operates in the ultraviolet range of wavelengths and combines high power with good efficiency. With photon energies of 4 to 7eV, excimer laser beams are not only absorbed efficiently in most materials but are also able to break chemical bonds directly upon absorption. However, excimer laser is widely used for micro-machining [46, 48] and its UV wavelength is not efficient enough to penetrate a large class of transparent materials, including some glasses and plastics. Therefore, it is conclusive that CO_2 laser with operating wavelength of 10.6μm is currently the most suitable for splicing of silica based optical fibers.

From early 80's to late 90s', Williams and Phuoc [49] investigated the laser-induced breakdown of gases by using powerful laser beam irradiance on combustion gases. The laser material processing on solid targets such as metal, ceramic material and

semi-conductors have received more attentions than the aqueous materials in the 90s [49,51]. The studies on laser-liquid interaction were mainly focused in the fields of laser medicine such as photo disruption, ablation and intraocular microsurgery [51].

Laser as an indirect heating source, is an excellent alternative that brings new horizon into fusion technology. Laser induced heating of metallic or dielectric materials has become popular due to its efficiency and effectiveness and because of ease of control of the laser power and beam diameter. The work on the interaction of laser with *dielectrics* using Nd:YAG laser (1.06μm) has been extensively reported, but the studies involving laser-fiber interaction is scarcely found in the literature. PCF is a new kind of optical fiber that can trap liquid easily if the fiber end is not sealed. This thesis includes investigations of CO_2 laser interaction with PCF, which demonstrate its potential for variety of applications.

(i) Laser Induced Thermal Energy on Dielectrics

To understand the physics of dielectric breakdown [52] due to absorption of laser sources, it is essential to review the experimental measurements and study theoretical models. The dielectric optical breakdown may be caused by the absorption of laser radiation through direct ionization or partial ionization in solid, liquid or gas [53]. The ionization, in certain situations, may result in generation of charged particles called plasma, and this can result in increased absorption of the laser by the dielectric. Many investigations on the laser induced plasma formation in solid, liquid and gas have been carried out but not all are fully understood especially in the liquid-phase of the material.

When a photon impinges on an optical fiber, a few mechanisms can cause possible loss of photon energy. These may include (i) the imperfections in fiber geometry, (ii) electronic transitions across the energy levels in the material, and (iii) finally depending on the material property and the incident wavelength, excitation of another photon (of different wavelength) or phonon followed by non-radiative relaxation process. As a result, there is an increase of the thermal energy in the material. To date, three potential lasers CO_2, Nd:YAG and excimer operating in the IR and UV region are widely employed in the industry. The CO_2 and Nd:YAG lasers are commonly used for thermal processing of materials such as cutting, welding, cleaning and surface modification. In electronics industry, their potential for soldering joints [53] has also been demonstrated. They are also extensively used for marking applications [54], where CO_2 laser is applied on metals and YAG for non-metals such as plastics, quartz, glasses or organics. In fiber splicing, CO_2 laser is more efficient than YAG laser to melt the silica due to the close matching of the wavelength and the molecular vibrational frequency of the silica material. Majority of the material processing applications are carried out with laser intensities higher than of $10^3 W/cm^2$. For a CW laser, the interaction time depends on the power and exposure time of the laser spot focused on the targeted area. For the *pulsed laser interaction process*, the interaction time is dependent on the duration and duty cycle of the pulse. In material processing, both the total energy and the intensity of laser beams are important parameters.

In 1979, Tien and Lienhard [55] described that only rotational and vibration transitions are involved when a dielectric medium absorbs EM wave at room temperature. They also expressed that the occupation probability of electron at low temperature is small. In 1980s, the interest in laser-induced damage (LID) was demonstrated, for example, the use of a 3ns-pulse Nd:YAG (1.06μm) laser to generate

damage on the surface of optical glass. At the glass surface, pit-like damages were attributed to absorption centers on the polished layer. In the interior, two phenomena showed up, threadlike and point like damage at different threshold power levels. The investigations on laser interaction with silica (SiO_2) at short wavelength have been reported extensively [56,58], but there are only limited studies involving the use of long wavelength. Pitts [58] demonstrated the proportionality of crack propagation rate with the radius of targeted particles and the three quarters power of fluence. In 1989, the effect of self-focusing was observed in the LID and Wang [58] in 2002 found that the microstructures were formed with periodic parallel fringes and circular fringes on the front surface of silicon substrate. These periodic structures were supposedly formed by the thermal capillary wave effect and the laser induced periodic surface structure effect (LIPSS effect) during the melting and re-solidification of the material as shown in Figure 2-3. The phenomenon observed was claimed to be complex and was not understood properly. In our experiments on laser splicing of silica fibers, the long wavelength CO_2 laser impinging on condensed photonic crystal fiber has shown some similar phenomenon.

A 2 μs CO_2 laser (TEA) pulse with energy density of 12.0 Jcm^{-2} has been used to demonstrate the modification of the surface of p-type boron-doped single crystal silicon. It has been observed that the energy absorbed from the CO_2 laser beam was converted partially into thermal energy, which in turn generated a series of effects such as melting, vaporization of molten material, shock waves etc. A wave-like microstructure consisting of periodic parallel fringes with a period of about 0.8 μm on the silicon surface was also observed. The laser induced periodic micro-structural behavior has been reported in the past, but the interaction of laser with silicon is not

properly explained [61, 62]. The above experimental results show the generation of fringes on the surface of media that is perpendicular to the laser beam. The work related to the formation of wave-like fringes propagating along the direction of laser beam is not found in the literature, however this phenomenon has been observed in our experiments.

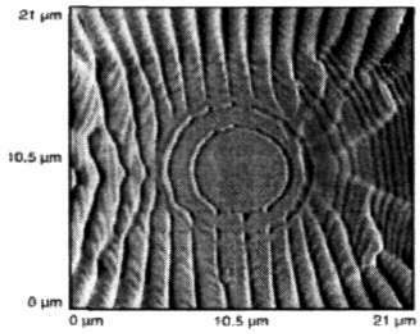

Figure 2-3 Periodic wave traveling on the silicon surface by CO_2 laser irradiation

To our knowledge, no study is reported to date on the laser interaction during the process of splicing in the enclosed silica cavity such as silica capillaries for the PCF. Our observations of laser-induced breakdown within the condensed PCF should provide a better understanding on the limits of laser splicing technology.

(ii) Ionization Collision

Bound Electrons generally do not absorb laser at low laser intensities. If the photon energy is less than the band-gap energy of the materials ($h\nu<E_g$), the electron will not make transition to a higher energy state. In a real dielectric material, very few free electrons are present; however, these can act as seed electrons to absorb laser power and gain sufficient kinetic energy to knock additional electrons from the inner shells

of lattice atoms in the material. The acceleration of these electrons enhances the impact ionization that can increase electron density by manifolds.

Even if the incident photon energy ($h\nu$) is close to band-gap energy E_g of the target material ($\mathbf{h\nu \approx E_g}$), it is still possible for the electron to make a transition to a higher energy state. We can consider the probability of this transition to be marginal and it may still be possible for the ionization collision to occur. The CO_2 laser (operating at wavelength of 10.6μm) with a photon energy $E_{h\nu}$ = 0.117eV is not likely to cause direct ionization of an oxygen or hydrogen molecule possessing energy gaps of 12.07eV or 15.35eV respectively. In term of laser interaction to material, two possible mechanisms are usually discussed, one is multi-photon ionization process [61, 64] and another one is electron cascade process [60-66]. If the laser energy is lower but closer to material band-gap, both processes may occur; whereas if the laser energy is much lower than the material band-gap, only the electron cascade process is possible if the laser intensity is sufficiently high. For example if the intensity of CO_2 laser is high enough, partial ionization in silica material may possibly occur. The rate of creation of new electrons is proportional to the rate of energy gain:

$$\frac{\partial n_e}{\partial t} = n_e \left(\frac{\partial E}{\partial t} \right) \frac{1}{E_g} \qquad \text{Equation 2-1}$$

The electron density increases exponentially with time if other effects (such as recombination) that cause loss of electrons are negligible.

(iii) Laser Induced Breakdown in Liquid

The interaction of high-intensity, pulsed laser radiation with liquid [67,68,69,70] is fundamental to many contemporary technologies including removal of water from the micro-circuits and micro-machines [65] and laser particles removal [71]. Most liquids are dielectrics at room temperature, as such, have large energy differences between electronic states and an insignificant number of free electrons; this is why most liquids are transparent at optical frequencies. In the early 80s to mid 90s, the investigations on laser interaction to ice or water have already attracted the interest from many researchers; the studies include the vacuum-UV reflectance spectrum of ice and the one-photon and multi-photon absorption for the vapor phase water spectrum. Crowell and Bartels [66] reported the transient absorption of hydrated electrons generated by the 3-5eV multi-photon ionization (MPI) of liquid water in picoseconds. The 2 or 3 photon-excitation in 3.02-3.47eV and 3.85-4.54eV energy range demonstrated the occurrence of low (≤15 %) recombination and medium (≥55%) recombination respectively. Crowell investigated the MPI under the short wavelength laser interaction with water.

At high incident laser intensities, liquid molecule can efficiently absorb few photons of laser to promote it to an excited electron state. If the total absorbed photon energy is high enough, the liquid molecule can ionize through the multi-photon absorption process or dissociate to form new species in the liquid. The decomposition is known as photolysis. Upon ionizing, an electron is ejected from the liquid molecule (ionization: $H_20 \rightarrow H_2O + e^-$), leaving behind a positively charge cation. Ionization in water occurs rapidly within a time interval in the order of 100fs [72, 73]. During dissociation, the molecule separates into simpler component species (Dissociation: $H_2O \rightarrow H^+ + OH^-$). The time required for dissociation is also approximately 100fs

[72]. For the photolysis products, in particular the ejected electron can exist for much longer period (~1μs) hence it is possible to enhance the deposition of laser energy in the liquid. Also the hydroxyl radical OH^- is the absorbing specie that absorbs UV light. The excited molecule can simply relax non-radiatively or radiatively back to ground state. Non-radiative transitions convert the absorbed photon into thermal energy, resulting in heating of the liquid. Radiative transition in liquids including water, are negligible. The studies show that water exposed to the short wavelength of 266nm and 532nm Nd:YAG laser radiation has improved the heating and reduced the skin depth by several order of magnitude. At 266nm wavelength, water exhibits a two-photon absorption, the probability of the water molecule ionizing is 0.30 and the non-radiative relaxing is 0.44. [74]. If some moisture or hydrogen is present in the synthetic silica fiber resulting hydroxyl groups chemically bonded to the silica network (Si-OH), the optical property of silica will be affected [75]. Most work has focused on OH band intensity, spectral position or shape. Determination of absolute hydroxyl content depends on the extinction coefficient, and these coefficients of 34 to 901 $mole^{-1}cm^{-1}$ have been studied [76,77]. The spectral position of the OH bands is influenced by the chemical composition of the silica sample such as the concentration of germanium, molecular hydrogen and water [75]. The fundamental and combination modes of the SiO_4 tetrahedron vibration are found to be shifted as a function of fictive temperature [75, 78].

In 1995, Kennedy [79] developed a first order model to determine the irradiance thresholds for laser-induced breakdown in ocular and aqueous media. The model established is based on the extension of Shen's simple rate equation [64] for the cascade breakdown in solids as well as the concept of multi-photon ionization in condensed media developed by Keldysh [80]. In the following year, Noack and

Vogel [81] investigated the generation of plasma in water by high power laser pulses for pulse duration ≅100ns. They calculated the rate of equation for the free electron density under the influence of an intense laser pulse, and demonstrated that the sudden rise in the absorption coefficient was due to the laser-induced breakdown as the plasma is formed. The article has stated that the generation of free electrons in distilled water is initiated by multi-photon ionization but subsequently dominated by cascade ionization generated by the nanosecond pulse. The laser wavelengths employed are short wavelengths of 580nm and 1064nm [61].

The presence of OH content in optical fiber deteriorates its physical quality and introduces losses in the transmission [75]. The relative intensities of the OH absorption bands in the silica fiber are measured between 0.4μm to 3.6μm wavelength range [75]. In the laser splicing investigations, the study of the OH content during the CO_2 laser interaction with the optical fiber are scarce because the CO_2 laser wavelength of 10.6μm is not used for transmission of optical signals. Further, for conventional silica fibers, the water condensation is not a serious problem as the water content is easily removed during the fusion process. However, this is not true in the photonic crystal fiber where the condensation inside the air holes may give constraint during the process of splicing. The study of photo-excitation and ionization in the 10.6μm laser energy regime in the silica fibers becomes extremely important and relevant to understand the mechanism of laser splicing process.

2.2 Theoretical Development and Modeling Review

The field of photonic crystal fibers has attracted a great deal of attention because these fibers are often perceived to be free of the constraints of conventional fiber and wave-guides. The work focused on modeling and development of PCF has being studied extensively in the past few years. Splicing of optical fibers is first emerged in the late 1970, but the investigation on splicing of PCF is new and needs intensive attention.

2.2 Characteristics of Photonic Crystal Fibers

The characteristics of PCF [63] are determined by the design of air holes and air hole-configuration, and subsequently these factors affect the important fiber parameters such as mode area, dispersion, non-linearity and core diameter. In one of the studies [85], it is shown that for an appropriate hole-diameter, the formation of a triangular core due to three missing neighboring air holes will significantly improve the *mode area* and *loss* properties. For large mode area (endlessly) photonic crystal fibers, the ~30% enhancement of the mode area is achieved without any increase in the fiber attenuation for the single mode operation.

A major drawback of the conventional optical fiber is its ability to support propagation of only a limited range of wavelengths (eg. 850nm, 1300nm or 1550nm). Also a standard fiber designed to operate at a specific wavelength is unsuitable at other wavelengths for single mode operation due to cut-off wavelength condition.

The problems of dispersion and resulting pulse broadening can be solved by an "endlessly photonic crystal fiber" which are classified under one of the categories of "photonic bandgap" crystal fibers.

The best way to understand the behavior of light in a photonic crystal is to compare it to the movement of electrons and holes in a semiconductor. In a silicon crystal, for example, the atoms are arranged in a diamond-lattice structure, and electrons moving through this lattice experience a periodic potential as they interact with the silicon nuclei via the Coulomb force. This interaction results in the formation of allowed and forbidden energy states. For pure and perfect silicon crystals, no electrons will be found in an energy range called the forbidden energy gap or simply the band gap. Considerimg photons moving through a block of transparent dielectric material that contains a number of tiny air holes arranged in a lattice pattern. The photons will pass through regions of high refractive index dielectric interspersed with regions of low refractive index air holes. To a photon, this contrast in refractive index looks just like the periodic potential that an electron experiences while traveling through a silicon crystal. Indeed, if there is large contrast in refractive index between the two regions, then most of the light will be confined either within the dielectric material or in the air holes. This confinement results in the formation of allowed energy regions separated by a forbidden region known as *photonic band gap (PBG)*. Since the wavelength of the photons is inversely proportional to their energy, the patterned dielectric material will block light with wavelengths in the photonic band gap, while allowing other wavelengths to pass freely. The potential of photonic-crystal structures [9] was first realized in 1987 by Eli Yablonovitch of Bell Communications Research in New Jersey. In 1991, Yablonovitch and co-workers [84] produced the first photonic crystal by mechanically drilling one-millimeter diameter holes into a block of material with a refractive index of 3.6. The structures with a complete out-of-plane PBG for 2D silica–air photonic crystal was first realized using a triangular arrangement of air holes. This arrangement was predicted to exhibit complete photonic band gaps, but

the requirement of large air hole sizes proved difficult to fulfill experimentally, and the fabricated photonic crystal fibers (PCFs) using triangular arrangements of air holes showed no evidence of PBG effects (albeit other highly unusual properties are found for these index-guiding PCFs). Attention therefore, shifted to so called honeycomb photonic crystals, which have been found to possess larger band gaps than triangular crystals, both for in-plane and out-of-plane propagation. Theoretical results suggested that PCFs based on such a honeycomb photonic crystal structures would be able to exhibit wave guidance by PBG at realistic parameters. These honeycomb-based low-index core PCFs have been fabricated and experimental results have confirmed the theoretical predictions of PBG guidance. Efficient numerical methods are needed for modeling large photonic crystal structures. A cross-section through the new type of fiber shows holes arranged neatly in an array like atoms in a crystal- hence the name, "crystal fiber". The fiber has a regular lattice of air cores running along its length and transmits a wide range of wavelengths without suffering from dispersion [85]

Depending on the air-hole design, photonic crystal fiber can also spread the light more evenly across the fiber cross-section, or increase the nonlinear effects. For example [86], a PCF can be fabricated with a narrow core to squeeze light into the core so that the intensity of the light becomes high enough to cause significant nonlinear effects. These nonlinear properties of this fiber cause the propagating light to undergo a shift to a range of other wavelengths. The photonic crystal fibers are used in the integration of two-dimensional micro structuring with one–dimensional longitudinal transmission. The outcome of this unique combination is the creation of fibers with *dispersive* and *nonlinear* characteristics. The effective non-linearity of a standard PCF

should be considered. The small effective area can be achieved in this type of fiber (i.e. PCF) so as to considerably increase its effective non-linearity in comparison to conventional fiber [87].

In conventional single-mode fibers (SMF), the single-mode optical bandwidth is typically limited by a higher-order mode cutoff at short wavelengths and macro-bend loss at long wavelengths. The characteristics of the photonic crystal fiber (PCF) are fundamentally different and it can be designed to be endlessly single-mode (ESM). A good way to illustrate the differences in the spectral properties of the SMF and the PCF is through the V-parameter. The V-parameter for the SMF, V_{SMF}, has traditionally been applied to determine the higher-order mode cutoff [88] as well as the MFD [89]. The V-parameter for the PCF [89], 90], V_{PCF}, shows that this also held the property of uniquely determining both the higher-order mode cutoff as well as the MFD [91]. The expressions for $\mathbf{V}_{smf}$, and $\mathbf{V}_{pcf}$, are given by:

$$\mathbf{V_{smf}} = \frac{2\pi\rho}{\lambda}\sqrt{\left(\mathbf{n_{core}^2} - \mathbf{n_{clad}^2}\right)} \qquad \text{Equation 2-2}$$

$$\mathbf{V_{pcf}} = \frac{2\pi\Lambda}{\lambda}\sqrt{\left[\mathbf{n_{fm}^2}(\lambda) - \mathbf{n_{fsm}^2}(\lambda)\right]} \qquad \text{Equation 2-3}$$

where, ρ is the core radius and $\mathbf{n}_{core}$ and $\mathbf{n}_{clad}$ are the refractive indices of the core and the cladding, respectively; $\mathbf{n}_{fm}(\lambda)$ and $\mathbf{n}_{fsm}(\lambda)$ are the wavelength dependent effective indices of the fundamental mode (FM) and the fundamental space filling mode (FSM), respectively. The decrease in effective index difference ($\mathbf{n}_{fm}^2 - \mathbf{n}_{fsm}^2$) with decreasing wavelength limits the number of modes and also has the effect that bend loss is observed at short wavelengths for the PCF [92]. The $\mathbf{V}$ value for the

triangular hole arranged-PCF is also first explained by Birks et al [1]. using the effective-index approximation of the cladding structure. In high frequency limit (low wavelength), the effective index of the cladding is approaching n_{fm} so that the index difference becomes small; similarly at longer wavelength, the effective index difference increases so that a stationary **V** value may be reached for PCF. The experimental results carried out by Nielsen et al [89] showed that PCF is significantly more robust towards bending at wavelengths from 400 nm to 1000 nm compared to the conventional SMF. The enhanced properties of the PCF are strongly dependent on the effective index difference between the guided mode and the cladding modes and therefore can be utilized for realizing a larger MFD with the benefit of improved power handling properties.

In general, the fiber characteristics are determined by two parameters: attenuation and dispersion. The latter limits the bandwidth of the transmitted signal through the fiber and the bit rate of the transmitted signal. Few mechanisms are responsible for signal attenuation within the optical fibers. One is the material absorption due to material composition and the fiber fabrication process. The absorption of light may be intrinsic, extrinsic, or atomic defects. Intrinsic absorption is a natural property of the glass. Another is the extrinsic absorption caused by impurities within the glass material. Linear scattering loss causes some of the optical power contained within one mode to be transferred linearly into a different mode. This tends to result in attenuation as the power transfer as a radiation mode, which does not continuously propagate within the fiber core. Non-linear scattering loss is caused by the optical power at certain wavelengths to be transferred in either the forward or backward direction to a different optical wavelength with a release of phonon. The most important types of non-linear scattering within optical fibers are simulated Brillouin

and Raman scattering. Stimulated Brillouin scattering may be regarded as the modulation of light through thermal molecular vibrations with the fiber. The incident photon in the scattering process produces a scattered photon of a different wavelength and a phonon of acoustic frequency. Brillouin scattering is significant only when the incident optical power is greater than a threshold power level given by:

$$P_{Brillouin} = 1.76 \times 10^{-2} d_{core}^2 \lambda^2 \alpha_{Att} \nu_{BW} \qquad \text{Equation 2-4}$$

where, d_{core} = diameter of fiber core, λ = operating wavelength in μm

α_{Att} = fiber attenuation in dB/km, ν_{BW} = source bandwidth in GHz

In the Stimulated Raman scattering, the non-linear interaction of the incident photon produces a high frequency optical phonon and a scattered photon of different wavelength. The Raman scattering occurs only when the power is above a certain threshold power P_{Raman}:

$$P_{Raman} = 0.236 d_{core}^2 \lambda \alpha_{Att} \qquad \text{Equation 2-5}$$

Brillouin and Raman scattering are not usually observed in the optical fibers (especially in MM fibers) because their threshold powers are relatively high especially if the operating wavelength is longer.

Another type of fiber loss is the bending loss including macro-bending and micro-bending losses. The macro-bending loss depends on the bend radius of the curvature as given below:

$$\alpha_{Bend} = c_1 \exp(-c_2 R) \qquad \text{Equation 2-6}$$

where, c_1 and c_2 are constant, R = radius of curvature of the fiber bend

Larger bending losses tend to occur at a critical radius of curvature $R_{critical}$, which can be estimated from:

$$R_{critical} \approx \frac{3n_{core}^2\lambda}{4\pi(n_{core}^2 - n_{clad}^2)^{3/2}} \qquad \text{Equation 2-7}$$

where, n_{core} = refractive index for fiber core, n_{clad} = refractive index for fiber cladding and λ = Operating wavelength

The increase of bending radius reduces the fiber attenuation. The fiber bend radius R should be larger than $R_{critical}$ to avoid significant bending losses.

The dispersion for PCF is a function of wavelength [10], the dispersion and dispersion slope can also be varied dramatically via the size and/or arrangement of the air holes. In the general rule, if the air-filling fraction (d/Λ) is very small, the influence of air holes is strongly limited and the dispersion curve is expectedly very close to material dispersion of the pure silica. As the diameter of the air holes is increased, the wave-guide dispersion becomes increasingly strong and dispersion is reduced significantly. It is interesting that an almost constant dispersion level around –60 ps/km/nm is predicted for a ratio d/Λ =0.4. This unique dispersion characteristic indicates that PCFs have potential applications as dispersion components [10].

A theoretical analysis is presented whereby through the proper selection of PCF geometry, these fibers will be able to be four times more efficient for second harmonic generation than for standard fibers [93].

2.2.2 An Overview of Fiber Splicing Techniques

Exceptional precision in fusion splicing is required to maintain the integrity of the most advanced optical components. A reliable and stable laser source ensures the quality of joint and an appropriate measurement technique determines the quality of splice.

(i) Splice Losses

Fiber-to-fiber end-face alignment is a very important coupling process before fibers are spliced. There are three misalignments are transverse (offset), longitudinal (end separation) and angular (tilt) misalignments. Nemoto [38] uses Gaussian field approximation to the fundamental mode in a single-mode fiber to determine the misalignment losses between two end faces of fibers F1 and F2 with rectangular co-ordinates (ξ, η, ζ) and (ξ', η', ζ') respectively.

$$\text{For F1: } \mathbf{E}_{\xi} = \left(\frac{2Z_0P}{\pi n_1 w^2}\right)^{1/2} \exp\left[-\frac{1}{2}(\tau\rho_r)^2\right]\exp(-j\psi) \qquad \text{Equation 2-8}$$

$$\text{For F2: } \mathbf{E}_{\xi'} = \left(\frac{2Z_0P}{\pi n_1 s_2^2}\right)^{1/2} \exp\left[-\frac{1}{2}\left(\frac{\rho_r'}{s_2}\right)^2\right]\exp(-j\beta\xi') \qquad \text{Equation 2-9}$$

$$\text{Coupling Coefficient: } \mathbf{C} = \left(\frac{n_1^2}{2Z_0P}\right)\int_0^{\infty}\int_0^{2\pi} \mathbf{E}_{\xi}\mathbf{E}_{\xi'}\rho_r' d\rho' d\phi \qquad \text{Equation 2-10}$$

Where, ρ is the radial co-ordinate and β is the propagation constant;

$$\tau = \frac{1}{w^2} + j\left(\frac{2\pi}{\lambda}\right)\left(\frac{1}{R}\right)$$

$$\psi = \left(\frac{2\pi}{\lambda}\right)\xi - \tan^{-1}\left(\frac{2\pi}{\lambda}\right)\left(\frac{w^2}{R}\right)$$

$$w = s_1\left[1+\left(\frac{1}{s_1^2}\times\frac{\xi}{2\pi/\lambda}\right)^2\right]^{\frac{1}{2}}$$

$$R = \xi\left[1+\left(\frac{2\pi}{\lambda}\times\frac{s^2}{\xi}\right)^2\right]$$

Also, **P** is the power carried by the mode in **F1** or by the Gaussian beam and is assumed that the gap between the fibers is filled with air or matching oil with the reflective index of n_1, λ is the wavelength, Z_0 the characteristics impedance of free space, ρ_r is the radial co-ordinate, **w** is dependent on spot size s_1 of F1, and spot size, of F2 is s_2. The power transmission coefficient $\eta = |C|^2$ and the splice loss is $-10\log_{10}\eta$ (dB).

Instead of using simulation program to determine splice loss, Ishikuar at el [94] determines single mode fiber splice loss based on fiber end face image detection using photodiodes and its accuracy with a setting error of 0.5μm. The principle of this method is to shine light source on the fiber ends, and the images of fiber ends cross the photodiodes (PD). At that moment, PD output voltage changes are detected. The object lens M is placed before the PD and is used to magnify the fiber end faces. A setting of accuracy A of fiber end gap is obtained by using the expression **A=q/M** where q denotes a PD detected output voltage changes. The fiber end gap T =Q/M is determined by the distance Q between both PDs. This method using fiber end face image detection by PD has a quick setting time of 5 seconds, but it is not easy to set up in the laboratory. Another type of splice loss measurement employs reflected light

from fiber, the light intensity distribution of the captured images are analyzed along the x y z observation planes [38, 39, 94, 95].

Another commonly used active splice loss measurement technique [96] is to use macro-bending technique. This method launches laser signal through the macro-bend in the vicinity of fiber edge and leaked light is captured by another nearby section of the macro-bend.

Regarding the splice losses in photonic crystal fibers, Bennett [99] in 1999 experimented with splicing of a particular step-index fiber (SIF) to holey fiber (i.e. high index PCF) and the measured splice loss was 1.7dB, however no detailed investigations of splice loss involving holey fiber were conducted. In year 2001, Lizier et al [100] reported the numerical calculations of splice loss based on the finite-difference time-domain (FDTD) simulation. It was to use a short pulse input with optical carrier at a particular wavelength was directed toward the splice from the SIF with LP_{01} field distribution and the results were calculated analytically. The splice loss was determined by the energies in the incident, transmitted and reflected waves. Due to the numerically intensive nature of FDTD calculations, it was common that only short section (approx. 30μm) of fiber could be modeled either side of the splice. The simulation shows that the splice loss was about 1.5dB that was quite close to the earlier experimental result. Furthermore, the determination of splice loss with variation in fiber parameters should be in agreement with analytical approximation based on effective index theory. Lizier [100] also mentioned that the FDTD simulation and computation for the lowest splice loss was determined by the holey fiber pitch where the mode field diameter was similar in both fibers. In the same year, Borzycki [101] suggested a few kinds of splicing techniques for PCF, which

employed one of these methods (i) ordinary fusion with large section of air hole collapse, (ii) short the fusion zone with less fiber collapse, (iii) ultrasonic welding of fiber ends, (iv) mechanical splice using index-matching gel. All these kinds of splicing techniques were introduced without any details about experimental studies.

(ii) Fiber's Temperature

In the arc fusion system, two fibers to be spliced are aligned and placed between two graphite electrodes. The voltage at the electrodes generates a high electric field across the fiber joint. This results in particle excess energies that are the excitation energy and the kinetic energy of free electrons. The mathematical theory [49] of heat conduction is based on the assumption that the heat flux at the plane $z=z_0$ as $\Phi(z_0)$, and the $\Phi(z_0)$ across a plane in a solid is proportional to the local temperature gradient dT/dz and is given as:

$$\Phi(z_0) = -K_c \left(\frac{dT}{dz}\right)_{z_0} \qquad \text{Equation 2-11}$$

Where, K_c = conductivity of the optical fiber.

The thermal energy over the time, Δt, for fusing of a fiber section of thickness Δz (from z to $z+\Delta z$) can be expressed as:

$$\left[\Phi(z) - \Phi(z+\Delta z)\right] \times \Delta t = \frac{C_{sp}}{V_{mol}} \Delta T \Delta z \qquad \text{Equation 2-12}$$

where, ΔT = change in temperature, Δt = time taken, c_{sp} = specific heat at constant pressure, and V_{mol} = molar volume

As the diameter of fiber is only 125 μm; it is reasonable to assume that $\Delta z \rightarrow 0$. So that the heat flow equation from Equation 2-6 can be rewritten as:

$$\frac{\partial}{\partial z}\left(K_c \frac{\partial T}{\partial z}\right) = \frac{c_{sp}}{V_{mol}} \times \frac{\partial T}{\partial t} \qquad \text{Equation 2-13}$$

When the optical fibers are heated to their melting point, their silica core and cladding layers expand, join and re-solidify after the thermal energy source is removed. For accurate calculations, we may allow to vary the laser power and laser exposure time to melt fibers' interface. When the electric field is removed, heating of the fiber also ceases. Electric arc fusion has been in the market for almost two decades and its functionality has been proven in spite of some drawbacks those can create problems under certain conditions. More details will be discussed in the next chapter.

In term laser splicing of optical fibers, K. Egashira [102, 103] and M. Kobayashi [104] proposed a simple analytical model of thermal condition in fiber splicing using CO_2 laser [102,103,105]. The laser source was assumed as a point source focused at the fiber joint where the fiber was treated as thin rod with constant physical parameters, non-existence of convection and radiation. With this assumption, the instantaneous temperature across fiber joint is given by

$$T_{inst,pt}(x,t) = \frac{2Q}{\pi d_{fiber}^2 c_{sp} \rho_{fiber} (\pi \kappa t)^{1/2}} \exp\left(-\nu t - \frac{x^2}{4\kappa t}\right) \qquad \text{Equation 2-14}$$

Where Q is the instantaneous heat liberated by the instantaneous point source, d_{fiber} is the fiber diameter, $\kappa = K/(c_{sp}\,\rho)$ with K the thermal conductivity, c_{sp} is the specific heat, ρ_{fiber} is the density of fiber material, S_{cond} is the surface conductance of material

and $v = 4S_{cond}/(c_{sp}\rho_{fiber}\, d_{fiber})$. For the continuous point source, the above equation will be integrated over time to obtain the fiber temperature. Subsequently, in 1977, the same group developed improved model by assuming continuous Gaussian laser source. Applying this assumption, they concluded that the temperature in the fiber is a function of distance from fiber joint as well as time **t**.

2.2.3 Laser Induced Thermal Energy

Plasma is the fourth state of matter. If the temperature increases, the solid eventually makes phase transitions to the liquid state, subsequently become gaseous. Finally the bonds between the ions and inner-shell electrons are broken and the gas becomes electrically conducting plasma [52]. In general, plasma maintains almost perfect charge balance as given by $-q_e n_e = q_{ion} n_{ion}$ where q_e and q_{ion} are the charge of electron and ion respectively, n_e is the electron density and n_{ion} is the ion density. For the plasma state to exist, electron collisions with neutral atoms or molecules must not be so frequent that the charged particle dynamics is governed by hydrodynamic forces rather than electromagnetic.

Relevant Parameters for Plasma Effect

(i) ***Plasma Parameter*** Λ_{plasma}: It is the dimensionless parameter expressed as:

$$\Lambda_{plasma} = n\left[\frac{\upsilon_{thermal}}{\left(ne^2/m\varepsilon_0\right)^{1/2}}\right]^3 \qquad \text{Equation 2-15}$$

where **n** = particle density, $\upsilon_{thermal}$ = particle thermal velocity and $(e^2/m\varepsilon_0)$ is the strength of the Coulomb interaction between free plasma charged particle assuming the $m = m_{ion}$ or $m = m_e$, where m_e is electron mass, and m_{ion} is ion mass

Two possible limits for Λ_{plasma}, are:

(i) $\Lambda_{plasma} << 1$, implies that the plasma is strongly coupled when the mean Coulomb energy of the ions is comparable to or less than the mean kinetic energy

(ii) $\Lambda_{plasma} >> 1$, means that a plasma is weakly coupled where the particle thermal motions are more important.

(ii) ***Debye Length*** λ_{Debye}: It is a measure of the distance in a plasma over which the electric field of a charged particle is "screened out" by the random thermal motions of the other charged plasma particles. The characteristics of Debye length (λ_{Debye}) correspond to the plasma frequency (ω_{plasma}) for a wave velocity and hence it is equivalent to the electron thermal velocity, $\upsilon_{thermal}$ [109].

$$\lambda_{Debye} \approx \frac{\upsilon_{thermal}}{\omega_{plasma}} = \left(\frac{k_B T}{4\pi n_e e^2} \right)^{1/2} \qquad \text{Equation 2-16}$$

where k_B is Boltzmann constant=$1.38 \times 10^{-16} cm^2 sec^{-2}$ and **T** = temperature (K).

$\omega^2_{plasma} = \left(\frac{4\pi n_e e^2}{m_e} \right)^{1/2}$, n_e= electron density, **e** =electron charge and m_e=electron mass. If $T_{(K)}$ is in Kelvin or $T_{(eV)}$ in **eV** then the respectively equations can be:

$$\lambda_{Debye} = 6.9\left(\frac{T_{(K)}}{n_e\left(cm^{-3}\right)}\right)^{1/2} = 743\left(\frac{T_{(eV)}}{n_e\left(cm^{-3}\right)}\right)^{1/2} \qquad \text{Equation 2-17}$$

The Coulomb force between particles in plasma is shielded by the space charge and is reduced in range from ∞ to λ_{Debye}. Once the particles become hotter, high mobility electrons are generated and λ_{Debye} spreads over a wider range. When the electrons density n is high, the Debye length shrinks. The Debye shielding occurs when there are enough particles in the charge cloud for the weakly coupled plasma as given by

$$\Lambda_{plasma} = \frac{4}{3}\pi\lambda^3_{Debye} >> 1 \qquad \text{Equation 2-18}$$

In the laser-induced plasma due to the inverse Bremsstrahlung process or other collective processes, the absorbed energy is transported to the high-density region by electron thermal conduction.

Under the effect of high power laser radiation, the electrons are accelerated to the electron thermal velocity, $\upsilon_{eTherrmal}$ [160].

$$\upsilon_{eThermal} = \sqrt{\frac{eT_e}{m_e}} \qquad \text{Equation 2-19}$$

Where, e = electron charge, T_e = electron temperature and m_e = electron mass.

Irradiance and Plasma Temperature

Experimental investigations on optical breakdown by lasers have been extensively reported. However, the first paper on the computational model of laser-induced

breakdown in condensed media was first reported by Kennedy [79] in 1995. His computation was based on the simple rate equation formalism given by Shen [64] for cascade breakdown in solids and on the model developed by Keldysh [80] for multi-photon ionization in condensed media. The interaction of a high-energy ultra-violet pulsed laser beam with solid materials has been investigated extensively over the past several years [106]. Many factors affect the laser-interaction such as irradiance, wavelength, pulse duration, ambient gas and pressure. Amongst all of them, the irradiance is the most important in controlling the mechanism of the laser-material interaction. Liu [106] used spectroscopic methods to diagnose the early phase of the laser-induced plasma in the pure single crystalline silicon (99.9%), using Nd:YAG laser (Coherent, Infinity) operating at 266nm with 3ns pulse duration. The plasma temperature (T_e) and electron density (n_e) were measured throughout the experiment, which showed the variation of T_e and n_e as the function of irradiance, ranging from 1 to 60GW/cm^2. At a threshold of ~20GW/cm^2, the electron density and temperature change dramatically. In the irradiance region lower than this threshold value, the electron density (n_e) and temperature (T_e) increased with the irradiance ($I_{h\upsilon}$) following the power law as $n_e \propto (I_{h\nu})^{0.24}$ and $T_e \propto (I_{h\nu})^{0.54}$ respectively.

Once the irradiance went beyond this threshold (i.e. $I_{h\upsilon} \Rightarrow$ 20GW/cm^2), the electron density increased at a faster rate according to the relation $n_e \propto (I_{h\nu})^{1.45}$; whereas the plasma temperature increased at much slower rate as $T_e \propto (I_{h\nu})^{0.24}$. The above experiment demonstrated that below its irradiance threshold, the temperature rise was dependent on the laser irradiance ($I_{h\upsilon}$) [106].

When there is an increase of laser intensity goes higher, the inverse Bremsstrahlung absorption of laser light decreases due to the increase in electron temperature and the steepening of density profile. When the inverse Bremsstrahlung absorption decreases, not only the laser light is reflected at the turning point, but also a significant amount of laser energy tunnels from the turning point through the evanescent region to the critical density region. At the critical point, the frequency of the charge density fluctuations can increase resonantly and propagate out to the under-dense region as an electron plasma wave [107].

Critical Electron Density n_{cr}

The critical electron density for plasma is given as:

$$n_{cr} = \frac{1.1 \times 10^{21}}{\lambda_{\mu}^{2}} \qquad \text{Equation 2-20}$$

Where λ_{μ} is the laser wavelength in micron.

Laser may penetrate slightly past the n_{cr}, and result in an exponential decay of electron concentration over a distance determined by the plasma density [108]. It is possible for the inverse Bremsstrahlung effect and Resonance absorption to occur with (i) low intensity **I** when $I\lambda_{laser}^{2}$ falls between 10^{12} W.μm^2/cm^2 to 10^{17} W.μm^2/cm^2 , (ii) long pulse interactions or in some ultra short-ultra-intense laser-solid interactions.

The plasma is dependent on the laser wavelength, the interacting materials and laser power. With large number of electrons generating a plasma cloud at the focused

volume and the laser intensity near to the threshold value, several problems are likely to be encountered. Firstly, for ion-electron density below the Bremsstrahlung value, the coupling efficiency of the laser beam into the focused area is enhanced. Secondly, when the ion-electron density is above the Bremsstrahlung value, it shields off the laser beam incident onto the focused area and sometimes defocuses the laser beam [110]. Under this condition, the laser beam is shielded by the plasma and cannot reach the interaction point if the electron density is higher than the critical value (n_{cr}). Of course, there are few techniques to reduce the plasma at high incident laser intensity. The techniques include the inert gas side jet plasma control [111] and introduction of electromagnetic field at the focused area to reduce the plasma density [112].

Some *phenomena* in the different level of electron density:

(a) For lower electron density, the total energy transferred into the medium remains well below the heat of evaporation and the formation of a vapor bubble is always observed during the optical breakdown in liquids, a phenomenon, which is not easily explained [81]. For efficient coupling, the plasma frequency, ω_{plasma}, must remain below the light frequency ω_{laser}.

(b) For electron density is greater than ($\frac{\omega_{laser}^2 m_e \varepsilon_0}{e^2}$), the plasma becomes highly reflective. The incoming laser light would not result in any further increase of the electron density [113].

CHAPTER 3 SYSTEM & PROCESS DEVELOPMENT OF LASER SPLICING FOR OPTICAL FIBERS

This chapter briefly illustrates the differences between electric arc and laser splicing technology, and describes the advantages of implementing laser fusion technique to splice optical fibers. The considerations for determining the splicing parameters for achieving good splice are also discussed. Finally, details on the design and development of a computer-aided CO_2 laser splicing system are presented.

3.1 Optical Fiber Splicing Technology

Mechanical splice, the first splicing tool introduced in 70s, involves the use of mechanical fixtures to align and join optical fibers. The basic components for such a technique include tubes made of glass, plastic, metal and ceramic; V-groove and more recent inclusion of rotary devices. Materials that assist mechanical splicing of fibers include transparent adhesives and index matching gels. The handling of mechanical splicing is relatively not convenient compared to the fusion splicing technique and its splice loss is also relatively high. Fusion splicing developed in late 70's, involves use of heat to melt and fuse the ends of two optical fibers, and it can provide splice loss as low as 0.01dB. Initially, nichrome wires have been used as the heating element for fusing of optical fibers. New fusion-splicing techniques have been attempted with replacement of the nichrome wires by gas flame, electric arc and carbon dioxide (CO_2) laser to heat the fiber ends. The portable electric arc splicing system [115] has become the most popular and widely used splicing technique that has left laser-

splicing technology [102, 103] being put in the backyard since 1990. Laser induced splicing has many advantages over the electric arc fusion technique, but the size of CO_2 laser source is relative large and the stability of laser source still needs to be improved. Although, due to its bulkiness, the laser-splicing system is currently not so suitable for field use, its potential remains great in many aspects. A brief description on the electric arc and laser splicing systems is shown below.

(a) Electric Arc Splicing System

In the electric arc splicing system [118], two electrodes are placed a few millimeters apart with the two fiber-ends aligned in between. The heating process uses an electric arc to ionize the space between prepared fibers to eliminate air and heat the fibers to the required temperature (1300 ~1800°C). The fibers then reach the semi-liquid and molten state resulting in the fusion of fibers and this can yield a splice loss of 0.05-0.2 dB if process parameters are appropriately controlled. The important process parameters for electric arc fusion include pre-fusion, arc current, arc exposure time, arc gap and overlap (stuffing) which can vary significantly for splicing systems from different manufacturers.

(b) Laser Splicing System for Optical Fibers

An attempt to splice optical fibers [119] by lasers was first made in 1979, however, very little work has been carried out or reported in the later years. Due to this, laser splicing is still not employed commercially for fiber splicing. In the early 80s, electrical technology was more mature than optical technology; and the electric arc fiber splicing technology has successfully demonstrated its capability to handle the

task. The 10.6 μm operating wavelength of CO_2 laser is strongly absorbed by the silica fiber, which results in the rapid rise of their melting temperatures to effectively form a firm splice joint. Several factors affect splice loss between two different types of fibers such as mismatch of refractive index [120], core/cladding diameter, numerical aperture and also due to their structural differences. Experimentally we have shown that laser-splicing technique gives better tensile strength and superior quality of splice joint if the splicing is performed with optimum process parameters. Important splicing parameters include laser power, beam size, exposure time, fiber-overlapping and beam positioning; these will be discussed in the following sections.

3.1.1 Advantages for Laser Fiber Splicing System

The limitations described above should not be the perpetual obstacle if the laser splicing gains sufficient attention; and efforts are focused to improve the performance of various components required for a laser splicing system. If we set aside the size of laser source, the advantages of using laser splicing over the electric arc fusion can be summarized in the following lines:

1) **Absence of Electrodes**

   The firing of fiber ends in an electric arc splicing system depends on the design of two electrodes. Due to the corrosion of electrodes during the splice operation, maintenance and a frequent change of electrodes are necessary at regular time intervals. This is the reason that electric arc fusion system is not so efficient and costly for mass production in the factory or heavy work environment. On the other hand, the CO_2 laser as a heating source does not have any electrodes, is

more reliable and its operating lifespan can be as long as 5-10 years; and hence the overall operating cost should be much lower.

2) No fiber Contamination

As mentioned earlier, the electric arc fusion technique uses the arc energy to ionize and heat the fibers to be spliced, as well as its surrounding atmosphere, therefore, it is easier to attract unwanted air-particles to be embedded in the spliced joint. The absorption of CO_2 laser by the atmospheric gases is extremely low, therefore the loss of laser energy through the air is negligible and most of the laser is absorbed by the fiber. Furthermore, in the case of electric arc heating, electrodes are easily corroded and the corroded particles may be deposited at the fiber joint during splicing. Therefore, the CO_2 laser as a fusion source can ensure a clean splicing and provide contamination free environment in the vicinity without high voltage arcing.

3) Localized Heating

The advantage of using laser beam for heating is that it occurs in a localized mode, both in space and in time. By matching the wavelength to the optical and the thermal material properties, and with suitable beam power, the amount of heating can be adjusted accurately to suit the needs of a process. If surface heating is required and/or volume heating is to be avoided, a large absorption coefficient and a short interaction time can be selected. Sharply delimited areas can be heated by laser-induced heat while the remainder of the work-piece stays virtually cold. Using short pulses or rapidly moving beams can achieve rapid cooling of the heated material. Apart from localization, laser beams, which are

chemically pure and free of inertia, can be moved easily and passed through windows to reach remote or inaccessible parts of a fiber-piece.

4) Accelerated Heating by Laser-induced Thermal Energy

The heating process by CO_2 laser is different from electric arc as it relies on the absorption of photons by silica, mostly to create resonant conditions in lattice of the material, and under certain situations by generating plasma at high laser intensities. Not all the photon wavelengths can cause heat generation in silica fiber. The excitation of the phonons generated by the CO_2 laser results in rapid heating of the fiber as the resonant wavelength of Si-O bond is very close to CO_2 operating wavelength (10.6μm). At this wavelength, the intense thermal excitation occurs through phonon absorption and possibly by Inverse Bremsstrahlung absorption. Hence laser radiation results in generation of photo-electrons and thermal electrons in silica, which absorb laser power through the laser plasma effect that may further enhance the photon absorption to accelerate the heating process. At the wavelength of 10.6 μm, the absorption coefficient of Si-O is about 10dB/μm [116]

In order to melt PCF to a semi-liquid state, the energy from the fusion source propagates alternately from the silica capillary to air holes. In the electric arc splicing system, the thermal energy from the electric arc is first absorbed and the fiber surface temperature increases, but the heat propagation in the air hole is slower than in silica due to poor thermal conductivity of air. For larger air holes in the fiber, the thermal energy penetration in the PCF would be slower. In the laser fusion technique, the laser absorbed by the fiber results in an increase in the number of electrons and ions, the dynamic electrons in turn absorb laser

resulting in electron multiplication and generation of plasma. This causes strong absorption of laser in the material and rapid generation of heat over the fiber cross-section faster than the electric arc. The bubble formation in PCF spliced by electric arc demonstrates the inefficient heat transfer from the arc system. Hence, there are several incentives to adopt laser to splice the photonic crystal fibers.

5) Small Fusion Area

The fusion area in laser splicing depends on the effectiveness of firing laser beam, whereas in an electrical arc splicing system, the emitting arc from the electrodes affects the fusion zone. Since laser provides highly localized heating, it is easy to limit the beam size close to target area. In this project, the laser used is a Gaussian beam with a width of 6mm and average lasing power is 10~14W. To improve the efficiency of fusion, the beam size should be reduced close to the fiber diameter. If the laser beam is stationary, it is efficient to reduce the beam-size approximately to 2-3 times of the targeted area. In this report, a focusing lens is used to reduce the beam to 400~500μm in diameter. For electric arc splicing, the arcing area depends very much on the design of electrodes and electric current. Generally, the arcing area onto the fiber is considerably much larger than the laser irradiating in its focal plane onto the fiber. Smaller fusion area has an advantage to avoid damage to the other part of the fibers away from the spliced region and therefore should reduce fiber loss.

6) Easier Laser Beam Positioning

The maximum temperature induced at the fiber joint is at the peak of Gaussian beam, and temperature slides accordingly at the declining slope of the intensity

profile. When there is a requirement of different thermal energies, it is possible to adjust the Gaussian beam towards the area that needs higher temperature or to run the laser beam at different scanning speed to achieve various hot zones. The scan along the fiber is done using a galvanometer mirror, which is controlled by the computer. Designing a moving electric arc to run across the fiber is not easy and not cost effective. In general, it is much more convenient to bend or lead the laser beam to any location by the lenses or special types of optical fibers.

7) Improved Fiber Tensile Strength

Laser induced heating at the splice between the two fibers is rapid and even, therefore temperature over the entire fiber ends should be evenly distributed within a short period. We have experimentally verified that the electric arc spliced SM fibers are weaker than their laser spliced counterparts.

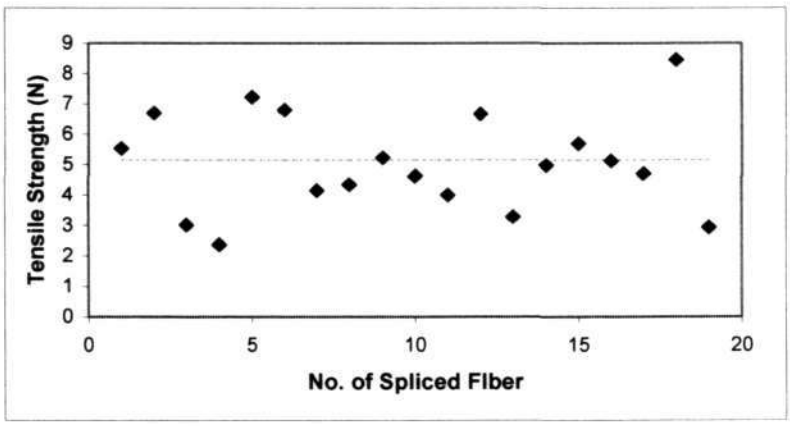

Figure 3-1 Tensile strength of single mode fibers spliced by commercial electric arc splicing system

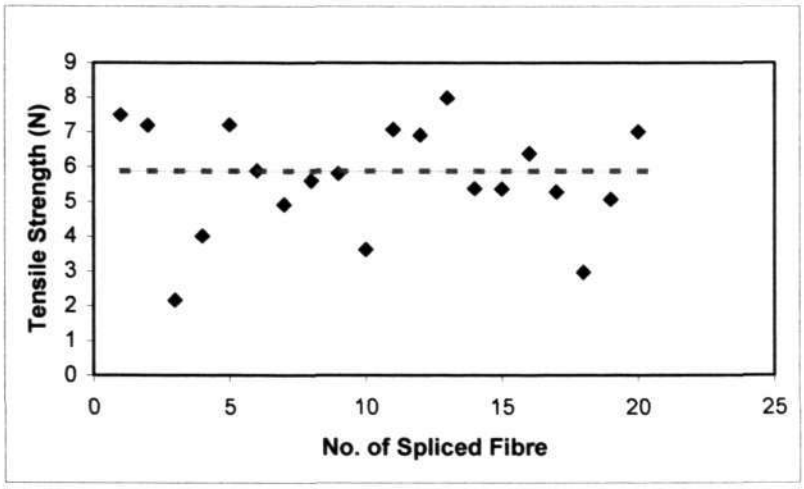

Figure 3-2 Tensile strength of single mode fibers spliced by laser fiber splicing system developed in our laboratory

3.1.2 Process Optimization for Laser Splicing of Optical Fibers

To achieve a good splice between two different types of optical fibers is more complicated than splicing of two similar optical fibers. This section describes the investigations performed on the splicing process to join photonic crystal fiber (PCF) to a standard single mode fiber (SMF). Every PCF has its specific structure such as size of air hole, air hole arrangement or the fiber material. PCF mainly made of pure silica has a melting temperature close to that of SMF, but the required laser power to melt these two types of fibers depends very much on their physical composition. For splicing of PCF to SMF, the amount of laser power must be carefully controlled for melting of these fibers to the semi-liquid state as well as to prevent any physical deformation to the fibers.

To design a good laser splicing system [117], the parameters those must be carefully considered include fiber-to-fiber alignment, reduction of OH ion content, fiber end-face overlapped stuffing stroke, laser power and laser exposure time.

(1) Fiber-to-Fiber Misalignment Losses

Three possible misalignments [115] may occur before and during the splicing of optical fibers: (i) Transverse offset (ii) Tilt offset (iii) Longitudinal separation. In fiber splicing process, transverse offset should be kept as low as possible (≅0.1dB) and the tilt angle should not be greater than 5°. The variation of surface tension across the fiber joint of two fibers during the fusion process may be affected by the irradiating laser power, unevenness of the cleaved surfaces and the overlapped stuffing stroke applied between two fiber ends. A proper fibers preparation, careful handling and precise control of laser parameters are imperative in order to ensure a balanced surface tension between the two fibers and to achieve low splice loss.

(2) OH Absorption in Optical Fiber

The simple structure of silica glass has the tetrahedron (SiO_4) that joins preferentially into rings, each containing six tetrahedral. Any deviation from the chain linking is considered as structural defect. In practice, the silica has stoichiometric defect and may appear as SiO_{2-x} where x is the number of missing oxygen or the presence of OH groups occurring between the (SiO_4) tetrahedron as shown in Figure 3-3, and hence the silicon atoms are not surrounded by 4 oxygen ions as in the case of perfect silica materials.

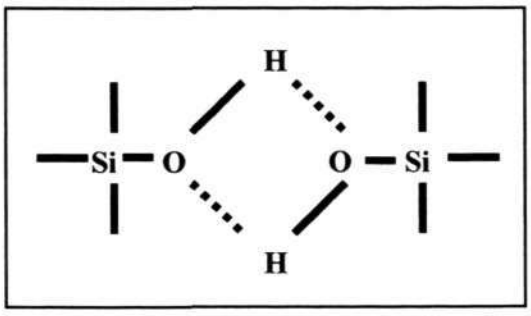

Figure 3-3 Structure of silica – $Si(OH)_2$ tetrahedron

Water reduces viscosity and causes structural de-polymerization, therefore the Si-O structural connectivity is affected. The optical fibers for the telecommunications require the highest purity and extremely low OH^- ion content to maintain optimum transmission performance and fiber's tensile strength [75]. The presence of OH ions in fibers attenuates the transmitting signal in the spectrum between 1300 and 1500nm [121]. Hence, the fiber end faces must be almost free from OH ion content and impurities before the laser is applied to fuse the fibers together.

(3) Fiber End-face Stuffing Stroke

The introduction of fiber end face stuffing is to compensate the irregularities of the fiber surface after cleaving. Low splice loss can be achieved by maintaining the equilibrium of (a) the axial force F_p caused by the pressure applied to the fiber ends, (b) the expansion force F_T due to thermal expansion, and (c) the inner surface tension force F_s of molten glass [122].

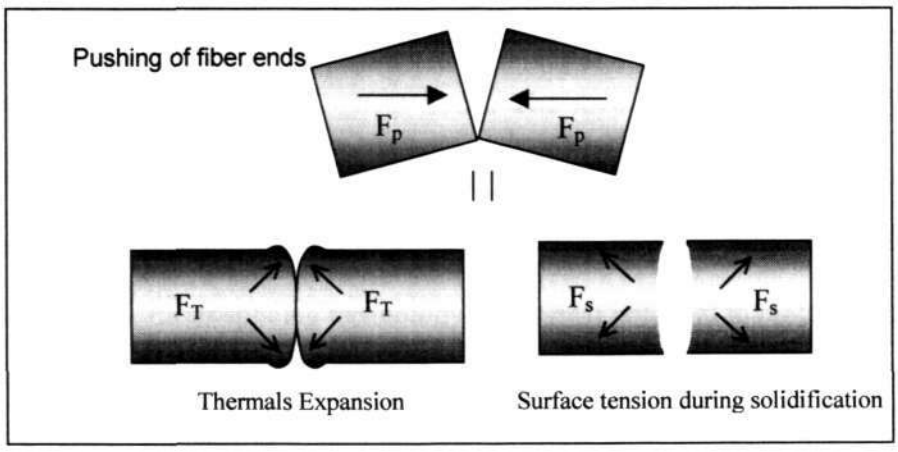

Figure 3-4 Overlap stuffing is introduced to balance the expansion force, inner surface force, and to compensate the unevenness of the fiber end-faces

(4) Laser Power and Laser Exposure Time

Low laser power will not cause the fibers to melt but it can be used to clean the fiber surface, reduce condensation and to strengthen the splice joint after the fibers are spliced. Fiber temperature is dependent on the laser power and laser exposure time, therefore an appropriate control of these two parameters is important to maintain low splice loss.

3.1.3 CO_2 Laser Fusion Technology and Photonic Crystal Fiber

The industrial CO_2 lasers are widely used for cutting, welding or material processing in the heavy industries. The studies on the use of CO_2 laser for processing of optical fiber began in late 70s, which included tasks such as fiber end preparation [41, 96, 122] fiber tapering and fiber splicing [124]. In the 90s, there was no serious activity to study or implement the laser splicing technology due to the widespread use of electric arc splicing technology. One reason for this could be due to the physical size of laser itself as mentioned previously. If the size of laser can be reduced, it may become more attractive for processing of optical fibers. The invention of photonic crystal fibers rekindles the interest of using CO_2 laser fusion technology for splicing of PCF as the laser-induced rapid heating over the fiber can keep the deformation of air holes in PCF to minimum. Laser splicing technology has a great potential to replace electric arc splicing technology for splicing of PCF and other specialty fibers.

3.2 Design Considerations for Laser Splicing System

In general, a basic laser splicing system would involve the design of the following subsystems.

(i) *Fiber Alignment and Control Subsystem* – to provide a precise alignment between the two fiber ends, the required tolerances for xyz alignments are in the range of ≅0.5~1μm.

(ii) *Laser Beam Positioning and Control Subsystem* – to control the laser intensity and laser positioning. For the smallest CO_2 laser available commercially, the laser intensity range is 0~14W, and it is desirable that additional system should be designed to swing the laser beam horizontally and vertically.

(iii) *Imaging and Measurement Subsystem* – to observe the magnified image of optical fibers on the monitor screen through high resolution CCD cameras Fiber splice loss can also be estimated by the processing the captured image.

(iv) *System Integration* – The personal computer interface may be developed to and control of laser parameters, fiber alignment and fiber image. The block diagram of a complete laser splicing system is shown in Figure 3-5.

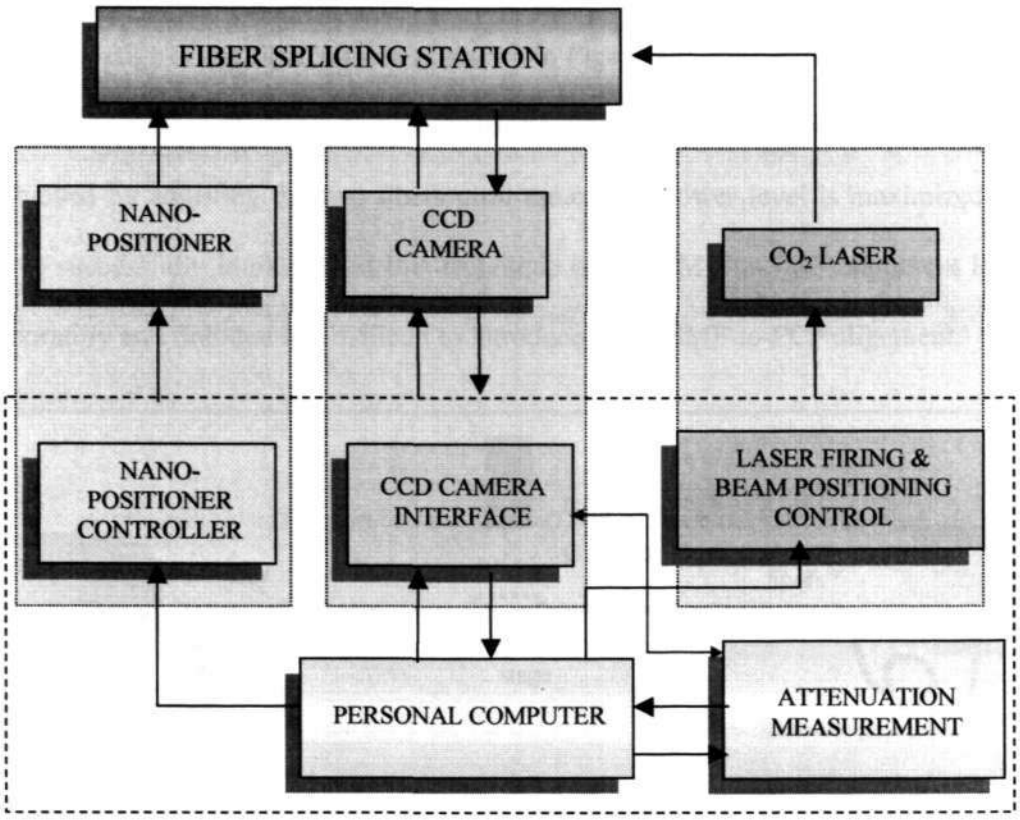

Figure 3-5 Functional block diagram of the laser splicing system

3.2.1 Fiber Alignment and Control

To achieve a good splice, the fibers must be aligned with high precision. Several alignment methods [123]and techniques have been reported in the literature and they are generally grouped into two main categories: active alignment and passive alignment methods.

In active alignment, a low power LED or Laser diode injects the light from one end of the fiber and the output is monitored at the other fiber end. This method known as

power monitoring method is illustrated in Figure 3-6. Alternatively, light injection and detection is performed by local monitoring of optical power from two points near the outer edge of the fiber surface as shown in Figure 3-7. This technique is known as local monitoring or macro-bending method [97, 98]. The optimum alignment is achieved by adjusting the two fibers until the output power level is maximized. We have successfully implemented this technique on the SMF-to-SMF alignment in our laboratory and find that it is difficult to introduce in the SMF-to-PCF alignment.

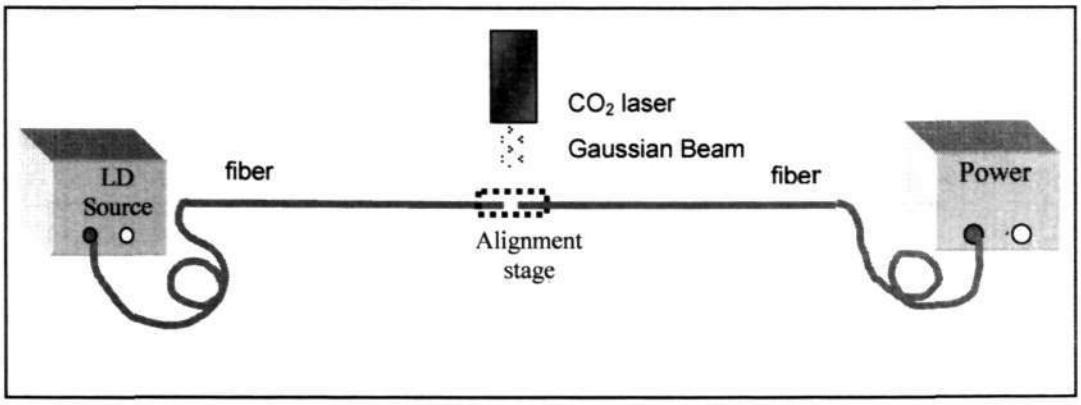

Figure 3-6 Power Monitor Method for fiber Alignment

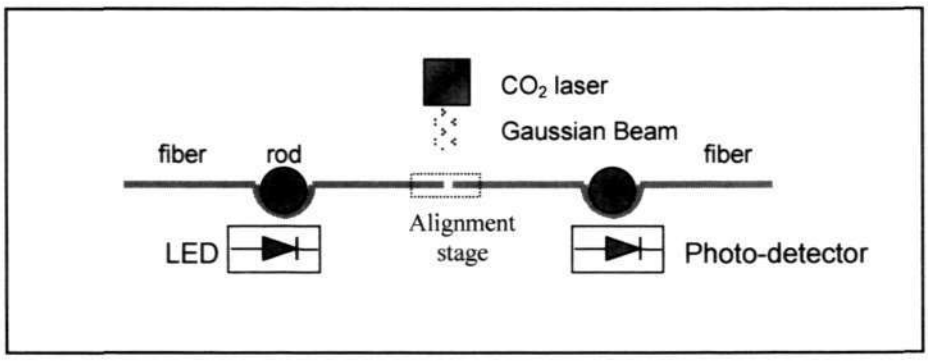

Figure 3-7 Marco-Bending Alignment Method

The passive alignment method has been employed in our laser splicing system. Two CCD cameras positioned at an angle of ≈45° with respect to each other are used for

monitoring of the 3D image of the fiber ends. This method performs physical alignment of the fibers by imaging the core or cladding reflective profiles [123]. In the core reflective profile method, the illuminating white light incident onto the fiber is reflected by the narrow core diameter of the single mode fiber and is seen as an enlarged core diameter within cladding. The cross-sectional images of the fibers are captured and analyzed on CCD cameras. By identifying the darker cladding image and brighter core image, it is useful for achieving core-to-core alignment for the single mode fibers. This technique is useful for the SMF-to-SMF alignment, but not for the PCF-to-SMF alignment because of the core of PCF is not easily identified under the camera view.

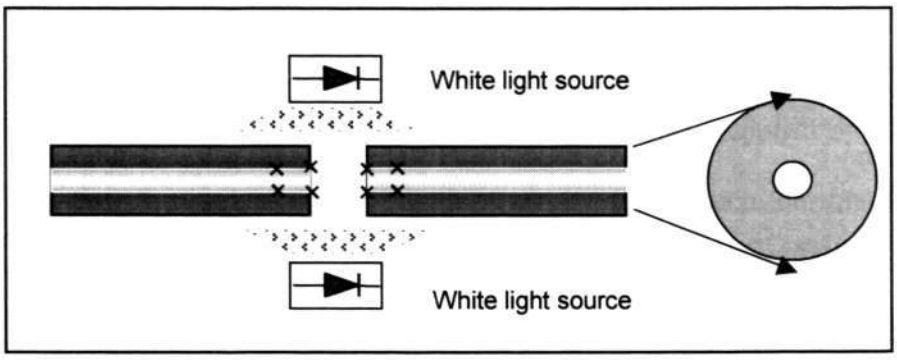

Figure 3-8 Core alignment by CCD camera, the core diameter is widened by light reflection at the core region

The profile alignment method has several advantages over the power monitoring and the local monitoring methods. Firstly, profile alignment does not need additional equipment such as laser sources or power meters for fiber link. Since its alignment is done at the fiber ends, it is not affected appreciably by fiber bending. Moreover, profile alignment method makes it possible to splice fibers at arbitrary splicing points simultaneously over the whole transmission line length at a cheaper cost. It is also

very convenient to align fibers of different diameters and also dissimilar fibers with different structural cross-sections.

3.2.2 CO_2 laser Beam Control Subsystem

CO_2 laser operating in continuous-wave (CW) mode produces relatively steady beam. It makes use of the method of RF excitation to maintain discharge stability, to control output power and modulation with ease, as well as to achieve convenient interfacing for systems automation. Also, its long operating life and with no frequent replacement of parts, it is very attractive and economical than electric arc system which uses electrodes requiring regular maintenance as mentioned previously. In our splicing system, *Series 48-1* CO_2 laser from *Synrad Corp* [125] is used. The Gaussian-profile beam waist at the output aperture of the laser before the goniometer is 6 mm, and its beam power is controlled by PC. The *palmScan* goniometer supplied by *SCANLAB*, has two precision galvanometer scanners and two deflection mirrors to ensure uniform laser power over a targeted area (Figure 3-9). The *palmScan* focuses the CO_2 laser to a beam size of ≅500μm diameter. As the power of the laser is approximately at 10 W, the laser power levels can be programmed to suit different processes in the laser splicing system such as fiber cleaning, cladding removal, fiber splicing and fiber annealing. The CO_2 laser has a very high efficiency compared to other common gas lasers [125]. Unlike the other lasers producing visible or near-IR light, the CO_2 laser operating at medium-IR wavelength at 10.6 μm is strongly absorbed by various types of glasses, plastics and water.

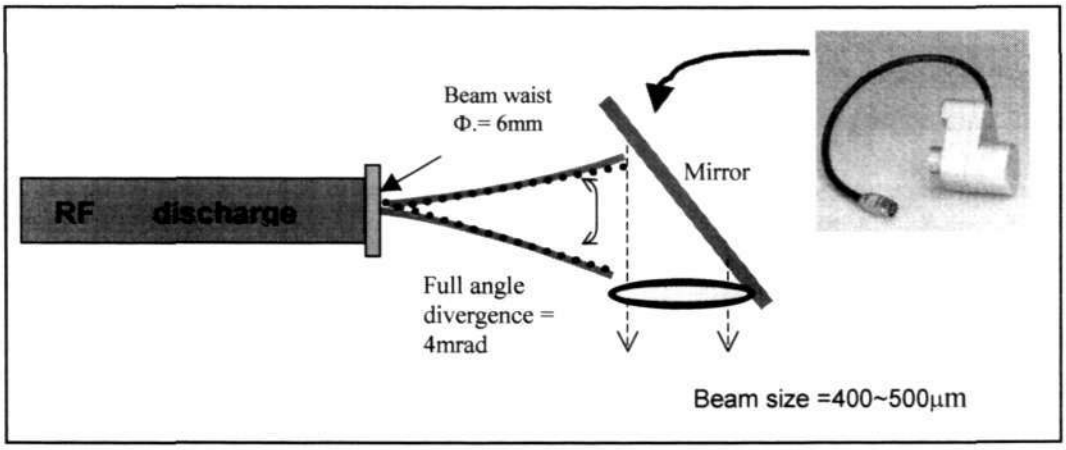

Figure 3-9 CO_2 laser redirected by the *palmScan* (picture at top right corner) to the fibers to be spliced

The level of laser power is digitized and controlled by the computer; the conversion table is shown in *Appendix A1*. The laser beam can be swung *horizontally for clearing condensation* of fiber ends and scanned *vertically for multi-fiber splicing*.

3.2.3 Imaging and Measurement Subsystem

Using image to analyze the position of fiber depends on the quality of camera and background lighting. It is preferable to have an enclosure for the system so as to shield it from the effects of ambient light. The 3D images of the two fiber ends (x-y plane and y-z plane) illuminated by white light sources, are captured by two cameras positioned at an angle of 45° between them. The cameras with the field of view of 0.7 mm are capable of achieving micron displacements and provide fiber images with a pixel resolution of ±0.5 μm. The fiber image captured by a CCD camera is digitized and an array of pixels (**PIC**ture **EL**ements) represents the digitized image. Many

image-processing methods are based on linear algebra using Fourier analysis or Discrete Convolution. Linear algebra is important in image processing as it can be used for compression, de-noising and edge detection on an image. The manipulation of visible image data is probably the predominant method of image processing. It can be used to produce visible image of purely numeric data enhanced in some manner to highlight some aspect of the data. Examples of this kind of image processing can be found in magnetic resonance based medical imaging equipment, sonar, radar, ultrasound equipment, heat-sensing equipment and fractals.

Image processing on real-time visible fiber images is generally used to align two fibers accurately. In most of the arc fusion splicing machines, core-to-core alignment has been used due to the high cladding eccentricity (than that of core) that existed in the past. However, with the improved manufacturing techniques, the current fibers have very low cladding eccentricity (typically less than 0.2 μm). To achieve high alignment accuracy, detection of the edges of the cladding of two fiber end-faces is adequate. Since, the reflective core image of PCF is difficult to visualize, the edge detection and image threshold are the best choices available for aligning the two fibers if the image processing technique is employed.

3.2.4 System Integration

The CPU is the master control of all the subsystems in our system. Visual C++ programming tools and three hardware interface cards are integrated to control the splicing parameters and automate the splicing process. The "PC-AHV 150" PCI plug-in card from *Piezomechanik Company* generates high output voltage directly to the piezo-actuator to control the xyz movement of one of the micro-alignment stages.

The xyz movement of the micro-alignment stage consists of manual coarse and fine (nano-meter) alignments. The automation for fiber-to-fiber alignment is obtained by three sets of high precision piezoelectric actuators, each actuator having a maximum stroke of 40μm. The piezoelectric actuator is controlled by voltage from the computer via the interface card of PC-AHV (model 150/3).

The laser power is controlled by a laser controller (CIO-DDA06), which has six-channels of analog output and 24 digital inputs/outputs and is installed on the ISA bus of the computer. *Matrox Imaging Library* has been used to detect the edge of the fiber and provides the necessary feedback to align the fibers with nanometer accuracy. The system performs necessary computations to provide an estimate of the splice loss.

The software has been developed to integrate all the subsystems and achieve optimum splice result under a user-friendly environment. It controls fiber-alignment positioners through piezo-controller and presets the power and duration of the CO_2 laser during the splicing process. Furthermore the laser splicing system displays real-time images by using two CCD cameras and controls image threshold levels by filtering noise and sharpening edges. The software displays dialog boxes such as "control power and duration of laser", "control fiber xyz alignment stage", "detect and measure misalignment of fibers and "measure and display splice-loss through image processing". Lastly the interactive program permits "Automatic" or "Manual" mode of operation.

A complete system set up is shown in Figure 3-10 and its system operation is described in the flow chart shown in Figure 3-11.

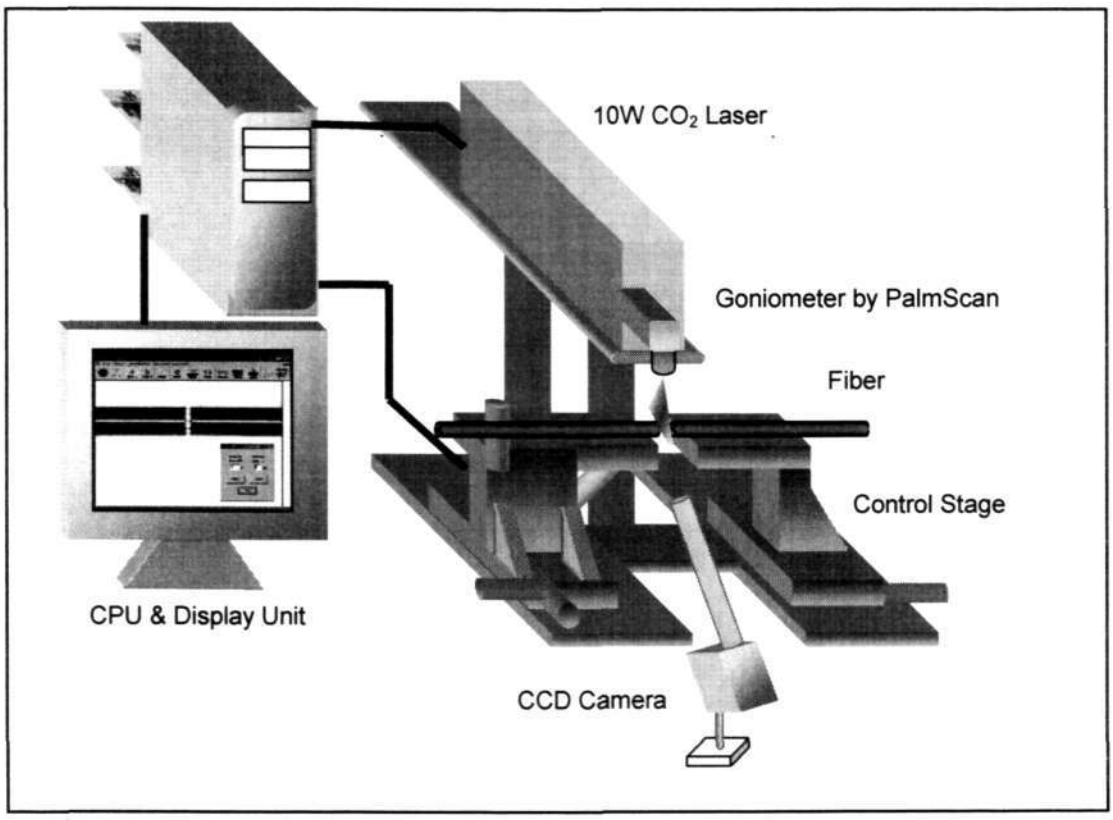

Figure 3-10 Complete Setup for Laser Splicing System

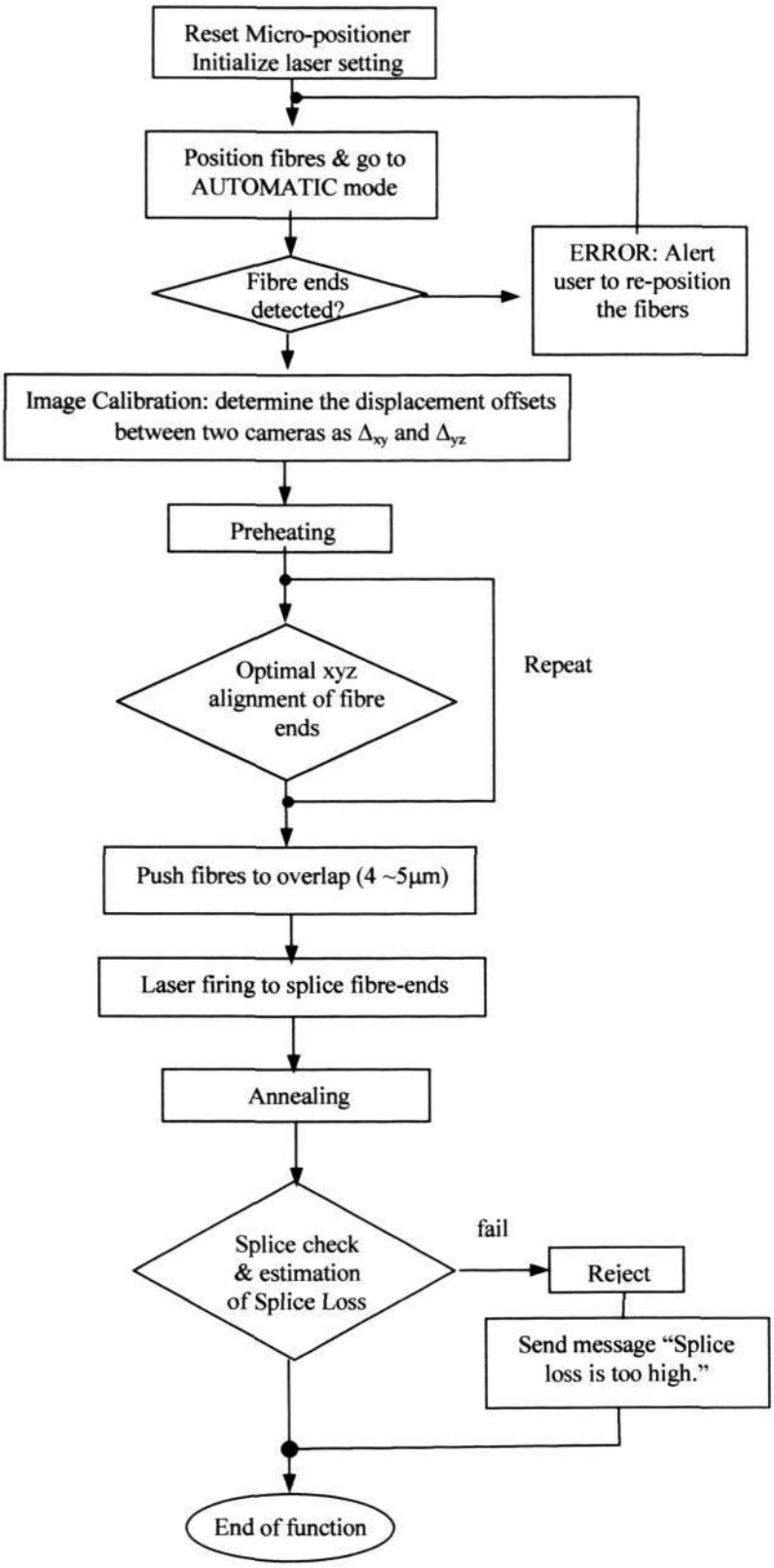

Figure 3-11 Flow chart for a complete splicing process.

3.3 Operational Parameters on Splicing of SMF-to-PCF

Photonic crystal fiber is an all-silica optical fiber with an array of longitudinal air holes around a solid central core. A hexagonal array of air holes with diameter (d_{hole}) and pitch (Λ) form low effective index cladding that makes the PCF to be visualized as a new form of single mode fiber. In the splicing of photonic crystal fiber to standard single mode fiber, the splice loss is affected both by parametric mismatch and by various misalignments similar to the conventional fibers. The parametric mismatch losses are due to mismatch of numerical apertures, core/clad diameters or refractive index profiles of the fibers to be joined. The misalignment losses are caused by the physical misalignment or macro bending of fibers. The micro-structural formed PCF is sensitive to laser power that makes splicing process very delicate. To minimize splice loss, three additional factors have been carefully considered in the system design: one is the structural loss caused by the deformation of PCF geometry (especially the hole-size and hole spacing); another is the scattering loss caused by the unevenness of the cleaved surfaces of the fibers. The last and most important factor is the contamination loss caused by condensation trapped inside the air holes.

Splicing of two fibers with different core diameters (between 2 μm to 9 μm) is a very complex process and any mismatch due to alignment; fusion power or other related components will result in high splice loss. Based on the assumption that mechanical constrains of the alignment stage and the tolerance effects of V-grooves to be negligible, a few operational parameters are discussed in the following section.

3.3.1 Laser Power and Control

Laser induced heating is not a normal heating process; the rapid rise of thermal energy over the fiber joint has improved the splicing quality. Higher laser power gives rise to fiber temperature and in general, solids expand when heated. If the initial volume is V_0, the increase in volume, ΔV, on the raising the temperature by ΔT at constant pressure may be expressed by $\Delta V=V_0\beta\Delta T$, where β is the coefficient of volume expansion. Thermal expansion of the crystal is due to the increase in the separation between the two atoms or ions with rise of temperature. As temperature increases, the amplitude of vibration of lattice atoms also increases. If the overlap stuffing applied to fiber to be spliced is sufficient, then the temperature rises to ~1500°C, the volume of silica will be 1.7mm^3 (coefficient of volume expansion = 1.2x10^{-6}°C^{-1}) larger than its original volume due to the excess of laser power as shown in Figure 3-12(a). If the laser power is slightly below the required power and the overlapped stuffing is insufficient, the two fiber ends are molten to join but a small neck at the joint is formed as shown in Figure 3-11(b).

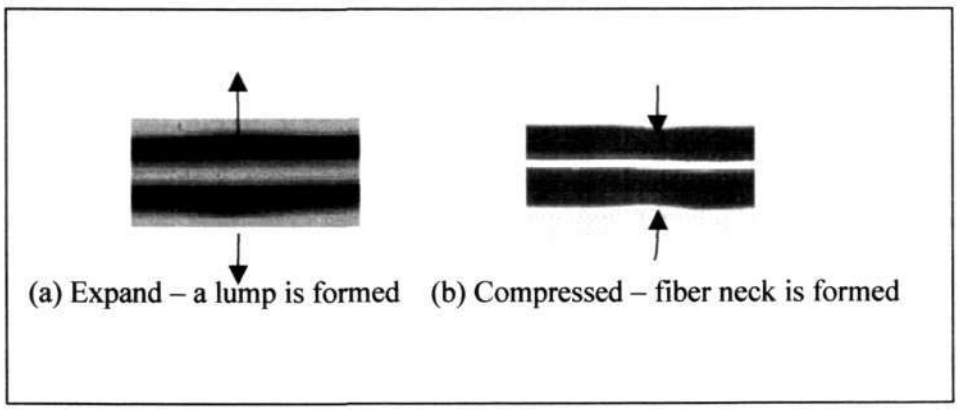

Figure 3-12 (a) Volume expansion when excess laser power is applied to the splice joint (b) Volume compression at slightly low laser power

The prevention of fiber slump, fiber neck or round fiber ends without joining, the appropriate selections of laser power and exposure time are very critical for achieving optimum fiber splice. In the splicing of PCF, the melting temperature is chosen to melt the fiber to the semi-liquid state is 1650°C

3.3.2 Mode Field Discrepancy

In general, higher losses are observed in the SMF-to-PCF splice as compared to SMF-to-SMF splice. One of the major contributors to the splice loss is the Mode Field Diameter (MFD) Mismatch. MFD describes the mode field (cross-section area of light) traveling down a fiber at a given wavelength. The splice loss incurred by the MFD mismatch [126] is estimated using the following relationship:

$$\textbf{Splice Loss} = 20\log\frac{1}{2}\left(\frac{\mathbf{MFD_1}}{\mathbf{MFD_2}}+\frac{\mathbf{MFD_2}}{\mathbf{MFD_1}}\right)\mathbf{dB} \qquad \text{Equation 3-1.}$$

The overlapped stuffing of the fibers, laser power and exposure time are factors that can affect the MFD and the splice loss.

3.3.3 Fiber End-face Overlapped Stroke and Laser Exposure Time

As pointed out previously, when the two fibers are to be spliced, a good control of fiber end-face stuffing stroke must be introduced to overcome the unevenness of the cleaved fiber end-faces. The requirement of overlapped stroke is determined based on the amount of laser power, the fiber material and cleaved surface of the fiber end-faces. Although SMF and PCF are made of silica material, the number of air holes for PCF can be one of the factors affecting the overlapped stroke. Based on our experience, overlapping is dependent to a large extent on the laser power. If the laser power is higher, overlapped value can be smaller vice versa. The overlapped stroke of

3-5μm has been used in our experiments to determine the splice loss for SMF-to-SMF and SMF-to-PCF splicing.

In conclusion, a complete laser splicing system has been developed to investigate and to achieve an optimum splice between SMF and PCF. The manual operation is convenient for us to explore and study all the possible parameters that may affect the quality of splice. Furthermore the system should enable the users to fabricate long period gratings [127] on various types of fibers, fiber tapers and other fiber based devices.

CHAPTER 4 STUDIES ON LOSSES IN PHOTONIC CRYSTAL FIBERS

This chapter presents some important results simulated for this project on high index photonic crystal fibers that may affect the splice losses for the fibers. The fiber types to be studied include large mode area PCF and non-linear PCF. A simulation program is used to determine the fiber-to-fiber misalignment losses and measurements have been performed to study the bending losses.

4.1 Introduction

Structurally, a high index PCF consists of a solid defect (core) surrounded by a ring of air holes; and the low index PCF has hollow defect (core) and rings of air hole as cladding as mentioned in Chapter 2. The high index core PCF [127] shares many common features with the conventional optical fibers, attributed to its operation based on the well-know mechanism of total internal reflection (TIR). The hollow structural defect in low index PCF allows transmission signal by using photonic band-gap mechanism.

An investigation on PCF is constrained due to the limited availability of PCF in the market or the test samples from the foreign institutions. At the time of our investigation on PCF, only high indexes PCFs were available, therefore we focused only on the large mode area PCF (LMA-PCF) and the non-linear PCF (NL-PCF). The cross-section of a high index PCF is illustrated in Fig. 4-1.

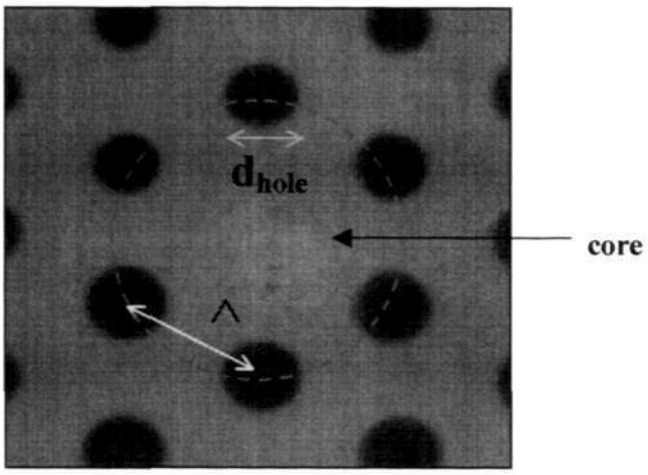

Figure 4-1 Hole-spacing or pitch = Λ and hole size = $\mathbf{d_{hole}}$ of PCF

The structure has air-holes of diameter ($\mathbf{d_{hole}}$). The pitch (Λ) and air filled fraction ($\mathbf{d_{hole}/\Lambda}$) of PCF exhibit a complete band-gap for certain value of propagation constant; any changes in the fabrication parameters affect the transmission characteristics. The core radius of PCF is generally chosen to be $\mathbf{0.62\Lambda}$ [3]. However, for different structures of PCF, different choices of equivalent core radius may be used, for example for the endlessly PCF a core radius of $\mathbf{0.45\Lambda}$ is used for single mode operation [17]. To date, there is no entirely satisfactory method for ascribing parameters to the equivalent fiber [10,12-20]. The group velocity dispersion (GVD) induced by the air holes at the fixed pitch is dependent on the transmission wavelength λ [129].

The single mode operation of PCF covers a wide range of wavelengths, and very much depends the effective refractive index [1,2,3]. Photonic crystal fibers are similar to single mode fibers: they are light- weight, flexible and not easy to handle if they are not well protected by insulated jackets or housing.

Similar to standard silica fibers, the splicing losses of photonic crystal fibers can be attributed to many factors such as fiber-to-fiber misalignments, bending losses, and condensation. Once fibers are spliced, the structural configuration of PCF may be affected causing change of its hole-size and pitch. Therefore a discussion is provided on the fiber properties those are likely to be affected due to the splicing. We are able to perform more detailed analyses on LMA-PCF than on NL-PCF due to the fact that the large mode area PCF (LMA-PCF) is much cheaper than non-linear PCF (NL-PCF). Also the LMA-PCF is more readily available and its core diameter is closer to that of SMF.

4.1.1 Properties of Photonic Crystal Fibers

In majority of our investigations, the high index PCF having a triangular configuration has been used. The operation of high-index triangular PCF in many respects resembles to that of standard step fiber as both these fibers achieve light confinement by *total internal reflection*. The triangular PCF, with an air-filling fraction less than 10%, has large frequency-bandwidth for wavelengths (λ) less than $\wedge$, that is meant $\mathbf{d_{hole}}/\Lambda$ is small.

In conventional optical fiber, the light propagates within the central core by total internal reflection. The core is doped, to give a higher refractive index than the surrounding glass cladding, and it is very narrow (diameter$\cong$ 5 μm or 9 μm), so that only the zero-order mode of signal is allowed to propagate within it. However, doping increases attenuation, narrow core limits the allowable optical power level. PCF consists of pure silica without any doped material and therefore has the benefit to

allow optical power over a wider spectrum. For example, the endlessly single mode holey fiber has remarkable wide wavelength range of operation from 400nm to 2000nm. Its operation can be explained by effective refractive index of the cladding (n_{eff}) and propagation constant (β) in the core. To maintain single mode operation, the PCF needs to have the effective V-parameter (V_{eff}) value near to 2.405. The V-parameter expressed below is sufficient to describe the characteristics of PCF:

$$V_{eff} = \frac{2\pi \Lambda}{\lambda}\sqrt{(n_{core}^2 - n_{eff}^2)} \qquad \text{Equation 4-1}$$

For PCF, it is assumed that the refractive index of the core (n_{core}) is independent of wavelength λ [1,2,3], and is always higher than the effective cladding mode index n_{eff} which is dependent on the wavelength. Therefore the light propagates within the core of the PCF by total internal reflective similar to a standard single mode fiber. For achieving $V_{eff} < 2.405$, it is possible by adjusting the d_{hole}/Λ ratio. In the laser splicing of PCF, the high melting temperature may reduce the size of air holes and even may result in complete collapse of air holes. The reduction in the size of air-hole diameter may eventually increase the effective area and result in smaller numerical aperture (**NA**) [130] as given by the following equation:

$$NA = \sin\theta = \left(1 + \frac{\pi A_{eff}}{\lambda^2}\right)^{-\frac{1}{2}} \qquad \text{Equation 4-2}$$

The effective area is an important measure of non-linearity of fiber. A high effective area requires high power density for non-linear effects to occur. The effective area is

related mode field diameter (**MFD**) through $A_{eff} = \pi(MFD/2)^2$. The effective non-linearity, γ [130.] is given by

$$\gamma = \frac{2\pi n_2}{\lambda A_{eff}} \qquad \text{Equation 4-3}$$

Where, n_2 is the nonlinear coefficient of the material, which approximately equal to $20.x10^{-20}$ m^2/W for pure silica [16], and λ is the free space optical wavelength. The equation shows that smaller effective area increases the non-linearity coefficient of fiber. Due to the high index difference between silica and air, it is possible to obtain a much tighter mode confinement in PCF over a wide wavelength range.

4.1.2 Types of Photonic Crystal Fibers Used

In this project, 4 types of PCF have been used but they are classified as (i) small air hole PCF (ii) large air hole PCF (iii) large mode area PCF and (iv) highly non-linear PCF (NL-PCF). Free samples of the first two PCFs were provided to us separately by two Foreign Research Institutes. The other two types have been acquired commercially.

Large mode area PCF (LMA-PCF) can provide high power delivery without exciting unwanted non-linear effects. This type of PCF consists of large mode areas for single-mode operation over a large wavelength range. One of the special characteristics of this type of fiber is its potential to be endlessly single-mode implying to the absence of higher-order modes regardless of the optical wavelength. In the case of conventional fibers, the effective area is limited by the fact that an increasing core size requires a correspondingly decreasing index step between the core and the

cladding in order to maintain single-mode operation. This imposes strict control of the index profile, which is difficult to realize with index-raising doping of the glass.

The cladding structure of LMA-PCF consists of a triangular array of air holes of diameter d_{hole} and pitch Λ corresponding to an air filling fraction f as [85]

$$f = \frac{\pi}{\left(2\sqrt{3}\right)}\left(\frac{d_{hole}}{\Lambda}\right)^2 \qquad \text{Equation 4-4}$$

In this type of LMA-PCF, the effective index n_{eff} of cladding in short- and long-wavelength limits is given as

$$\lim_{\lambda<<\Lambda} n_{eff} = n_{SiO_2} \qquad \text{Equation 4-5}$$

$$\lim_{\lambda>>\Lambda} n_{eff} = f n_{air} + (1-f) n_{Si} \equiv \bar{n} \qquad \text{Equation 4-6}$$

where n_{air} = refractive index in air, n_{Si} = refractive index of Si for PCF

For intermediate regime

$$n_{eff} \approx \bar{n} + (n_{Si} - \bar{n}) \cosh^{-2}\left(\frac{\alpha\lambda}{\Lambda}\right) \qquad \text{Equation 4-7}$$

Where $\alpha \cong 1$, and is only weakly dependent on d_{hole}/Λ. The last equation shows that the presence of air holes results in the effective cladding index n_{eff} to be strongly wavelength dependent.

The core diameter of the LMA-PCF employed in this project is 10.5 μm, which is slightly larger than the standard SMF with diameter=9μm. Splicing of these two types of fibers is expected to have mode-area mismatch loss between their joints.

Highly Non-linear Photonic Crystal Fiber (NL-PCF) has large air-hole and thin strut width between the air-holes; it has small mode area and exhibits non-linear characteristics. Generally, the range of possible values of the waveguide dispersion increases when the hole-size is large relative to their spacing. In the splicing of this kind of PCF to SMF, many constraints are encountered due to the large air holes, which are easily condensed. Further the ~1μm thick strut between holes may collapse once the fiber end is cleaved or the fibers are spliced. Another serious constraint in splicing of NL-PCF to SMF is its core diameter of 2.6μm, which is much smaller than the 9μm diameter of standard SMF.

The specifications of the single mode optical fiber and the commercially available photonic crystal fibers used for this project are summarized below:

(i) Specifications for Single Mode Fiber supplied by Yang

Cladding diameter: 125μm.

Average core diameter: 9μm

Effective area A_{eff}=66.5651 μm^2 at 1.55μm (simulated by R-soft software)

(ii) Specifications for LMA-PCF supplied by Crystal Fibre A/S

Cladding diameter: 126 ±3μm.

Average core diameter: 10.5±1.0μm

Average pitch to hole-size ratio (d/Λ): ~0.5

Far field width 2ω=10±2° (ω= Gaussian Beam Width)

Gaussian Mode field diameter ($2\lambda/\pi\sin(\omega)$) =11.32μm

Effective area A_{eff} =100.64μm^2 (calculated at 1.55μm)

Fiber loss < 0.0022dB/m

(iii) NL-PCF supplied by BlazedPhotonics (specifications measured at 810 nm)

Cladding diameter: 125μm.

Average core diameter: 2.6μm

N.A.= 0.43

Mode Field Diameter at 810nm=1.4μm

Effective area A_{eff}=3.9235 μm^2 (simulated at 1.55μm)

Fiber loss at 810nm: 0.041dB/m

In addition, we obtained two other types of PCF provided separately by two foreign research institutes. However, we have not included the specifications of these PCFs due to their poor design and inconsistent hole-size along the fiber length.

4.2 Misalignment Losses and Simulation Results

To estimate the possible splice losses, it is imperative to measure of coupled power between a PCF and SMF before splicing. As the transmitted signal propagates from SMF to PCF, the coupled power is influenced significantly due to differences of MFD, NA and material types.

Due to the complexity of the cladding structure of the PCFs, the traditional fiber theory for light propagation and confinement cannot be directly applied. A wide variety of numerical algorithms for modeling such as beam propagation, finite-difference time domain, localized mode expansion, multi-pole methods, and plane wave expansion (PWE) are currently available. Each method has advantages and disadvantages. For propagation problems, commercial tools based on beam propagation and finite-difference time-domain algorithms are adequate to analyze the coupling and loss effects for the PCF. In this report, we have used a optical software provided by R-Soft Beam propagation method (BPM) [15] and FDTD [132] to study light transmission in PCF.

For the Scalar BPM, the electromagnetic wave equation is to be recast into the Helmholtz equation using the scalar approximation for the optical field. As Eggleton et al. [133] states that BPM provides a simple method to determine the modal spectrum and model profiles for complex wave-guides in the field of micro-structured optical fibers or PCF.

Another theoretical study of guided modes in PCF is the Finite-Difference Time-Domain (FDTD) method which was proposed by Qui [134] and Town et al. [135] for the full wave analysis. The FDTD approach is based on a direct numerical solution of

the time-dependent Maxwell's curl equations. It has the ability to model light propagation, scattering, diffraction, reflection and polarization effects. It is also a powerful tool for performing analysis of sub-micron devices with very fine structural details and hence should be important for optimization of PCF characteristics. .

4.2.1 Misalignment Losses between SMF and PCF

Large mode area PCF (LMA-PCF) is different from non-linear PCF (NL-PCF), as it consists of very small air holes spreading over the fiber cross section. The core diameter of LMA-PCF (≈9.37μm) is closer to that of single mode fiber (SMF), whereas the NL-PCF has a core diameter of ≈2.6μm. Similarly the mode area discrepancy between SMF and LMA-PCF is smaller if compared to the NL-PCF. The simulation results illustrated in (Figures 4.3-4.5, 4-7-4.8) shows that the direct coupling losses between the SMF-to-LMA-PCF and SMF-to-NL-PCF are approximately 0.088 dB and 5.69 dB respectively if the misalignment losses are assumed to be negligible.

Splicing of SMF-to-SMF is much simple than splicing of SMF-to-PCF, as the slight misalignment between SMF-to-SMF is self regulated during the splicing process due to the presence of surface tension and cohesive forces between similar fibers. This internal self-alignment process does not apply fully to the dissimilar fiber splicing. PCF and SMF are both made of silica material. However, PCF consists of pure silica and SMF is made of different doped elements in the core and the cladding. The achievement of good splice for SMF-to-PCF, the fiber end faces must be well-cleaved and well alignment to prevent slipping of fiber ends when irradiated with laser.

In order to estimate the splice loss, the BMP and FDTD are used to analyze the PCF and its coupling loss with SMF.

The simulation of the coupling loss of LMA-PCF and SMF is performed by launching a 1550nm wavelength signal with Gaussian beam profile from the SMF to LMA-PCF is shown in the Figure 4-2. Figure 4-3 shows the normalized output after the signal propagates in PCF. Due to the software limitation, the simulation can be performed for a propagation distance of only 8000μm, and the coupling loss obtained for this distance is 0.98 (–0.088dB).

With a launched optical power ϕ from SMF, the fractional transmitted power, **T** [13], in the PCF at a distance **L** is given by:

$$T(\lambda,L)=\frac{\iint_{PCF}\phi(\lambda,x,y,L)\phi^{*}(\lambda,x,y,z=L)dxdy}{\iint_{SMF}\phi(\lambda,x,y,L)\phi^{*}(\lambda,x,y,z=L)dxdy} \qquad \text{Equation 4-8}$$

T (λ, L) is equivalent to the coupling loss and can be treated as the minimum splice loss for LMA-PCF to SMF splice. The **T (λ, L)** can be simplified as $LOSS_{splice(min)}$[130]

$$LOSS_{splice(min)} \cong \frac{4A_{eff1}A_{eff2}}{(A_{eff1}+A_{eff2})^{2}} \qquad \text{Equation 4-9}$$

Based on the specifications given above, the effective areas for SMF and LMA-PCF are $\mathbf{A_{SMF}}=66.565\mu m^2$ and $\mathbf{A_{LMA\text{-}PCF}}=100.64\mu m^2$ respectively. Using the above Equation 4-8, the minimum calculated splice loss of these two fibers is found to be 0.958 (–0.1842dB), which is close to the simulated coupling loss. This implies that if there is no significant deformation and misalignment between these two fibers, the minimum splice loss is about 0.1 to –0.18dB.

The simulation results (Fig 4.4) also show that for an axial misalignment of 1μm between the fibers, the total loss $\mathbf{LOSS_{axial}}$ between the fibers is expected to be about 0.546dB, and the angular misalignment of 3° introduces another additional loss of $\mathbf{LOSS_{angular}} \cong 0.004$dB to the fiber-joint. The net fiber loss due to axial/angular misalignments and MFD mismatch without any fiber deformation would be

$$\mathbf{LOSS_{net}} = \mathbf{LOSS_{splice(min)}} + \mathbf{LOSS_{axial}} + \mathbf{LOSS_{angular}} \qquad \text{Equation 4-10}$$

Therefore the net loss after splice would be 0.73dB without fiber deformation and the coupling loss is assumed to be –1.8dB.

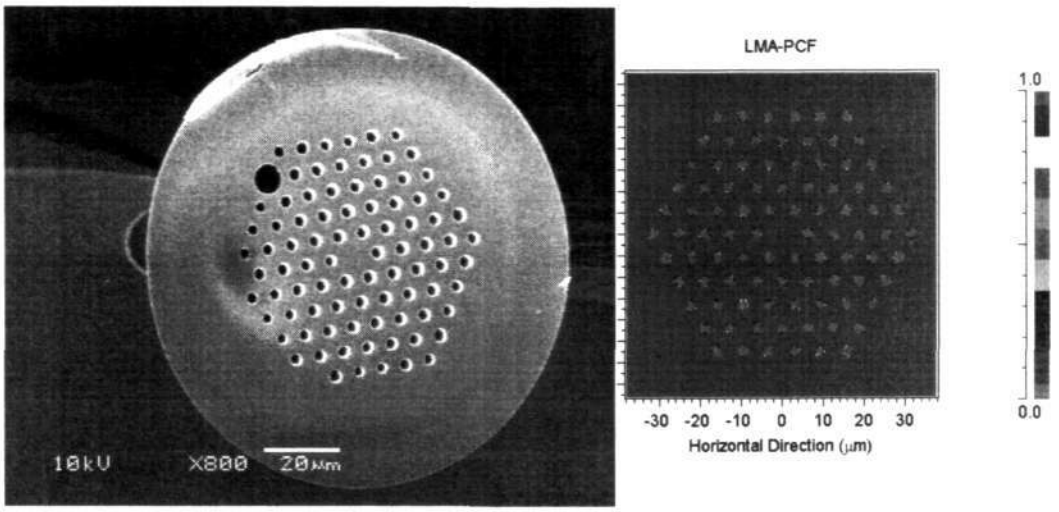

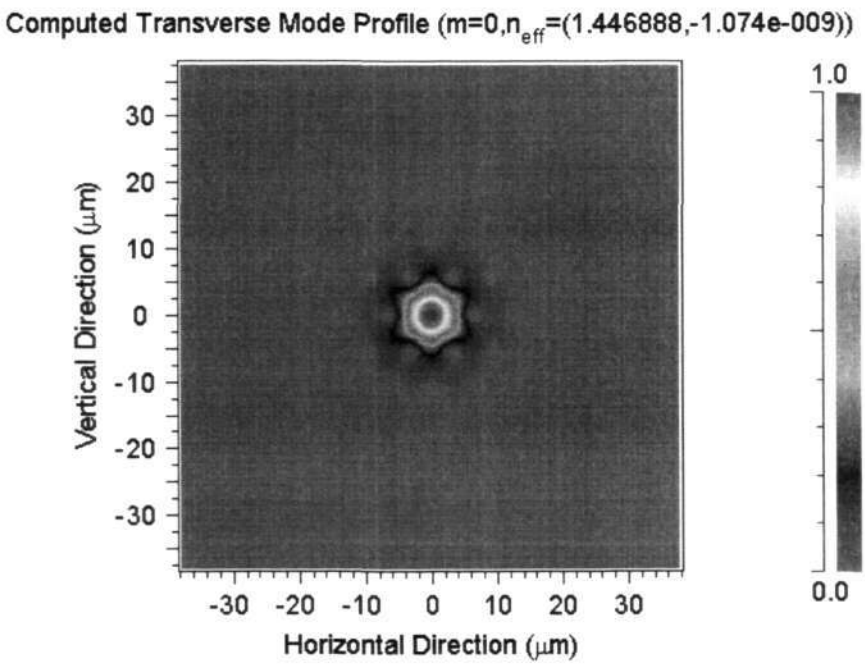

Figure 4-2 LMA-PCF with d=1µm, period= 3.2 µm, core diameter = 9.375µm

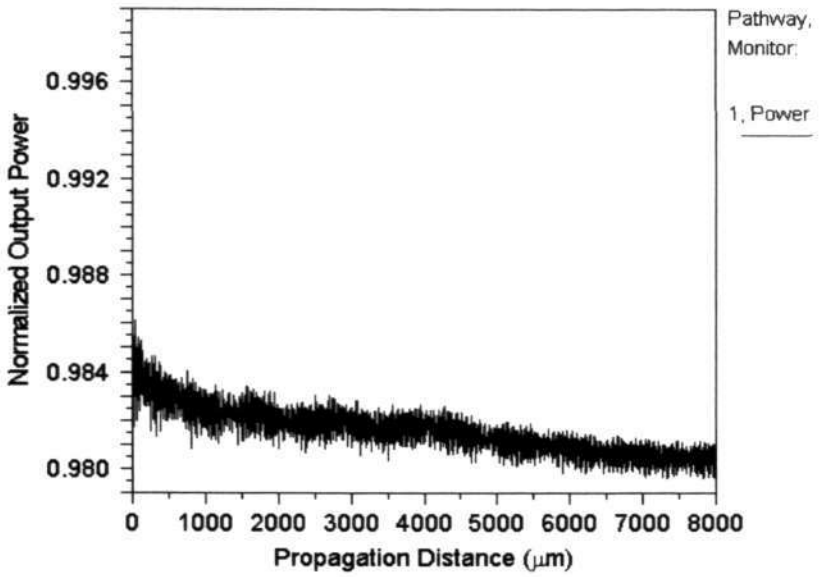

Figure 4-3 Direct Coupling Loss between SMF to LMA-PCF

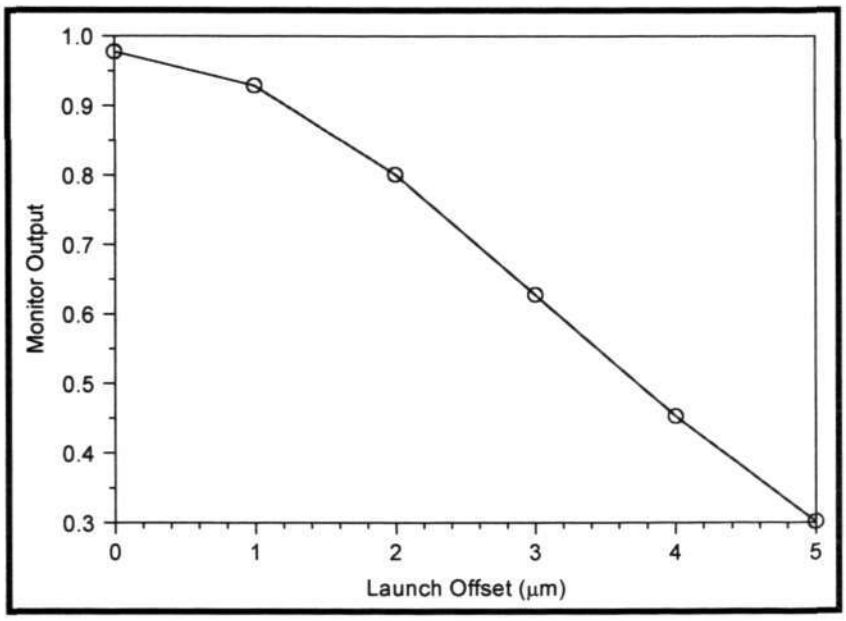

Figure 4-4 Axial Misalignment Loss between SMF and LMA-PCF

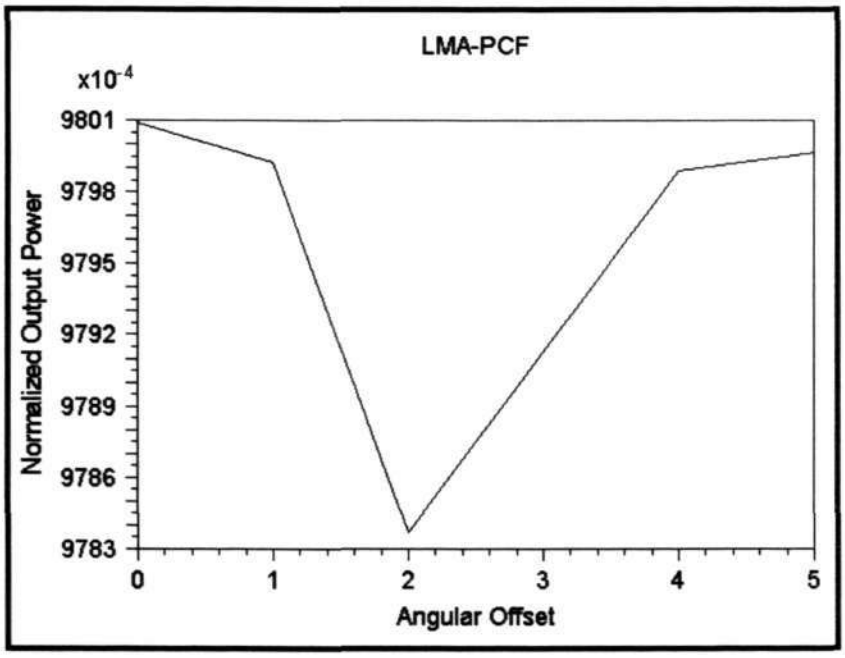

Figure 4-5 Tilt Misalignment Loss between SMF and LMA-PCF

The intensity profile for the fundamental mode of NL-PCF simulated by BPM method is shown on Figure 4-6, which is agreeable with the manufacturer. Direct coupling loss between 9-μm-diameter of SMF to a 2.6 μm-diameter of NL-PCF is significantly high due to large difference between the core sizes and dissimilar fibers. Based on the FDTD simulation, the coupling loss for launching 1550nm Gaussian beam from SMF to PCF at the propagation distance of 8000μm is 0.265 or -5.77dB. The calculated minimum splice loss based on Equation 4-9 is 0.2073 or -6.833dB. Therefore we can assume the minimum splice loss for SMF-to-NLPCL is $LOSS_{min}$ = –6.3 dB with no deformation in the fibers.

To overcome the problem of large core diameter mismatch in SMF and NL-PCF splicing, it is perhaps best to use of core-tapered fiber with constant cladding diameter as a buffer to reduce the effective area mismatch, but we are yet to find such a fiber.

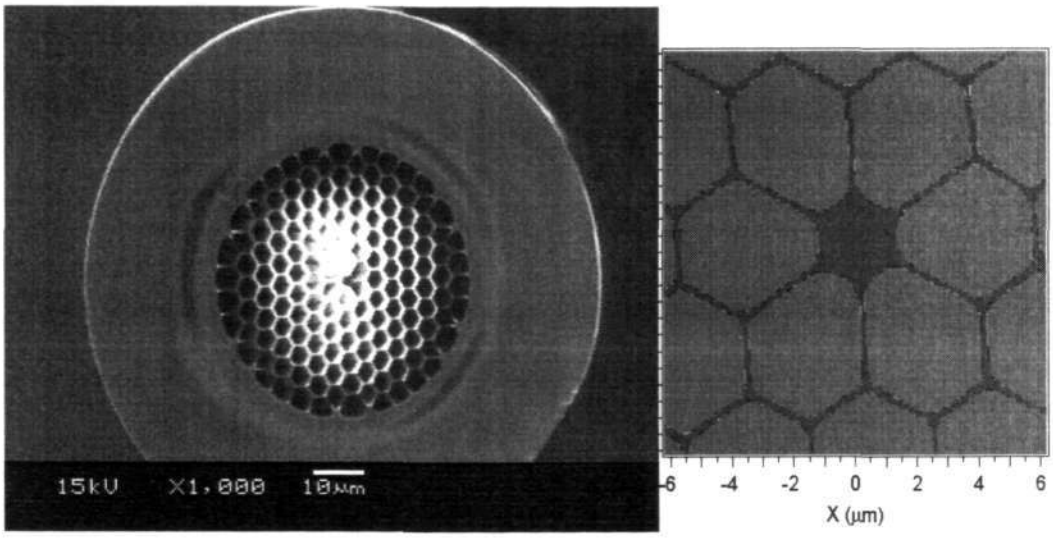

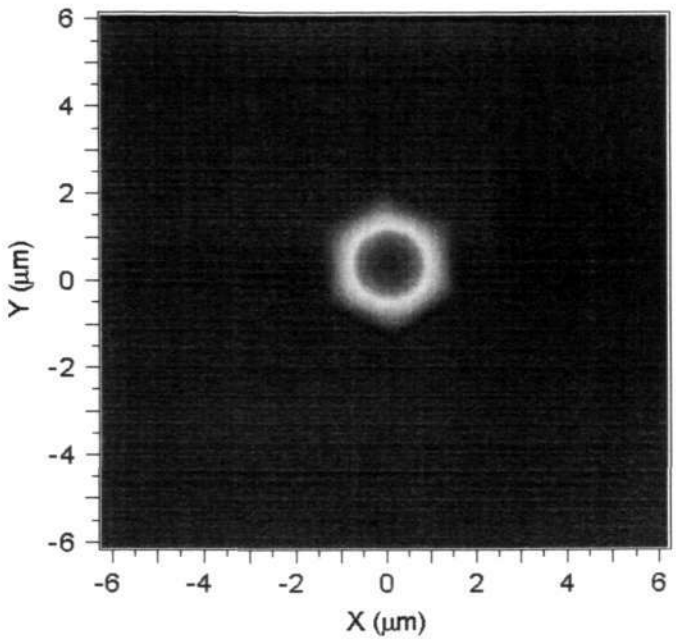

(b)

Figure 4-6 (a) Cross-section of NL-PCF with core diameter of 2.6µm. (b) Intensity distribution in the transversal plane

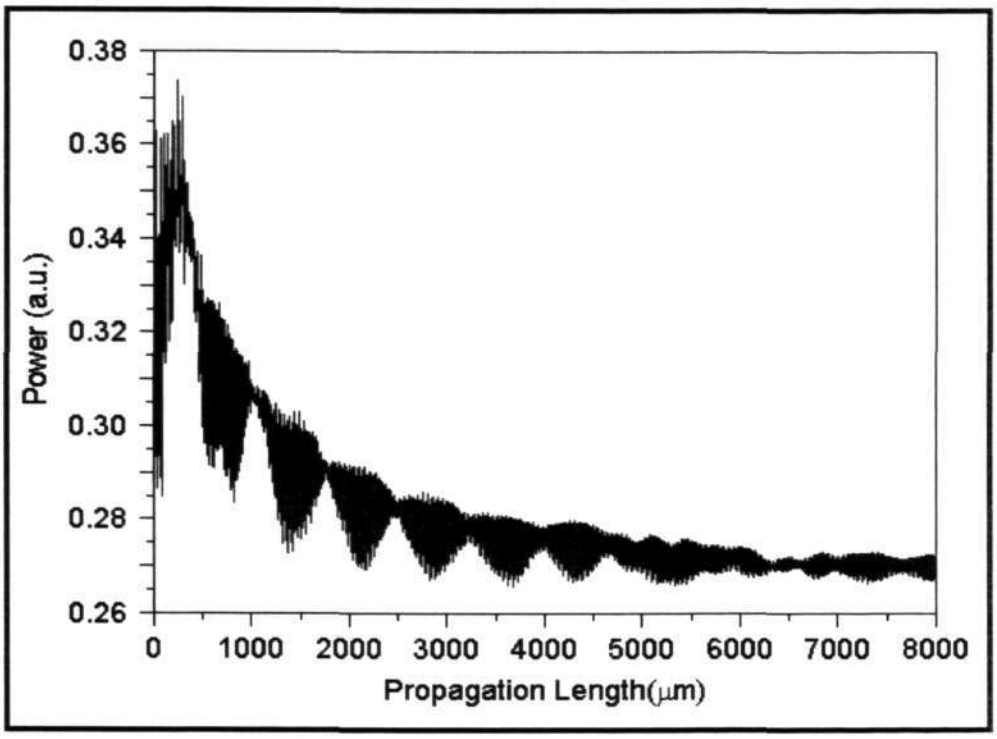

Figure 4-7 Direct Coupling Loss of SMF to NL-PCF

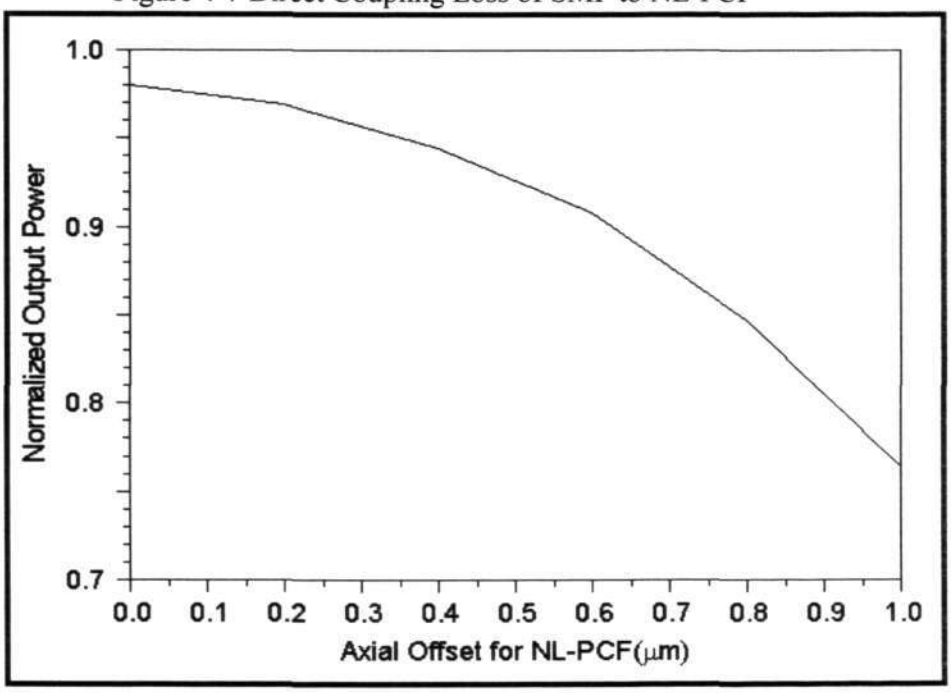

Figure 4-8 Axial Misalignment Loss between SMF and NL-PCF

4.3 Marco-bending losses in PCF

Due to the nature of optical fiber and the problems in handling of bare fibers, macro-bending loss in optical fiber becomes an important factor for practical applications. A common practical problem often encountered in the laboratory is the inaccurate measurement of laser power due to unintentional bends of the fiber. Another important factor is the critical bend radius, and it is essential to keep the radius of curvature of fiber bend above this critical value, otherwise excessive losses would be encountered. However, in order to quantitatively characterize the unique PCF bending properties including both a short-wavelength and a long-wavelength bend loss, we have adopted the following expression [178]:

$$\alpha = 4.343\left(\frac{\pi}{4\rho R_c}\right)^{\frac{1}{2}}\left[\frac{k_0\rho\sqrt{n_{si}^2-n_{cl}^2}}{VK_1(W)}\right]^2\left(\frac{1}{W}\right)^{\frac{3}{2}}\exp\left(-\frac{4R_cW^3\Delta}{3\rho V^2}\right) \quad \text{Equation 4-11}$$

where $\rho = 0.62\Lambda$ is the equivalent core radius, R_c is critical radius of curvature in the bend, V is the normalized frequency, W is the normalized decay parameter of the cladding, Δ is relative difference between the core and the effective cladding indices, K_1 is the modified Bessel function of first order, $k_0=2\pi/\lambda$ and λ is wavelength, n_{SiO_2} and n_{cl} are refractive indices of pure silica and PCF cladding respectively.

4.3.1 Experimental Studies on PCF Marco-bending

In our experiment, a 3m long large mode area PCF has been spliced to single mode fiber patch cords. The PCF is coiled on wheels with different bend radius values; the bending loss is measured by connecting the patch cords to a white light source

(*ANDO AQ-4303B*) and analyzed by an optical spectrum analyzer (*Agilent 86142B*). at wavelengths of 1300 nm and 1550 nm respectively.

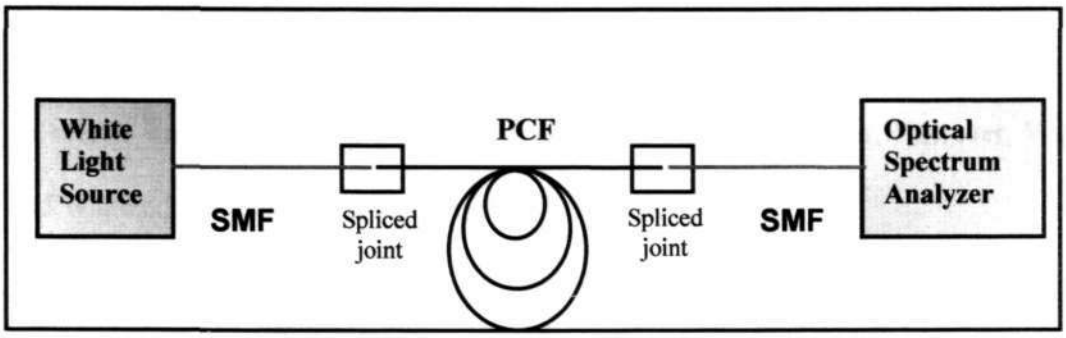

Figure 4-9 Experimental setup for Marco-bending measurement

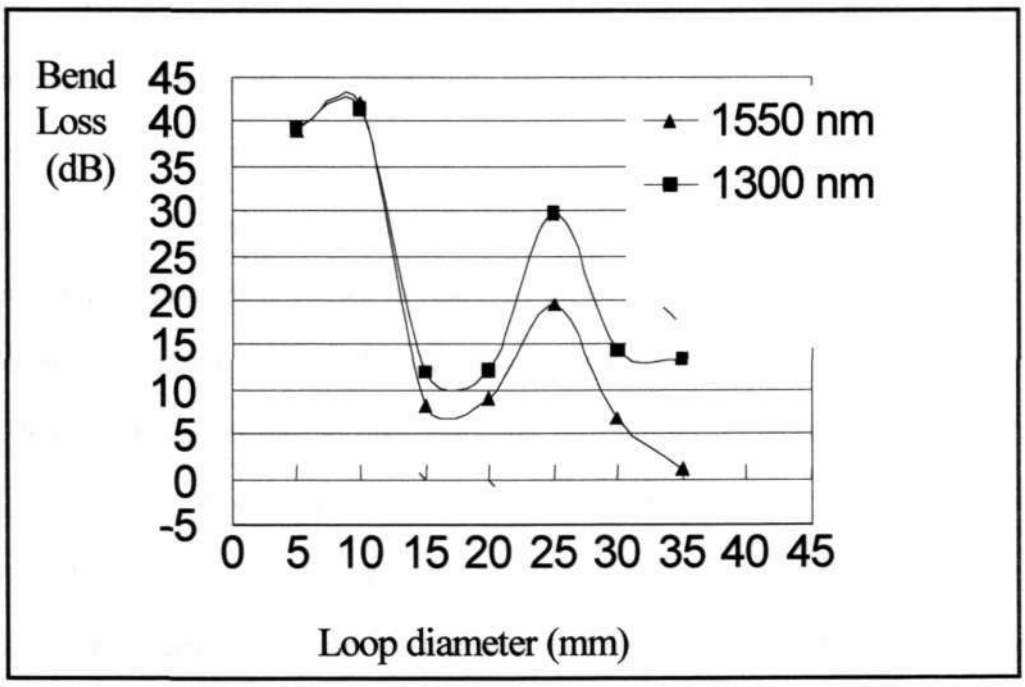

Figure 4-10 Marco-bending losses at λ=1300nm and λ= 1550 nm

With smaller N.A., the fiber is more susceptible to bending loss. Figure 4-10 shows that the longer wavelength permits higher bending tolerance as its critical bending radius. To obtain low bend loss, the radius of curvature of a bend **R** must be much higher than the critical bending radius as $\mathbf{R_c}$.

At shorter wavelength, $\mathbf{R_c}$ and λ are independent of the core diameter. However, V_{eff} and W are constant in the photonic crystal fiber, so R_c varies as

$$\mathbf{R_c} \infty \frac{\Lambda^3}{\lambda^2} \qquad \text{Equation 4-12}$$

4.4 OH^- ion Loss in PCF

The water contamination in silica fiber would result in attenuation of signal transmission due to OH^- ion absorption. The peak OH^- absorption is at ~1380nm in the transmission window of 1300 - 1550nm and its loss is about 0.6 to 6dB/km. As PCF consists of tiny air holes, moisture is easily trapped inside the fiber. The following experiment is carried to study the loss in PCF caused by condensation. In this experiment, the cleaved fibers are aligned and placed in close proximity. A wet cotton bud is tapped on the fiber ends and then the measurement is taken by the Agilent Optical Spectrum Analyzer. It is observed that the significant signal attenuation occurs across the transmission window of 1150 to 1700nm. However, this condensation can be reduced by exposing the fiber with ≅1W CO_2 laser before splicing. A 6dB improvement of signal strength is achieved without causing any deformation to the PCF and SMF as shown in Figure 6-9. . If PCF is seriously condensed, a complete removal of trapped liquid is very difficult. Hence, a careful preparation of fiber end-faces prior to splicing is very important.

CHAPTER 5 MODELING OF LASER-FIBER INTERACTION

In this chapter, the laser induced thermal effect for splicing of single mode fiber and photonic crystal fiber is discussed. The investigations on laser-induced optical breakdown due to laser interaction process between silica layer and air hole layer in the photonic crystal fibers are also presented. Some interesting phenomena caused by laser interaction in the silica layers are illustrated.

5.1 Laser Interactions with Photonic Crystal Fibers

Laser splicing of multi-mode silica fibers using CO_2 laser began in mid-70s, however, an analytical model of thermal condition in fiber splicing based on laser point source has been described in 1977 by Egashira and Kobayashi [102,103] as outlined in Chapter 2. Also, in the following years some researchers developed an improved model assuming laser beam as a continuous Gaussian laser source [105, 136] These models are useful for analyzing thermal distribution in the conventional fiber as well as to optimize the laser splicing parameters such as laser power and laser exposure time. Factors that are likely to affect the splice characteristics include the laser power, the beam size, the laser exposure time and the positioning of the laser beam, fiber overlap, cleanliness of fiber ends, cleaved angle and types of spliced fiber. Based on our earlier experiments for splicing of standard single mode fibers, it is possible to achieve a splice loss $\leq$ 0.1 dB by irradiating the fibers for 4 seconds with a 3W CO_2 laser having a beam width of $\cong$500μm. Also a significant reduction of exposure times is obtained if the laser power is increased (e.g. $\cong$4.4W). Splicing of standard optical fibers is much simpler than splicing of a photonic crystal fiber to a single mode fiber. Joining two different types of fibers together is indeed a very challenging task as the

fibers may have different melting temperatures, different fiber diameters etc. We consider the major stumbling block for splicing of PCF is the difficulty to maintain minimum deformation of air holes in PCF. Laser interaction in photonic crystal fibers (PCF) is a complicated process if the air holes contain some form of condensation. This thesis includes the work on the development of a modified 1-Dimensional heat transfer model to determine the optimum laser parameters for splicing of SMF to PCF. Additional, the 3D thermal transfer model has also been developed to analyze the heat distribution over the cross-section of fibers. Another model has been introduced to study the electron density in silica and condensate in the PCF caused by absorption of laser. The mechanisms of laser absorption in PCF may be caused due to phonon absorption or inverse Bremsstruhlung absorption or combination of both phenomena if condensation occurs. A PCF with a small hole-size and large silica strut-width (or $d_{hole}/\Lambda < 0.5$) is easier to splice than those with thin strut-width and large air hole-size. If the intensity of laser power exceeds slightly above the melting threshold, the walls of the silica capillaries may easily collapse for a strut-width of fraction of micrometer.

Condensation problem in PCF is difficult to avoid, especially during the process of fiber splicing. Condensation in the air holes decreases the PCF melting threshold and complicates the laser splicing process. Although extensive studies have been reported on the interaction of high intensity laser with liquid, including removal of water from microcircuit and micro-machines [75], contamination removal [137], laser-induced desorption of thin films [138,139], ophthalmic microsurgery [140], angioplasty [141] and laser induced gall-stone fragmentation [142]. *Perhaps, this thesis is the first to report the investigation on the laser interaction with PCF with or without condensation.*

The absorbed laser energy by the material may not necessarily result in direct heating of the material, in many cases; it may result in generation of high kinetic energy free electrons and subsequent creation of plasma. This is different from phonon absorption; where phonons interact with photons under resonant like conditions to increase the temperature of the material. Laser power at different levels affects the electron density over the targeted region. In the state of plasma, the free electrons generated by avalanche ionization reaches a high enough density to cause irreversible material breakdown and ablation. Once the electrons transfer energy to the ions and the lattice, an increase in the material temperature is observed. The amount of energy transfer or rate of heating is dependent on the intensity of laser, pulse duration and the electron flux. If the electron density at the focused area is higher than the critical value (10^{18} electrons/cm^3), the plasma may shield the CO_2 laser beam. In electric arc fusion of silica fibers, which is different from laser fusion, the thermal energy is directly converted from the electrical energy and is not dependent on the inverse Bremsstrahlung effect. High temperature melting normally causes vaporization of material and volume expansion as observed in electric arc fusion and reported on chapter 6. The laser fusion results in volume expansion or compression in optical fibers that is dependent on the laser power and exposure time applied to PCF.

The laser interaction with PCF is likely to occur at three layers: (i) *Atmospheric layer surrounding the fibers*: Laser passing through the atmospheric gases before being incident on the silica surface has limited chance to ionize the air molecules, therefore we assume that no laser excitation would occur in the atmospheric medium. (ii) *Silica layer in PCF*: Since CO_2 laser is transparent to atmospheric layer; it is very likely that laser would be absorbed by the silica material of the PCF. Phonon absorption dominates at low input power. In the event that the silica fiber is contaminated, the

increase in laser intensity may cause partial ionization and inverse Bremsstrahlung absorption in the silica layer. (iii) *Air-hole layer in PCF*: If the air-hole layer is filled with gas molecules, laser excitation may not occur. Air-hole layer may impede the heat conduction but it has not been observed during the laser fusion process of PCF. If air-hole layer is condensed, the laser interaction with the trapped liquid or with the condensed silica capillaries becomes unstable at high laser power levels.

For average CO_2 laser power levels of 3.1W and 4.4W that have been employed in our experiments, the power intensity profiles are depicted in Figure 5.2(a) and Figure 5.2(b) respectively.

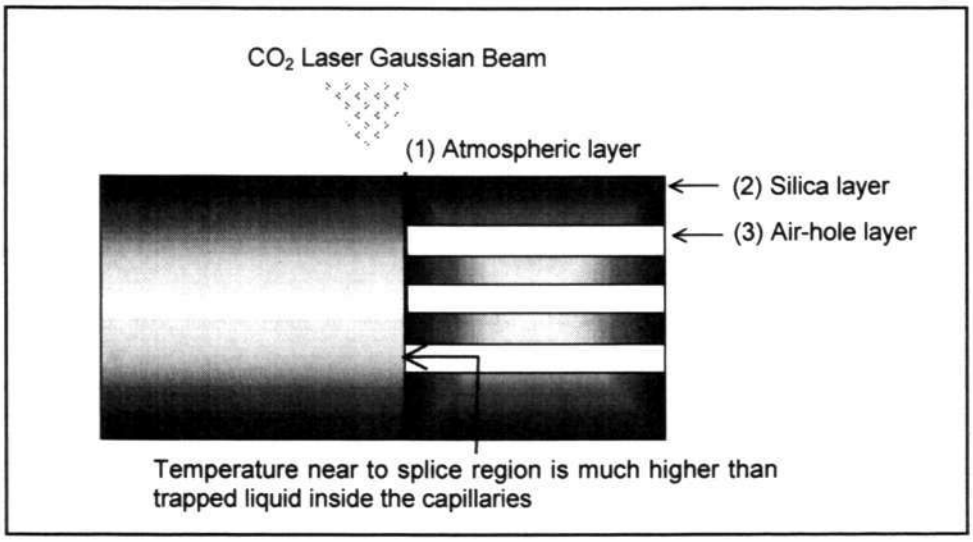

Figure 5-1 Laser beam positioned more towards the single mode fiber than the PCF during splicing. Three laser interaction layers are also shown.

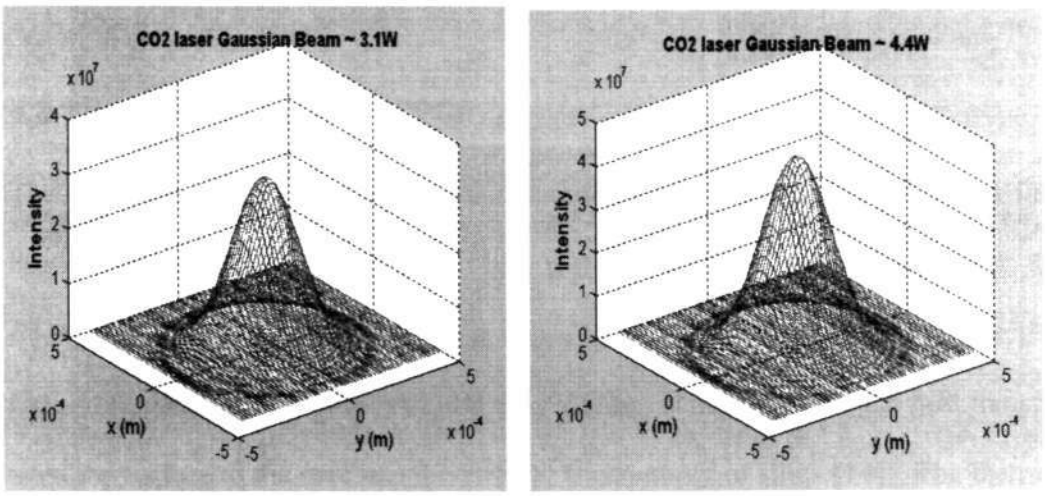

Figure 5-2 Laser Intensity Profiles for CO_2 laser sources with average power levels of (a) 3.1W (b) 4.4W

5.2 Thermal Energy Transfer in Optical Fibers

Splicing can be performed using flame, electric-arc or laser source. Using flame to splice optical fibers is not a practical solution; electric arc and laser splicing techniques are the better candidates. In the electric arc heating process, the electric arc generated by the electrodes is absorbed by the silica material as well as by it's surrounding. This causes temperature rise not only at the fiber joint but also that of the surrounding region. The thermal energy is then gradually transferred towards the core. The mechanism by which a CO_2 laser transfers heat to the fiber is very much different. The heating is highly localized and is caused by resonance in the lattice as well as due to the inverse Bremsstruhlung process.

5.2.1 Electric-Arc Heating in PCF

The arc generated by electrodes in the electric arc fusion-splicing machine at first heats up the surfaces of the optical fibers and then the heat propagates towards the fiber cores. The temperature rise in the single mode silica fiber, with slight refractive index difference between the core and the cladding, is dependent on the heat transfer from the surface to the core and the thermal conductivity of silica [144]. The thermal conductivity of silica K_{Silica}, at temperature 1300°C is about 7.8279 $Wm^{-1} K^{-1}$ and is given as

$$K_{Silica} = 0.78 - 0.054 \exp\left(\frac{T+379}{354}\right) + 0.165 \exp\left(\frac{T+379}{405}\right) \quad \text{Equation 5-1}$$

In the electric arc fusion, as the heat propagates in PCF, the air-filled capillary tends to slow down the heat transfer rate. The thermal conductivity for air [145], K_{air}, is about 0.0862 at 1300°C (which is about 91 times lower than that of silica) is given by the following equation

$$K_{air} = 3.3.84 \times 10^{-3} + 7.66 \times 10^{-5} T - 1.54 \times 10^{-8} T^2 \qquad \text{Equation 5-2}$$

Figure 5-3 depicts the above thermal conductivity relationships for silica and air respectively.

The thermal conductivity of the PCF would be lower if the air holes are large, as the air-holes slow down the heat propagation. As a result the temperature inside the core would be lower and hence the electric arc fusion technique is not well suited for splicing of PCF to SMF. Furthermore, the thermal expansion of the silica layer is much lower than that of the air; this may cause relative volume increase of air capillaries.

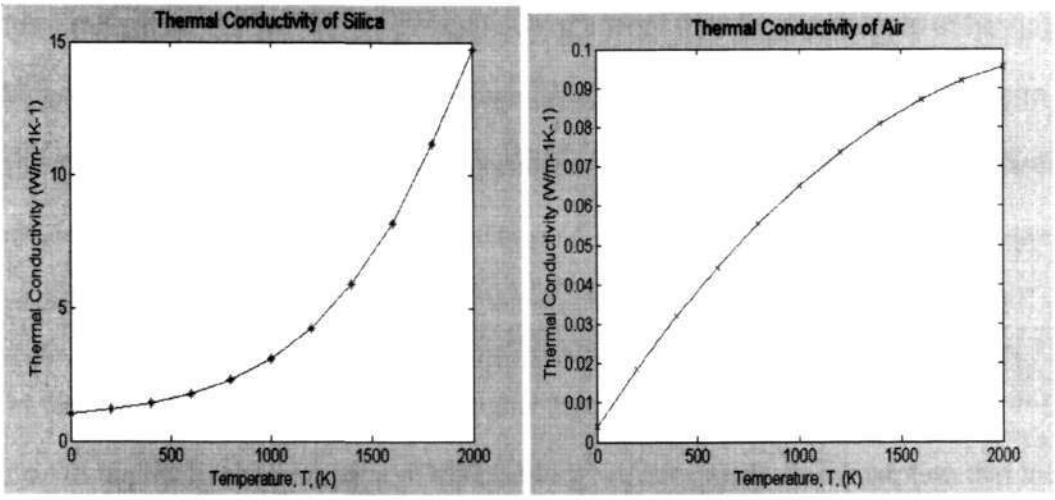

Figure 5-3 (a) Thermal conductivity for silica (b) Thermal conductivity in air

However, the laser induced thermal energy is different from the electric heat mechanism. The photons from the CO_2 laser are absorbed by the fiber to cause thermal excitation of the silica molecules. The heating induced by laser is very much faster than the electric arc fusion; therefore the rise of temperature over the cross-section of fibers should be more rapid than the conventional heating method.

5.2.2 Laser-Induced Thermal Energy and Temperature Distribution

The photon energy of 0.112eV of CO_2 laser is not sufficient to cause direct ionization in the silica material, which has a band-gap of ≅12.6eV. However, photons-phonon interaction in the above case will generate heat as well as free electrons. Also, the free electrons absorb laser energy that may increase the number of electrons due to avalanche ionization. Once the electron density reaches to a value $\cong 10^{18}/cm^3$, irreversible material breakdown and ablation may begin. These electrons absorb laser energy and the electron collisions will increase the temperature of the material. At the same time, the electrons *transfer* energy to the lattice that will further increase the temperature of material. The magnitude of energy transfer and the rate of heating induced by laser depend on the laser power level, laser exposure time and the laser-to-fiber coupling efficiency. In our experiment, the optimum laser power and laser exposure time are investigated for melting of PCF and SMF into semi-liquid state without vaporization.

In the SMF, the Ge-doped core has higher laser absorption than the cladding [146]. Due to the relatively large area of the cladding, we have made an assumption that the laser absorption in the core and cladding to be the same. Hence, the one-dimensional model for heat distribution in the cladding is sufficient to analyze the temperature distribution in the fiber as shown in Figure 5-5. Assuming the absorption of CO_2 laser

in the atmosphere and un-contaminated air holes to be negligible, the requirement of estimated power for melting of PCF can be based on the net volume of silica without air holes. Hence, the effective silica diameter of PCF (d_{epcf}) can be expressed as:

$$d_{epcf} = 2\sqrt{\frac{1}{\pi}\left[\frac{\pi d_{pcf}^{\,2}}{4} - \sum_{0}^{n} n_{hole}\left(A_{hole}\right)\right]} \qquad \text{Equation 5-3}$$

Where, n_{hole} = number of air holes, A_{hole} = cross-section area of air hole and. d_{pcf}= PCF diameter

The propagation of optical waves can be described by three separate phenomena including transmission, reflection and diffraction. In the geometrical optics, the propagating optical wave front is represented as the propagation of rays as shown in Figure 5-4. This ignores the effect of diffraction. In the Snell's Law, the incident light traveling to a planar interface obeys the following relationship:

$$\frac{n_i}{n_r} = \frac{\sin\theta_i}{\sin\theta_r} \qquad \text{Equation 5-4}$$

where, n_i = refractive index of material at the incident ray, θ_i = angle of incident

n_r= refractive index of material at the refracted ray, θ_r = angle of refracted

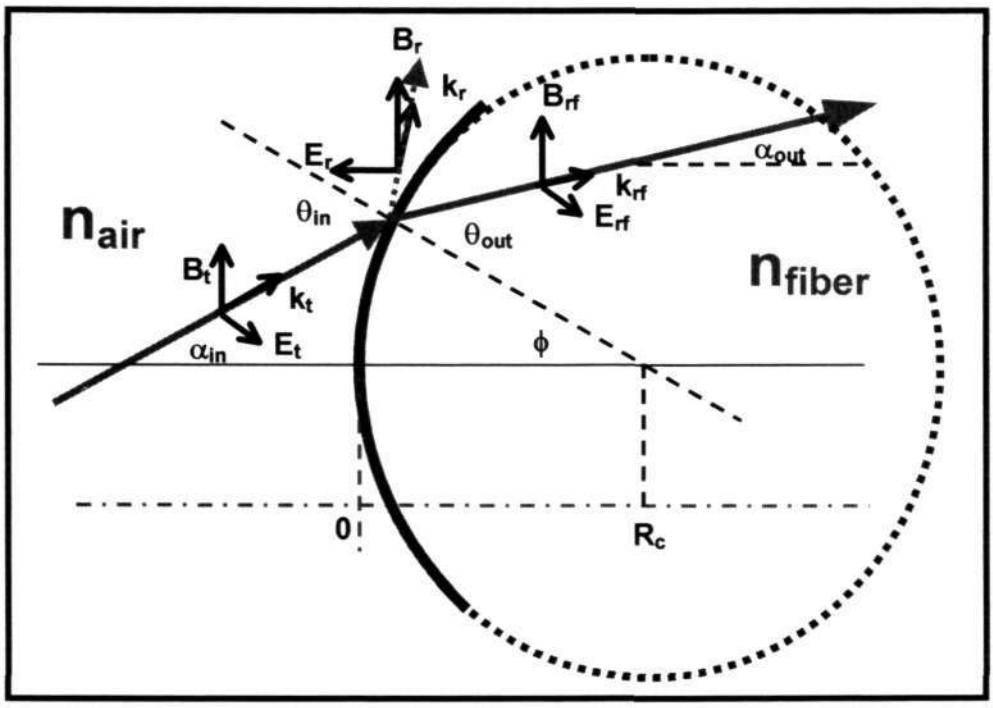

Figure 5-4 Refraction at the interface between atmosphere and fiber

The incident ray making an anlge α_{in} with respect to the horizontal axis undergoes refraction at the surface and the refracted ray emerges at an angle of α_{out}. It can be seen that

$$\alpha_{in} = \theta_{in} - \phi, \qquad \alpha_{out} = \theta_{out} - \phi$$

For air n_{air} =1, hence Equation 5-4 can be re-written as

$$\sin\theta_{in} = \frac{\sin\theta_{out}}{n_{fiber}} \qquad \text{Equation 5-5}$$

In general, the reflectivity is defined as:

$$R = \frac{E_r}{E_t} \qquad \text{Equation 5-6}$$

For TE polarized wave propagating through a fiber, the reflectivity becomes

$$R_{TE} = \frac{E_r}{E_t} = \frac{\cos\alpha_{in} - n\cos\alpha_{out}}{\cos\alpha_{in} + n\cos\alpha_{out}} = -\frac{\sin(\alpha_{in} - \alpha_{out})}{\sin(\alpha_{in} + \alpha_{out})} \qquad \text{Equation 5-7}$$

For TM polarized wave propagating through a fiber, the reflectivity becomes

$$R_{TM} = \frac{E_r}{E_t} = \frac{n\cos\alpha_{in} - \cos\alpha_{out}}{n\cos\alpha_{in} + \cos\alpha_{out}} = -\frac{\tan(\alpha_{in} - \alpha_{out})}{\tan(\alpha_{in} + \alpha_{out})} \qquad \text{Equation 5-8}$$

Combining of the above Equations (5-5 to 5-8), represents a ray that enters at various angles between ±90°. The average Reflectivity (**R**) on the cylindrical fiber surface determined by TE wave and TM wave can be integrated as:

$$R = \frac{1}{\pi}\int_0^{\pi/2} \frac{\sin^2(\alpha_{in} - \sin(\sin\alpha_{in}/n_{fiber}))}{\sin^2(\alpha_{in} + \sin(\sin\alpha_{in}/n_{fiber}))} + \frac{\tan^2(\alpha_{in} - \sin(\sin\alpha_{in}/n_{fiber}))}{\tan^2(\alpha_{in} + \sin(\sin\alpha_{in}/n_{fiber}))} d\alpha_{in}$$

Equation 5-9

Reflectivity **R** is one of the important parameters for describing the temperature distribution over the optical fiber.

For a Gaussian CO_2 laser beam impinging on the optical fiber as illustrated in Figure 5-5, the temperature distribution in the fiber would depend on the laser power P_{laser}, laser beam offset δ with respect to the fiber axis, the beam position z_{offset} relative to fiber joint, laser beam-diameter $2r_{beam}$ and diameter of fiber. Since the difference between the core and cladding refractive indices is very small, we can assume that the

fiber to be made up of single refractive index of silica material. The required laser power to bring the PCF to semi-liquid state would be dependent on the net quantity of silica, hence the effective diameter ($\mathbf{d_{epcf}}$) of PCF for laser fusion is equivalent to the diameter of PCF with no air holes as described in Equation 5-3.

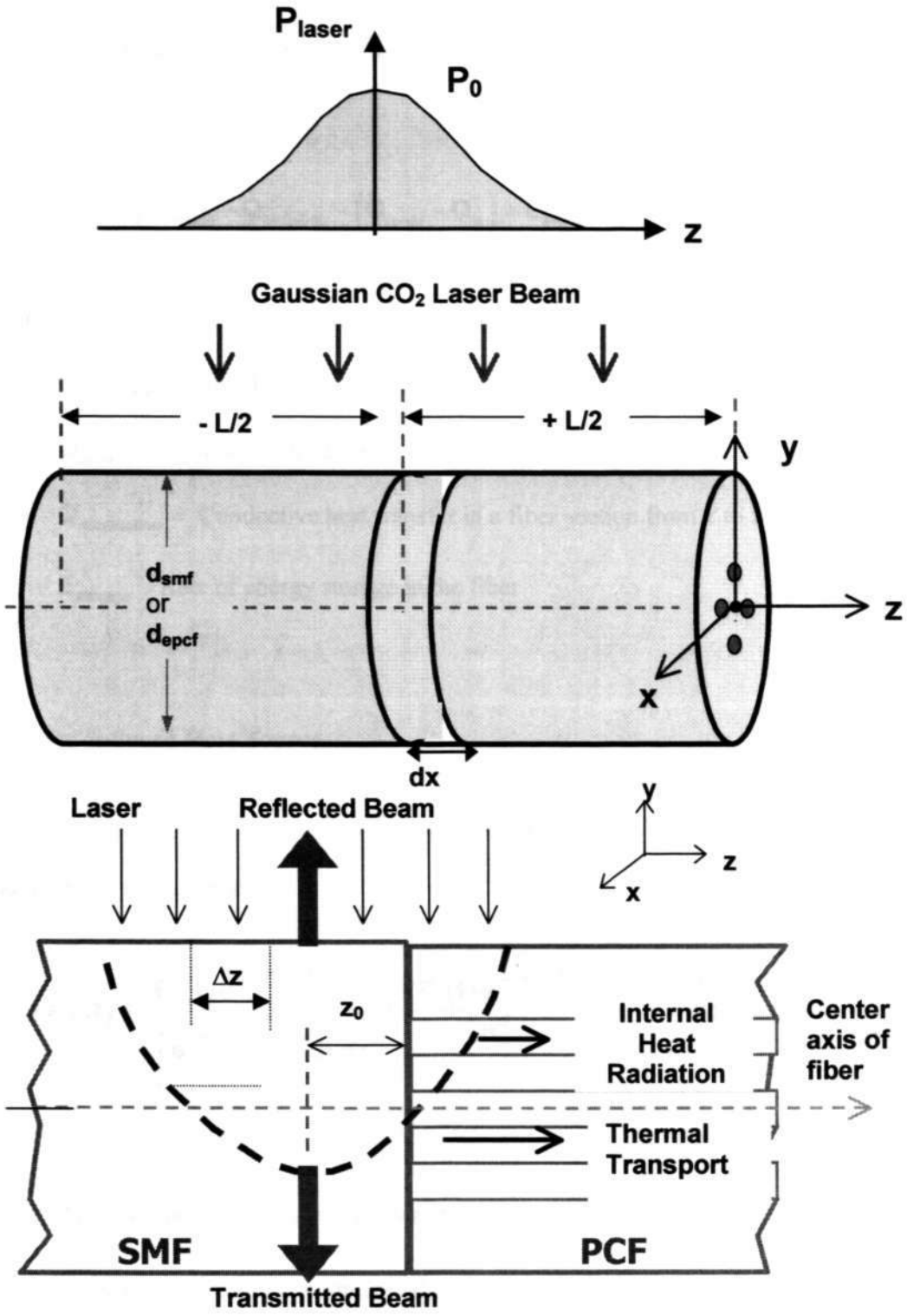

Figure 5-5 Schematic of one-dimensional thermal transfer model

The general heat transfer equation can be formulated as:

$$\dot{E}_{heat} - Q_{convection} - Q_{radiation} - Q_{conduction} = \dot{E}_{storage} \qquad \text{Equation 5-10}$$

$$\dot{E}_{heat} - Q_{convection} - Q_{radiation} - \left(Q_{|z+\delta z} - Q_{|z}\right) = \dot{E}_{storage} \qquad \text{Equation 5-11}$$

Where $\dot{E}_{heat}$ = heat energy generated due to the absorption of CO_2 laser energy

$Q_{convection}$ = Heat loss due to convection from fiber to the ambient

$Q_{radiation}$ = Radiation heat loss

$Q_{conduction}$ = Conductive heat transfer in a fiber section from z to $z+\delta z$

$\dot{E}_{storage}$ = Rate of energy storage in the fiber

(a) Laser-Induced Heat Source

The optical power of CO_2 laser is a Gaussian beam profile [38] and its laser beam irradiance can be expressed as:

$$P''_{laser}(x,z,t) = \frac{P_0(t)e^{-2\left(x^2+z^2\right)/r_{beam}}}{\int_{-\infty}^{+\infty} e^{-2\left(x^2+z^2\right)/r_{beam}}\,dxdz} = \frac{2P_0(t)e^{-2\left(x^2+z^2\right)/r_{beam}}}{\pi r_{beam}^2} \qquad \text{Equation 5-12}$$

Where, P_0 = laser power, r_{beam} = beam waist radius

If the laser beam is positioned with a small offset of z_0 from the fiber joint at the x-z plane, the Equation 5-12 becomes

$$P''_{laser}(x,z,t) = \frac{P_0(t)e^{-2\left((z+z_0)^2+x^2\right)/r_{beam}}}{\int_{-\infty}^{+\infty}\int_{-\infty}^{+\infty} e^{-2\left((z+z_0)^2+x^2\right)/r_{beam}}dxdz} = \frac{2P_0(t)e^{-2\left((z+z_0)^2+x^2\right)/r_{beam}^2}}{\pi r_{beam}^2}$$

Equation 5-13

In our experiments, the laser beam size is about 3-4 times the fiber diameter; therefore only part of laser power would be absorbed by the fiber. Assuming that the equivalent thickness of fiber absorption in the 1-D thermal transfer model to be $d_{efiber} = \sqrt{\frac{\pi d_{fiber}^2}{4}} = \sqrt{\frac{\pi}{4}} d_{fiber} = 0.8863 d_{fiber}$ and a reflectivity of the fiber to be **R**, the total energy absorbed by a cross-section of fiber of thickness, **dz** is given by:

$$\dot{E}_{heat} = dQ_{souce} = (1-R)\left[\int_{-\frac{d_{efiber}}{2}}^{\frac{d_{efiber}}{2}} P''_{laser}(x,z,t)dx\right]dz \qquad \text{Equation 5-14}$$

where, d_{fiber} =diameter of fiber and $d_{efiber}=0.8863 d_{fiber}$

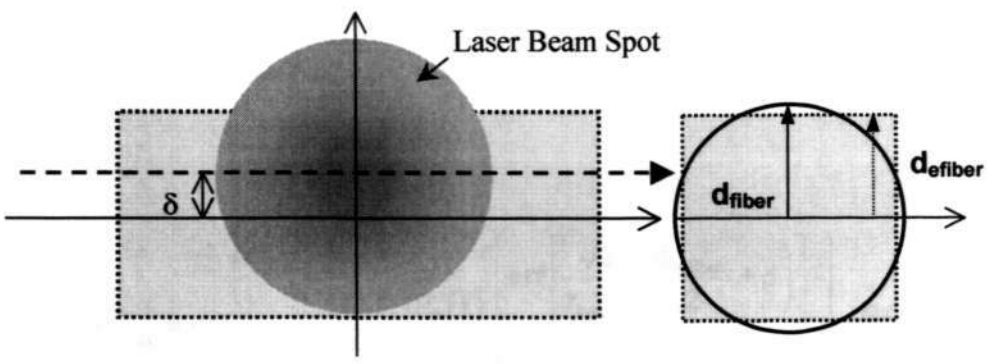

Figure 5-6 (a) Top view for laser beam falls on the fiber at x-z plane
(b) side-view for cross-section of fiber

Furthermore, if the peak of laser beam is located with an offset of δ from the center of fiber axis (Figure 5-6), the expression can be written as

$$\dot{E}_{heat} = dQ_{souce} = (1-R)\left[\int_{-\frac{d_{efiber}}{2}+\delta}^{\frac{d_{efiber}}{2}+\delta} P''_{laser}(x,z,t)dx\right]dz$$

Equation 5-15

$$\dot{E}_{heat} = dQ_{souce} = \frac{(1-R)P_0(t)}{\pi r_{beam}^2}\left\{\int_{-\frac{d_{efiber}}{2}+\delta}^{\frac{d_{efiber}}{2}+\delta} e^{-2y^2/r_{beam}^2}dx\right\}e^{-2(z)^2/r_{beam}^2}dz$$

Equation 5-16

As the serpentine bracket in the above equation is an error function, the Equation 5-16 can be re-written as

$$\dot{E}_{heat} = dQ_{souce} = \left[\frac{(1-R)P_0(t)}{\pi r_{beam}^2}\times\frac{r_{beam}\sqrt{\pi}}{2^{3/2}}\right]\left\{\begin{matrix}\mathrm{erf}\left[\frac{\sqrt{2}}{r_{beam}}\left(\frac{d_{efiber}}{2}+\delta\right)\right]-\\ \mathrm{erf}\left[\frac{\sqrt{2}}{r_{beam}}\left(-\frac{d_{efiber}}{2}+\delta\right)\right]\end{matrix}\right\}e^{-2z^2/r_{beam}^2}dz$$

Equation 5-17

$$\Rightarrow \quad \dot{E}_{heat} = dQ_{souce} = \frac{(1-R)P_0(t)}{2^{3/2}\sqrt{\pi}r_{beam}^2}\left\{\begin{matrix}\mathrm{erf}\left[\frac{\sqrt{2}}{r_{beam}}\left(\frac{d_{efiber}}{2}+\delta\right)\right]-\\ \mathrm{erf}\left[\frac{\sqrt{2}}{r_{beam}}\left(-\frac{d_{efiber}}{2}+\delta\right)\right]\end{matrix}\right\}e^{-2z^2/r_{beam}^2}dz$$

Equation 5-18

(b) Radiation Heat Loss

The radiation heat loss over the perimeter of fiber cross-section of thickness **dz** is given as

$$dQ_{radiation} = \sigma\varepsilon\left(\pi d_{efiber} dz\right)\left(T^4 - T_{air}^4\right) \qquad \text{Equation 5-19}$$

where, ε = Emissivity of fiber, σ = Stefan-Boltzmann constant

(c) Convection Energy Loss in Fiber

The heat energy transfer through the convection is given as :

$$dQ_{convection} = h_{convection}\pi d_{efiber}\left(T - T_{air}\right)dz \qquad \text{Equation 5-20}$$

Where, $h_{convection}$ = convective coefficient

(d) Conduction Energy Loss

$$dQ_{conduction} = d\left(Q_{|z+\delta z} - Q_{|z}\right) = \left[K_\theta A\left(\frac{\partial T}{\partial z}\right)\Big|_{z+\delta z} - K_\theta A\left(\frac{\partial T}{\partial z}\right)\Big|_{z}\right] \qquad \text{Equation 5-21}$$

As $$\nabla f = \frac{\partial f}{\partial z} = \lim_{\delta z \to 0}\left(\frac{f(z+\delta z) - f(z)}{\delta z}\right)$$

$$dQ_{conduction} = K_\theta A\left(\frac{\partial^2 T}{\partial z^2}\right) \qquad \text{Equation 5-22}$$

Where, K_θ= thermal conductivity and

the cross section area of the fiber $A = \frac{\pi d_{fiber}^2}{4}$

(e) Energy stored in Fiber

$$\dot{E}_{store} = \rho_D c_{sp} \frac{\partial T}{\partial t} A dz \qquad \text{Equation 5-23}$$

where, ρ_D = fiber density, c_{sp}=specific heat of fiber,

As the relationship of $\frac{\rho_D c_{sp}}{K_\theta} = \frac{1}{\kappa_{ext}}$

The extinction coefficient, κ_{ext} is the imaginary part of the complex refractive index of the fiber and the absorption coefficient $\alpha_{absorption} = 4\pi\kappa_{ext}/\lambda$ is dependent on κ_{ext} and λ. Based on the work done by McLahlan at el [147.]:, the variation of κ_{ext} can be expressed as a function of the temperature (Kelvin)

$$\kappa_{ext} = 1.82\times10^{-2} + 10.1\times10^{-5}(T - 273.15) \qquad \text{Equation 5-24}$$

(f) 1-Demensional Thermal Transfer Equation

The general equation for the *1-Dimensional Thermal Transfer* can be expressed as:

$$\begin{aligned}\dot{E}_{heat} &= dQ_{source}(z) \\ &= h_{convection}(\pi d_{efiber})(T - T_{air}) + \sigma\varepsilon(\pi d_{efiber})(T^4 - T_{air}{}^4) \\ &\quad + \rho_D c_{sp} A\left(\frac{\partial T}{\partial t}\right)dz - KA\left(\frac{\partial^2 T}{\partial z^2}\right)\end{aligned} \qquad \text{Equation 5-25}$$

Rearrangement of the equation (5-26) gives:

$$\begin{aligned}dQ_{source}(z) &= h_{convection}(\pi d_{efiber})(T - T_{air}) + \sigma\varepsilon(\pi d_{efiber})(T^4 - T_{air}{}^4) \\ &\quad + \rho_D c_{sp}\left(\frac{\sqrt{\pi} d_{efiber}}{2}\right)^2\left(\frac{\partial T}{\partial t}\right)dz - K\left(\frac{\pi d_{efiber}^2}{4}\right)\left(\frac{\partial^2 T}{\partial z^2}\right)\end{aligned}$$

Equation 5-26

Substitution of Equation 5-18 into Equation 5-27 and rearrangement of the terms, gives:

$$\frac{(1-R)P_0(t)}{2^{3/2}\sqrt{\pi}r_{beam}^2}\left\{\mathrm{erf}\left[\frac{\sqrt{2}}{r_{beam}}\left(\frac{d_{efiber}}{2}+\delta\right)\right]-\mathrm{erf}\left[\frac{\sqrt{2}}{r_{beam}}\left(-\frac{d_{efiber}}{2}+\delta\right)\right]\right\}e^{-2(z+z_0)^2/r_{beam}^2}$$

$$=h_{convection}(\pi d_{efiber})(T-T_{air})+\rho_D c_{sp}\left(\frac{d_{efiber}}{2}\right)^2\left(\frac{\partial T}{\partial t}\right)+$$

$$\sigma\varepsilon(\pi d_{efiber})\left(T^4-T_{air}{}^4\right)-\kappa_{ext}\rho_D c\left(\frac{\partial^2 T}{\partial z^2}\right)$$

Equation 5-27

(g) Boundary Conditions

The boundary conditions for the fiber at time **t=0** are as follows:

The fiber temperature is same as the ambient temperature before irradiation by laser

$$T(z,0)=T_{air}$$ Equation 5-28

Within the fiber

At $z = L/2$ $$h_{convection}\left(T_{L/2}-T_{air}\right)+K_\theta\frac{\partial T}{\partial z}=0$$ Equation 5-29

And $z = -L/2$ $$-h_{convection}\left(T_{-L/2}-T_{air}\right)+K_\theta\frac{\partial T}{\partial z}=0$$ Equation 5-30

The above equations contain several parameters including specific heat (c_{sp}), convective heat transfer coefficient ($h_{convection}$), extinction coefficient (κ_{ext}), thermal

conductivity (K_θ), refractive index of fiber (**n**), emissivity (ε) and fiber density (ρ_D); all these parameters are summarized in Appendix –A3.

The temperature distribution across the optical fiber as illustrated in Figure 5-7, shows that the temperature at **z=0** is highest and decreases gradually from the center of the laser beam spot. In an attempt to minimize the deformation during the laser splicing process, the laser power is adjusted to bring the fibers to semi-liquid state. Based on the data available for electric-arc systems [148], we have chosen a temperature value around 1600~1700K for splicing of PCF to SMF. This value is close to the fictive temperature of silica. In Figure 5-7, the simulate results are shown at three laser power levels (3.1W, 3.84W and 4.4W), which we have used frequently in our experiments. The diagram demonstrates that higher laser power would increase laser absorption as well as the temperature of the silica fiber.

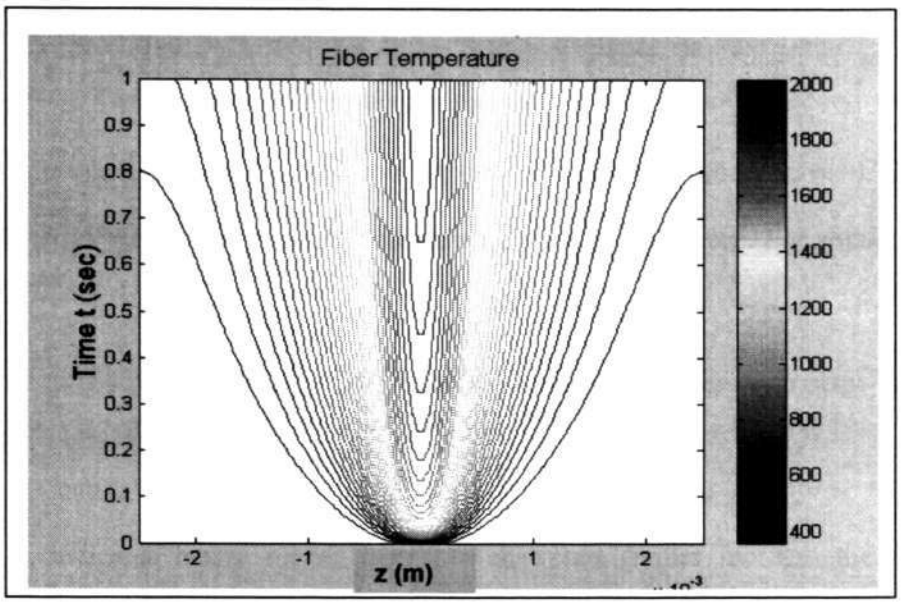

Figure 5-7 Temperature Distribution across the fiber from **z** = -200μm to 200 μm with laser power≅4.4W.

Although the melting temperatures of silica material in SMF and PCF are almost the same, these two types of fibers need different laser exposure times due to their structural differences. A practical approach is to adjust the laser beam position slightly away from the fiber joint and more towards the SMF that needs higher laser power than PCF.

Based on the simulation result, with a laser power of 4.4 W, the laser exposure time of about 120ms is necessary to melt LMA-PCF and reach the temperature of ≅1650K [149] Once the laser irradiation is stopped, the cooling rate of the fiber would depend on the fictive temperature of silica, the temperature at which the silica liquid is frozen into glass. Higher fictive temperature glass cools down more rapidly than those

glasses with lower fictive temperatures. The fictive temperatures of single mode optical fiber measured by infrared reflection method are found to be 1150~1300°C for the core, 1450 ~1550°C for the inner cladding and 1620~1660°C for the outer cladding [146]. Generally, the fiber needs less than a fraction of a second to re-crystallize implying that the average cooling rate of a few thousand degrees Celsius per second. Also the cladding should cool down earlier than the core. For splicing of SMF and PCF, the choice of laser power and laser exposure time is determined by the temperature (≅1640K=2000°F) that is necessary to bring the fibers into semi-liquid state. [148].

Figure 5-8, indicates that a higher laser power would further increase the fiber temperature; hence fiber splicing would need shorter laser exposure time. The results on fiber temperature for the three types of fibers including SMF, LMA-PCF and NL-PCF are shown in Figure 5-9 and Figure 5-10. NL-PCF consists of large air holes and hence its net volume of silica is small. If a single laser source is used to irradiate these 3 types of fibers, the temperature of NL-PCF would be the highest. Figure 5-10 shows the variation of fiber temperature (**T**) with distance (**z**) along the fiber axis and laser exposure time (**t**). Figure 5-11 shows that if the laser beam is offset away from the fiber axes, the temperature of the fibers will be significantly lower to melt the fiber and hence no splicing is achieved.

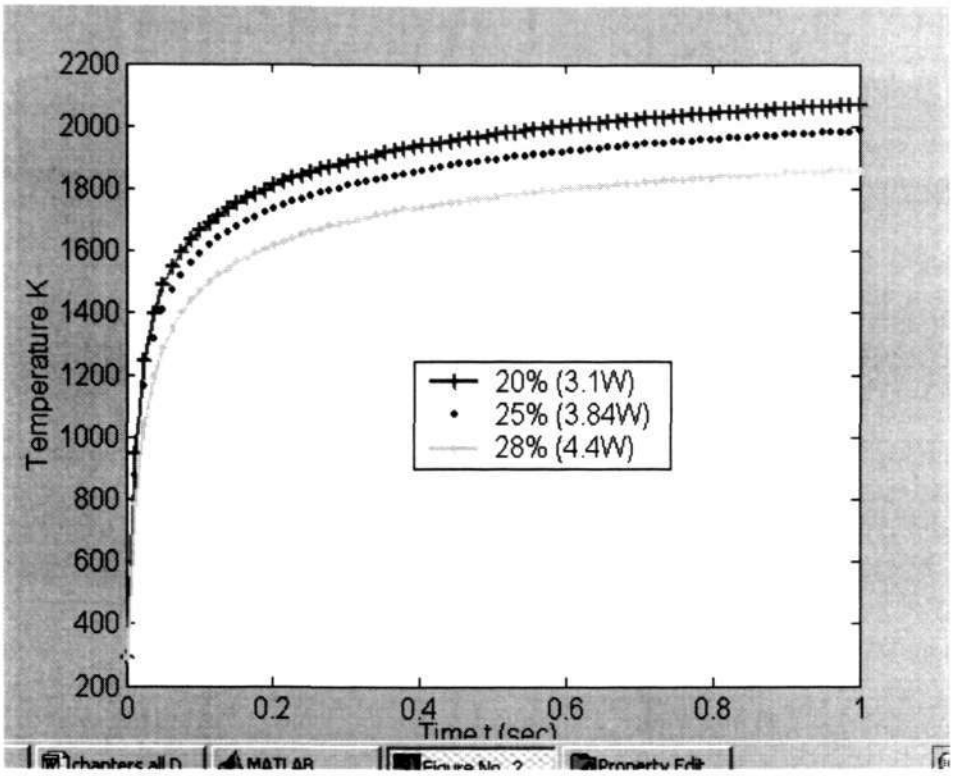

Figure 5-8: Higher laser power needs shorter laser exposure time for melting the fibers into semi-liquid state

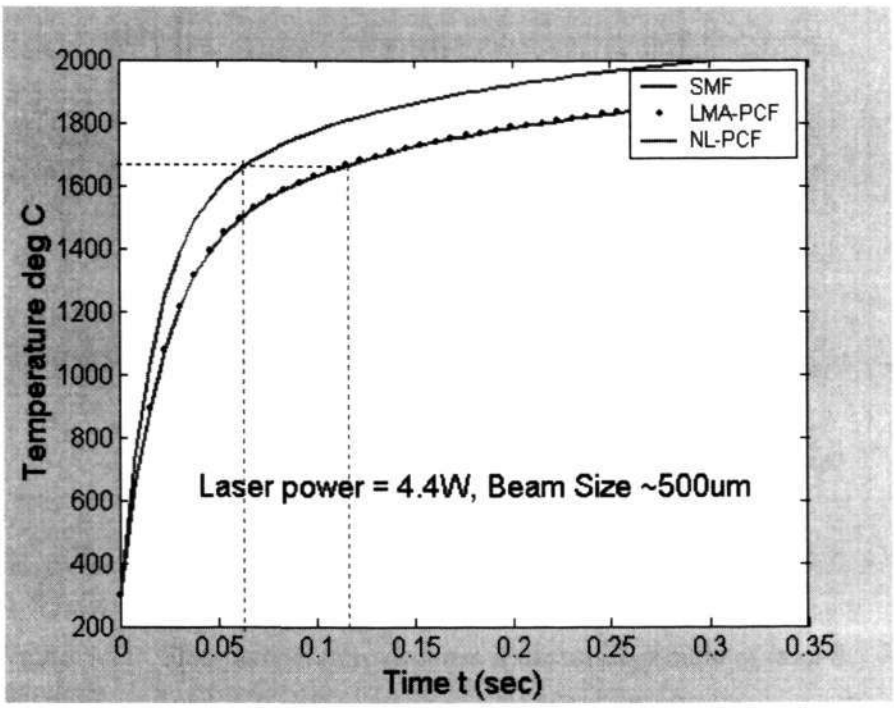

Figure 5-9 Temperature of Fibers vs laser exposure time

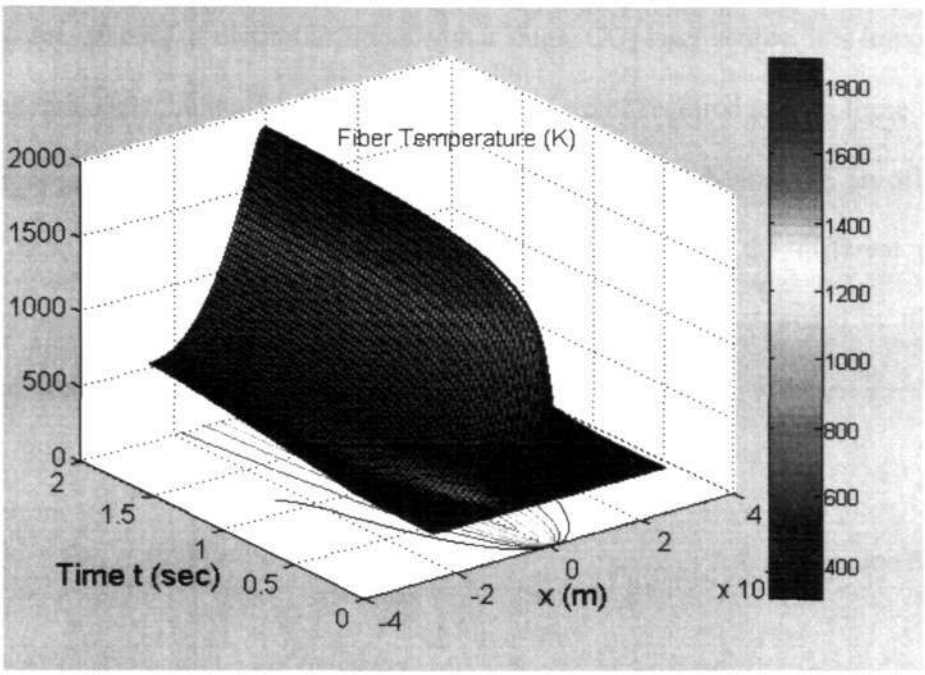

Figure 5-10 Overview of temperature distribution over time and width of fiber

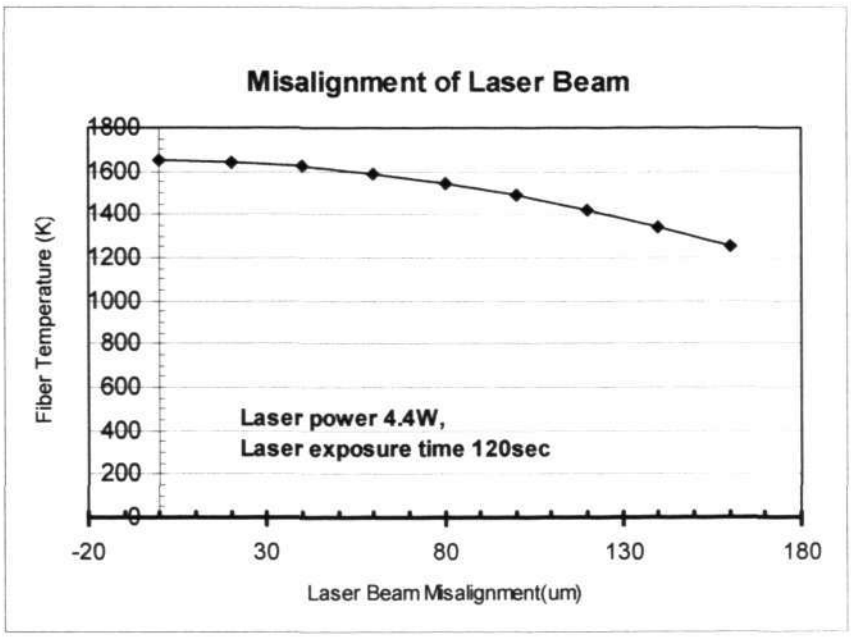

Figure 5-11 Fiber temperature declines if the misalignment of laser δ increases

5.2.3 Beam Offset Consideration

During the splicing of dissimilar fibers with a single CO_2 laser source, it is impossible to simultaneously maintain two different exposure times required to melt these fibers. Hence the practical solution is to shift the peak of Gaussian beam with an offset $\mathbf{z_0}$ away from PCF and more towards the SMF to compensate the different power requirement for these two fibers. The extent of laser beam offset would be directly proportional to the net silica content in the fibers:

$$P_{Fiber1}(z,t) = \int_{-\infty}^{x_0} \frac{2P_0(t)e^{-\frac{2z^2}{r_{beam}}}}{\pi r_{Beam}^2} dz \qquad \text{Equation 5-31}$$

$$P_{Fiber2}(z,t) = \int_{z_0}^{-\infty} \frac{2P_0(t)e^{-\frac{2z^2}{r_{beam}}}}{\pi r_{Beam}^2} dz \qquad \text{Equation 5-32}$$

$$\frac{P_{Fiber1}}{P_{Fiber2}} = \frac{d_{smf}}{d_{netPCF}} \qquad \text{Equation 5-33}$$

The $\mathbf{z_0}$ has been computed using Matlab software. For example, to splice a 125μm diameter single mode fiber with a PCF having an equivalent diameter (deduction of air holes) of 100μm, the beam-offset ($\mathbf{z_0}$) should be about 29μm towards the SMF.

5.3 Thermal Transfer Mechanism and Scattering Loss in Single Hollow Core Photonic Crystal Fiber

The 1-Dimensional thermal transfer model is a good approach to determine the requirement of optimum laser power and laser exposure time for fiber splicing, but it is inadequate to analyze the thermal energy distribution over the cross-section of the fiber. In this section, a 3-D thermal transfer model is introduced to analyze the heat flux inside the SMF and Single-Hollow-Core PCF, it also illustrates the back-scattered light. Figure 5-12 shows the cross-section of these two types of fibers.

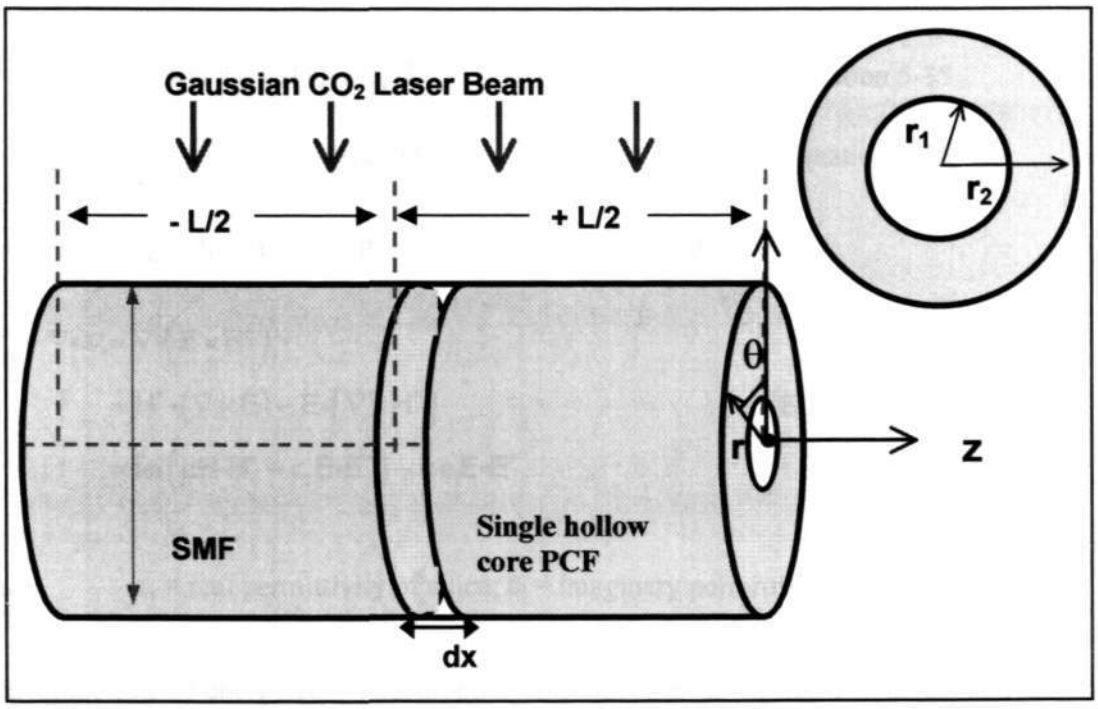

Figure 5-12 Three-Dimensional Optical fiber comprising inner core of solid silica or air-hole and cladding layer

To analyze the thermal energy distribution over the cross-section of these fibers, we adopt the approach of Barton et al [42] where a laser beam is assumed to be fifth order corrected fundamental Gaussian beam impinging onto the fiber. The thermal transfer rate is determined by using the Maxwell's equation that gives the rate of energy change per unit volume by Poynting vector as follows:

$$\vec{s} = \vec{E} \times \vec{H}^* \qquad \text{Equation 5-34}$$

Where $\vec{E}$ = Electric field intensity, $\vec{H}^*$ = Complex conjugate of magnetic field intensity

Absorption within the fiber is dependent on the fiber's permittivity (imaginary part) and can be determined by Maxwell's equation in frequency domain:

$$\nabla \times \mathbf{H} = -i\omega\left(\varepsilon_r + i\varepsilon_i\right)\mathbf{E} \qquad \text{Equation 5-35}$$

$$\nabla \times \mathbf{E} = -i\omega\mu\mathbf{H} \qquad \text{Equation 5-36}$$

The rate of energy change per unit volume can then defined as:

$$\begin{aligned} \nabla \cdot \mathbf{s} &= \nabla \cdot \left(\mathbf{E} \times \mathbf{H}^*\right) \\ &= \mathbf{H}^* \cdot \left(\nabla \times \mathbf{E}\right) - \mathbf{E} \cdot \left(\nabla \times \mathbf{H}^*\right) \\ &= i\omega\left(\mu \mathbf{H} \cdot \mathbf{H}^* - \varepsilon_r \mathbf{E} \cdot \mathbf{E}^*\right) - \omega\varepsilon_i \mathbf{E} \cdot \mathbf{E}^* \end{aligned} \qquad \text{Equation 5-37}$$

Where ε_r = real permittivity of silica; ε_i = imaginary permittivity of silica

The average rate of energy (q_{vol}) absorbed by the fiber per unit volume is dependent on the electric field strength and the imaginary part of the permittivity:

$$\begin{aligned} q_{vol} &= \frac{\omega}{2}\varepsilon_i \mathbf{E} \cdot \mathbf{E}^* \\ &= \frac{\omega}{2}\varepsilon_i |\mathbf{E}|^2 \end{aligned} \qquad \text{Equation 5-38}$$

Hence the Rate of heat generated per unit length can be expressed as

$$Q_{source}(z)dz = \left[\int_{-\pi}^{\pi}\int_{0}^{r} q_{vol}(r,\theta,z)\cdot r dr\cdot d\theta\right]dz \qquad \text{Equation 5-39}$$

To determine the temperature distribution along the fiber, we assume the fiber to be divided into many segments of tiny cores of length of **dz**. With heat source given by equation 5-40, the 1-D thermal transfer model Equation 5-26 for each segment of fiber takes the form of 3-D heat transfer equation as given below:

$$dQ_{source} - dQ_{convection} - dQ_{radiation} + K\frac{\partial^2 T}{\partial z^2}Adz = \rho c_{sp}\frac{\partial T}{\partial t}Adz$$

Equation 5-40

The rate of energy absorption per unit volume is proportional to the square of electric field amplitude at a given point. In order to know the thermal distribution in the separate layers of fiber (e.g. inner layer r_1 = core or air-hole and outer layer r_2 = cladding), the electromagnetic field inside the fiber must be analyzed.

The detailed treatment of heat flux distribution in the layered cylindrical fiber is illustrated in Appendix A4, where it is assumed that the Gaussian beam spread of CO_2 laser in a homogenous medium satisfies the vector Helmholtz equation. Figures 5-13, 5.14 and 5.15 show the simulation results for the distribution of thermal energy over three types of fibers: (i) single mode fiber with core and cladding, (ii) PCF with small air-hole and (iii) PCF with single large air-hole. Due to a limitation in the software used, the simulation could be performed with the smallest air hole size of 5μm. In the simulation process, the single small air-hole represents LMA-PCF and the large single air-hole represents NL-PCF.

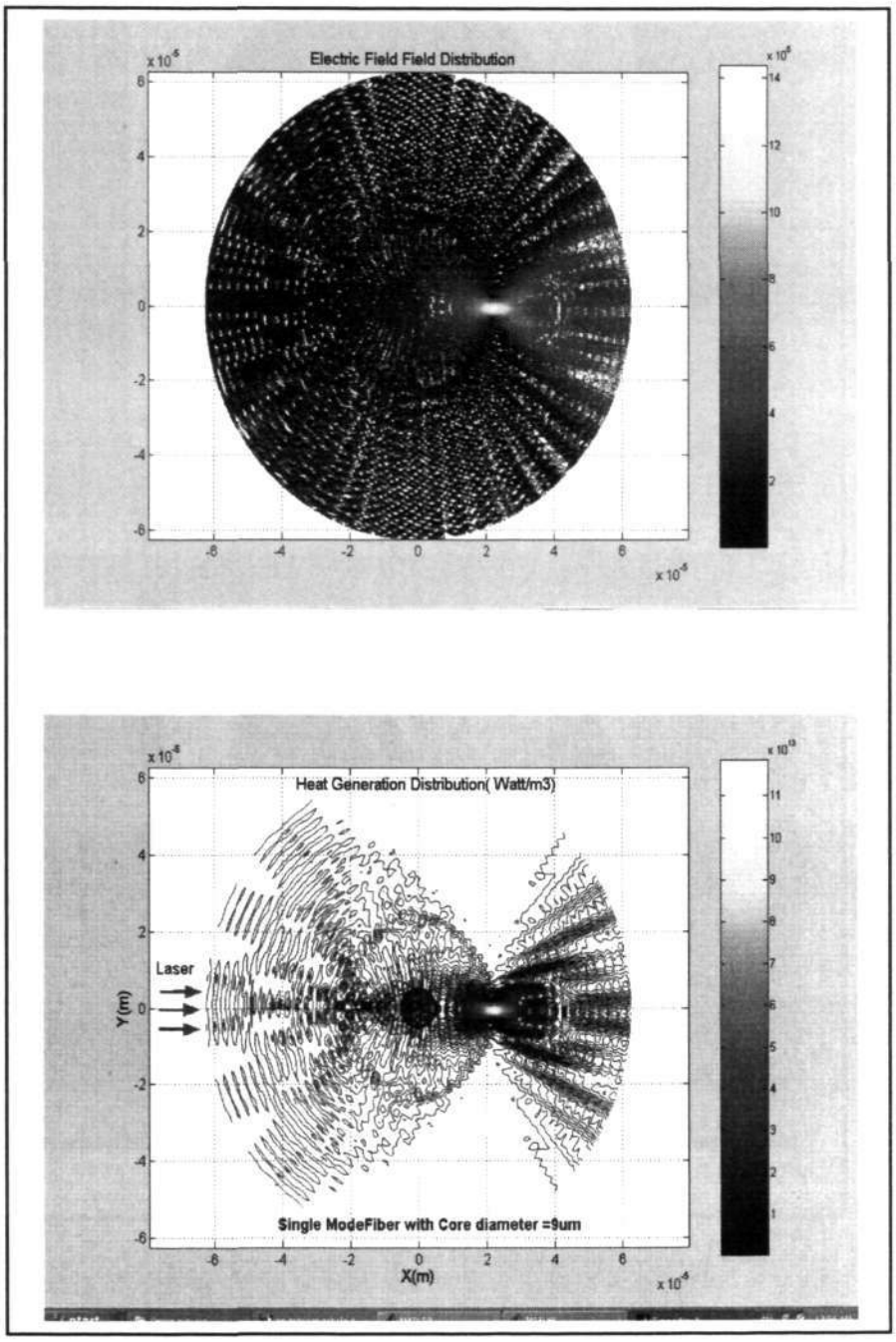

Figure 5-13 Thermal Energy Distribution in the SMF cross section

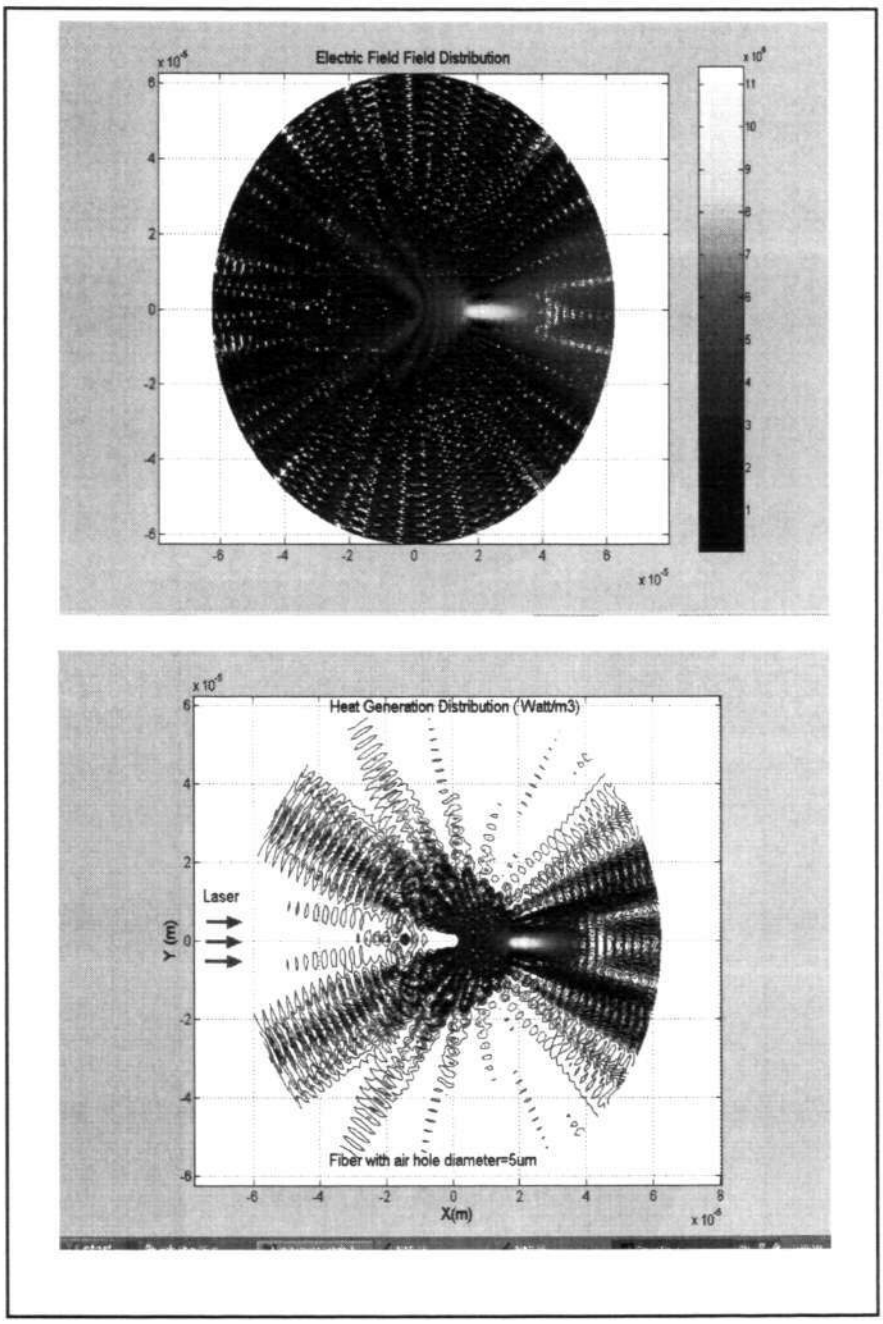

Figure 5-14 Thermal Energy Distribution in the cross section of hollow core fiber with hole-size of 5μm

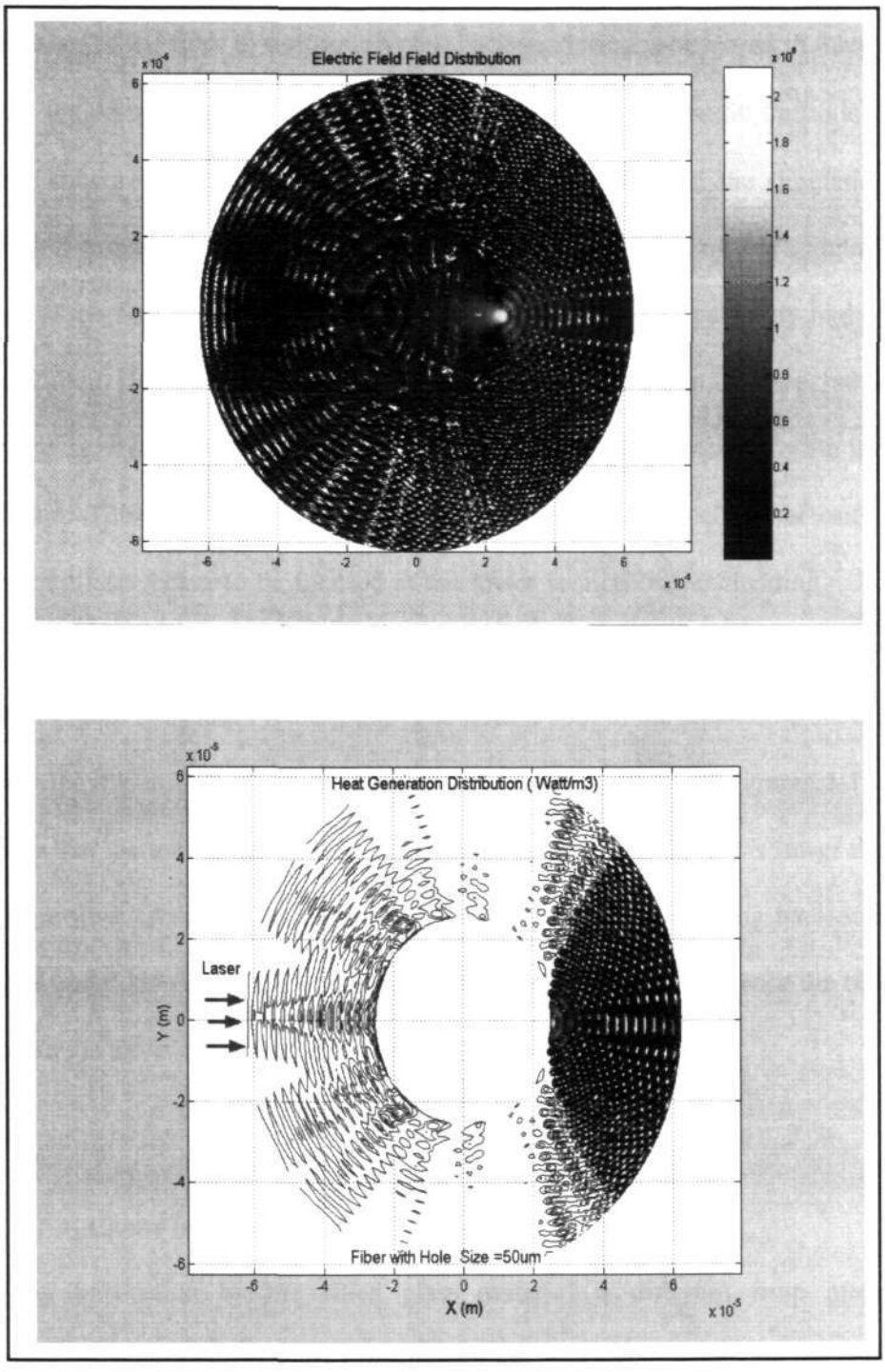

Figure 5-15 Thermal Energy Distribution in the cross section of hollow core fiber with hole-size of 50μm

A laser beam passing from the cladding to the core (or air hole) causes the temperatures of the fiber to rise rapidly, but back-scattering is observed in three types of fibers including single mode fiber, 5μm hollow core fiber and 50μm hollow core fiber are shown in Figures 5-13, 5.14 and 5-15 respectively. In the simulation, the assumption is made that the CO_2 laser is transparent to air hole of PCF. Figure 5-13 shows that the heat generation in the Ge-doped core of SMF is generally higher than in its cladding. However the hottest spot in the SMF is not within the core, rather it is found at a spot in the lower section of the cladding directly opposite to the incident laser beam. This spot occurs due to the lensing effect of the core that causes the propagating laser beam to be focused at the lower section of the cladding. For the hollow core fibers, their hottest spot is near to the air-hole under the laser beam as shown in Figure 5-14 and Figure 5-15. The hottest spot in the small air-hole is much more obvious than in the large air-hole PCF. The above figures (Figures 5-13 to 5-15) show that the temperature in the cladding near to the laser beam is lower than the rest of the fiber cross section. The smaller air-hole PCF has a strong back-scattered beam traveling opposite to the direction of incident laser beam and hence the cladding temperature is lower compared to that in large air-hole PCF.

5.4 CO_2 Laser Interaction with Silica

The laser absorption by the silica glass material is different from metals or semiconductors. In semiconductors, the absorption depends primarily on the band-gap energy ($\mathbf{E_g}$) of the material and generally occurs if the photon energy ($\mathbf{h\nu}$) is greater than the material band gap. Laser absorption in a dielectric is characterized not only by the material band-gap but also by a set of optical parameters such as frequency-

dependent absorption coefficient, reflectivity, the concentration of dopants or free carriers and level of surface and bulk defects. The band-gap energy of the dielectric is typically above 3eV and that electrons in dielectrics are tightly bound in the valence bands, hence electron excitations are possible only at UV wavelengths. The following section presents results on the interaction of CO_2 laser (photon energy $\mathbf{h\nu} = 0.112$eV) with optical fibers (SMF and PCF) that generally have band-gap energies in the range of 8.9eV to 12.6eV.

5.4.1 Photonic Thermal Effects

As is well known, a phonon represents quantization of lattice vibrations and the phonon energy is usually less than 0.1eV. When a photon is absorbed, it may cause generation electrons, photons of different wavelength or phonons. The energy absorption by phonons occurring in fiber determines the fundamental quantum limit of attenuation.

The basic structure of silica fiber is tetrahedral SiO_4 and it may be isolated as ortho-silicate or combined with oxygen atom and another SiO_4 to form Si_2O_7. [151, 152]. Silica has very strong absorption near to 10 μm wavelength, but has low absorption in the near IR wavelengths used in optical fiber communications. The high phonon absorption in silica is mainly caused by the valence bond stretching in **Si-O-Si** structure [153]. Silica fiber doped with GeO_2, P_2O_5 or Be_2O_3, has several vibrational modes in the wavelength range of 8.7μm ~ 12.9μm. Also the Ge-doped core generally has higher absorption than its cladding. If the fiber is condensed, the laser absorption in the fiber is further enhanced during the splicing process due to the increased OH^- ion content.

For a silica fiber with condensation, the hydroxyl group may be bonded to the silica network (i.e. SiOH) and this may affect its optical properties. One of the overtones of the OH^- absorption has a peak at λ=1.38μm. Hence it affects the performance of optical communications in the wavelength range from 1300-1700nm. In laser-silica interaction, significant phonon generation may occur at long wavelengths even if the laser intensity is low.

5.5 Computation of Laser Optical Breakdown

Dielectric breakdown through optical absorption of laser radiation is also called optical breakdown or laser-induced breakdown. It can be either the partial or complete ionization, depending on the laser wavelength and the band-gap of the material. We have used 10.6μm CO_2 laser for laser splicing of SMF to PCF, a laser plasma generation may occur during the fusion process. In this section, a model is presented to analyze the laser induced breakdown threshold in the silica fiber and the condensed fiber.

We have used the model first developed by Kennedy [79] to calculate irradiance thresholds for laser-induced breakdown in condensed media including ocular and aqueous media. This model is primarily an extension of Shen's simple rate equation [64] and Keldysh model for the multi-photon ionization [80]. Several studies have been reported on the optical breakdown in the fluid and the occurrence of plasma decay in the cavitations bubble formation, but no studies have been reported for this effect in the silica fiber and condensed PCF.

Once the laser is absorbed by the dielectric, the optical breakdown can be caused by complete (direct) or partial (indirect) ionization depending on $h\nu > E_g$ or $h\nu < E_g$ respectively. The ionization results in plasma, which rapidly absorbs laser power through the inverse Bremsstrahlung process. The rapid heating of plasma can cause significant increase of temperature, plasma expansion, and emission of audible acoustics or visible plasma. Two laser-induced breakdown mechanisms are possible: one is through the direct ionization of the medium by multi-photon absorption and another is cascade ionization (or called avalanche ionization). *Cascade absorption* that is different from the multi-photon ionization requires one or more free electrons (also called seed electrons) to be present in the focal volume to begin the ionization. We believe that if the PCF is not contaminated with liquid or other material, the laser-induced breakdown occurring in SMF and PCF should be quite similar. However, the capillary effect in the small air hole of PCF trapped with liquid can change the characteristics of optical breakdown during the laser splicing process as the impurities in the fiber may act as shallow donors of the seed electrons for cascade or multi-photon absorption. Additionally, the resonance condition between the CO_2 laser and silica material increases the temperature through the phonon absorption and hence it may further enhance the ionization through thermal induced collisions. Pure silica with energy gap of 9.6eV is usually considered to have no seed electron, therefore, it is impossible to generate direct ionization and also difficult to create multi-photon absorption in the laser interaction process with CO_2 laser which has a low photon energy of 0.112eV. We assume that the phonon absorption initially dominates in the laser absorption process by increasing the energy of lattice vibrations. This process increases the temperature of silica and the probability of ionization by releasing more

free electrons to increase the carrier density; hence the probability of cascade breakdown or multi-photon ionization may increase significantly.

In order to illustrate the complete process for the laser-induced breakdown, these two processes will be illustrated in the generic rate equation even though the multi-photon ionization may not be significant in our experiments.

5.5.1 Rate Equation for Optical Breakdown

To determine the irradiance required for producing optical breakdown, a generic rate equation [27] is used which describes the electron generation through multi-photon absorption $(\mathbf{d\rho/dt})_{mp}$, cascade ionization $(\eta_{casc}\rho)$ and diffusion loss of electrons out of the focal volume $(\mathbf{g}\rho)$ and recombination losses $((\eta_{rec}\rho^2)$:

$$\frac{\mathbf{d}\rho}{\mathbf{dt}} = \left(\frac{\mathbf{d}\rho}{\mathbf{dt}}\right)_{\mathbf{mp}} + \eta_{\mathbf{casc}}\rho - \mathbf{g}\rho - \eta_{\mathbf{rec}}\rho^2 \qquad \text{Equation 5-41}$$

The *cascade ionization rate*, $\eta_{\mathbf{casc}}$, is the probability that a free electron will encounter an ionization collision with the bound electron per unit time.

The *multi-photon absorption rate* is determined by the *density of bound electrons* $(\rho_{\mathbf{bound}})$ having a binding energy $\mathbf{E_{ion}}$ at time $\mathbf{t}$, where the *density of bound electrons* is dependent on molecular density (ρ_{mole}) and the density of free carrier ρ_{free}.

$$\left(\frac{\partial\rho}{\partial\mathbf{t}}\right)_{\mathbf{mp}} = \eta_{\mathbf{mp}}\rho_{\mathbf{bound}}(\mathbf{t}) \qquad \text{Equation 5-42}$$

Or,

$$\left(\frac{\partial \rho}{\partial t}\right)_{mp} = \eta_{mp}\left(n_e \rho_{mole} - \rho_{free}(t)\right) \qquad \text{Equation 5-43}$$

For condensed media, the initial free carrier density is low (even during the breakdown) and can be neglected in the calculations [154]. Therefore, the rate equation can be simplified as:

$$\frac{d\rho}{dt} = \eta_{mp}\rho_{bound} + \eta_{casc}\rho - g\rho - \eta_{rec}\rho \qquad \text{Equation 5-44}$$

$$\frac{d\rho}{dt} - (\eta_{casc} - g)\rho = \eta_{mp}\rho_{bound} - \eta_{rec}\rho \qquad \text{Equation 5-45}$$

As the second term (η_{casc} - g) on the L.H.S. and the R.H.S. terms of the rate equation are almost constants, the equation can be rewritten as

$$\frac{d\rho}{dt} - a\rho = b \qquad \text{Equation 5-46}$$

Where, $a = (\eta_{casc} - g)$; $b = \eta_{mp}\rho_{bound} - \eta_{rec}\rho$

The solution for free carrier density is in the form of,

$$\rho(t) = e^{at}\left[\int_0^t be^{(-at)}dt + C\right] \qquad \text{Equation 5-47}$$

$$\rho(t) = e^{at}\left[\left(-\frac{b}{a}e^{-at}\right)_0^t + C\right] \qquad \text{Equation 5-48}$$

Where, C is a constant of integration.

Assuming that the initial free carrier density ρ_0 comes from thermal collisions, then,

$$C = \rho(0) = \rho_0 \qquad \text{Equation 5-49}$$

$$\rho(t) = \rho_0 e^{at} + \left(\frac{b}{a}\right)\left(e^{at} - 1\right) \qquad \text{Equation 5-50}$$

$$\rho(t) = \rho_0 e^{at} + \left(\frac{\eta_{mp}\rho_{bound} - \eta_{rec}\rho}{\eta_{casc} - g}\right)\left(e^{at} - 1\right) \qquad \text{Equation 5-51}$$

Numerical simulation of the free carrier density can be obtained from the above equation.

(1) Cascade Breakdown

Cascade breakdown occurs easily in the condensed media, because the quasi-free electrons that are bound to a molecule or lattice site have enough kinetic energy to move through the lattice without being trapped by localized potential wells. Cascade ionization and electron multiplication would occur as long as these quasi-free electrons have sufficiently mobility to undergo collisions and absorb photons.

In the classical model, a free electron of effective mass $\mathbf{m_e}$ and charge **e** interacts with an *alternating electric field of frequency* ω and r.m.s. field strength $\mathbf{E_{rms}}$ that is similar application to a laser with *laser frequency* ω_{laser} irradiating to the a dielectric, the change of electrons energy occurs due to field and also during collisions with atoms or molecules through the inverse Bremsstrahlung process at a rate given [155]

$$\frac{dE_{gain}}{dt} = \left(\frac{\varepsilon^2 E_{laser}^2}{m_e \omega_{laser}^2}\right)\left(\frac{\omega_{collision}^2 \omega_{laser}^2}{\omega_{laser}^2 + \omega_{collision}^2}\right) \qquad \text{Equation 5-52}$$

Where $\omega_{laser} = \frac{2\pi c}{\lambda}$, and collision frequency $\omega_{collision} = \rho_{atom} \upsilon_e \sigma_e$ is dependent on the at atomic density (or molecular density) ρ_{atom}, electron velocity υ_e and electron transport cross section σ_e.

Irradiance I_0, defined as the power per unit area (W/m^2) of a light beam striking a surface of the target, is related to the rms field E_{laser} by

$$E_{laser}^2 = \frac{I_0}{cn\varepsilon_0} \qquad \text{Equation 5-53}$$

Where, **c**= speed of light, **n** = materials refractive index, permittivity for free space ε_0 = 8.854×10^{-12} Fm^{-1} and the average electron energy $E_{av} = \frac{E_{ion}}{2}$

If photon absorption does not occur due to electrons and the electrons do not collide with heavy particles (ions or molecules), then the electron energy loss can be expressed as

$$\frac{dE_{loss}}{dt} = -\left(\frac{2m_e}{M}\right)\left(\frac{\omega_{laser}^2}{\omega_{laser}^2 + \omega_{collision}^2}\right)\omega_{collision} E_{av} \qquad \text{Equation 5-54}$$

Where, **M** = Atomic or molecular mass.

Therefore, the average rate of change of electron energy can be expressed as

$$\frac{dE_e}{dt} = \frac{dE_{gain}}{dt} - \frac{dE_{loss}}{dt} \qquad \text{Equation 5-55}$$

Substitution of Equation 5-52 and Equation 5-54 into Equation 5-55, gives

$$\frac{dE_e}{dt} = \left[\left(\frac{e^2E_{laser}^2\omega_{collision}}{m_e\omega_{laser}^2}\right) - \left(\frac{2m_e\omega_{collision}E_{av}}{M}\right)\right]\left(\frac{\omega_{laser}^2}{\omega_{laser}^2 + \omega_{collision}^2}\right)$$

Equation 5-56

An electron with kinetic energy close to the ionization energy E_{ion} may produce another free electron. Dividing the above equation 5-56 by E_{ion} gives the cascade ionization rate;

$$\eta_{casc} = \frac{1}{E_{ion}}\left[\left(\frac{e^2E_{laser}^2\omega_{collision}^2}{m_e}\right) - \left(\frac{2m_e\omega_{collision}E_{av}}{M}\right)\right]\left(\frac{\omega_{laser}^2}{\omega_{laser}^2 + \omega_{collision}^2}\right)$$

Equation 5-57

The electron mean time between collisions (or momentum transfer collision time) is given as

$$\tau = \frac{1}{\omega_{collision}}$$

Equation 5-58

Hence, the ***cascade ionization rate*** becomes

$$\eta_{casc} = \left[\left(\frac{e^2I_0}{m_e c n \varepsilon_0 E_{ion}}\right) - \left(\frac{m_e\omega_{laser}^2}{M}\right)\right]\left(\frac{\tau}{1+\omega_{laser}^2\tau^2}\right)$$

Equation 5-59

Where, ω_{laser} is the laser frequency at $\omega_{laser} = \frac{2\pi c}{\lambda}$, n = material refractive index.

(2) Multi-photon ionization

Ionization in the condensed media refers to an electron transition from the valence band to conduction or excitation band, creating an electron-hole pair. Ionizing an atom or molecule with an effective ionization energy E'_{ion} needs $n_{h\nu}$ photons, where $n_{h\nu}$ is defined as

$$n_{h\upsilon} \approx \frac{E'_{ion}}{\hbar\omega_{laser}} + 1 \qquad \text{Equation 5-60}$$

Where $\hbar = \frac{h}{2\pi}$ and h =Planck's constant

The probability of multi-photon ionization in silica having band-gap of 9.6 ~12.6eV [156,157] due to CO_2 laser (photon energy of 0.112eV) is very low, therefore the multi-photon ionization rate is assumed to be negligible in our analysis:

$$\eta_{mp} \cong 0 \qquad \text{Equation 5-61}$$

(3) Reduction in Electron Density

The reduction in electron density is contributed from the recombination, trapping and diffusion. The recombination during the breakdown can be neglected if the electron lifetime > 10^{-8} s [79]. Due to the low binding energy (≅0.5 eV) of cascading electrons, the high probability of re-ionization is high and the trapping effect would be insignificant. [158]

With the above assumptions, the reduction in electron density is primarily contributed from the diffusion and the rate of diffusion of electrons, g is given as

$$g = \frac{\text{Electron Diffusion Coefficient}}{(\text{Diffusion Length})^2} = \frac{D}{\Lambda_{diffusion}^2} \qquad \text{Equation 5-62}$$

Where, $$D = \frac{E_{ion}}{3m_e\omega_{collision}}$$

and $$\frac{1}{\Lambda_{diffusion}^2} = \left(\frac{4.8}{d_{beam}}\right)^2 + \left(\frac{1}{z_{rayleigh}}\right)^2 = \left(\frac{4.8}{d_{beam}}\right)^2 + \left(\frac{4\lambda}{\pi d_{beam}^2}\right)^2$$

Where, d_{beam} = beam waist diameter, $z_{rayleigh}$= Rayleigh Length, λ = laser wavelength

Small focal volumes and spot sizes would produce higher rate of diffusion and cause a higher breakdown threshold for pulses longer than the diffusion time. The rate of diffusion of electrons can be written as

$$g = \frac{E_{ion}}{3m_e\omega_{collision}}\left[\left(\frac{4.8}{d_{beam}}\right)^2 + \left(\frac{4\lambda}{\pi d_{beam}^2}\right)^2\right] \qquad \text{Equation 5-63}$$

Alternatively, g can also be expressed as

$$g = \frac{\tau E_{ion}}{3m_e}\left[\left(\frac{4.8}{d_{beam}}\right)^2 + \left(\frac{4\lambda}{\pi d_{beam}^2}\right)^2\right] \qquad \text{Equation 5-64}$$

Where τ is the meantime between the electron-heavy particle collisions and is assumed to be ≅1fs, d_{beam} is the Gaussian beam waist diameter and λ is the optical wavelength.

5.5.2 Optical Breakdown by CO_2 laser

In principle, any laser can provide sufficiently high energy density to create conditions for high temperature plasma, however, for the CO_2 laser having a photon energy of 0.112eV, it is difficult to create direct ionization or partial ionization if the initial free carrier density of the targeted media is low. As mentioned, silica has high intrinsic absorption at the wavelength of 10.6μm. The initial free carrier density ρ_0 of a focused media, may come from ionization of molecules in the medium, ionization of impurities, ionization of carriers in local shallow traps. The ionizing mechanisms are optical absorption of one or more photons or thermal excitation. In silica or condensed silica, thermal excitation can be due to the molecule-to-molecule collision or from the molecular interaction with lattice vibrations (i.e. phonon), hence the initial free carrier density of a focused media can be expressed as

$$\rho_0 = \rho_{thermal} + \rho_{mp} \qquad \text{Equation 5-65}$$

Initially, the ionization in silica may take place due to thermal excitation caused by the phonon absorption and hence the initial free carrier density would be given as:

$$\rho_0 = \rho_{thermal} \qquad \text{Equation 5-66}$$

The probability P_r for the ionized electrons to be in the excited state is given by Maxwell-Boltzmann Distribution:

$$P_r(e) = \exp\left(-\frac{E_{ion}}{k_B T}\right) \qquad \text{Equation 5-67}$$

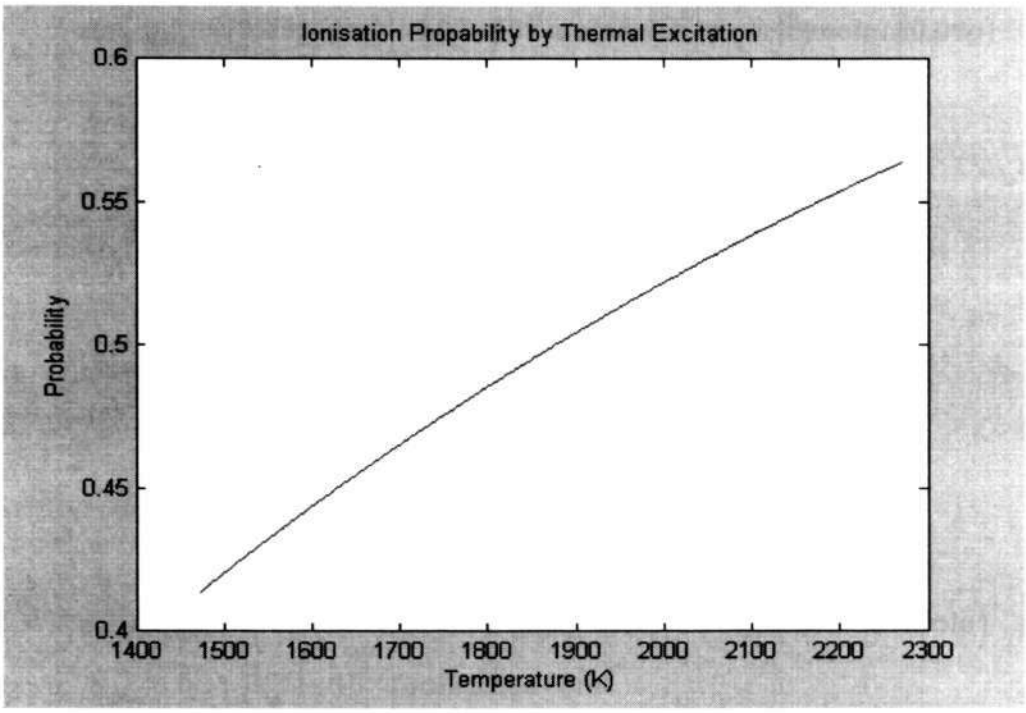

Figure 5-16 Temperature dependence of Ionization Probability

The initial electron density due to thermal excitation can be estimated by

$$\rho_{thermal} = P_r \times \rho_{bound} \qquad \text{Equation 5-68}$$

Where, the bound electrons density ρ_{bound} is dependent on the existing electron density (n_e) and molecular density (ρ_{mol}) of the medium

$$\rho_{bound} = n_e \rho_{mol} \qquad \text{Equation 5-69}$$

Where ρ_{mol} for a material is given as

$$\rho_{mol} = \frac{\text{Material Density}(g/cm^3) \times \text{Avogadro Constant}}{\text{Mole}}$$

(a) The molecular density of silica would be

$$\rho_{mol-Silica} = \left(2.29g/cm^3\right)\left(6.02\times10^{23}molecules/mole\right)\left(1mole/60.09g\right)$$
$$= 2.29\times10^{22}molecules/cm^3$$
$$= 2.29\times10^{28}molecules/m^3$$

Since SiO_2 has a pair of such bound electrons, the net bound electron density is

$$\rho_{bound-Silica} = 2\times2.29x10^{22}\ \ bound\ electrons/cm^3$$
$$= 4.58x10^{28}\ \ bound\ electrons/m^3$$

(b) The molecular density of water would be

$$\rho_{mole-water} = \left(1g/cm^3\right)\left(1mole/18g\right)\left(6.02\times10^{23}molecules/mole\right)$$
$$= 3.34\times10^{22}molecules/cm^3$$
$$= 3.34\times10^{28}molecules/m^3$$

Since water has a pair of such bound electrons, the net bound electron density is

$$\rho_{bound-water} = 2\times3.34x10^{22}\ \ bound\ electrons/cm^3$$
$$= 6.68x10^{28}\ \ bound\ electrons/m^3$$

(c) The molecular density of $Si(OH)_4$ would be

$$\rho_{mole-Si(OH)_4} = \left(2.0g/cm^3\right)\left(1mole/45.098g\right)\left(6.02\times10^{23}molecule/mole\right)$$
$$= 2.67\times10^{22}molecule/cm^3$$
$$= 2.67\times10^{28}molecule/m^3$$

Because of twin pairs of such bound electrons, the net bound electron density is

$$\rho_{bound-Si(OH)_4} = 4\times2.67x10^{28}\ \ bound\ electrons/m^3$$
$$= 10.68x10^{28}\ \ bound\ electrons/m^3$$

5.5.3 Electron Density by Cascade Ionization in Condensed PCF

If the recombination rate and multi-photon rate are negligible, then Rate of ionization

$$\frac{d\rho}{dt} - (\eta_{casc} - g)\rho = 0 \qquad \text{Equation 5-70}$$

And electron density, $$\rho = \rho_0 \exp(\eta_{casc} - g)t \qquad \text{Equation 5-71}$$

Where, ρ_0, the initial electron density is assumed to be caused by thermal excitation at 1640K (with probability P_r=0.46), hence the initial density for silica, water and $Si(OH)_4$ can be computed as

$$\rho_{0(Silica)} = \rho_{thermal(Silica)} = 0.46 \times 4.58 \times 10^{28} \text{ free electrons/m}^3$$
$$= 2.107 \times 10^{28} \text{ free electrons/m}^3$$

$$\rho_{0(water)} = \rho_{thermal(water)} = 0.46 \times 6.68 \times 10^{28} \text{ free electrons/m}^3$$
$$= 3.073 \times 10^{28} \text{ free electrons/m}^3$$

$$\rho_{0(SiOH_4)} = \rho_{thermal(SiOH_4)} = 0.46 \times 10.068 \times 10^{28} \text{ free electrons/m}^3$$
$$= 4.631 \times 10^{28} \text{ free electrons/m}^3$$

We use the above values to determine the electron density for laser-induced plasma effect in Silica, water and $SiOH_4$.

The following data has been used to determine the cascade ionization in silica, water and $SiOH_4$:

Material band-gap energy	$E_{ion(Silica)} = 9.6eV \times (1.602 \times 10^{-19} J)$ $E_{ion(water)} = 5.6eV \times (1.602 \times 10^{-19} J)$ $E_{ion(SiOH_4)} = 5.6eV \times (1.602 \times 10^{-19} J)$
Electron charge	$e = 1.602 \times 10^{-19} C$
Irradiance laser power	$I = 5 \times 10^{10} W/m^2 \sim 5.5 \times 10^{10} W/m^2$
Electron mass	$m_e = 9.109 \times 10^{-31} kg$
Material mass of molecule	$M_{Silica} = 9.967 \times 10^{-26} kg$ $M_{water} = 3 \times 10^{-26} kg$ $M_{SiOH_4} = 7.49 \times 10^{-26} kg$
Mean time between collisions	$\tau = 1\ fs$
CO_2 Laser frequency	$\omega_{laser} = \frac{2\pi c}{\lambda} = \frac{2\pi \times 3 \times 10^8 m/s}{10.6 \times 10^{-6} m} = 1.778 \times 10^{13} Hz$

For laser impinging on PCF or silica fiber, the electron density is dependent on cascade ionization as well as the diffusion loss. Every electron whose kinetic energy exceeds the ionization E_{ion} energy (i.e. first term of Equation 5.65) would produce another quasi-free electron. Some energy loss may occur due to elastic collision between the electron and the molecule (i.e. second term of Equation 5.65), and the relationship between these two terms is shown in Figure 5-17. The Figure 5-17 shows that for irradiance below $I < 5.482\ W/m^2$, cascade ionization for $Si(OH)_4$ would not occur due to high elastic collision loss.

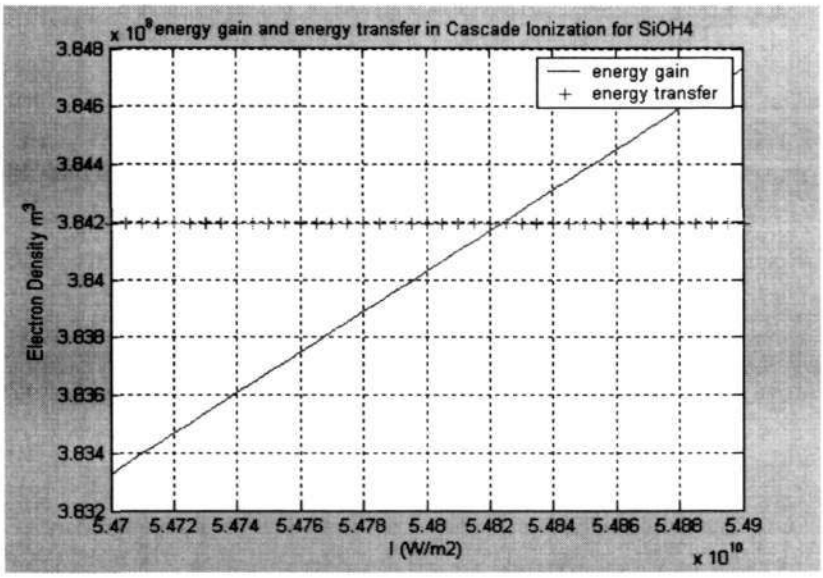

Figure 5-17 Dependence of electron density on irradiance for **Si(OH)$_4$**
Cascade ionization may not occur if **I**< 5.482 W/m^2

The electron density of laser-induced material is dependent on the cascade ionization rate η_{casc} and electron diffusion rate **g**. For laser intensity > threshold intensity, η_{casc} > **g**, hence the electron density in irradiated volume rises rapidly with lasing time. For laser intensity **<** threshold intensity, $\eta_{casc} < g$, therefore the electron density declines rapidly with lasing time

The electron density would increase if the elastic collision and electron diffusion effects are low, and the increase of laser intensity would increase the rate of cascade ionization as well as the electron density as shown in Figure 5-18.

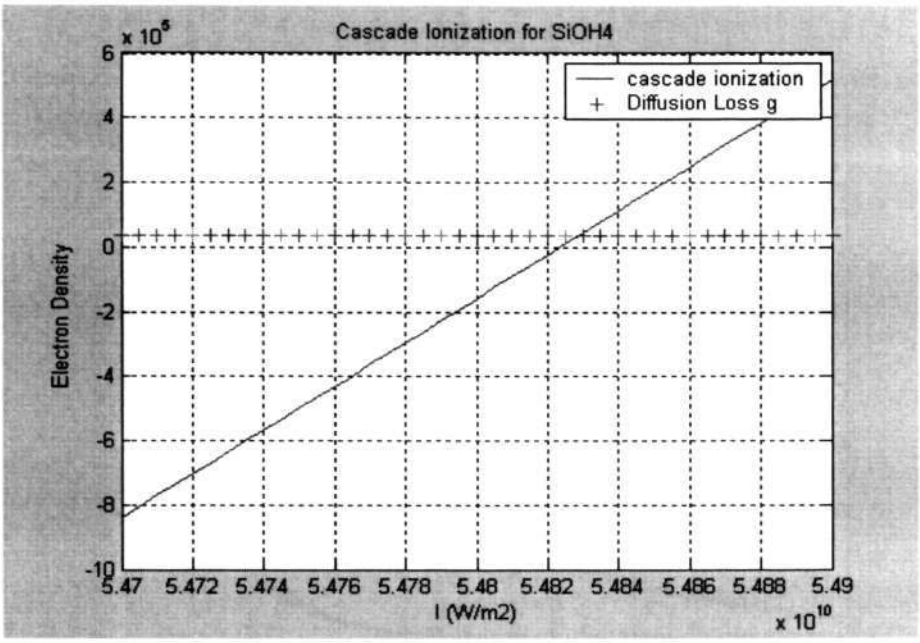

Figure 5-18 Dependence of electron density on irradiance for **$Si(OH)_4$** with cascade ionization and diffusion loss

Since PCF is easily condensed due to the capillary effect, the water condensation causes structural de-polymerization as given by the following reaction

$$SiO_2 + 2H_2O = 2\ Si(OH)_4$$

The formation of silica hydroxide due to water vapor causes reduction of the viscosity and material degradation of silica fiber or PCF. This affects the optical properties of the fibers.

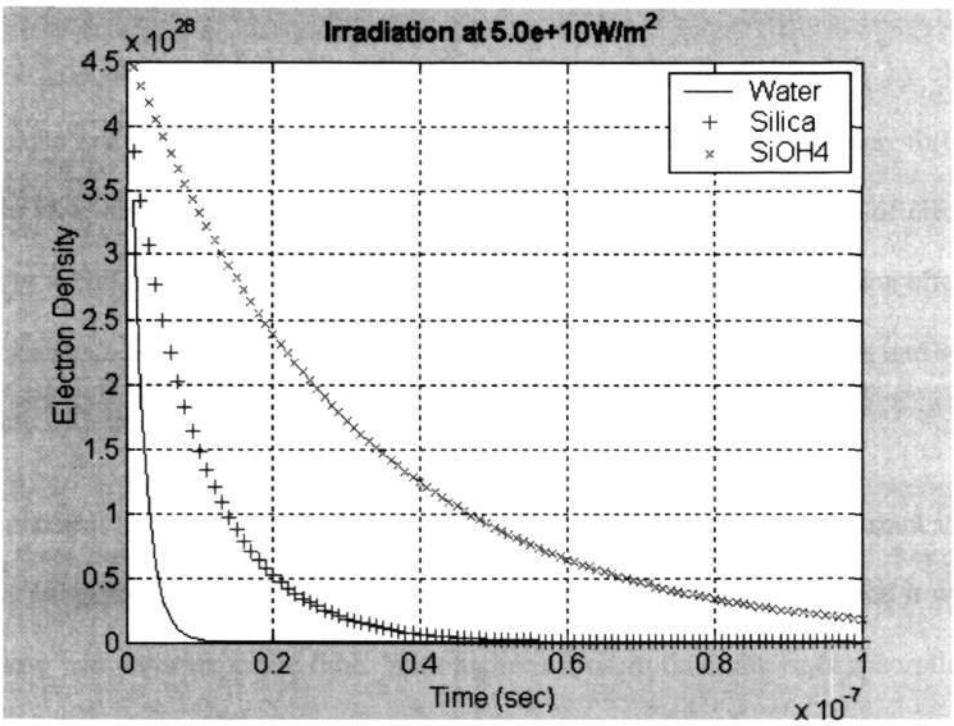

Figure 5-19 Electron density declines with time if the ionization rate is lower than the electron loss rate

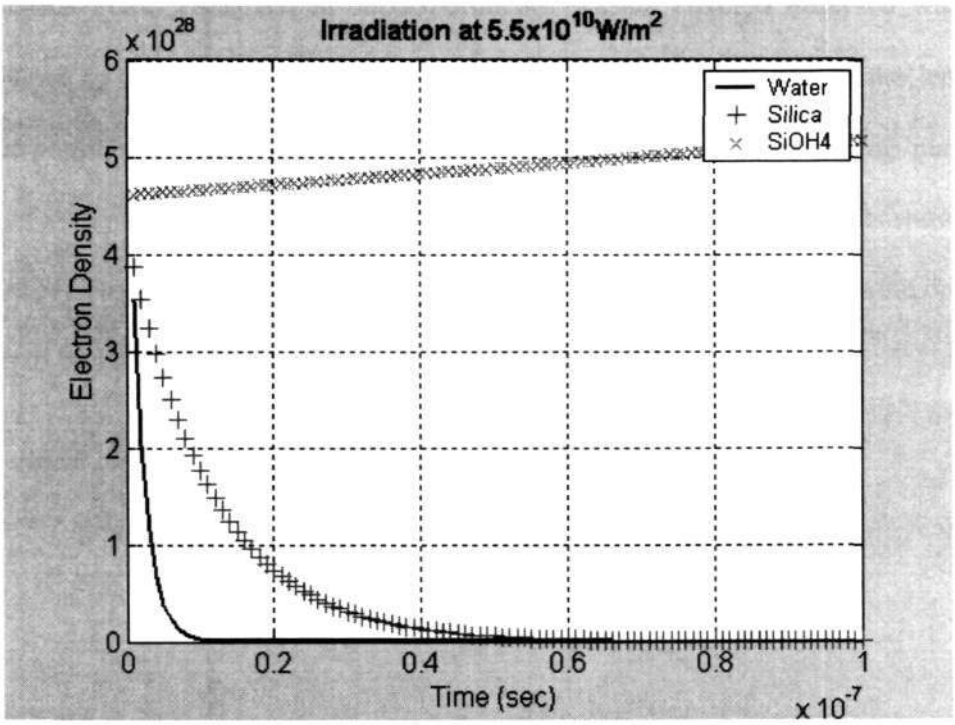

Figure 5-20 The increase of electron density of condensed silica fiber is primarily contributed by the **$Si(OH)_4$** content. The electron densities of SiO_2 and water decline with time.

Figure 5-19 shows that the decrease of electron density is caused mainly by elastic collisions and Figure 5-10 shows that at higher irradiance power of laser, $Si(OH)_4$ would have higher electron density than **SiO_2** and water. The net growth of electron density in $Si(OH)_4$ occurs due to higher cascade ionization than the diffusion effect at the irradiance $\mathbf{I_0}$ of $5.5x10^{10}W/m^2$, even though electron densities of **SiO_2** and water decline with time.

The material absorption of the CO_2 laser in fibers is assumed to be a constant in the above simulation. In reality, the CO_2 laser absorption is time dependent, and it would increase with laser exposure time. With higher exposure time, the laser absorption is likely to be enhanced due to plasma generation in the fiber, and from the simulation results, an irradiance exceeding $5.482x10^{10}W/m^2$ is necessary to create plasma in condensed PCF. However, in our experiments, plasma effect is observed with an irradiance of $\cong 3.585x10^8$ W/m^2 on the NL-PCF, which may be due to the lensing effect possibly created by various effects including shape of surrounding plasma, molten material and capillaries in the PCF. Based on the simulation results shown in Figure 5-13 to Figure 5-15, the lensing effect may change the irradiance in the optical fibers to be $10^{11} \sim 10^{12}$ W/m^2, hence plasma effect may occur.

The critical electron density for Inverse Bremsstrahlung is given as

$$n_{cr} = \frac{1.1 \times 10^{21}}{\lambda_{laser}^2} cm^{-3}$$

Where, λ_{laser} = laser wavelength (μm)

Hence the critical electron density induced by CO_2 laser in optical fiber should be $\cong 10^{19}$ cm^{-3}. For electron density exceeding the critical value, the damping of light does not occur, hence, for efficient thermal effect due to laser plasma, the number of electrons should be below the critical electron density.

Inverse Bremsstrahlung arises from electrons that have gained energy from laser and lose this energy by collisions with ions. In the cascade ionization, the increase of laser irradiance would increase the density of electron cloud that gives rise of plasma effect. Once the laser is removed, the plasma effectively damps the light wave and heats up the materials.

In conclusion, splicing of SMF to PCF depends on the laser intensity (P_0), higher P_0 shortens the splicing time based on 1-D thermal transfer model. As the structure of PCF is different from that of SMF, it is necessary to offset the laser by a few micrometers towards the end face of SMF. 1-D thermal transfer model is an effective model to determine the required laser power and laser exposure time to meet the optimum splice, but it is not sufficient to illustrate the thermal transport mechanism within the fiber. Therefore 3D thermal model for optical fibers (SMF and hollow core Fiber) based on electromagnetic wave theory is used to study the beam propagation and beam scattering mechanisms within the fibers when the laser is absorbed. Finally, rate equations have been used to emphasize the rise of inverse Bremsstrahlung. The increase of electron density occurs only if the rate of cascade ionization is higher than the rate of electron loss. The condensation in optical fibers modifies the optical property of fiber and affects laser absorption accordingly.

CHAPTER 6 EXPERIMENTAL INVESTIGATIONS, RESULTS AND DISCUSSIONS

This chapter presents the experimental investigations performed for splicing of various types of photonic crystal fibers (PCFs) to the standard single mode fiber (SMF). First, the limitations and problems encountered for splicing of PCF to SMF with commercial electric arc splicing systems are described. This is followed by the introduction of the laser splicing technique for obtaining high performance splicing of these types of fibers. The laser induced splicing of PCF is a type of laser-fiber interaction process with a very high probability for involvement of laser induced plasma effects. Hence it is imperative to study these possible laser plasma effects observed on PCF.

6.1 Introduction

In majority of PCF applications, it is necessary to splice photonic crystal fibers (PCF) to standard single mode optical fibers and the choice of implementation of a specific technique is yet to be resolved. Some models of electric arc splicing machine may splice the PCF to SMF but deformation of air holes is always unavoidable, which may cause serious problems for certain applications [4]. In the following sections, we describe the use of the electric arc splicing machine in our laboratory to perform splicing of PCF to SMF and also demonstrate the feasibility of laser fusion for splicing of SMF-to-PCF. An in-house developed laser-splicing system has been

developed to perform these studies. Fusion of PCF using laser is not just a simple melting process; it is very likely that a complex interaction between laser and condensed silica would occur and it is important that such phenomena should be studied to better understand the laser processing of PCF.

The energy transfer from a material consisting of atoms or molecules occurs mainly through three mechanisms: rotational, vibration, and electron transition [159, 161] For a high power laser irradiating a material, the high photon flux increases the possibility of cascade ionization and absorption. The degree of freedom of a molecule is dependent on the level of laser excitation determined by the irradiating wavelength and the energy level in the targeted material such as silica, water moisture or methanol. Therefore in the laser splicing process for fusing SMF-to-PCF, the effectiveness of laser-fiber coupling is largely determined by the matching between photon energy and energies for various transitions in the material.

The requirement of cleaning of PCF prior to splicing may condense the air holes and may complicate the laser interaction process. Methanol, a commonly used cleaning solvent, like water, has vibration energy relaxation, which is complex due to the broad stretching transitions [159, 160]. The molecule may de-localize as the OH excitation may undergo rapid intermolecular hopping to nearby condensation site, hence optical breakdown in the condensed silica is possible at low laser intensities. If the liquid is trapped inside the air holes of PCF, laser scans across the fiber end-face can be employed to minimize the trapped water droplets, but there is no guarantee that the liquid particles would be completely eliminated, especially if the liquid is trapped far away from the fiber end. Once the condensed fiber absorbs sufficient laser energy during the splicing process, there is very high possibility for occurrence of plasma

effect. The increased kinetic energy of electrons in the plasma would further enhance the laser absorption in the material and hence speed up the melting process. If laser power is too high, it may cause damage to the PCF and degrade the splice joint.

The required steps those must be completed prior to laser splicing are (i) cleaning of fibers (ii) proper cleaving of fiber ends and (iii) precise fiber-to-fiber alignment. During the splicing process by CO_2 laser, the parameters such as overlapped stroke, beam's positioning, laser power and laser exposure time must be carefully controlled.

6.1.1 Types of PCFs and their Specifications used in this project

The photonic crystal fibers are new products and have become available in the market only in the recent years. During the progress of our experimental investigations, only limited types of PCFs were available. Another problem was their extremely high cost which restricted us to acquire only a small quantity of these fibers. However, we have attempted to get PCFs from different sources including corporations and research organizations. We are thankful to some of these organizations for providing us with free samples. Mainly four types of PCFs have been used in our experiments. The first two types were provided by the Research Centers from China (Sample 1) and Taiwan (Sample 2). The sample 1 consists of large air holes and sample 2 has much smaller air holes, they are named as $LPCF_C$ and $SPCF_T$ respectively in our experimental studies. Subsequently, we purchased the Large Mode Area photonic crystal fiber and highly non-linear photonic crystal fiber from the manufacturers termed as LMA-PCF and NL-PCF respectively.

The two samples $LPCF_C$ and $SPCF_T$ do not have regular sizes of air-holes traveling along the length of the fiber especially for $LPCF_C$. Their losses are relatively high, but

they have been useful for the fiber splicing investigations in the initial stages when we were not able to get adequate support from the commercial suppliers. The configuration of $LPCF_C$ and $SPCF_T$ are shown in Figure 6-1 and Figure 6-5 respectively. The LMA-PCF and NL-PCF, have low losses and uniform structure, therefore we have concentrated our studies on these fibers. The characteristics of these four types of PCFs are summarized in the table below. *It must be emphasized that information about several parameters (e.g. pitch, number of air-holes) were not provided by the suppliers and we had to estimate these parameters using SEM and other techniques:*

Type	**$LPCF_C$**	**$SPCF_T$**	**LMA-PCF**	**NL-PCF**
Core diameter	≈ 9.584μm	≈ 10.3μm	10.5 ±1μm*	2.6μm*
Cladding diameter	≅100μm	≅125μ m	125μ m*	125μ m*
No of air-holes	14	36	30	>120
Hole size (d)	≈8.33μm	≈ 2.5 μm	2.2μm	~2.6μm
Pitch (Λ)	≈15.83μm	≈ 8.33μm	~7μm	~4.8μm
Image of Fiber	Figure 6-1	Figure 6-5	Figure 6-6	Figure 6-8
Fiber Loss	Not available	Not available	<20dB/km* at λ_{cutoff}=700~1000nm)	0.67dB/km* at zero dispersion wavelength
Features	Very large air holes	Small air-holes	Small air holes	Strut-width to pitch Ratio ≅0.6, Air-filling fraction ≅ 87%

(*) Provided by manufacturers

Fiber splicing technology is not new, but splicing of PCF is very different from the splicing of solid core fiber SMF or erbium-doped fiber. The following section describes the problems encountered to splice PCF to SMF with the electric arc fusion technology.

6.2 PCF-to-SMF Splicing by Electric Arc Method

The electric arc fusion machine is designed for splicing of standard silica fibers but not for PCF. In electric-arc method, high electric field generated by two electrodes at the fiber joint melt the fibers. Even though, this technique has been proven to be effective for SMF splicing, it is not found very suitable for splicing PCF. In the following section, we describe the experimental studies on splicing of PCF-to-SMF by electric arc machine and relevant results are presented.

6.2.1 Technical Limitations on Electric Arc Splicing System

Majority of electric arc splicing machines currently available in the market are either based on core-to-core profile alignment or macro-bending alignment method. [97].

As mentioned in Chapter 4, photonic crystal fiber (PCF) consists of an array of air capillaries along the entire fiber length. Its core (or defect) is made up of pure solid silica (without any doped impurity) surrounded by cladding comprising of staggered capillary tubes. In our attempts to splice the PCF-to-SMF by electric-arc machine, we have, like many others, have encountered serious problems to identify the core-images of PCF using the CCD cameras of the machine. Without clear identification of the core image, most of the existing splicing machines fail to recognize the PCF and

hence fiber alignment by profile projection cannot be performed. Even if the splicing system employs macro-bending alignment technique, it is not highly recommended for PCF alignment since this method may not be applied to all types of PCF. Till now, fiber profile alignment is probably one of the best solutions to align two dissimilar fibers. We also realize that the large heating zone generated by the arcing is another problem with the electrical arc splicing technique [35] as it causes a severe deformation of PCF air holes that may result in very high splice loss at SMF-to-PCF joint.

6.2.2 Experimental Results for Electric Arc Splicing of SMF-to-PCF

Before splicing, the normal stripping, cleaning and cleaving processes are carried out on the fibers. Although the cleaning tissue is only dipped with a thin layer of methanol, the capillary effect in PCF will cause a small amount of liquid to be sucked into the air holes of the PCF. This problem is unavoidable as long as the fiber ends are not sealed. In the splicing process, the SMF and PCF are placed onto the electric arc splicing machine and the standard automated procedures are carried out. We have observed that after fiber alignment and triggering of the arc by the electrodes, the air bubble grew bigger with substantial increase of size in the splicing region as shown in Figure 6-1. At the same time, the electric-arc machine halts suddenly. We have used several models of electric arc splicing machines; unfortunately most of them failed to recognize the PCF.

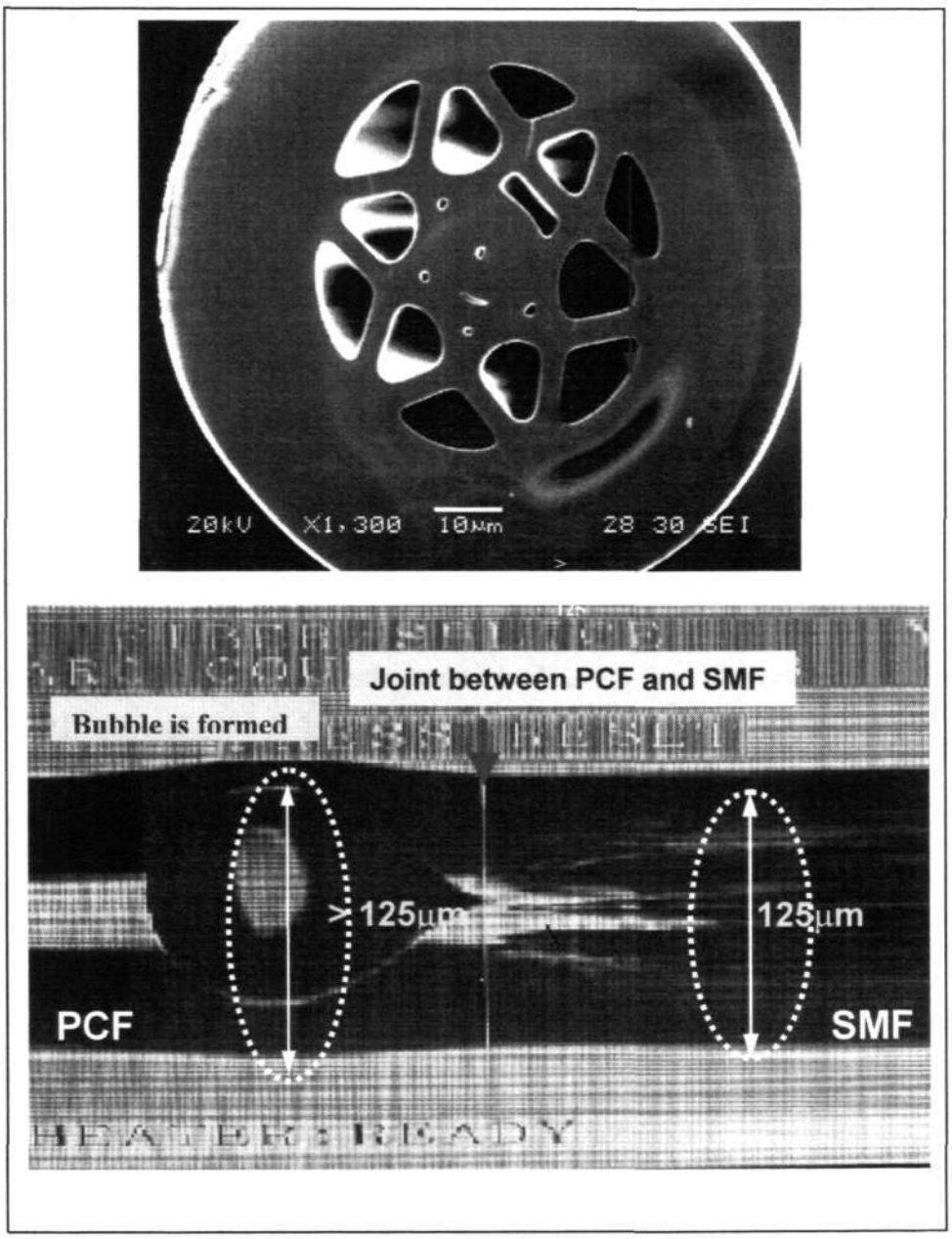

Figure 6-1 (a) Type of PCF used for splicing (b) Bubble formation at the fiber ends in the electric arc splicing process

6.2.3 Discussion on Electric Arc Splicing of SMF-to-PCF

The heat transfer rate and heat propagation in electric-arc generated thermal energy are very much different from the laser-induced fusion in the optical fibers. The heat generated by two electrodes positioned across the splicing region propagates from fiber's cladding surface to the core based on the conductivity of the materials. The electric arc temperature (**T**) affects the thermal conductivities of silica ($\mathbf{K}_{SiO2}$) and air $\mathbf{K}_{air}$ as given by the following relationships [69]:

$$\mathbf{K}_{SiO2} = 0.78 - 0.054\exp\left(\frac{T+379}{354}\right) + 0.165\exp\left(\frac{T+379}{405}\right) \qquad \text{Equation 6-1}$$

$$\mathbf{K}_{air} \approx 4.675\times10^{-4}\sqrt{T} \qquad \text{Equation 6-2}$$

Using the above expressions, the thermal conductivities for silica and air at the temperature of **T**=1573 K are estimated to be $\mathbf{K}_{Si}$ = 8 $Wm^{-1}K^{-1}$ and $\mathbf{K}_{air}$ =1.87x10^{-2} $Wm^{-1}K^{-1}$ respectively, whereas the thermal conductivity of methanol, $\mathbf{K}_{m}$, is given to be approximately 0.18 $Wm^{-1}K^{-1}$ [163]. The data show that the heat generated on the silica surface has higher resistance to pass to the core as the transmission medium is air, or air-holes filled with liquid. Therefore it is difficult to maintain a constant temperature over the cross-section of the fiber within a short period. With increase in the number of air-holes and size of air hole, the heat transfer rate from outer silica-surface to inner core would be significantly lower especially if it is condensed.

Although the thermal conductivity of the silica is about ≅40 times larger than that of the methanol, its vaporization temperature ≅21 times higher. In the Figure 6-1, the volume expansion of PCF is obvious. Thermal expansion ΔV of PCF is dependent on

the thermal expansivity (β) and temperature (T) and is given as $\Delta V=V_0(T)$, where V_0 is the initial volume . The volume expansion for liquid is much higher than that of the solid. The thermal expansivities for silica, methane alcohol, and water are $\beta_{Si}=1.2\times10^{-6}/°C$, $\beta_m=1.19\times10^{-3}/°C$, and $\beta_{H_2O}=2.1\times10^{-4}/°C$ respectively. If a constant temperature of 1300°C is assumed across the full cross-section of the fiber, the volume expansion at of PCF in silica should be 1031 and 167 times lower than methanol and water respectively. The rate of heat flow drops slightly towards the core due to air holes, but the overall temperature still remains high. At high temperature, the methanol is vaporized with rapid volume expansion that forces the bubble out of the fiber end as shown in Figure 6-1. The process has been observed more than 10 times and no splicing could be performed. Successful splicing could only be obtained by using the laser fusion system as shown in Figure 6-2. Detailed explanation of laser splicing process and phenomena will be discussed in the later sections.

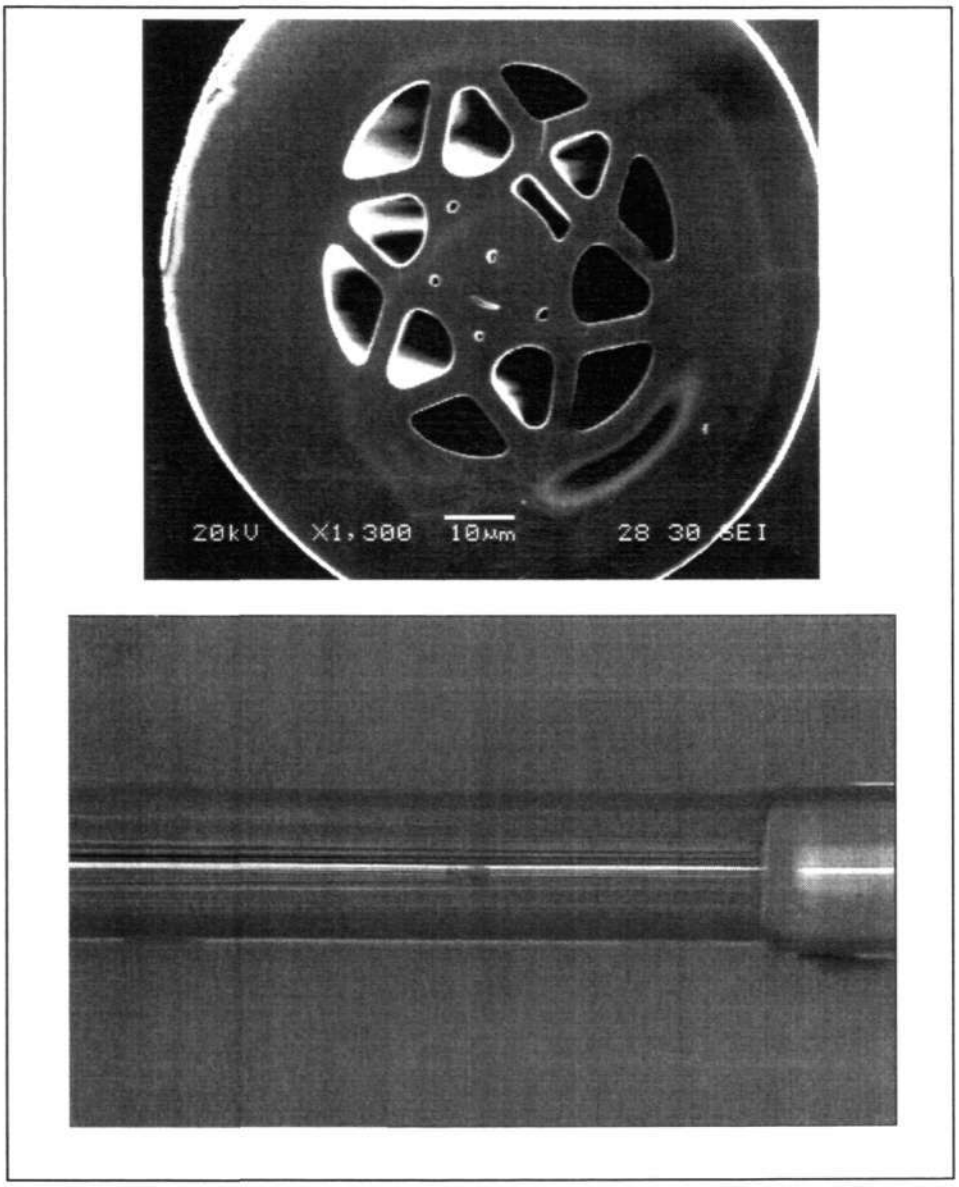

Figure 6-2 First successful splice obtained between non-standard diameter $LPCF_C$ and SMF by laser splicing system

6.3 PCF-to-SMF Splicing Using Laser Fusion Technique

Laser interaction in photonic crystal fibers (PCF) is a complicated coupling process due the micro-structural cross section of the PCF. The regimes for laser interactions to PCF and SMF may include: air on fiber's surface or above the fiber's surface, silica and air hole layers as discussed in Chapter 5. Every type of PCF has its unique air-hole size, hole-to-hole spacing, and hole pattern according to its functionality and applications; therefore it is not an easy task to have standard parameters for splicing of PCF. In the following experiments, we report the results on splicing of $SPCF_T$ (similar type to LMA-PCF), LMA-PCF and NL-PCF with the standard single mode fiber of diameter ≅125μm. The $LPCF_C$ with large air-holes is quite similar in structure to NL-PCF, hence the experimental results obtained from this fiber may provide a good basis for explaining effects in NL-PCF. However, a 0.2m long of $LPCF_C$ given by the institution has been completely utilized for experiments with electric arc splicing process. The $SPCF_T$ and LMA-PCF have low air-filled fraction, hole-to-hole spacing larger than the air-hole diameter, and core diameter comparable to SMF; therefore it is much easier to splice these types of fibers compared to the NL-PCF. The NL-PCF consists of high air-filled fraction with thin silica strut, which can be easily damaged during the splicing process and may result in high splice loss. Also, due to its small core diameter of NL-PCF, core-to-core alignment between this fiber and SMF is extremely difficult to achieve and a slight core-to-core mismatch would further worsen the splicing performance.

Trapping of moisture or methanol inside the air holes of PCF is a common problem. In addition to introducing high transmission loss due to OH^- ion absorption, this contamination also affects the fiber-melting threshold and temperature distribution

over the fiber cross-section. Hence, the studies of laser power interactions with the PCF and condensed PCF would provide us a better understanding of temperature changes and thermal effects in these fibers.

In this project, a 10W CO_2 laser with a Gaussian beam diameter of ≅500 μm is used to splice the fibers. The required laser power in the splicing process is varied between 1W to 5W. With a view to obtain a good splice joint and keeping in mind the various problems in fusing of dissimilar fibers, the following steps have been implemented:

- While cleaning the fiber tips by wet tissue, the quantity of methanol is kept to minimum and the wiping is done as swiftly as possible. This should reduce migration of cleaning solvent into the air holes of PCF.
- Once the fibers are placed on the xyz alignment stages, a laser beam with a power of 1 W is irradiated onto the fiber end-faces or scanned axially along the length of the fibers for ~ 1 second. This step should reduce condensation trapped inside the air holes. If the condensation is excessive, this section of fiber should be cut and removed.
- Condensation might be more serious for PCFs with large air-holes than those PCFs with smaller air holes. Also large air hole PCF usually has thin strut width and therefore control of laser power would be more critical.
- In the case for splicing of similar fibers, a slight alignment mismatch is compensated easily due to self-alignment during the fusion process and splice loss may not increase significantly. For the dissimilar fibers like SMF and PCF, self-alignment is very limited, and even with slight misalignment between two fibers ends, the increase in splice loss can be severe. Hence, the cleaved surfaces for SMF and PCF must be extremely

flat and smooth to prevent fibers slipping against each other which otherwise can cause serious alignment mismatch during the splicing process. The situation is further complicated due to necessity of maintaining the fiber-overlapped stroke in the laser splicing process.

- For a PCF with higher air-filled fraction, the overlapped stroke can be lower. For example, the fiber end-face overlaps for NL-PCF and LMA-PCF are 3μm and 5μm respectively.
- Laser is placed more towards the SMF than the PCF from the joint at the fiber end-faces. This is to maintain low deformation of air-hole since the laser power to melt SMF is generally higher than that for the PCF.

In the splicing process, stripping and cleaving steps of PCF are similar to those used for standard single mode silica fibers. After cleaning, about 0.5cm long fiber ends are cleaved and even then, there is no guarantee that condensation would not be left inside the air capillaries. Based on the common occurrence of bubble formation during the electric arc splicing, we believe that low condensation still remains inside the capillaries. These tiny water droplets cannot be easily detected under the microscope. In order to understand the laser-interaction in the PCF, we have used a high-speed camera with 1000 fps (frame per second) to capture the real time images of the splicing process as shown in Figure 6-3.

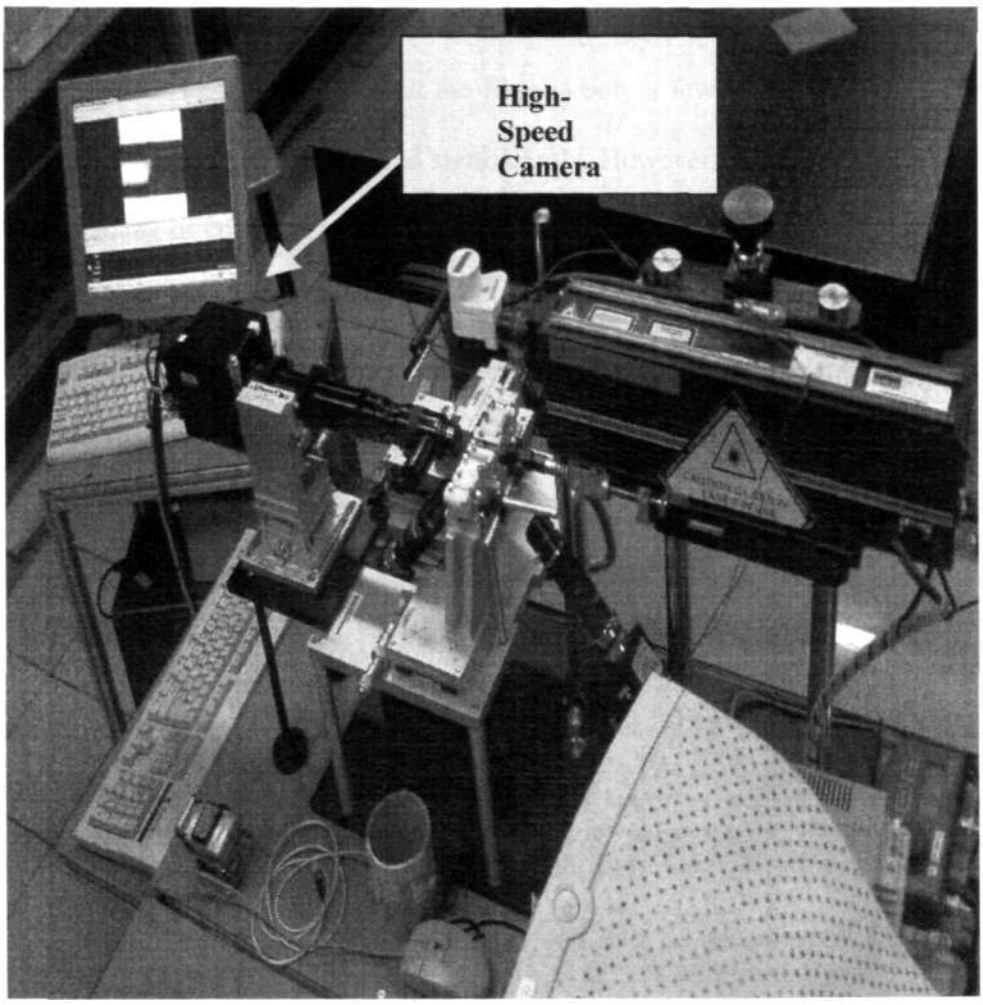

Figure 6-3 High Speed Camera with recording time 1000fps is placed horizontally towards the spliced fibers

6.3.1 Experimental Results on Laser Splicing of $SPCF_T$/LMA-PCF to SMF

As the required laser power to melt the fiber is only a few watts, it might seem that the size of CO_2 laser can be reduced significantly. However, this, in reality, is not true as the majority of commercially available CO_2 lasers have a minimum output power of 10 W. The size of the CO_2 laser, in general, increases with its output power and we did manage to acquire a custom made 5W CO_2 laser with a physical size of $300x100x100mm^3$ for our laser splicing system. Due to the poor stability of output power of this laser, we could not use it for our system. If a stable and reliable laser operating at a wavelength of 10.6μm with an output power ≤5W, then the size of laser splicing system can be reduced significantly. In our experiments with a 10W CO_2 laser having a beam size of 500 μm, a typical power of 3W is required to splice the fibers. With the hope that CO_2 lasers with 5W (or lower) power would be available in the future. In our experiments, we have employed 3-5 W of power for splicing of $SPCF_T$-to-SMF and LMA-PCF_T-to-SMF, which will be described in the following section. Depending on the beam diameter, the power requirement to melt the fiber may be different compared to the above values.

(a) **Laser splicing of $SPCF_T$ using low laser power**

The $SPCF_T$ used in this experiment is quite similar to the LMA-PCF with small size of air-hole (d_{hole}), index profile d_{hole}/Λ = 0.388 and period Λ =9.01μm. A 3.1W laser beam is positioned with an offset of about 5~10μm towards the SMF than PCF from the fiber joint. The complete splicing process is summarized in Figure 6-4 and the total time for splicing of these fibers is about 3 - 4 seconds,

including the time required for preheating (~1sec), fusing (~2sec) and annealing (~1 sec).

The image of the spliced fiber is shown in Figure 6-5, which illustrates the air hole deformation in the $SPCF_T$ to be quite small and the capillary section near to the spliced region can still be seen. The overall splice loss is obtained for these types of fibers is about 0.6-09dB if the excluding discrepancy due to MFDs.

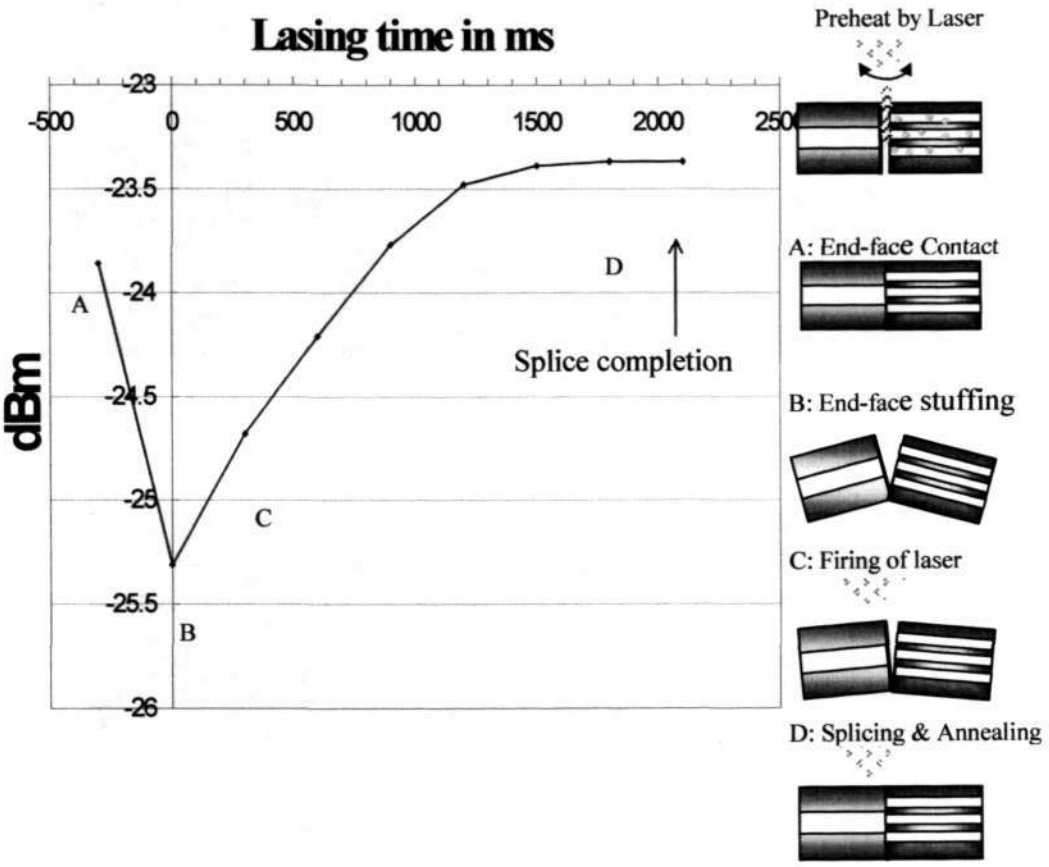

Figure 6-4 A complete Splicing Process for Splicing of $SPCF_T$ to SMF

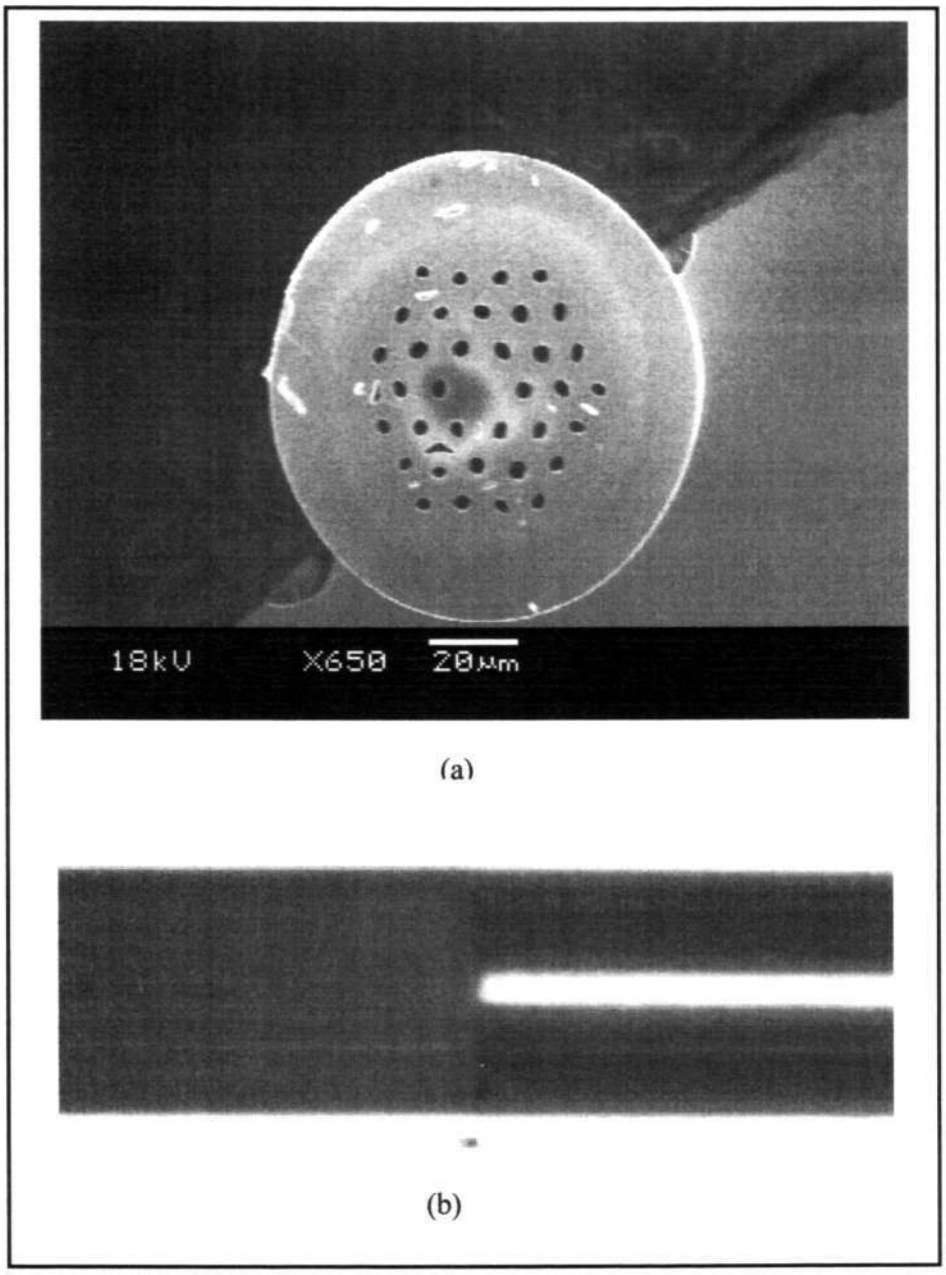

Figure 6-5 (a) Top image illustrates the cross-section of $SPCF_T$ with an index profile of $d_{hole}/\Lambda = 0.388$ and period $\Lambda = 8.5\mu m$. (b) Bottom image shows the $SPCF_T$ -to–SMF splice joint.

(b) Time Reduction on Splicing of SMF-to-LMA-PCF by Higher Laser Power

For very low laser power, melting of fibers and splicing may not occur at all. Similarly the fibers may completely evaporate at very high power from the laser. However, we have observed that, splicing of fibers would occur at several power levels, but a low laser power (approximately 3W) requires longer splicing time. Hence, to improve the efficiency of splicing, experiments have been performed with high laser power of 4.4 W and a set up involving high-speed camera has been used to monitor a complete splicing process.

Based on the theoretical simulation results obtained in Chapter 5, approximately 120msec of exposure time is required for splicing of LMA-PCF (Figure 6-6) to SMF with a 4.4 W power from the CO_2 laser. The laser beam is positioned with an offset is about ~5μm towards the SMF which to bring the fibers to the desired [125] semi-liquid state having a temperature of about 1640K.

A real time imaging (Figure 6-7) performed during the splicing of SMF-to-LMA-PCF shows that the time required for reaching the semi-liquid state in the fibers is 110ms to 120ms. This is in good agreement with the theoretically calculated value of 120ms and also gives a good splice joint with very little air-hole deformation.

In the SMF-to-SMF splicing, if laser exposure time is slightly higher (120-140ms) and due to the absence of capillaries, this does not have any adverse affect on the splice performance as compared to the splicing of PCF- to-SMF. In order to optimize the laser exposure time and minimize the deformation of PCF, we have utilized high-speed camera as a tool to determine the best splice based on the images taken within a

time frame of every millisecond. From the images, it is observed that the air hole deformation occurs only near the upper section of fiber surface where the laser beam impinges with an exposure time greater than 120ms. A slight collapse of air holes (2~4 air holes nearest to the fiber surface) is observed far away from the defect and the measured splice loss of about 1.0dB has been obtained. This shows that the splice loss is not seriously affected due to air-hole collapse as the splice loss is affected by many factors such as alignment, laser stability etc.. PCF is very sensitive to fluctuation of laser power; a slight variation of power can affect the fiber temperature and hence the splicing performance. Therefore, the laser power and laser exposure time must be determined correctly to prevent collapse of air-holes.

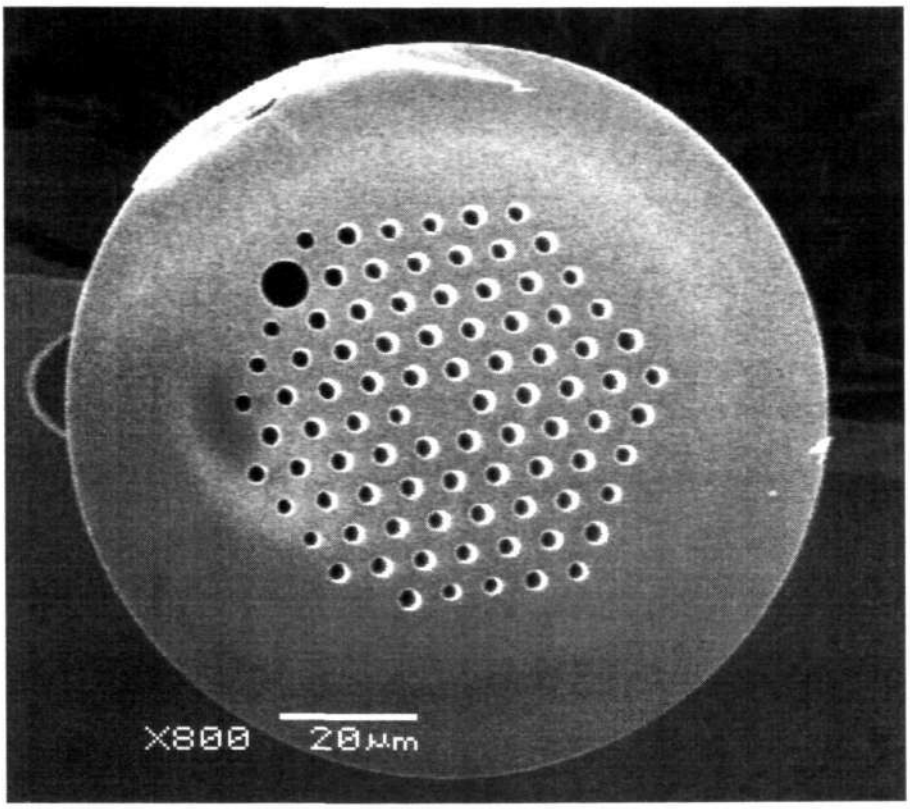

Figure 6-6 Configuration of Large mode area - PCF (LMA-PCF)

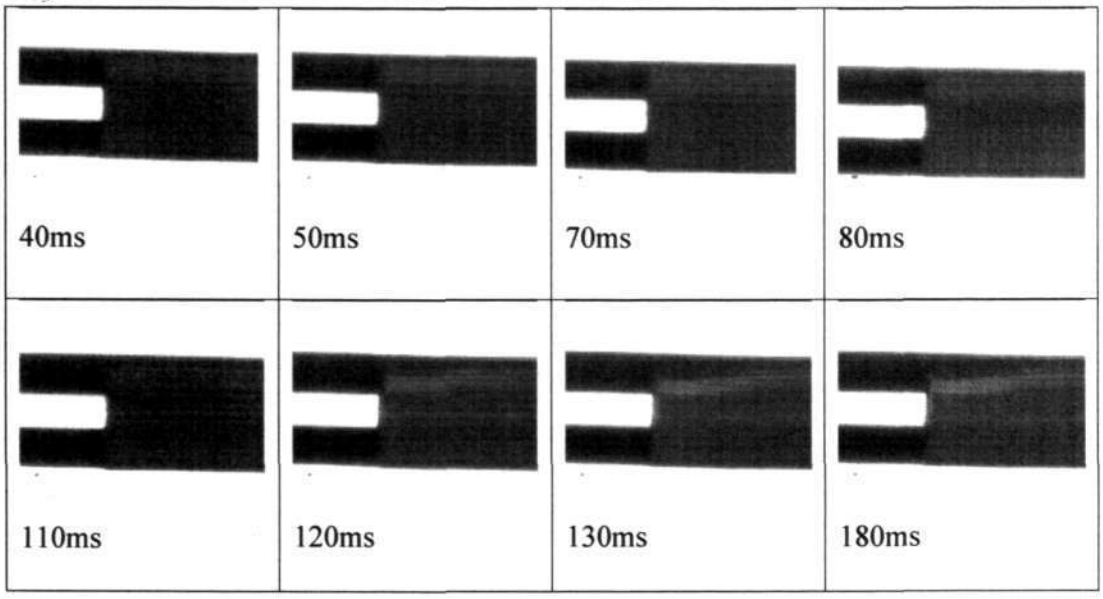

Figure 6-7 Time resolved fiber splicing process under the 4.382W laser irradiation

6.3.2 Experimental Results on Laser Splicing of NL-PCF-to-SMF

The core diameter of NL-PCF used in this experiment is ≅2.6μm, which is about 1/3 of SMF diameter; and its direct fiber end-face coupling loss to SMF end-face is simulated by the FDTD is about 5.686dB. Furthermore, the large air-holes of NL-PCF generally traps more of the cleaning solvent (than the LMA-PCF), therefore to reduce the condensation, it is recommended that the fiber ends be exposed for more than 1 second with 1~1.2W of laser power. In this experiment, an *Optical Spectrum Analyzer* is used to measure the fiber-to-fiber coupling loss caused by condensation. In Figure 6-9, the transmission signals over the wavelength of 1200-1700nm are almost lost if the air holes of PCF are seriously trapped with methanol. Further, Figure 6-10 shows improvement in the transmitted signal by ~6dB (at λ=1315nm) after scanning the fiber ends with ≅1.2W of laser power. This experiment gives a good indication about the level of laser power that can reduce the moisture trapped in air holes.

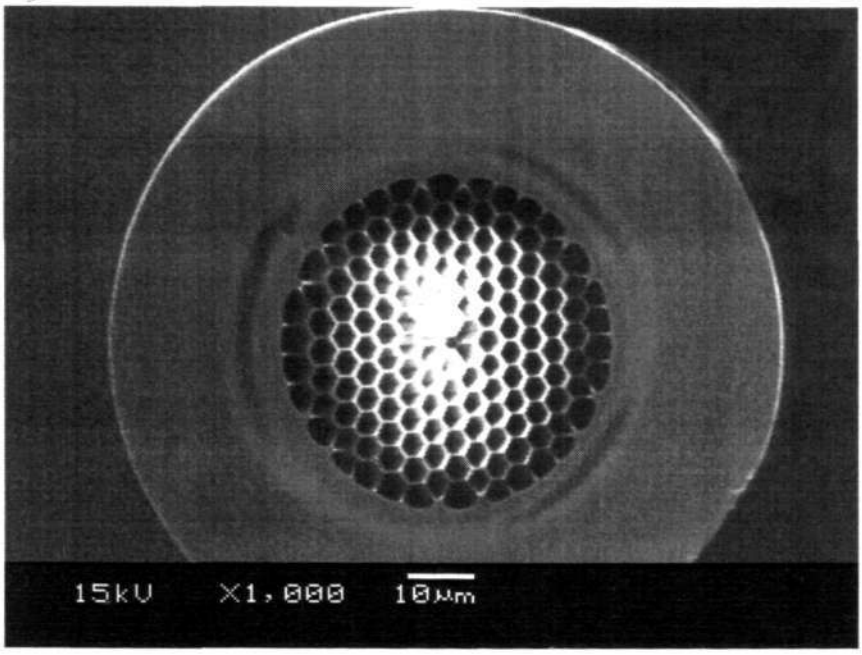

Figure 6-8 Configuration of Highly Non-Linear PCF (NL-PCF)

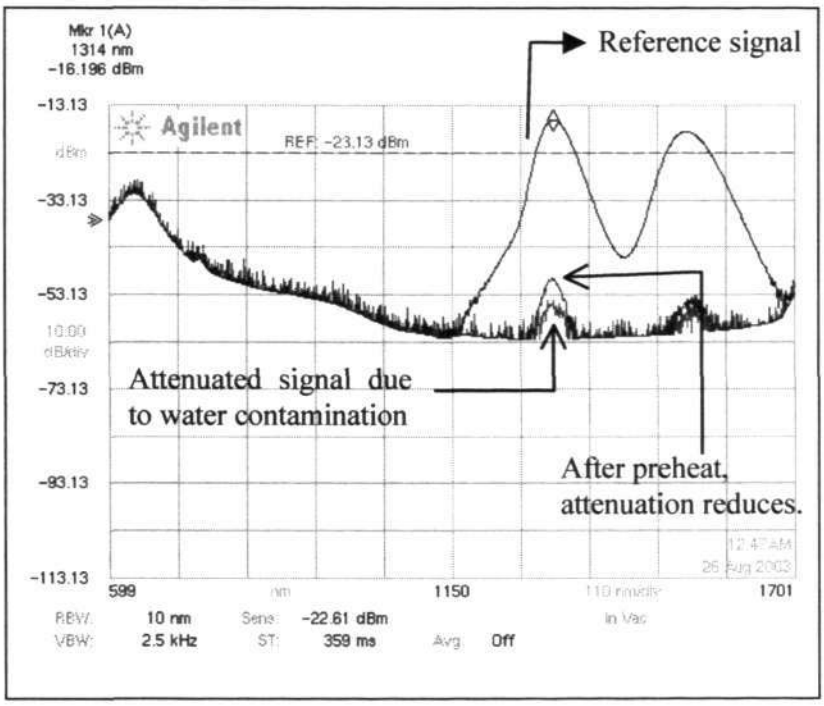

Figure 6-9 Transmitted signal over the wavelength of 1200-1700nm is almost absorbed by methanol.

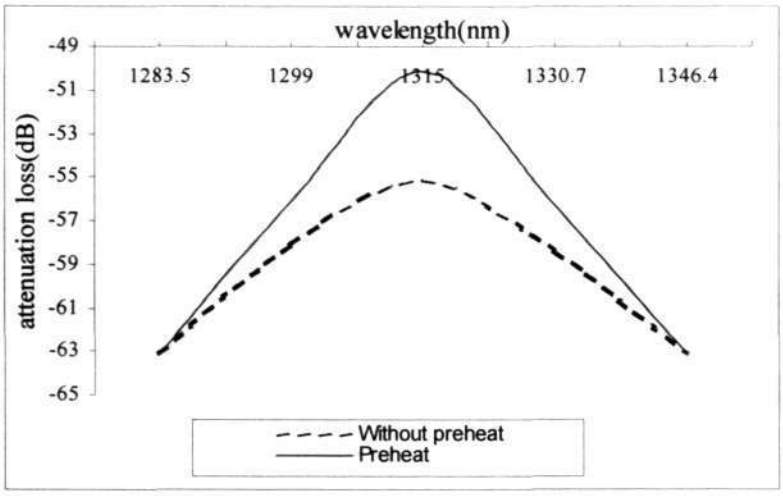

Figure 6-10 Improvement in the Transmitted power due to Reduced Condensation

Based on the simulation results, it is derived that the peak intensity of 4.4W laser beam should be positioned with an offset of about 29 μm towards the SMF from the fiber joint, and a fiber-overlapped stroke of ≈3μm should be introduced before splicing. On certain occasions it has been observed that, a gradual increase of laser power prevents fiber end-faces slipping against each other when the laser impinges onto the overlapped fibers. For example, a laser power of 2.5W with an exposure time of 100ms softens the fiber ends and gradually brings the two fibers closer. Subsequently, a laser of 4.4W with exposure time of ≅120ms is used to splice the two fibers with minimum splice loss. The high-speed imaging system mentioned earlier records the complete process to confirm the simulated values given in Chapter 5. Even though, the ideal exposure time for splicing is estimated to be 120 ms, a higher laser exposure time of 300ms has been employed to monitor and efficiently capture the complete splicing process as illustrated in Figure 6-11.

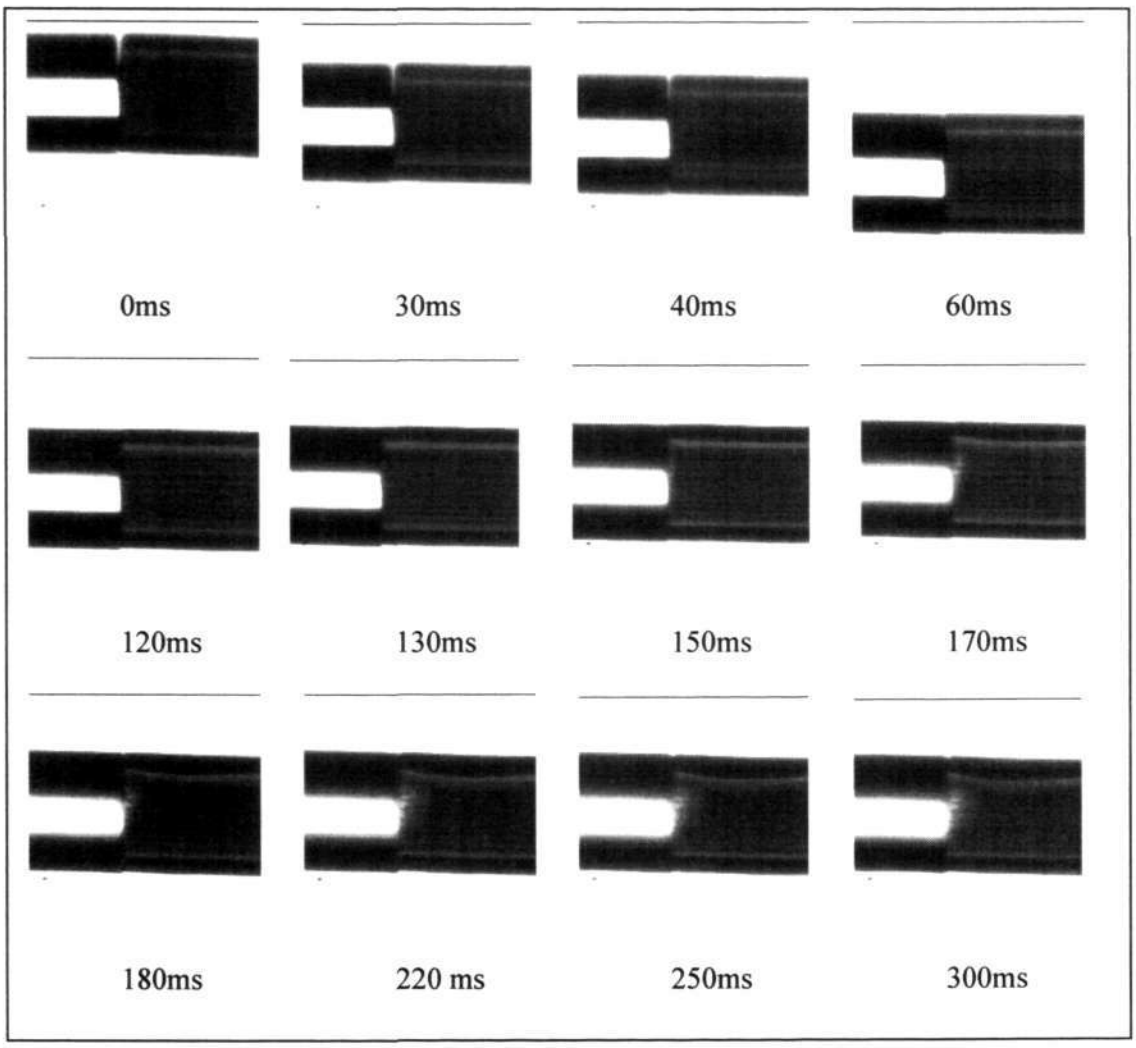

Figure 6-11 Real time imaging of laser splicing process for joining of Time resolved splicing process of SMF to NL-PCF

The effective splicing of fibers with an exposure time of ≈120ms is in good agreement with the calculated value based on the 1-D thermal transfer model. For exposure time >130ms, we observe that the plasma grows from the center of splice joint and moves axially towards the NL-PCF as shown in Figure 6-11. As lasing time increases, the plasma moves farther away from the splice region and the extra bending of air capillaries is observed near to the uppermost layer of air-capillaries.

In order to fully understand the movement of plasma, another experiment with an extended laser exposure time ≅1 second has been carried out. A serious deformation of the NL-PCF is observed far away from the fiber joint, which is out of the field of view (FOV) of the high speed camera; hence its image (Figure 6-12) is captured by one of the cameras in the laser splicing system. The deformation is more severe at the uppermost surface compared to the lower surface of PCF.

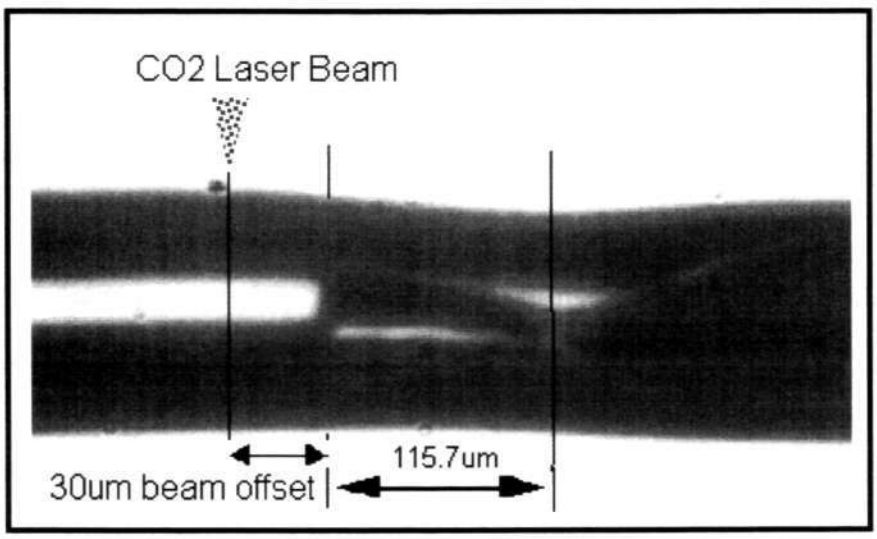

Figure 6-12 Air holes of NL-PCF are compressed and deformed far away from the center of the laser beam spot placed ~30μm away from the fiber joint at the SMF. The image shows the migration of the hottest spot by 115.7 μm away from the fiber joint.

From the above experiments, it is noted that, as the laser exposure time increases, the fiber's hottest spot in the PCF is shifted away from the center of the laser beam spot. Based on the images shown in Figure 6-11, the shift of air-hole deformation for laser exposure times of 220ms and 300ms are at 53.8μm and 71.42μm respectively; hence the velocity of the shift is 0.22mm/sec approximately assuming linear behavior.

6.4 Discussions and Analysis

A good splice between PCF-to-SMF is achievable if the fiber contamination and fiber alignment mismatch are kept in minimum. As it has been mentioned in the last chapter, the laser interaction with PCF might involve any of the three layers of PCF (i.e. atmospheric layer, silica layer and air-hole layer). If the surface of optical fiber is clean, the atmospheric layer above it should be transparent to CO_2 laser and hence the top layer of silica fiber absorbs laser directly. The resonance between laser frequency and silica lattice enhances the thermal energy propagation in the silica layers of the PCF as air holes are transparent to laser, therefore the heat transfers rapidly into the fibers. This process enhances the temperature distribution over the fiber-cross section consequently reduces the air-hole deformation of PCF and strengthens the fiber joint if the PCF is not condensed.

In the splicing process, it is not easy to check that whether the PCF to be spliced is condensed or not, especially if the PCF consists of large sized air-holes. If PCF is trapped with liquid, laser interaction with PCF is not only at the silica layer, but also extends to the condensed layer.

With increased condensation in PCF, the optical breakdown threshold declines and the liquid affects the splicing process, making it difficult to get a good splice. The condensation in PCF increases the rate of absorption of laser, resulting in increased kinetic energy of existing (seed) electrons and enabling them to knock out additional electrons from the lattice. Continuation of this process would lead to generation of plasma, which further enhances the laser absorption in the PCF.

In the following sections, analysis of the splice results obtained on splicing of commercial available PCF fibers (i.e. LMA-PCF and NL-PCF) to SMF is carried out. Subsequently, the analysis on the splicing of condensed PCF and effects observed with high laser power are reported.

6.4.1 Splicing Results

In general, the CO_2 laser impinging on optical fiber generates thermal energy with uniform spread across the fiber cross-section and hence it is effective and efficient process to splice PCF to SMF. Our experimental results confirm the formation of good splices between LMA-PCF-to-SMF and NL-PCF-to-SMF using 4.4W laser beam with exposure time of 115~120ms and beam offset of 2-5mm and 29mm respectively. In practice, a slight fiber-to-fiber misalignment or imperfect fiber-cleaved angles may be present prior to splicing. Hence, it is necessary to consider the possible coupling losses caused by mode field diameter (MFD) mismatch, tilt angle, and the axial misalignment between PCFs to SMF. Table 6-11 summarizes the simulated coupling losses of PCFs-to-SMF. In addition the attenuation losses for PCFs are included.

Table 6-1 Possible Losses in the Splicing of PCF-to-SMF

Status / *Coupling of SMF-to-*	5° tilt (dB)	0.2um Axial Misalignment (dB)	Direct Coupling Loss (dB)	PCF Attenuation Loss (dB/km)
LMA-PCF Core diameter = 10.5 ±1.0μm	0.001	0.05	0.09	20
NL-PCF Core diameter = 2.6μm	0.004	0.25	5.735	41

Table 6-2 Practical Results for Splicing of PCF-to-SMF

Splicing SMF-to-	Beam Offset	Recommended Overlapped Stuffing	Measured Splice loss
LMA-PCF	≈5μm	≈4~5μm	0.6~0.9dB
NL-PCF	≈29μm	≈3μm	7.9 ~9.3 dB

Quantitative loss estimation for SMF-to-SMF splice is simpler than PCF-to-SMF splice as the possible splice loss for the latter is affected much more by core-to-core misalignment and the fiber deformation at the splice regime. Also, the splice loss of PCF-to-SMF is not so straightforward since they are dissimilar fibers with different MFD, different refractive indices etc. The objective of achieving a good splice of

PCF-to-SMF is to maintain the original structure of PCF and SMF; hence it is imperative to maintain low deformation of PCF in order to achieve a low splice loss. The direct coupling loss caused by MFD mismatch for LMA-PCF-to-SMF is low as seen from the simulation result. However, this loss is very high for NL-PCF to SMF joint. High splice loss is mainly contributed by fiber-to-fiber misalignment and deformation of PCF and SMF. The following example illustrates the method used for determining the splice loss.

Example: Splice loss of LMA-PCF-to-SMF

Direct measured loss after splicing = 0.88dB

Based on the simulation result, the direct coupling loss = 0.09dB (since $MFD_{LMA\text{-}PCF} \cong MFD_{SMF}$)

Actual Splice loss = Actual loss – Direct coupling loss =0.88dB - 0.09dB = 0.71dB

Therefore, the splice loss of 0.71dB is caused by fiber-to-fiber misalignment, fiber deformation and other unknown losses due to unknown factors in the splicing process. Table 6-2 shows the splice losses of LMA-PCF-to-SMF and NL-PCF-to-SMF. The splice loss for $SPCF_T$-to-SMF is around 1.3~2.8 dB. The splice loss calculations for $LPCF_C$ are not performed due to its non-uniform hole-sizes along the length of fiber and extremely high attenuation fiber loss.

6.4.2 Volume Expansion and Compression in PCF During the Splicing Process

In this section, we examine the impact on splicing of PCF-to-SMF if the PCF is seriously condensed. In the electric arc splicing, we observe the formation of a single bubble at the fiber joint because the electric arc induced thermal energy propagates from the top surface towards the inner core of the fiber and the condensation vaporizes slowly. However, we have never observed a single bubble escaping out from the PCF-to-SMF interface during the laser splicing process. Laser interaction with the fiber is a process of inverse Bremsstrahlung (IB) absorption, which depends on the kinetic energy of electrons and electron density in the plasma. If the fiber is condensed, the laser interaction with the PCF easily leads to the generation of quasi-free electrons in the conduction band. The photon absorption does not result in direct conversion to thermal energy; therefore, the depth of penetration of fiber keyhole is not only caused by the thermal conductivity but also due to the damping of electrons during the IB absorption. The thermal coupling is efficient if the electron density is lower than the critical level of 10^{18} electrons/cm^2.

In this section, we focus on the laser induced heating process for the splicing of SMF-to-condensed PCF and explore the formation of any bubbles in the laser fusion technique. This experiment was carried out before we acquired the commercial PCFs. In order to monitor the laser-fiber interaction effect, a $LPCF_C$ having large air-holes over the fiber cross-section has been fused with SMF by using a 3.8W laser pulse having an exposure time of 50 ms. Two such laser pulses are sufficient to join the fibers together and no bubble formation is observed (Figure 6-13a) but the spliced joint is weak and contains trapped solvent. This demonstrates that the laser-induced thermal energy rapidly penetrates into the PCF, vaporizes and clears the condensation

near to the edge of fiber ends, but leaves some solvent in the fiber section far away from the fiber edge. In order to confirm the trapping of condensation inside the PCF, a few more pulses of laser are applied to the fiber joint. In this process, we observe a gradual volume expansion of PCF as the laser exposure time increases due to the trapping of vaporized liquid inside the air-holes is unable to escape through the fiber joint. Figure 6-13(b) shows the presence of bubble pockets in the PCF, which has been captured by one of the cameras in the laser system. A continual laser power applied to the fiber joint would burst the bubble pockets as shown in Figure 6-13(c, d). After the release of trapped liquid (Figure 6-13e), a lump is formed at the fiber joint in the direction of the laser beam as shown in Figure 6-13(f).

This above experiment confirms that the laser-induced thermal energy spreads faster into the fiber-joint compared to the electric arc induced thermal energy.

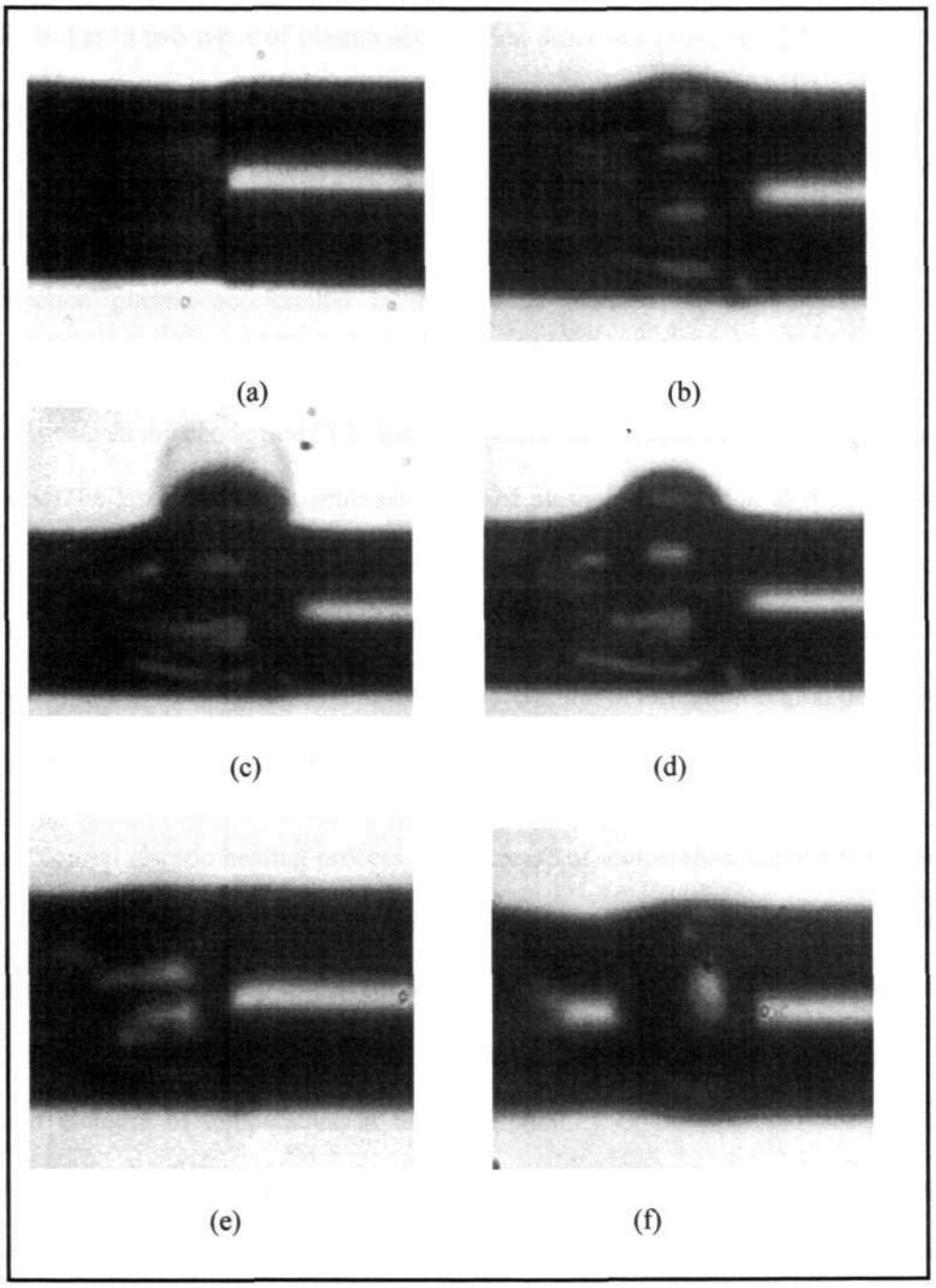

Figure 6-13 (a) The interface between $LPCF_c$ and SMF is joined but it is weak. (b) Few more laser pulses cause the trapped water to expand faster than the silica capillaries, *bubble-Pockets* are formed within the PCF. (c) Water bubble is formed and gradually bursts out to the ambience (d) Water bubble disappears (e) Last two process repeat as more laser pulses apply, less water is trapped. (f) Water bubble is pushed into the lump after molten silica compressed.

Why the lump is formed in the direction of laser and not in other directions? Perhaps this is due to two types of plasma acceleration processes [164, 165.] during the laser fusion processes namely, *Forward Plasma Acceleration* and *Reflection Plasma Acceleration*. Forward plasma acceleration is the plasma formation accelerating in the direction of laser beam and from the lower surface of the fiber. However, the reflection plasma acceleration is the plasma induced on the target fiber and accelerated against the incident laser pulse. These two types of plasma formations may occur in the condensed PCF due to the unstable characteristics of liquid in the air holes. The laser pulse first generates forward plasma acceleration at the silica layer and subsequently causes thermal breakdown in liquid with a strong reflective acceleration. This phenomenon is observed when the laser pulses are continuously applied to the splicing region and the keyhole at the deformation region does not go deeper.

In a normal electric heating process, the increase of temperature vaporizes the liquid and the expansion of volume depends on random movement of molecules. However, laser induced heating onto the condensed silica is caused initially through phonon absorption followed by the IB absorption as explained in the previous chapter. The rapid increase of temperature in the close vicinity of the spot induces a sudden vaporization and ionization of material along the narrow channel of keyhole along the beam axis. The increase of temperature gives rise to the photon absorption and speeds up the fusion process. If the air holes are not completely free of condensation, the light source quickly interacts with the lower forbidden band-gap of liquid near to the SMF-to-PCF splicing region. The molten silica and liquid diffuse rapidly, followed by their rapid cooling after the laser power is removed. The process of redistribution of

the solute most likely freezes up the molten glass and hence no volume expansion occurs in the PCF. The sudden drop of temperature reduces the inner pressure within the air holes, hence compresses the fiber joint to generate a lump at the splice regime, which have observed in our experiments.

The $SPCF_T$ has smaller air-holes and thicker silica layer than the $LPCF_C$, therefore the amount of trapped liquid and the resulting volume expansion is much smaller. With longer laser exposure time, the trapped liquid inside the PCF vaporizes to the atmosphere, hence compression, instead of expansion is observed in the PCF during the splicing process.

6.4.3 Asymmetrical Air hole Deformation in PCF

Thermal transfer in optical fiber satisfies the thermal thinness conditions hence the 1-D thermal transfer mechanism has been used to analyze the fiber temperature. The temperature distribution over the fiber ends is found to be uniform [143, 166, 167] for laser exposure time longer than 2μs $\left(\tau = \frac{\text{Fiber Diameter } d_{Fiber}}{4 \times \text{Thermal Diffusivity } \kappa}\right)$. This implies that any expansion or compression in the fiber joint should be symmetrical and uniform. However, the experiments show that the slight deformation at the upper surface of PCF in the silica capillary layers for slightly longer laser exposure time. In order to explain this phenomenon, a 3D thermal transfer simulation program described in the previous chapter is useful to determine the temperature distribution over the SMF and hollow air-core PCF. Figure 6-4 and Figure 6-5 illustrate the temperature distributions in SMF, small single hollow core PCF (representing the size of air hole LMF-PCF or $SPCF_T$) and large single hollow core PCF (representing the

size of air hole for NL-PCF or $SPCF_T$). Based on these three images, it is obvious that the strength of backscattered beam is strongest for single air hole PCF, followed by large single air-hole PCF and the SMF has the weakest backscattered beam. The temperature on the uppermost layer of PCF exposed directly to the laser is lower than bottom layer of the PCF.

In convection, heat transfer occurring by flow of gas or liquid is also affected by surface tension. With uneven temperature distribution, hotter surface fluid is pulled toward colder surface fluid. Figure 6-11 shows that the temperature distribution over the fiber cross-section is not uniform especially near to the fiber upper surface in the direction of laser beam. The deformation occurs only at the outer layer of air capillaries. The inner layer of air holes under the laser beam (or called active region) is compressed and deformed. The air hole deformation of PCF near to the surface of fiber perhaps is due to the rapid change of temperature or the surface tension driven convection (or called oscillation mechanism in the thermo-capillary flow) [168]. The non-symmetrical heat distribution is caused by the rise of heat flux that goes beyond the critical value and results the heat flow to be oscillatory. This type of convection has been explained as thermo-capillary convection by the team of NASA scientists [169]. The heat flow along the fiber length is called surface flow and the flow toward the heated region in the interior is called the return flow as shown in Figure 6-14. The fluid particles move back and forth in the azimuthal direction as the laser beam is scattered unevenly to the fiber's surface and cause the heat flow to be oscillatory. The heated region is relatively small and the fluid velocity is large, therefore the convection time scale in the region is small compared to the overall convection time. The small convection time causes the rapid change of surface flow in the heated

region, and the return flow would not respond immediately, therefore the surface at active region must deform first to generate sufficient pressure gradient due to this time lag of return flow. There is more heat transported out of the active region, so that the temperature outside the region increases and heat propagates towards the cold wall, driven by the radial temperature gradient near to the surface. This convection of hot fluid toward the cold wall is clearly seen in the image captured by the high-speed camera during the process of splicing. In Kamotani's oscillatory thermo-capillary [168] flows experiment in the open cylindrical container induced by CO_2 laser heating, it is also explained that the surface deformation is due to time lag of return flow. The sizes of cylindrical container under test are 1.2cm to 2cm, which are very different from the optical fibers with diameter of 125μm. For the small diameter of cylindrical optical fiber, the return flow of heat should not be an issue. However, the 1~2μm air holes spread over the LMA-PCF's cross-section may cause the reflection of impinging laser beam in the active region as a form of scattering loss. In the 3 D thermal transfer model, a single air hole at the center of the fiber (hollow core fiber) is used to simulate to propagation of heat energy within the fiber and determine the strong back-scattering (equivalent to return flow) with smaller air hole, the back-scattered beam is stronger (Figure 6-14). Since LMA-PCF has many small air holes in the cross-section, the strong return flow causes rapid change of temperature near to the fiber surface. High ambient temperature results in high-pressure acting onto interface of the SMF and PCF. Only the air capillaries cannot withstand pressure, therefore the compression occurs in the air hole and a bending near to the fiber interface as shown in Figure 6-14.

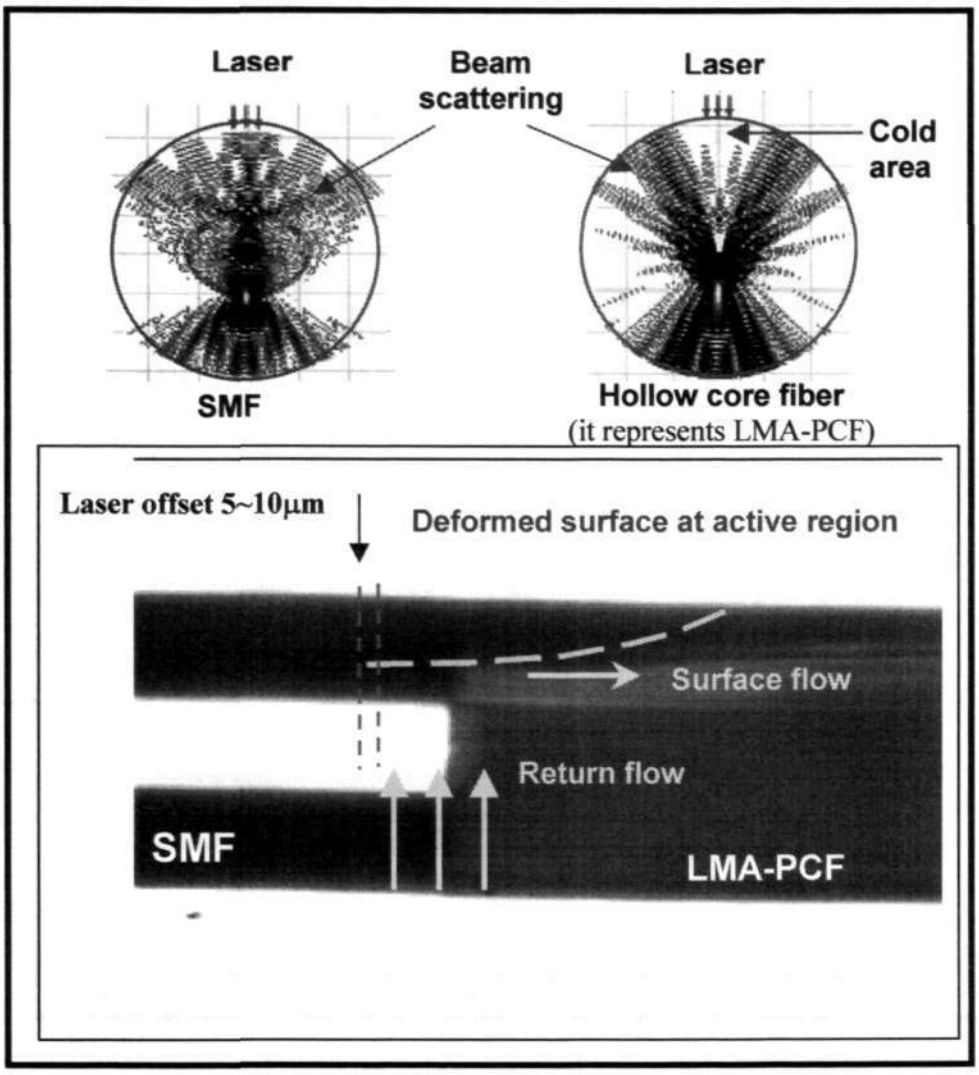

Figure 6-14 Inner-surface (air-holes) deformation at active region due to failure of the air capillaries to sustain the pressure caused by the rapid change of temperature near the fiber surface closer to the impinging laser.

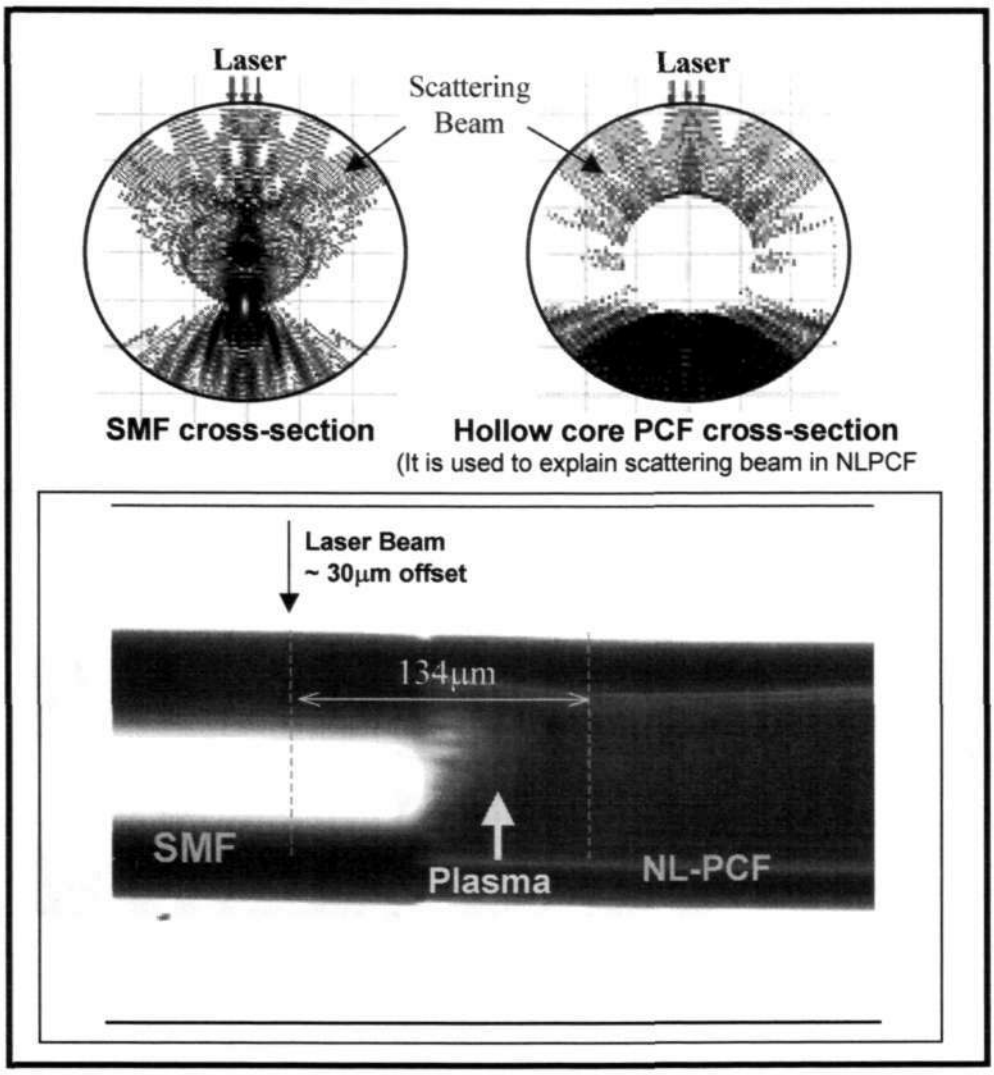

Figure 6-15 Laser plasma speeds up heat flow and results in the further azimuthal shift of air hole deformation away from the center of beam

The NL-PCF having large air holes would have weaker back-scattered beam in the direction of laser (Top-right image of Figure 6-15). As shown in bottom image of Figure 6-15, the plasma is generated at the center of NL-PCF with slight condensation in the splicing region and the growth of plasma accelerates the surface heat flow azimuthally. Therefore, the plasma travels azimuthally away from the laser beam and causes the deformation of air holes far way from the peak of laser beam spot. If the air

holes are condensed, the quick absorption of laser by the trapped liquid leads to inverses Bremsstrahlung (IB) effect. IB arises from electrons and further increases the laser absorption in the condensed medium. In the cascade ionization, the high laser power at the condensed fiber increases the density of electron cloud, and once plasma is damped it heats up rapidly. As the lasing time prolongs, the plasma shields the laser and the shift of fiber collapse is observed far away from the laser beam as shown in the shown in Figure below.

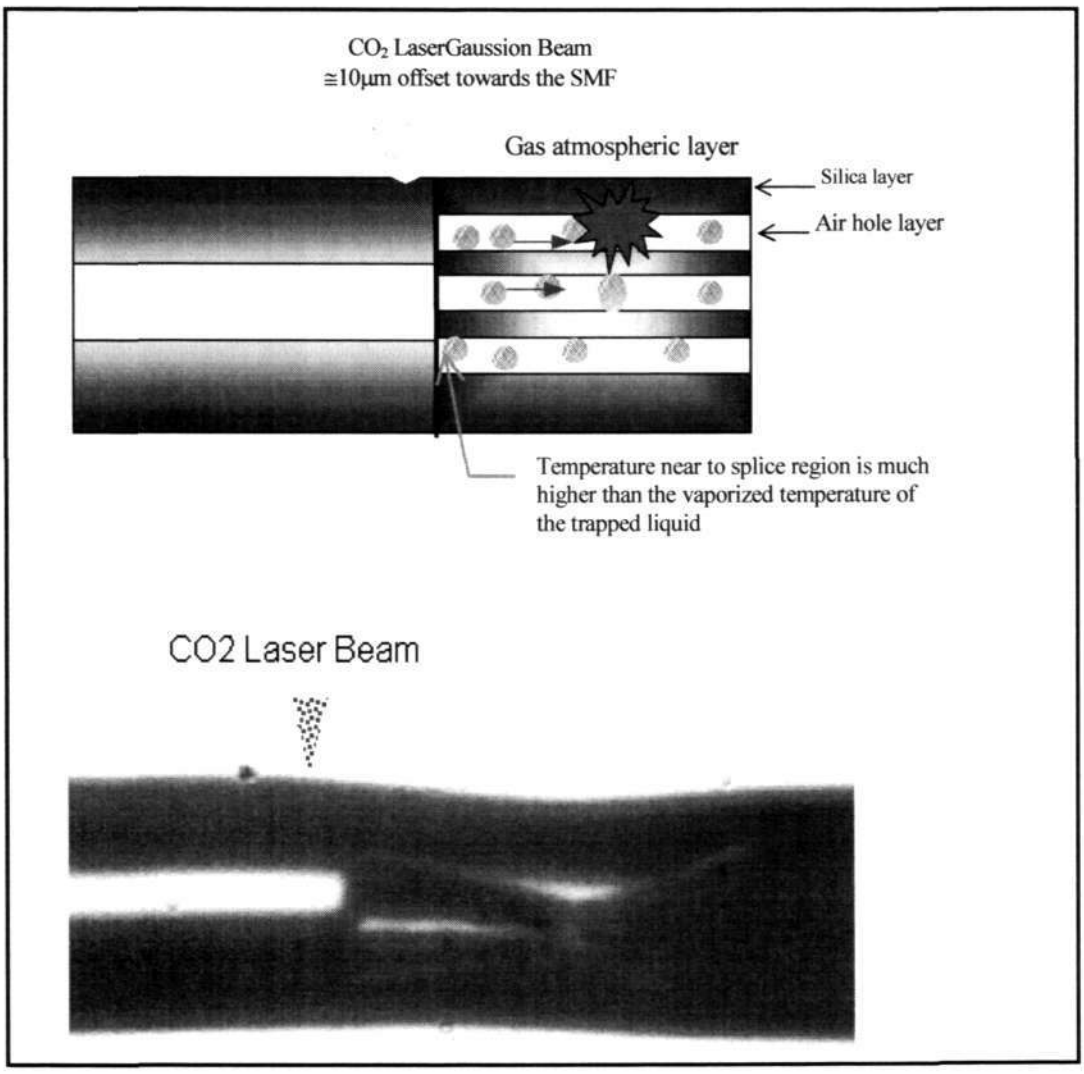

Figure 6-16 Collapse of air holes far away from the peak of laser beam spot

6.4.4 Periodic Fringes Inside the Fiber Cross-section

The study on the formation of lump at the spliced region caused by high laser irradiation is not our main objective; however it may worth reporting the results that we have obtained in this phenomenon that is observed during our investigations with laser splicing of PCF.

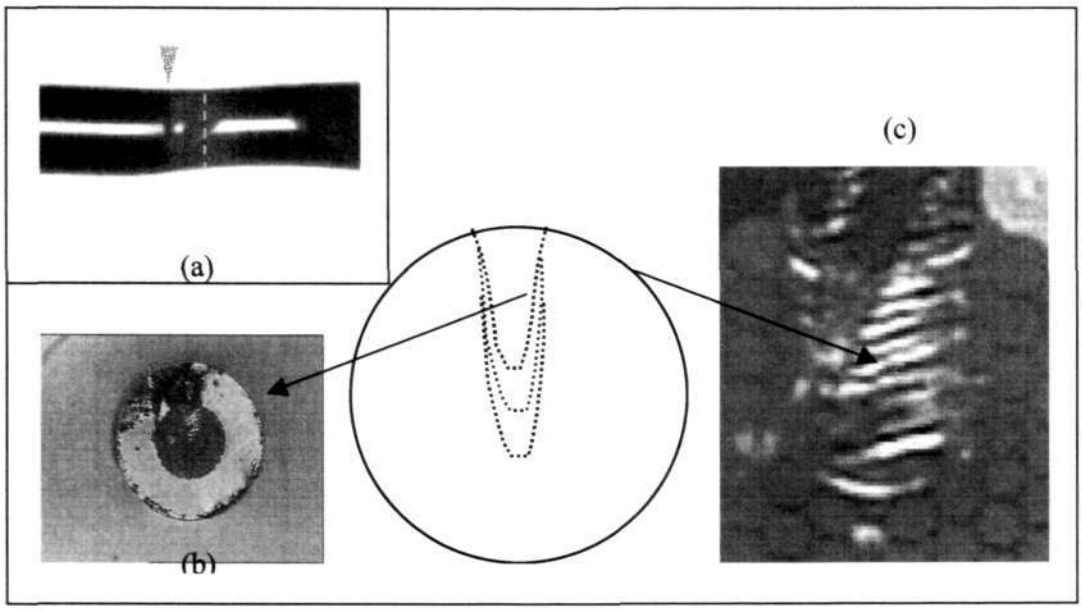

Figure 6-17 (a) High laser power at the splicing region squeezes a silica lump (b) Cross section of PCF near the spliced region. (c) Magnified view of periodic fringes seen moving towards the center of the PCF

As Wang et. Al [58] has reported that when a laser impinges onto the silica substrate coated with a thin layer of paint or gold, periodic parallel fringes and circular fringes appear on the upper surface of substrate. Similar phenomenon is also observed at the cross-section of NL-PCF near to the spliced region where the lump is formed. The main difference is the position of fringes, the ring of fringes on the substrate mentioned above propagates perpendicular to the direction of laser beam, whereas the

fringes in the cross-section of PCF is observed to be rippling along the direction of laser beam as shown in Figure 6-17. The period of fringes is almost equivalent to the radius of air-hole, hence we believe that it may be caused by the periodical microstructure of the PCF. According to some reported articles, the characteristics of fringes is dependent on the intensity of laser and the *backside effect* [58] caused by the strong reflection of the molten materials such as condensed silica, however, not much information has been provided on the above effect. We believe that the *backside effect* observed in our experiments is perhaps a type of reflective plasma acceleration created during the laser irradiation of the NL-PCF. With condensed PCF, the forward plasma acceleration is likely to be slower than the reflective acceleration; hence the depth of penetration by the laser appears to be limited even if the laser pulses are still continuously incident to the splice region. Strong reflective plasma acceleration is likely to occur during the fusion process to gradually push the molten silica upwards and hence a lump formation is observed above the fiber's surface.

CHAPTER 7 CONCLUSION AND RECOMMENDATIONS

This chapter presents the conclusion on the work done for this project and gives some recommendations for future work that may be undertaken for project upgrading, development and applications. The achievement of laser-splicing technique for splicing of photonic crystal fiber to standard single mode fiber shows great promise and we are optimistic about its potential for practical applications.

7.1 Conclusion

Optical fiber splicing is an essential process in the field of optical fiber communications and fiber-based products [20, 170, 171]. Most of the splicing work for joining of two fiber ends is commonly performed by electric arc fusion or epoxy injection technique and it is very rare to find the use of CO_2 laser fusion technique for this purpose. CO_2 lasers have been extensively used in material processing applications such as welding, soldering, and marking etc., and its potential for splicing of standard optical fibers has been realized, however, no serious efforts have been made to implement and deploy it commercially. As a result, the research activity on this topic has been scarce since early 90s. The advent of photonic crystal fibers leads us to put more attention on the laser splicing technique than the current electric arc splicing systems due to some limitations those have been observed with the use of electric-arc technique for splicing of SMF to PCF.

So far, no published work is found in the literature that presents work on the laser splicing of PCF-to-SMF and currently no such commercial system is available in the market. In 1999, one report demonstrated the measured splice loss of PCF to be 1.5dB [100] and another report showed the simulated splice loss of SMF-to-PCF to be 1.7dB [99], but no detailed description has been given on the practical methodology to achieve the splice. In 2004, B. Bourliaguet [172] was the first to present a detailed description on the practical aspects on the splicing of SMF and PCF using conventional electric arc technique. His approach was to use a low power electric arc with short pulses to join PCF to SMF with collapse of air-holes in the PCF at the spliced region. The collapse of air holes for the kind of PCF used in his experiment did not cause serious splice loss, but this technique is not always suitable or feasible to other types of PCF. Based on his paper, we further confirm that electric arc fusion causes the significant collapse of air holes and therefore the laser splicing technique is a better solution for splicing of various types of PCF. Some of the advantages for laser-splicing technique include localized heating by delivery of intense energy over a small area due to small beam diameter of the laser, precise control of laser power and uniform temperature distribution over the fiber cross-section. The melting temperatures of silica material in PCF and SMF are very close, but each of these fibers may need different laser power due to difference in their structure. In general, PCF needs lower laser power than SMF, and the amount of laser power for melting the fiber depends on the total volume of the air holes in the PCF – larger air hole needs lower laser power. In order to estimate optical lasing parameters for given fibers, a simple 1-Dimensional thermal transfer model has been established to determine the optimal laser power and laser exposure time. Laser exposure time can be reduced from few seconds to about a hundred milliseconds if the laser power

increases from 3.1W to 4.4 W. In the 1-D thermal transfer model, it is assumed that the air holes of PCF are transparent to CO_2 laser and simulation results for laser power and laser exposure time are in agreement with the experimental results. Since there is only one laser source impinging onto end faces of the SMF as well as the PCF, the optimized solution is to offset the laser beam more towards the SMF than at the PCF. For splicing of LMA-PCF to SMF and NL-PCF to SMF, the theoretical simulation results show that the respective offsets should be of the order of 5 μm and 30μm.

The 3-D thermal transfer model represents an extension of 1-D model for analyzing the heat distribution over the fiber cross-section. The 3-D model simply depicts the thermal energy distribution for SMF and hollow core PCF as the laser beam runs across the fiber cross-section. The simulation shows that the back-scattered beam from an optical fiber with small single air hole may cause the rise of ambient temperature at the upper surface of the optical fiber. The rapid change of thermal conditions across the fibers causes collapse of the air holes near to the upper surface of PCF. Due to sudden changes in temperature, the air capillaries in LMA-PCF would not withstand the rise of ambient pressure on its surface; therefore asymmetrical deformation of air hole is observed. The deformation appears near to the surface of PCF and far away from the defect (or core) and may affect the splice loss.

Some unique phenomena have been observed in the CO_2 laser induced splicing of PCF. Splicing of two different types of fibers is considerably more complex than it may appear at a first glance. Extensive studies have been carried out to characterize the laser splicing parameters as well as to study the laser-silica interaction. The rate equation has been used for this purpose.

The laser-interaction in SMF and PCF depends on laser intensity and laser exposure time that gives rise to different electron densities. If the cascade ionization is higher than the rate of electron loss that would cause rapid absorption through inverse Bremsstrahlung effect if the electron density near to $10^{18}/cm^3$, plasma shields the laser beam when electron density exceeds the critical density at higher laser irradiance. Imaging with high-speed camera in our experiments has been useful to further confirm the information about the optimum laser exposure time to achieve best possible splice results.

Generally, for studies on laser dielectric interaction, YAG, excimer or He-Cd laser have been used. Laser with shorter wavelength (high photon energy) may easily cause multi-photon ionization or direct ionization in the dielectrics, and long wavelength CO_2 laser has been rarely used for processing of high band-gap materials. However, CO_2 laser is strongly absorbed by the silica material through photon-phonon interaction, and therefore is a good candidate for splicing of silica fibers. The generic rate equation has been used to analyze the electron density in silica (SiO_2), hydroxyl group in $Si(OH)_4$, and water content. It is more difficult to clear the moisture in the larger air holes, for example in the case of NL-PCF. Time resolved recorded images show that the rise of plasma begins from the hottest spot (i.e. center) of the fiber and spreads azimuthally away from the fiber interface towards the PCF. This is also partially due to the rise of electron density that forces the shielding plasma away from the laser beam. Therefore the deformation on the PCF does not occur directly below the laser beam, but at a distance away from the center of the beam spot. On top of this, the back-scattered beam brings the air hole deformation near to the fiber's upper surface, and such a similar deformation is also observed with NL-PCF in our

experiments. However, compare to LMA-PC, this deformation in NL-PCF is shifted farther away from the spliced region due to the plasma effect.

For PCF splicing, the rapid heating by CO_2 laser should effectively splice the fibers to minimize the deformation of air holes, hence further investigations may be useful to obtain additional process details. The development of laser splicing system is a multi-disciplinary project, which involves work on electronic circuit design, image processing, computer interfacing, micro-alignment and laser technology. Additional studies on the heat transfer mechanism and the inverse Bremsstrahlung effect between CO_2 laser and silica should be useful to further improve the characteristics of laser spliced PCF.

7.2 Recommendations

A complete laser splicing system [173], has been developed for splicing of standard single mode and photonic crystal fibers and this is shown in Figure 7-1. The splicing of LMA-PCF-to-SMF and NL-PCF-to-SMF has been successfully demonstrated.

Considering variation and encounters during the progress of this project, the following recommendations are suggested for further improvements and modifications based on the limitations involved in this project:

a) Laser Beam Shaping or Scanning at Different Laser Power Levels

It may be possible to improve the results on splicing of SMF-to-PCF by using beam shaping or scanning of the CO_2 laser as this may assist in satisfying the requirement of different laser intensities for two different types of fibers. The

beam size after reshaping must be small to ensure that only the small-spiced region is exposed to the laser (Figure 7.2). This should be beneficial especially for certain types of PCF such as the NL-PCF with thin strut width. Another possible approach to provide varying laser intensities to the spliced region is to rapidly scan a laser beam of smaller diameter (≤50μm) across the spliced region as shown in Figure 7-3.

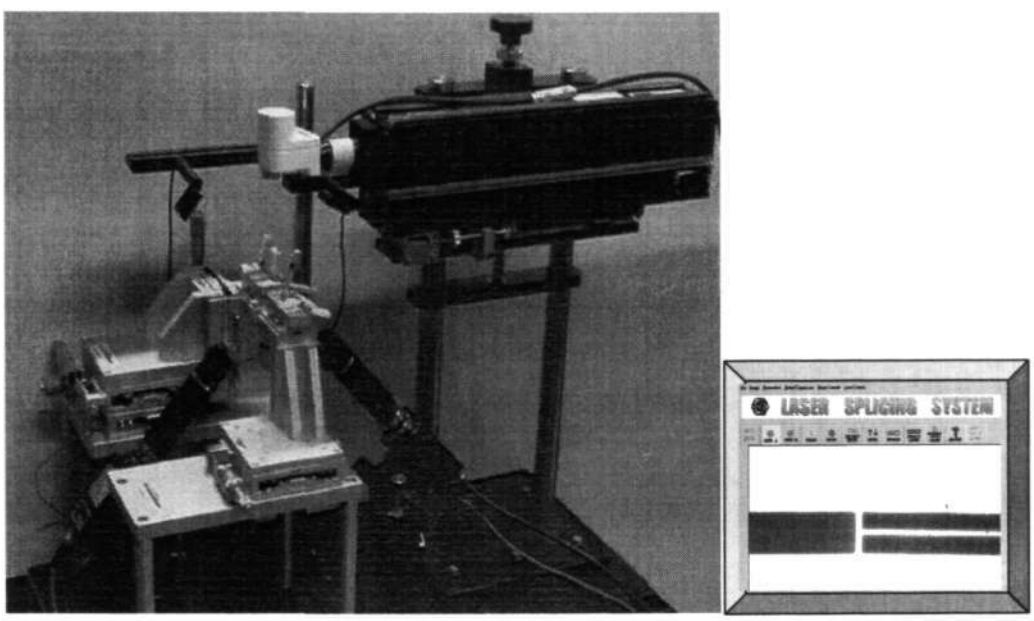

Figure 7-1 CO_2 Laser Splicing System

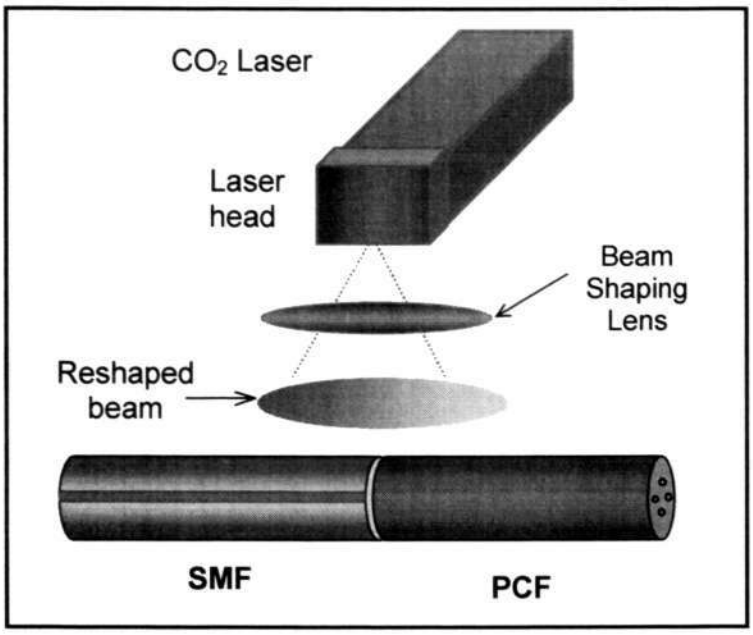

Figure 7-2 Beam shaping may provide different laser intensities to different types of fibers

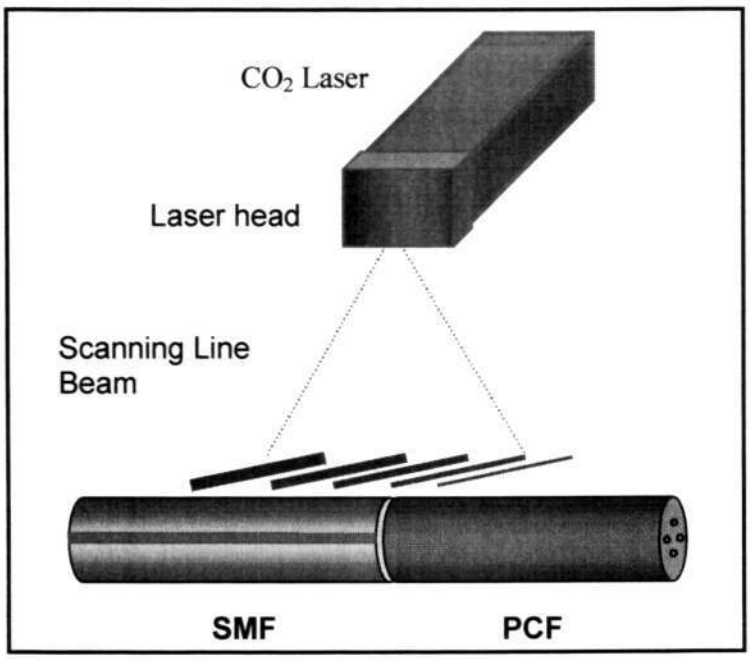

Figure 7-3 Beam scanning to obtain varying laser intensities across different fibers

b) Tapered Core Fiber

The MFD discrepancy between SMF and NL-PCF contributes to very high coupling loss and also introduces high misalignment loss among them due to its relatively small core diameter. To minimize this mismatch, it is best to introduce a *tapered-core* fiber as a buffer between SMF and PCF as shown in Figure 7-4. Currently only the tapered fibers and not the *tapered-core* fibers are available in the market.

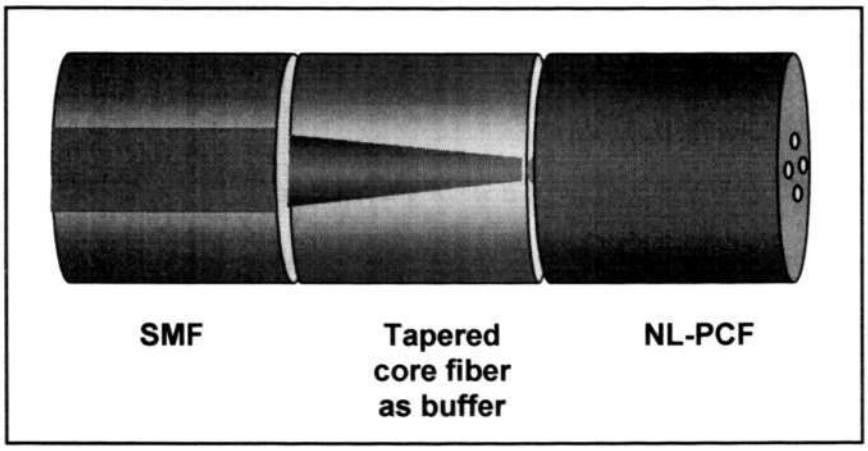

Figure 7-4 Tapered-core fiber can be used as a buffer to match the different mode field diameters between SMF and NL-PCF

c) Powerful PC

Based on the current capacity of personal computer (PC), the 3D thermal transfer model for hollow core fiber can only be simulated with minimum air hole diameter of 5μm. For smaller air-hole diameter, the present PC fails to calculate the heat distribution over the cross section. A more powerful PC is needed to simulate the 3D heat distribution for PCF.

d) Intensity fluctuation of CO_2 laser

The laser resonator determines the stability of laser beam. To reduce uncertainty in the splice results due the intensity fluctuations (typically 10%) of commercially available CO_2 lasers, it is highly desirable to put additional efforts to improve the stability of the laser beam.

e) Stand-alone System using micro-controller

PC is not portable and it is not a cost effective for field usable laser-splicing system. A combination of micro-controller, miniature CCD cameras, and LCD screens powered by portable re-chargeable batteries is recommended to replace the PC based laser splicing system for field use.

In summary, a complete laser splicing system has been developed and built that is suitable for the laboratory use. In future, with availability of better components for the imaging, laser control and alignment subsystems; the overall system can be fabricated with small size and improved performance.

BIBLIOGRAPHY

[1] Joo Hin Chong and M. K. Rao, "Development of a system for laser splicing photonic crystal fiber," Pg. 1365-8, Vol. 11, No. 12 16 June 2003, Optics express.

[2] Joo Hin Chong, M. K. Rao, Yinian Zhu, and Ping Shum, "An Effective Splicing Method on Photonic Crystal Fiber Using CO_2 Laser," IEEE Photonics Technology Letters, Pg 942-4 Vol.15, No. 7, July 2003.

[3] Yinian Zhu, Ping Shum, Joo Hin Chong, M. K. Rao, and Chao Lu "Strong resonance and a highly compact long period grating in a large-mode-area photonic crystal fiber," Optics express, Pg. 1900-5, Vol. 11, No. 16,August 2003

[4] Joo Hin Chong, Yinian Zhu, M.K. Rao, Ping Shum, "Splicing on Condensed Photonic Crystal Fiber using CO_2 laser," OECC 2003

REFERENCES

1. T.K Birks, J.C. Knight and P. St. J Russell "Endlessly single mode photonic crystal fiber," Optics Letters, Vol.13 July 1 1997.

2. J. C. Knight, T. A. Birks, P. St. J. Russell and D. M. Atkin, "All-silica single-mode optical fiber with photonic crystal cladding," Vol. 21, No. 19, pp.1547-9, Optics Letters, October, 1996.

3. A. B.Jarklev, J. Broeng, A.S. Bjarklev, "Photonic crystal fibres," Kluwer academic publishers, 2003.

4. Joo Hin Chong, M.K. Rao, Yinian Zhu, and Ping Shum, "An Effective Splicing Method on Photonic Crystal Fiber using CO_2 Laser" Photonics Technology Letters, vol. 11, no. 12, July 2003.

5. John Senior, "Optical Fiber Communications Principles and Practice," Prentice Hall International Series in Optoelectronics, 2nd Edition, pp. 11-12, 1992.

6. John Midwinter, "Optical fibers for transmission," Wiley, pp. 101-109, 1979.

7. "Optical fibers carry information of the age," Laser Focus World, pp. 101-109, Mar 1997.

8. E. Yablonovitch, "Photonic crystals: semiconductors of light," Scientistic American Inc., http://www.sciam.com, pp. 47-555, December 2001.

9. E. Yablonovitch, "Inhibited spontaneous emission in solid-state physics and electronics," Physical Rev. Lett, 58, pp.2059-2062, 1987.

10. J. Broeng, " Photonic crystal fibers: A new class of optical waveguides," Optical fiber technology vol. 5, pp. 305-330, 1999.

11. T. M. Monro, J.C. Bagget, W. Belardi, K.Frusawa, "International conference of on transparent optical network," Poland: IEEE Catalog number ISBN 0-7803-7096-1, pp. 88-91, conference proceeding, ICTON 2001.

12. J.C. Knight, J.Broeng. T.A. Birks, and P.St. J. Russell, " Photonic bandgap guidance in optical fibers," Science, vol. 282, pp. 1476-1478, 1998.

13. A. K. Abeeluck, N. M. Litchinitser, C. Headley, and B. J. Eggleton, Analysis of spectral characteristics of photonic bandgap waveguides," pp 1120-33, vol.10, No.23, Nov 2002.

14. T.A. Birks, P.J. Roberts, P.St. J. Russel, D.M. Atkin, and T. J. Shepherd, " Full 2-D photonic bandgaps in silica/air structures," IEE Electronics Letter, vol. 31, pp. 1941-1943, 1995.

15. M. Monro, P.J. Bennett, N.G.R. Broderick and D.J. Richardson, "Holey fibers with random cladding distributions," Optics Letts., vol.25, pp. 206-208, 2000.

16. A. Bjarklev, J. Rishede, S.E.B. Libori, J. Broeng, "Photonic crystal fibres – Novel Fibres, New Applications," pp. 172-177, IEEE, ICTON 2002.

17. N. A. Mortensen, J. R. Folken, P.M.W Skovgaard, and J. Broeng, "Numerical aperture of single mode photonic crystal fibers," IEEE photonics Technology Letters, pp. 1094-1096, vol. 14, No. 8, August 2002.

18. Jes Broeng, Stig E.Barkou, Anders Bjarklev, Thomas Sondergaard, Erik Knudsen, " Review paper: Crystal fiber technology", Proceedings of Danish Technical Research Council, pp 22-28, 2000.

19. Ren Guobin, Wang Zhi, Lou Shuqin, Jian Shuisheng, "Mode classification and degeneracy in photonic crystal fibers", Optics Express, Vol. 11, pp1310-1321, June 2003.

20. J. H. Chong, P. Shum, H. Hartono, and Y. Aleta, "Investigations on the Characteristics of Point-by-point CO_2 Laser Induced Long-Period Grating on Optical Fiber," Presented at Fourth International Conference on Information, Communications & Signal Processing, and Fourth IEEE Pacific-Rim Conference on Multimedia (ICICS-PCM'2003), December 15-18, 2003, Singapore.

21. Yinian Zhu, Ping Shum, Joo-Hin Chong, M. K. Rao, and Chao Lu," Strong resonance and a highly compact long period grating in a large-mode-area photonic crystal fiber," Opt. Express 11, 1900-1905 (2003).

22. T. T. Larsen, A. Bjarklev, D. S. Hermann, and J. Broeng, "Optical devices based on liquid crystal photonic bandgap fibres," Opt. Express **11,** 2589-2596, 2003.

23. A. Bjarklev, Optical fiber amplifiers: Design and System Application, Artech House, Boston/London, 1993.

24. Splicing is Taken a New Heights, Fiberoptic Product News, pp. 17-22, Oct 1996.

25. Loose tube splice for optical fibres, C.M. Miller, Bell Syst. Tech. Pp.1215-25, vol.75 (7), 1975.

26. J.P. Longtin and C.L. Tien, "Efficient laser heating of transparent liquids using multiphoton absorption," Journal of heat mass transfer, vol. 40, No. 4, pp. 951-959, 1997.

27. A. Vogel, K. Nahen, D. Theisen and J. Noack, "Plasma formation in water in picoseond and Nanosecond Nd:YAG laser pulses –part I: Optical breakdown at threshold and superthreshold irradiance," IEEE Journal of Quantum Electronics, vol. 2, pp. 847-860, No.4, December 1996.

28. B.G. Shin, J.H. Park, and Jang-Joo Kim, "Low-loss, high-bandwidth graded-index plastic optical fiber fabricated by the centrifugal deposition method," Applied Physics Letters, vol. 82(26), pp. 4645-4647. June 30, 2003.

29. K. Hara, K. Horiuchi, S. Kim, I. Nakano, T. Takebayashi, K. Takikawa, K. Yasuoka, M. Koyano, S. Matsui and H. Takeuchi "Heat splicing of plastic fibers using a PEEK tube," vol. 348, Issue 1, 21 pp. 139-146 August 1994.

30. Y. Hayato, I, Takeharu, S. Tetsuo, "Plastic star coupler" Proc. SPIE, vol. 1592, p. 2-11, Dec 1991.

31. A. J. Fielding, K. Edinger and C.C. Davis, "Experimental observation of mode evolution in single mode tapered optical fibers," Journal of Lightwave Technology, vol. 17, pp. 1649-1656, no.9, September 1999.

32. 3M fusion splicing of Erbium-doped optical fiber

33. Fusion splicer eyes erbium-doped fiber, 20-Aug 2002, fiber.org. http://fibers.org/articles/news/4/8/17/1

34. H.K.Ceo, J.U. Jeon, Y.K Cho, K.T. Joeong, "Gain and noise figure improvement of erbium doped-fiber amplifiers by optimizing spectral splicing conditions," pp. 236-8, Technical Digest, OFC 98.

35. Y. Mohanna, "Electric arc temperature estimation of a fiber splicer," IEE proc-optoelectron. Vo. 142, no.6, pp313-5, Dec 1995.

36. A. Ishikura, Y. Kato, T. Ooyanagi, and M. Miyauchi, "Loss factors analysis for single mode fiber splicing without core axis alignment," vol. 7, pp. 577-583, No. 4 Journal of lightwave technology, April 1989

37. T. Onodera, I. Suzuki, T. Yamada, Y. Osato, O. Watanabe and T. Kato, "The Development of an Optical Fiber Splicer using a profile alignment system," pp.13-20, Fujikra Technical Review 1987.

38. S. Nemoto, T. Makimoto, "Analysis of splice loss in single mode fibres using a Gaussian field approximation," vol. 11, pp. 447-457, Optical and Quantum Electrons, 1979.

39. W. Zheng, O. Hulten, S. Esmaeli, "Splice-loss estimation for an automated ribbon-fiber fusion splicer," Journal of lightwave technology, vol. 17, no. 8, pp. 1366-77, August 1990.

40. H. E.Ghandoora, I. Nasserb, A. Al-Hadyc, A.Al-Shukrib, "A comparative study of spliced optical fibers," Optics and Lasers in Engineering, vol. 41 pp. 277–287, 2004.

41. K. Kinoshita and K. Egashira, "Optical fiber end preparation using a CO_2 laser," Applied Optics, vol. 17, No.8, pp. 1210-12, April 1978.

42. M.C. Fowler and D.C. smith, Journal applied. Phys., vol. 46, 1975.

43. K. Klaus, D, " Integration of laser processing in machine tools and their economy," Jan. Proc. SPIE, vol. 3102, pp. 105-6, Sept 1997.

44. R.A. Kleijhorst, H.L. Offerhaus and P.Bant, "Micro-machining workstation for a diode pumped Nd:YAG high brightness laser system", Rev. Sci. Instrum. vol. 69(5), pp. 2118-2119 (1998)

45. Hecht, Jeff. The Laser Guidebook. Blue Ridge Summit: McGraw-Hill, Inc., 1992.

46. Kenyon, W. Basic Welding and Fabrication. Singapore: Longman Singapore Publishers Pte Ltd., 1979.

47. A. K. Nayak, V. Parthasarathy, S. K. Sarkar, "Parametric studies on generation of short CO_2 laser pulses for IR-laser chemistry," Infrared physics & technology, 42, p535-540, 2001.

48. http://www.lasersolutionsandsystems.com/

49. W. Williams, M. Soileau, E. Van Stryland, Picosecond air breakdown at 0.45mm, Applied Physics Letter 43, pp.352-354, 1985

50. M. V. Allmena, A. Blatter, "Laser Beam Interactions with materials", Physical principles and applications, 2nd Edition, page 1-2, 1995.

51. "Ultrashort laser pulases tackle precision machining", Laser Focus World, page 101, August 1997.

52. B. Medres, Thermal and plasmas effects in laser material processes, AS USSR, 1987.

53. D.G. Whitehead, A.V. Polihanczuk, "Reflow soldering by laser," American Society of Mechanical Engineers, vol.143, page 47-48, 1990.

54. F.Y. Genin, K. Michlitsch, "Laser induced damage of fused silica at 355 and 1046nm initialed at aluminum contamination particles on the surface", SPIE 2966, Paper #2966-33, 1997.

55. C.L. Tien and J.H. Lienhard, *Statistical Thermodynamics*, Hemisphere Publishing Corp., New York, 1979.

56. Larry D. Merkle, N. Koumvakalis, and M. Bass, "Laser-induced bulk damage in SiO_2 at 1.064, 0.532, and 0.355 um," *Journal of Applied Physics*," Vol. 55, Issue 3, pp. 772-775, February 1, 1984.

57. J. H. Pitts, "Modelling laser damage caused by platinum inclusions in laser glass" LLNL 17th Annual Symposium, Oct.1985.

58. W. J. Wang, Y.F. Lu, C.W. An, MH. Hong, T.C. Chong, "Controllable periodic structures on silicon wafer by CO_2 laser irradiation," Applied surface science, vo. 189, pp. 549-598, 2002.

59. M. S. Trtica, B.M. Gakovic, "Pulse TEA CO_2 laser surface modifications of silicon," Applied surface science, vol. 25, pp. 336-342, 2003.

60. M. V. Allmen, "Laser Beam Interactions with materials," Springer Series in materials science, vol. 2, Springer, Berlin, 1987.

61. Sander, M.U Luther, K, J Troe, " Journal of phys. Chem Vol. 97, page 11489, 1993.

62. T.X. Phuoc and F.P. White, " Laser-induced spark ignition of CH_4/air mixture," combustion and Flame110: 203-216,1999.

63. John C. Travis and Gregory C. Turk "Laser-Enhanced Ionization Spectroscopy," April 1996.

64. Y.R. Shen, "The principles of nonlinear optics," pp. 528-39 New York: Wiley, 1984.

65. J. K. Fushinobu, L.M. Phinney and N.C. Tien, Ultra-short pulse laser heating of silicon to reduce microstructure adhesion, Int. J Heat Mass Transfer, vol. 39, pp. 3181-86, 1996.

66. R. A. Crowell and D.M. Barter, " Multiphoton Ionization of Liquid water with 3.0-5.0eV Photons," J. Phys. Chem, vol. 100, page 17940-17949, 1996.

67. P.V. Torek, D.L.Hall, M.S. Woodridge, H_2O absorption spectroscopy for determination of temperature and H_2O mole fraction in high-temperature particle synthesis systems," Applied Optics, v 41, n 12, p2274-2284 Apr 2002.

68. C.A. Sacchi, " Laser-induced electric breakdown in water," J. Opt. Soc. AM. B. B8, 99.337-345, 1991.

69. G.W.C. Kaye & T.H. Laby, Tables of physical and chemical constants, 16th edition, Longman 1995.

70. S.J. Gitomer and R.D. Jones," Laser-produced plasmas in medicine," IEEE Trans, Plasma Sci., Vol. 19, pp 1209-1219, 1991.

71. H.K. Park, C.P. Grigoropoulos, W.P. Leung and A.C. Tam, "A practical excimer laser-based cleaning tool for removal of surface contaminants, IEEE Trans. Components Packaging Mfg. Technol. A 17, pp. 631-4, 1994.

72. D.N. Nikogosyan, A.A. Oraevsky and V.I. Rupasov, two photon ionization and dissociation of liquid water by powerful laser UV Radiation, Chem. Phys. 77, pp.131-143, 1983.

73. C. Pepin, D. Houde, Hremita, T. Goulet and J.P. JayGerin, Evidence for resonance-enhance multiphoton ionization of liquid water using 2-eV laser

Light: variation of hydrated electron absorbance with femtosec on pulse intensity, Phys. Rec. Lett, 69, pp. 3389-3392, 1992.

74. J.P. Longtin and C.L. Tien, " Efficient laser heating of transparent liquids using mult-photon absorption," Int. J. Heat Mass Transfer, vol 40, no. 4, pp951-959, 1997.

75. O. Humbach, H. Fabian, U. Grzesik, U. Haken and W. Heitmann, "Analysis of OH absorption bands in synthetic silica," Journal of Non-Crystalline Solids, vol. 203, pp. 19-26, 1996.

76. J.P Williams, Y.S. Su, W.R. Strzegowski, B.L. Bulter, H.L. Hoover and V.O Altemose, Am, Ceram. Soc. Bull, vol. 55, 524, 1976.

77. J.E. Shelby, J. Vitko Jr., and R.E. Benner, J. Am. Ceram Soc. 65 C59, 1975.

78. A. Agarwal, K.M. Davis and M. Tomozawa, J. Non-cryst. Solids, vol. 185, pp. 191, 1995.

79. P.K.Kennedy, "A first-order model for computation of laser-induced Breakdown thresholds in ocular and aqueous media: Part-Theory," IEEE Journal of Quantum Electronics, vol. 31, No.12, pp. 2250-2257, December 1995.

80. L.V. Keldysh, "Ionization in the filed of a strong electromagnetic wave," Sov. Physics. J ETP, vol. 20, pp.1307-1314, 1965.

81. J. Norack and A. Vogel, "Laser-induced plasma formation in water at nanosecond to femto-second time scales: calculation of thresholds, absorption coefficients, and energy density," IEEE journal of quantum electrons, vol. 35, No. 8, pp. 1156-1167, August 1999.

82. Alastair M. Glass, David J. DiGiovanni, Thomas A. Strasser, Andrew J. Stentz, Richart E. Slusher, Alice E. White, A. Refik Kortan, Benjamin J. Eggleton, "Advances in fiber optics," Bell Labs Technical Journal, Vol.5, Issue 1, pp. 168-187, January/March 2000.

83. M. Ohnishi; N. Yoshizawa; Y. Miyajima.; O. Kawata; Y. Negishi "Loss stability assurance against hydrogen for submarine optical fiber cable," Lightwave Technology, Journal of , Volume: 6 , Issue: 2 , Pages:203 – 20, 9Feb. 1988.

84. E. Yablonovitch, T. J. Gmitter, and K. M. Leung, "Photonic band structure: The face-centered-cubic case employing nonspherical atoms," *Phys. Rev. Lett.*, vol. 67, p. 2295, 1991.

85. N.A. Mortensen, M.D. Nielsen, J.R. Folkenberg, A. Petersson, H.R. Simonsen, "Improved large-mode-area endlessly single-mode photonic crystal fibers", Optics Letters, Vol.28, No.6, pp. 2309-2311, March 2003.

86. J. Lægsgaard and A. Bjarklev, "Reduction of coupling loss to photonic crystal fibers by controlled hole collapse: a numerical study", Optics Communications, In Press, Uncorrected Proof, Available online 15 April 2004.

87. N.G. Broderick, T.M. Monro, P.J. Benett, and D.J. Richardson, " Nonlinearity in holey optical fibers: measurement and future opportunities", Optics Letters, Vol.24, No. 20, pp 1395- 1397, October 1999.

88. W.A.Gambling, D.N. Payne, and H. Matsumyra, "Cut-off frequency in radially inhomogeneous single-mode fibre," Electron. Lett. **13**, 139-140 (1977

89. M.D. Nielsen, J.R. Folkenberg1, N.A. Mortensen1, and A. Bjarklev, "Bandwidth comparison of photonic crystal fibers and conventional single-mode fibers" Vol. 12, No. 3 , Optics Express, February 9, 2004.

90. N.A. Mortensen, J.R. Folkenberg, M.D. Nielsen, and K.P. Hansen, "Modal Cut-off and the V-parameter in Photonic Crystal Fibers," Opt. Lett. **28**, 1879-1881 (2003).

91. M.D. Nielsen, N.A. Mortensen, J.R. Folkenberg, and A. Bjarklev, "Mode-field radius of photonic crystal fibers expressed by the V-parameter," Opt. Lett. **28**, 2309-2311 (2003).

92. T. Sørensen, J. Broeng, A. Bjarklev, E. Knudsen, and S.E.B. Libori, "Macro-bending Loss Properties of Photonic Crystal Fibre," Electron. Lett., **37**, 287-289 (2001).

93. G. Chang, Theodore B. Norris, and H. G. Winful, "Optimization of supercontinuum generation in photonic crystal fibers for pulse compression", Optics Letters, Vol.28, No. 7, pp, 546-548, April 2003.

94. A. Ishikura, Y. Kato, T. Ooyanagi and M. Mityauchi, "Loss factors analysis for single mode fiber splicing with core axis alignment," Journal of Lightwave Technology, vol. 7. no. 4, pp. 577- 583, April 1989.

95. T. Onodera, I. Suzuki, T. Yamada, Y. Osato, O. Watanabe and T. Kato, " The development of an optical fiber splicer using a profile alignment System," Fujikura Technology Review, pp13-20, 1987.

96. A. Ide, M. Tachikura and Y. Nomura, "Fiber misalignment method by the reflected light from fibers," Journal of lightwave technology, vol. 8, no. 8, pp. 1243- 9, August 1990.

97. S.M. James, "Non-intrusive optical fibre identification using a high-efficiency macro-bending 'clip-on' optical component, Electronics Letters," vol. 24, no.19, pp. 1221-1222, 15 September1988.

98. M. Y. Loke, J.N. McMullin, "Simulation and measurement of radiation loss at multimode fiber macrobends," Journal of lightwave technology, vol. 8 no. 8, pp.1250-1256, August 1990.

99. P.J. Bennett, T. Monro, and D.J. Richardson, "Toward practical holey fiber technology: Fabrication, splicing, modelling, and characterization," Opt. Lett., vol. 24.1203-1205, Sept.1999.

100. J.T. Lizier and G.E. Town, "Splice Losses in Holey Optical Fibers", IEEE Photonics Technology Letters, Vol.13, No. 8, pp. 794-796, August 2001.

101. K. Borzycki, " Holey fibers-application issues," IEEE ICTON 2001

102. K. Egashira and M. Kobayashi, "Optical fiber splicing with a low-power CO_2 laser," Applied Optics, vol. 16. No. 6, pp. 1636, July 1977.

103. K. Egashira and M. Kobayashi, " Analysis of thermal conditions in CO_2 laser splicing of optical fibers," Applied Optics, vol. 16, no. 10, pp. 2743-6, Oct 1977.

104. Kobayashi, K. K. Phys. Chem. Vol. 87, page 4317, 1983.

105. S. Kozaki, "Scattering of Gaussian beam by a homogeneous dielectric cylinder," J. Appl. Phys. 53, 7195 –7200, 1982.

106. H.C. Liu, X.L. Mao, J.H. Yoo, R.E. Russo, "Early phase laser induced plasma diagnostics and mass removal during single-pulse laser ablation of silicon," Splectrochimica Acta Part B 54, pp. 1607-24, 1999.

107. K.Mima, H.A.Baldis, A. Nishiguchi, H.Takabe, C. Yamanaka, "Laser Plasma Theory and Simulation," Harwood academic publishers, 1994.

108. S. C. Wilks and E. L. Kruer, "Absorption of ultra-short, ultra-intense laser light by solids and over-dense plasmas," IEEE Journal of Quantum Electronics, vol. 33, no. 11, pp. 1954-1967, Nov. 1997.

109. H. Hora, "Plasmas at high temperature and density", Applications and implications of laser-plasma interaction," Spring-Verlag Publications1991.

110. H.T. Tse, H.C. Man and T.M. Yue, "Effect of electric and magnetic fields on plasma control during CO_2 laser welding," Optics and lasers in Engineering vol. 32, pp55-63, 1999.

111. Z.Sun, AS Salminen, TJI. Misio, "Quality improvement of laser beam welds by plasma control," J. Mater Science Letters, vol.12, pp. 1131-3, 1993.

112. H.L. Wei, "Electron diffusion in a non-uniform electric field and a uniform magnetic field." Acta Physica Sinca, 5(2), pp.90-9 1996.

113. A. Vogel, K. Nahen, D. Theisen, and J. Noack, "Plasma formation in water by pico-second and nanosecond Nd:YAG laser pulses-I: Optical breakdown at threshold and superthreshold irradiance," IEEE J. Select. Topics Quantum Electron., vol. 2 pp. 847-860, 1996.

114. A.G. Gnedovets, O.M. Portnov, I. Smurove, G.Flamant, " Kinetic model of mass transfer through gas-liquid interface in laser surface alloying,: Applied surface science 109/110, page 143-9, 1997.

115. K. Inada, O. Watanabe and H.Taya, "Splicing of fibers by the fusion method," IEEE Journal on selected areas in communications, Vol.Sac-4 No5, pp. 706-703, August 1986.

116. John Gower, "Optical communication systems," 2nd edition, Prentice Hall pp. 91, 1993.

117. E. Serfini, "Statistical approach to the optimisation of optical fiber fusion splicing in the field," Journal of lightwave technology, vol.7, no. 2, pp.431-35, Feb 1989.

118. http://www.corning.com/opticalfiber, Single fiber splicing fusion, Application note, Corning, AN301, September 2001.

119. F. Espstp, E. Vezzoni, " Connecting and splicing techniques," Optical fibre communication, McGraw- Hill, pp. 541-643, 1981.

120. H. El Ghandoor, I. Nasser, Afaf Abdel-Hady and A. Al-Shukri, "A comparative study of spliced optical fibers, Optics and Lasers in Engineering, Volume 41, Issue 2, Pages 277-28, February 2004

121. M. Bredol, D. Leers, L. Bosselaar and M. Hutjens, "Improved Model for OH absorption in Optical Fibers," Journal of lightwave technology, vol. 8, no.10, pp. 1536-40, Oct. 1990.

122. A.K. Das, S. Bhattacharyya, "Low-loss fusion splices of optical fibers," Journal of Lightwave Technology, vol. LT-3, No.1, pp.83-92, February 1985.

123. O. Tsutomu, S. Isao, Y. Takeshi O. Yasukuni, W. Okosu and K. Takamasa, "The Development of an Optical Fiber Splicer Using a Profile Alignment System," Fujikura Technology.

124. W. Zheng, "Real time control of arc fusion for optical fiber splicing," Journal of lightwave technology, vol.11, no. 4, pp.548-53, April 1993.

125. http://www.synrad.com/search_apps/Default.htm

126. S.A.Cooper, R.W. Erskine Jr. Corning Cable System "Practical Guidelines for mass splicing," National Fiber Optic Engineers Conference, 2001.

127. Yinian Zhu, Joo Hin Chong, Ping Shum, M. K. Rao, and Chao Lu, "Experimental investigation of macro-bending losses in large-mode-area photonic crystal fiber," Presented at the 8th OptoElectronics and Communications Conference (OECC'2003), October 13-16, 2003, Shanghai, China.

128. Joo Beom Eom, Kun Wook Park, Youngjoo Chung, Won-Taek Han, , Un-Chul Paek,Dug Young Kim, and Byeong Ha Lee "Optical properties measurement of several photonic crystal fibers"; Department of Information & communicatins, Kwangju Institution of Science & Technology, leebh@kjit.ac.kr

129. T.M. Monro, D. J. Richardson and N.G. Broderick, "Efficient modelling of holey fibers," FG3-1, pp.111-113, 1999.

130. N.A. Mortensen, "Effective area of photonic crystal fibers," Optics Express vol. 10, n0. 7, pp.341-348, 2002.

131. http://www.rsoft/ BeamPROP/FullWAVE CAD, 2002

132. A. Taflove and S. C. Hagness, Computational Electrodynamics: The Finite-Difference Time-Domain Method, 2nd ed., Artech House, 2000.

133. B. J. Eggleton, C. Kerbage, P.S. Westbrook, R.S. Windeler, A. Hale, "Micro-structured optical fiber devices," Vol. 9, No. 3, pp. 698-713, Optics Express Dec. 2001.

134. M. Qiu, " Analysis of guided modes in photonic crystal fibers using the finite-difference time-domain method," Microwave and Optical Technology Letters, Vol. 30, No. 5, pp. 327-330, Sept. 2001.

135. G. E. Town and J. T. Lizier, "Tapered holey fibers for spot size and numerical aperture conversion," pp. 261, Proc. CLEO, 2001.

136. T. Kojima and Y. Yanagiuchi " Scattering of an offset two dimensional Gaussian Beam by a cylinder, " J. Appl. Phys. Vol.50, pp. 41-46, 1979.

137. K. Fushinobu, L.M. Phinney and N.C. Tien, "Ultra-short –pulse laser heating of silicon to reduce microstructure adhesion," Int. J. Heat Mass Transfer 39, pp.3181-3186, 1996.

138. H. K Park, C.P. Grigoropoulos, W.P. Leung and A.C. Tam, "A practical excimer laser based cleaning tool for removal of surface contaminants," IEEE Trans. Components Packaging Mfg, Technol., A17, pp.631-643, 1994.

139. A.Vertes, " Laser desorption of large molecules: Mechanism and models," Methods and mechanisms for producing ions from large molecules, Plenum Press, 1991.

140. S.D. Allen, J. O. Porteus, W.N. Faith and J. B. Franck, " Contaiminant and defect analysis of optical surfaces by infrared laser induced desorption," Appl. Phys. Lett. 45, pp.997-999, 1984.

141. R.F. Steinert and C. A. Puliafito, " the Ni-YAG laer in Opthalmology," Philadelphia, PA: Saunders, 1985.

142. M. R Prince, G.M. La Muraglia, P. Teng, T. F. Deutsch, and R. R. Anderson, " Preferential ablation of calcified arterial plaque with laser-induced plasmas," IEEE J. Quantum Electron., vol QE-23, pp. 1783-1786, 1987.

143. G.E. Myers, Analytical Methods in conduction heat transfer," Mc.Graw Hill, 1971.

144. D.R. Fairbank. Thermal visco-elastic simulation model for tapering of laser heated fused silica fiber. *SPIE* Fiber Optic Components and Reliability, 1580:196, 1991.

145. F.Keeith, "Principles of heat transfer, 2nd edition, International Textbook Company, 1965.

146. D.L.Kim, M. Tomozawa, S. Dubois, "Fictive temperature measurement of single mode optical fiber core and cladding," Journal of lightwave technology, vol. 19, No.8, pp. 1155-1158, August 2001.

147. A.D.McLahlan and F.P. Meyer. Temperature dependence of the extinction coefficient of fused silica for CO_2 laser wavelengths," Applied Optics, 26(12): pp. 1728-1731, 1 May 1987.

148. P Rosenberg, "The Basics of Fiber Optics, Part 3," http://www.ecmweb.com/ar/electric_basics_fiber_optics/" Electrical Wholesaling, Sep 1, 1999.

149. A.H. Rose, "Annealing Optical fiber: Applications and properties," The American Ceramic Society Bulletin, vol. 79 (3), 2000.

150. J. P. Barton, D.R. Alexander ''Fifth Order Corrected Electromagnetic Components for a Fundamental Gaussian Beam,'' J. Appl. Phys. 66(7), 2800–2802, 1989.

151. R.S. Krishnan, "Raman spectrum of Quartz," Nature, p. 155-452, 14 April 1945.

152. I. Simon and H.O. McMahon, "Study of the structure of quart, critobalite, and vitreous silica by reflecion I infrared. J. Chem, Physics, 21 (1): 23-30, 1953.

153. T. Isawa and N. Shibata, " Optical attenuation in pure and doped fused silica in the ir wavelength," Applied physics letter, 31 (1): 1794-1795, July 1979.

154. P.A. Barnes and K.E. Riechkhoff, "Laser induced underwater sparks," Appl. Phys. Lett., vol. 13, pp. 282-4, 1968.

155. C. DeMichelis, "Laser induced gas breakdown: A bibliographical review," IEEE J. Quantum Electron., vol. 5 QE-5, pp. 188-202, 1969.

156. A.V Kabashin, M. Meunier, "Fabrication of photoluminescent Si-based layers by air optical breakdown near the silicon surface," Applied surface Science 186, pp. 578-582, 2002.

157. K. Sugioka, K. Obata, K. Midorikawa, M. H. Hong, D. J. Wu, L.L. Wong, Y.F. Lu, T.C. Chong, "Advanced materials processing based on interaction of laser beam and a medium," Journal of Photochemistry and Photobiology A: Chemistry 6253m pp. 1-8, 2003.

158. A. Migus, S. Pommeret, N. Yamada, A. Antonetti, and Y. Gauduel, " Trapping and solvation of electrons in aqueous media," in Ultra-fast Phenomena VI," Springer Verlag, 1988, pp. 527-531.

159. D.D. Dlott, "Vibrational energy redistribution in polyatmoic liquids: 3D infrared- Raman spectroscopy," Chemical Physics 266, pp.149-166, 2001.

160. M.A. Lieberman, A.J. Lichtenberg, "Principles of plasma discharges and material processing," New York: Wiley-Interscience, 1994.

161. R.A. Crowell and D.M. Bartels, "Multiphoton ionization of liquid water with 3.0-5.0eV photon," Journal of Phys Chem. 100, pp17940-17949, 1996.

162. V.S. Letokhov, N.D. Ustinov, "Laser power and their applications," Harwood academic publishers.

163. M.D. Podesta, "understanding the properties of matter," UCL press, 1996.

164. H. Horisawa, I. Kimura, "Fundamental study on plasma accelerator for propulsion applications," Surface engineering instrumentation and vacuum technology, vol. 65, p389-396, 2002.

165. A.G. Gnedovets, O.M. Portnov, I. Smurov, G. Flamant, "Kinetic model of mass transfer through gas-liquid interface in laser surface alloying," Applied surface science 109/110, pp. 143-149, 1997.

166. J. P Holman, "Heat Transfer, 2nd Edition, Chapter 4, Mc Graw-Hill, 1968.

167. A.J.C. Grellier, N.K. Zayer, C. N. Pannell " Heat transfer modelling in CO_2 laser processing of optical fibres", Optics Communications Vol.152, 324-328, July 1998.

168. Y. Kamotani, S. Ostrach, J. Masud, " Oscillatory thermocapillary flows in open cylindrical containers induced by CO_2 laser heating," International Journal of Heat and Mass Transfer, vol. 42, pp 555-564, 1999.

169. Y. Kamotani, J. Masud and A. Pline, "Oscillatory Convection Due to Combined Buoyancy and Thermo-capillarity," J. Thermo-physics & Heat Transfer, Vol. 10, No. 1, pp. 102-108, 1996.

170. Y. Zhu, P. Shum, J.-H. Chong, M.K. Rao, and C. Lu *"Deep-notch, ultracompact long-period grating in a large-mode-area photonic crystal fiber"*, vol. 28, pp. 2467, Optics Letters, 2004.

171. J H Chong, P Shum, H Hartono, Y Aleta, MK Rao, C. Lu, Y. Zhu, "Measurements of refractive index sensitivity using long-period grating refractometer," Optics Communications, vol. 229, pp.65-69, 2004.

172. B. Bourliaguet, C. Pare, F.Emond and A Croteau, " Micro-structured fiber splicing," pp. 3412-3417, vol. 11, No.25, Optics Express, 15 December 2003.

173. J. H. Chong, M. K Rao "System Development for Laser Splicing of Photonic Crystal Fibers" Optics Express, 11, 1365-1370, July 2003.

174. K. Mima, H.A. Baldis, A. Nishiguchi, H. Takbe and C. Yamanaka, "Laser simulation theory and simulation," Harwood academic publishers, 1994.

175. J. P. Barton, D.R. Alexander ''Fifth Order Corrected Electromagnetic Components for a Fundamental Gaussian Beam ,'' J. Appl. Phys. 66(7), pp.2800–2802, 1989.

176. J. P. Barton, ''Electromagnetic field calculations for irregularly-shaped, axisymmetric layered articles with focused illumination,'' Appl. Opt. 35, pp532–541, 1996.

177. *Bernd Jahne*, Practical Handbook on Image Processing for scientific applications, CRC, 1997.

178. A. W Snyder and J.D. Love, "Optical waveguide theory", Chapter 23, pp. 418, Chapman & Hall, 1983.

Appendix A- 1- CO2 Laser Power Table

Laser Power (%)	First Trial (w)	Second Trial (w)	Third Trial (w)	Average (w)
1	0.01	0.01	0.01	0.01
2	0.03	0.03	0.03	0.03
5	0.42	0.41	0.40	0.41
10	1.26	1.20	1.11	1.19
15	2.20	2.20	2.20	2.20
20	3.10	3.05	3.11	3.09
25	3.75	3.83	3.93	3.84
30	4.83	4.66	4.70	4.73
35	5.53	5.60	5.58	5.57
40	6.40	6.48	6.43	6.44
45	7.05	7.03	7.17	7.08
50	7.82	7.50	7.63	7.65
55	8.07	8.57	8.27	8.30
60	8.80	8.90	8.83	8.84
65	9.03	9.16	9.60	9.26
70	10.03	10.30	10.04	10.12
75	10.38	10.72	10.89	10.66
80	10.78	11.34	11.05	11.06
85	11.09	11.60	11.59	11.43
90	11.57	12.03	12.00	11.87
95	12.96	13.00	12.73	12.90
100	12.78	12.70	12.95	12.81

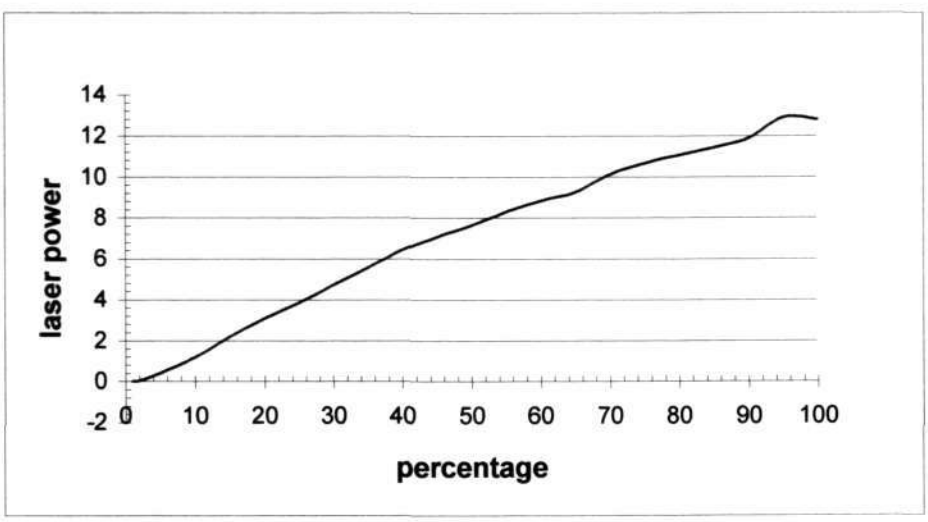

Figure A - 1- Laser Power

Appendix A- 2 Imaging System

Matrox Imaging Library Version 4.0 was used as a primary instrument for image processing in this project. It has various functions like character recognition, object detection, thresholding and digitizing that is applicable to most types of images.

(a) Edge Detection

Edges can be defined as pixel intensity discontinuities within an image. These may be different surfaces of the object, or perhaps a boundary between light and shadow falling on a single surface. The quality of edge detection is limited by what is in the image and are affected by noise present in an image.

The simplest edge detector is a filter that is to take a weighted sum of pixels around the current pixel in order to determine its new value. This is termed Discrete Convolutional Filtering [177]. The filter mask (or kernel) that is used in the development of the imaging software (Alignment.exe) is a 3x3 "Sobel Templates" of the form

for horizontal edge detection $\begin{bmatrix} -1 & -2 & -1 \\ 0 & 0 & 0 \end{bmatrix}$

and $\begin{bmatrix} -1 & 0 & 1 \\ -2 & 0 & 2 \end{bmatrix}$ for vertical edge detection.

A diagrammatic illustration of Discrete Convolutional Filtering is shown below.

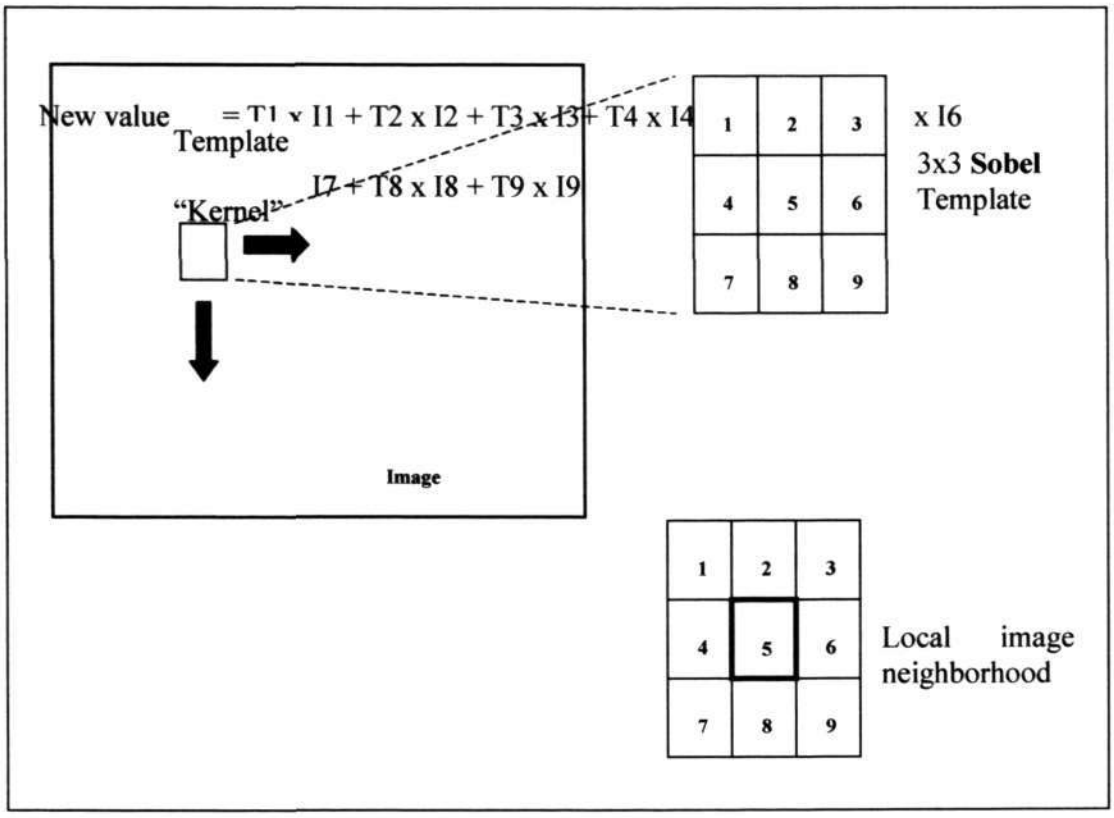

Figure A-2: Discrete Convolutional Filtering

The filter mask (kernel) is applied to every pixel in the image. It is easy to work out that in continous areas the above results in a total of zero and when the mask spans different colour values it sums to different values. The discrete convolution technique [9] can be written in the form:

$$G'_{mn} = \sum_{m'=-r}^{r} \sum_{n'=-r}^{r} H_{m'n'} G_{m-m',\, n-n'}$$

where G' = convolved image, G = original image, H = kernel, m (or m') = row and n (or n') = column

In order to apply Discrete Convolutional Filtering using programming language C++, the image is first digitized using MilDigitizer( ) function and the geometry coordinates of the fiber image is stored into a 2D buffer array using MbufGet2d( ) function from Matrox Imaging Library. Both horizontal and vertical edges are found after the conversion of each image bits to a new value using the "Sobel" template. An example of edge detection image with strategic crosses marked is shown in Figure 6.2 below.

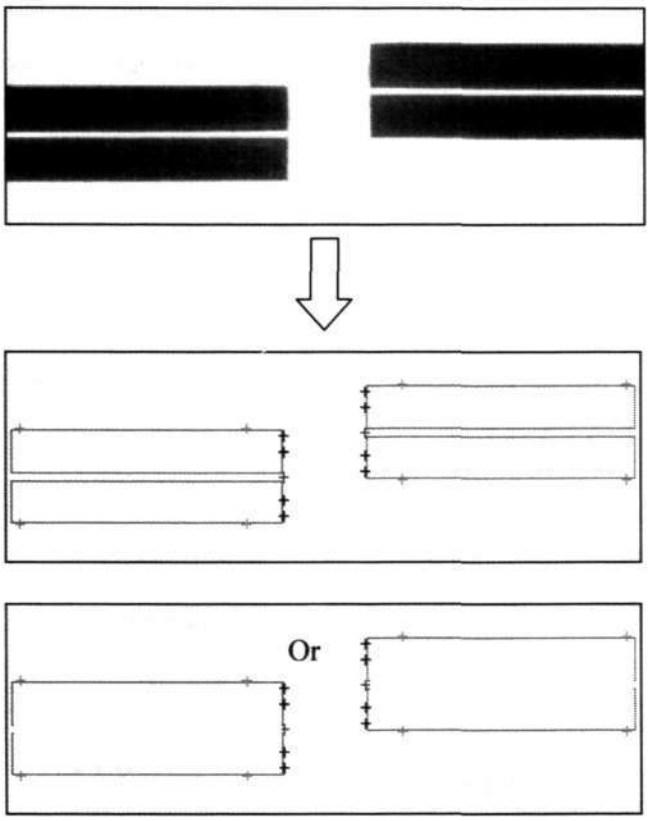

Figure A-3 (i) Core Profile Alignment Single mode fibers (ii) Cladding Profile Alignment for SMF to PCF

(b) Image Thresholding

In order to detect the edges of the fibers accurately and sharply, the image needs to be filtered to get rid of the effect of noise and to improve the signal-to-noise ratio.

Thresholding is a popular image segmentation method that converts a grey-level image into a binary image. By selecting a certain threshold value, and setting all pixel values below it to one (white), and all pixel values above it to zero (black), a black and white binary image can be obtained.

The selection of gray-scale intensity used for thresholding is arbitrary and it can be controlled. It is hard to find a way for automatic selection of a good threshold value because this project deals with live images. However, the selection of the best threshold value can be quickly found manually by changing the buffer value of the filter from 0 to 255.

The actual programming involves using Matrox Imaging Library function MimBinarize( ) which has 8 bits thresholding value (0 to 255) that is controllable. Examples of different threshold value of a two-fibers image are shown in Figure A-4.

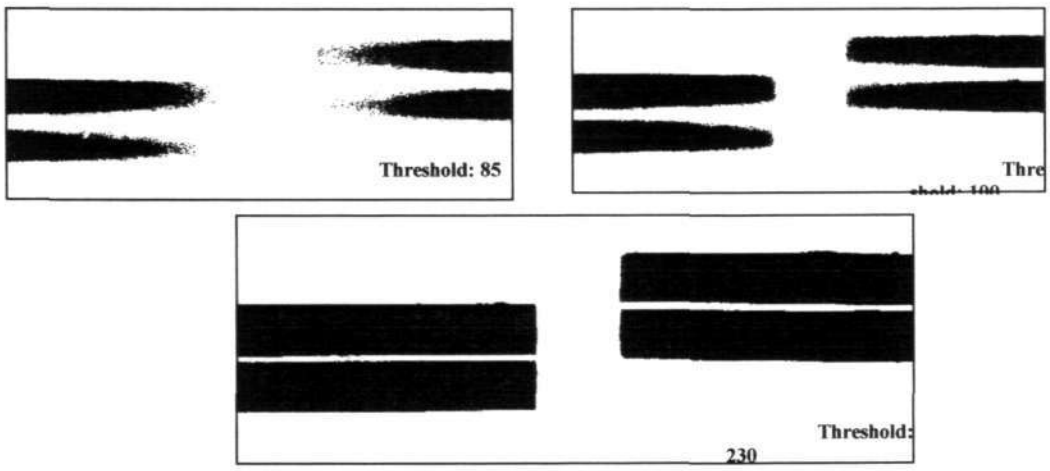

Figure A -4 Images for fiber profiles at different thresholds

Appendix A- 3: Thermal Parameters for Silica Fibre

Diameter of fiber d, Temperature T is in Kelvin.

Specific Heat, c_{sp} (unit is in $Jkg^{-1}K^{-1}$)

$$c_{sp} = \frac{-2\times10^{5} + T}{23.1992 + T} + 1.7\times10^{-3}\left(T + 8\times10^{5}\right)$$

Convection heat transfer coefficient, $h_{convection}$

$$h_{convection} = \frac{K_{air}}{d} 10^{\left(0.039+0.13\log\left(\psi d^{3}\Delta T\right)+0.01\left[\log\left(\psi d^{3}\Delta T\right)\right]^{2}\right)}$$

where

$$K_{air} = 3.84\times10^{-3} + 7.66\times10^{-5}T - 1.54\times10^{-8}T^{2}$$

$$\psi = 101\times10^{6}\, e^{\left(T-273.15/50.7\right)} + 43.5\times10^{6}\, e^{\left(T-273.15/138\right)}$$

Extinction coefficient, κ_{ext}

It determines the depth of radiation penetration being absorbed by fiber

$$\kappa_{ext} = 1.82\times10^{-2} + 10.1\times10^{-5}\left(T - 273.15\right)$$

Thermal Conductivity K_{θ} (in unit of $Wm^{-1}K^{-1}$)

$$K_{\theta} = 0.78 - 0.054e^{\left(T+379/354\right)} + 0.165e^{\left(T+379/405\right)}K$$

Refractive index of silica fiber, n

$n = 2 \pm 0.2$ at wavelength λ =10.6μm

Emissivity of cylindrical fiber, ε

$$\varepsilon = 4.445\times10^{-2}\left(\chi^{0.4859}\right) - 2.508\times10^{-4}\left(\chi^{1.4859}\right) + 7.593\times10^{-7}\left(\chi^{2.4859}\right)$$

where $\chi = \dfrac{d\times T}{500}$

Density of fiber ρ_D

$\rho_D = 2200 kgm^{-3}$

Appendix A- 4: Three Dimensional Heat Transfer Model

Three-dimensional heat equation is an expansion of one dimensional heat equation.

(a) ***Rate of Energy Generation inside a Particle***

The flow of energy and direction of the electromagnetic wave propagation are represented by Poynting vector as

$$s = E \times H^{*} \qquad \textbf{A- 1}$$

Where the asterisk denotes the complex conjugate, **E** and **H** are complex electric and magnetic fields, respectively.

Based on Maxwell's equation in frequency domain as

$$\nabla \times H = -i\omega\left(\varepsilon_r + i\varepsilon_i\right) E \qquad \text{A- 2}$$

$$\nabla \times E = i\omega\mu H \qquad \text{A- 3}$$

The rate of energy change per unit volume can then be defined as

$$\begin{aligned} \nabla \cdot s &= \nabla \cdot \left(E \times H^{*}\right) \\ &= H^{*} \cdot \left(\nabla \times E\right) - E \cdot \left(\nabla \times H^{*}\right) \\ &= i\omega\left(\mu H \cdot H^{*} - \varepsilon_r E \cdot E^{*}\right) - \omega\varepsilon_r E \cdot E^{*} \end{aligned} \qquad \text{A- 4}$$

where ε_r and ε_i are real and imaginary permittivity of the material.

For convenience, we define the real and the imaginary permittivity for the particle as ε_{tr} and ε_{ti}. The average rate of energy absorbed by the particle per unit volume is

$$q_{vol} = \frac{\omega}{2}\varepsilon_{ti} E \cdot E^{*} = \frac{\omega}{2}\varepsilon_{ti}|E|^{2} \qquad \text{A- 5}$$

(b) Electromagnetic Field Strength inside an Infinite Length Cylinder

As the rate of energy absorbed by the particle per unit volume is dependant on **E** and imaginary permittivity. Hence, it is necessary to obtain the electric field strength inside the fiber. J.P. Barton [175,176] shows the Internal and near-surface electromagnetic fields for an infinite cylinder illuminated by an arbitrary focused beam, and we extend his study to a layered cylinder such as optical fiber consists of core and cladding.

The electromagnetic interaction of an arbitrary monochromatic focused beam with an infinite layered circular cylinder located within an infinite, non-absorbing surrounding medium is considered. The cylinder and the surrounding medium are individually homogeneous, isotropic, and nonmagnetic ($\mu = 1$). An implicit time dependence of (e^{-iwt}) is assumed. The incident field (designated by the superscript *i*) is assumed known, and the electromagnetic fields within the layer (designated by the superscript *l*), the core (designated by the superscript *w*), and the electromagnetic field scattered from the particle (designated by the superscript *s*) are to be determined.

The solution is formulated in cylindrical coordinates, (r, θ, z), with the *z-axis* oriented along the length of the cylinder and the origin of the coordinate system located within the core and near the center of the particle. The layer, core, and scattered electromagnetic fields are expressed in terms of series expansions over products of cylindrical functions. The coefficients for the series expansions are then related to the known incident field by application of appropriate boundary conditions at the layer–

external medium and core–layer interfaces. The boundary conditions are matched with a cylindrical coordinate version of the boundary-matching method first introduced in [176]. The boundary-matching method is best suited for the analysis of near-circular geometries that have no sharp corners.

Important parameters for the analysis include the dielectric constant of the external medium (ε_{ext}); the complex relative refractive index of the layer ($\overline{n_2} = \sqrt{\varepsilon_2 / \varepsilon_{ext}}$); the complex relative refractive index of the core ($\overline{n_1} = \sqrt{\varepsilon_1 / \varepsilon_{ext}}$); the particle size parameter ($2\pi a / \lambda_{ext}$, where a is the characteristic radius of the outer particle surface and λ_{ext} is the external medium wavelength); and the various parameters associated with the propagation direction, polarization orientation, and general character of the incident field. The incident beam has a beam waist radius of ω_0 and a focal point location of (x_0, y_0, z_0).

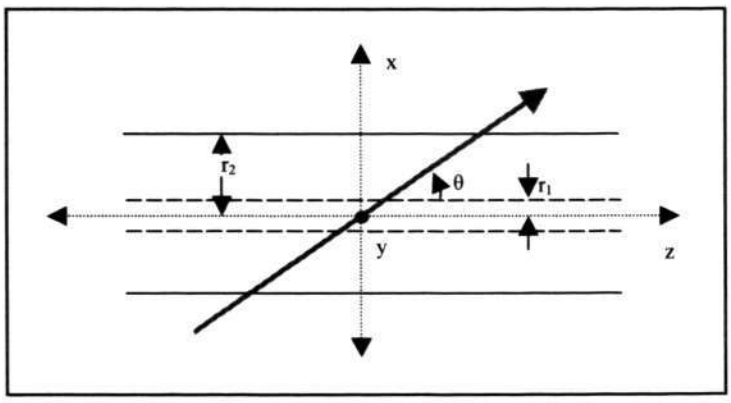

Figure A-1 Laser beam strikes at arbitrary angle.

Within a source free, homogenous medium, both electric field **E** and magnetic field **H** are solenoidal and satisfy the vector Helmholtz equation:

$$\nabla^2\mathbf{E} + k^2\mathbf{E} = 0 \qquad \text{A- 6}$$

$$\nabla^2\mathbf{H} + k^2\mathbf{H} = 0 \qquad \text{A- 7}$$

Following the approach of Stratton, independent solenoidal vector solutions M and N of the vector Helmholtz can be obtained from the scalar solution ψ of the scalar Helmholtz equation by the following vector operations:

$$\mathbf{M} = \nabla\times\left(\hat{e}_z\psi\right) \qquad \text{A- 8}$$

$$\mathbf{N} = \frac{1}{k}\nabla\times\mathbf{M} \qquad \text{A- 9}$$

where $\nabla^2\psi + k^2\psi = 0$

the cylindrical coordinates becomes

$$\frac{1}{r}\left(r\frac{\partial\psi}{\partial r}\right) + \frac{1}{r^2}\frac{\partial^2\psi}{\partial\theta^2} + \frac{\partial^2\psi}{\partial z^2} + k^2\psi = 0 \qquad \text{A- 10}$$

A separation of variables to equation (A-10) provides scalar Eigen functions if the form

$$\psi_m(k_z) \sim Z_m(k_r r)e^{ik_z}e^{im\theta} \qquad \textbf{A- 11}$$

where m is an integer index, $-\infty < m < \infty$ and k_r is related to k_z by

$$k_r^{\,2} = k^2 - k_z^{\,2} \qquad \text{A- 12}$$

For bounded solutions, k_z must be real, but otherwise $-\infty < k_z < \infty$. The generic function Z_m can be the cylindrical Bessel function of the first kind, J_m the cylindrical Bessel function of the second kind, N_m, the Hankel function of the first kind, $H_m^{(1)} = J_m + iN_m$, or the Hankel function of the second kind, $H_m^{(2)} = J_m - iN_m$.

Vector eigen functions that correspond to the scalar eigen function given in equation (A-7) can be determined by use of equations (A-3) and (A-4). For the scattered field, e general expressions for the electric field is then

$$\mathbf{E}^{(s)}(r,\theta,z) = \sum_{m=-\infty}^{\infty} \left\{ \int_{-\infty}^{\infty} \left[\begin{array}{l} a_m(k_z)\mathbf{N}_m^{(s)}(k_z,r) \\ +b_m(k_z)\mathbf{M}_m^{(s)}(k_z,r) \end{array} \right] \times e^{ik_z z}\, dk_z \right\} e^{im\theta} \qquad \text{A- 13}$$

where

$$\begin{aligned} \mathbf{M}_m^{(s)}(k_z,r) = & \left\{ \frac{1}{r} imH_m^{(1)}\left[k_r^{(s)} r\right] \right\} \hat{r} \\ & + \left\{ -k_r^{(s)} H_m^{(1)\prime}\left[k_r^{(s)} r\right] \right\} \hat{\theta} + [0]\hat{z} \end{aligned} \qquad \text{A- 14}$$

$$\begin{aligned} \mathbf{N}_m^{(s)}(k_z,r) = & \frac{1}{k^{(s)}} \left\{ ik_r^{(s)} k_z H_m^{(1)\prime}\left[k_r^{(s)} r\right] \right\} \hat{r} \\ & + \frac{1}{k^{(s)}} \left\{ -\frac{1}{r} mk_z H_m^{(1)}\left[k_r^{(s)} r\right] \right\} \hat{\theta} \\ & + \frac{1}{k^{(s)}} \left\{ k_r^{(s)2} H_m^{(1)}\left[k_r^{(s)} r\right] \right\} \hat{z} \end{aligned} \qquad \text{A- 15}$$

In equations (A-14) and (A-15) the Hankel function of the first kind, $H_m^{(1)}$, is chosen for the radial function since, in the limit of large *r*, this function corresponds to an outgoing traveling wave, which is the appropriate form for the scattered-field

solution. An expression for the scattered magnetic field can be derived from equation (A-13), from $\mathbf{H} = -(i/k_0)\nabla \times \mathbf{E}$ with additional relationships $\nabla \times \mathbf{M} = k\mathbf{N}$ and $\nabla \times \mathbf{N} = k\mathbf{M}$:

$$\mathbf{H}^{(s)}(r,\theta,z) = -i\sqrt{\varepsilon_{ext}} \sum_{m=-\infty}^{\infty} \left\{ \int_{-\infty}^{\infty} \begin{bmatrix} a_m(k_z)\mathbf{M}_m^{(s)}(k_z,r) \\ +b_m(k_z)\mathbf{N}_m^{(s)}(k_z,r) \end{bmatrix} \times e^{ik_z z}\, dk_z \right\} e^{im\theta} \quad \text{A- 16}$$

Similarly for the internal field,

$$\mathbf{E}^{(w)}(r,\theta,z) = \sum_{m=-\infty}^{\infty} \left\{ \int_{-\infty}^{\infty} \begin{bmatrix} c_m(k_z)\mathbf{N}_m^{(w)}(k_z,r) \\ +d_m(k_z)\mathbf{M}_m^{(w)}(k_z,r) \end{bmatrix} \times e^{ik_z z}\, dk_z \right\} e^{im\theta} \quad \text{A- 17}$$

$$\mathbf{H}^{(w)}(r,\theta,z) = -i\overline{n}_1\sqrt{\varepsilon_{ext}} \sum_{m=-\infty}^{\infty} \left\{ \int_{-\infty}^{\infty} \begin{bmatrix} c_m(k_z)\mathbf{M}_m^{(w)}(k_z,r) \\ +d_m(k_z)\mathbf{N}_m^{(w)}(k_z,r) \end{bmatrix} \times e^{ik_z z}\, dk_z \right\} e^{im\theta} \quad \text{A- 18}$$

where

$$\begin{aligned} \mathbf{M}_m^{(w)}(k_z,r) = &\left\{ \frac{1}{r} imJ_m\left[k_r^{(w)} r\right] \right\} \hat{r} \\ &+ \left\{ -k_r^{(w)} J_m{}'\left[k_r^{(w)}\right] \right\} \hat{\theta} + [0]\hat{z} \end{aligned} \quad \text{A- 19}$$

$$\begin{aligned} \mathbf{N}_m^{(w)}(k_z,r) = &\frac{1}{k^{(w)}} \left\{ ik_r^{(w)} k_z J_m{}'\left[k_r^{(w)} r\right] \right\} \hat{r} \\ &+ \frac{1}{k^{(w)}} \left\{ -\frac{1}{r} mk_z J_m\left[k_r^{(w)} r\right] \right\} \hat{\theta} \\ &+ \frac{1}{k^{(w)}} \left\{ k_r^{(w)2} J_m\left[k_r^{(w)} r\right] \right\} \hat{z} \end{aligned} \quad \text{A- 20}$$

In equations (A-19) and (A-20) the cylindrical Bessel function of the first kind, J_m, is chosen as the radial function for the internal field, since N_m is unbounded as $r = 0$.

Similarly for the layer field,

$$\mathbf{E}^{(l)}(r,\theta,z)=\sum_{m=-\infty}^{\infty}\left\{\int_{-\infty}^{\infty}\begin{bmatrix} e_m(k_z)\mathbf{N}_m^{(l1)}(k_z,r) \\ +f_m(k_z)\mathbf{M}_m^{(l1)}(k_z,r) \\ +g_m(k_z)\mathbf{N}_m^{(l2)}(k_z,r) \\ +h_m(k_z)\mathbf{M}_m^{(l2)}(k_z,r)\end{bmatrix}\times e^{ik_z z}\,dk_z\right\}e^{im\theta} \qquad \text{A- 21}$$

$$\mathbf{H}^{(w)}(r,\theta,z)=-i\overline{n_2}\sqrt{\varepsilon_{ext}}\sum_{m=-\infty}^{\infty}\left\{\int_{-\infty}^{\infty}\begin{bmatrix} e_m(k_z)\mathbf{M}_m^{(l1)}(k_z,r) \\ +f_m(k_z)\mathbf{N}_m^{(l1)}(k_z,r) \\ +g_m(k_z)\mathbf{M}_m^{(l2)}(k_z,r) \\ +h_m(k_z)\mathbf{N}_m^{(l2)}(k_z,r)\end{bmatrix}\times e^{ik_z z}\,dk_z\right\}e^{im\theta} \qquad \text{A- 22}$$

where

$$\begin{aligned}\mathbf{M}_m^{(l1)}(k_z,r)&=\left\{\frac{1}{r}imJ_m\left[k_r^{(l)}r\right]\right\}\hat{r}\\&\quad+\left\{-k_r^{(l)}J_m{}'\left[k_r^{(l)}r\right]\right\}\hat{\theta}+[0]\hat{z}\\ \mathbf{M}_m^{(l2)}(k_z,r)&=\left\{\frac{1}{r}imN_m\left[k_r^{(l)}r\right]\right\}\hat{r}\\&\quad+\left\{-k_r^{(l)}N_m{}'\left[k_r^{(l)}r\right]\right\}\hat{\theta}+[0]\hat{z}\end{aligned} \qquad \text{A- 23}$$

$$\begin{aligned}\mathbf{N}_m^{(l1)}(k_z,r)&=\frac{1}{k^{(l)}}\left\{ik_r^{(l)}k_zJ_m{}'\left[k_r^{(l)}r\right]\right\}\hat{r}\\&\quad+\frac{1}{k^{(l)}}\left\{-\frac{1}{r}mk_zJ_m\left[k_r^{(l)}r\right]\right\}\hat{\theta}\\&\quad+\frac{1}{k^{(l)}}\left\{k_r^{(l)2}J_m\left[k_r^{(l)}r\right]\right\}\hat{z}\\ \mathbf{N}_m^{(l2)}(k_z,r)&=\frac{1}{k^{(l)}}\left\{ik_r^{(l)}k_zN_m{}'\left[k_r^{(l)}r\right]\right\}\hat{r}\\&\quad+\frac{1}{k^{(l)}}\left\{-\frac{1}{r}mk_zN_m\left[k_r^{(l)}r\right]\right\}\hat{\theta}\\&\quad+\frac{1}{k^{(l)}}\left\{k_r^{(l)2}N_m\left[k_r^{(l)}r\right]\right\}\hat{z}\end{aligned} \qquad \text{A- 24}$$

In equations (A-23) and (A-24) the cylindrical Bessel function of the first kind, J_m, and the cylindrical Bessel function of the second kind, N_m, are chosen as the radial function for the layer field, since J_m and N_m are bounded.

The incident field $E^{(i)}$, $H^{(i)}$ (in this case, a focused beam) is assumed known. The unknown expansion coefficients for the scattered field, $a_m(kz)$ and $b_m(kz)$, the internal field, $c_m(kz)$ and $d_m(kz)$ and the layer field $e_m(kz)$, $f_m(kz)$, $g_m(kz)$, and $h_m(kz)$ are determined by applying the boundary conditions associated with the continuity of the tangential components of the electromagnetic field at the surface of the circular cylinder and at the interface between internal and layer. At the layer-external medium interface, $r = r_2$

$$E_z^{(l)} - E_z^{(s)} = E_z^{(i)}, \qquad \text{A- 25}$$

$$E_\theta^{(l)} - E_\theta^{(s)} = E_\theta^{(i)}, \qquad \text{A- 26}$$

$$H_z^{(l)} - H_z^{(s)} = H_z^{(i)}, \qquad \text{A- 27}$$

$$H_\theta^{(l)} - H_\theta^{(s)} = H_\theta^{(i)}. \qquad \text{A- 28}$$

At the internal-layer medium interface, $r = r_1$

$$E_z^{(w)} - E_z^{(l)} = 0, \qquad \text{A- 29}$$

$$E_\theta^{(w)} - E_\theta^{(l)} = 0, \qquad \text{A- 30}$$

$$H_z^{(w)} - H_z^{(l)} = 0, \qquad \text{A- 31}$$

$$H_\theta^{(w)} - H_\theta^{(l)} = 0. \qquad \text{A- 32}$$

With use of general expansions of equations (A-13), (A-16), - (A-18), (A-21),, and (A-24), equations (A-25) – (A-32) are each multiplied by $e^{-ik_z z}e^{-im\theta}dzd\theta$, integrated over the variable limits, $-\infty < z < \infty$ and $0 < \theta < 2\pi$, and then matched mode by mode. The result is the following set of eight linear algebraic equations that, for each m, k_z combination, can be used to solve for coefficients of the scattered field, $a_m(kz)$ and $b_m(kz)$, the internal field, $c_m(kz)$ and $d_m(kz)$, and the layer field $e_m(kz)$, $f_m(kz)$, $g_m(kz)$, and $h_m(kz)$.

$$\begin{aligned}&+\left\{\frac{1}{k^{(l)}}k_r^{(l)2}J_m\left[k_r^{(l)}r_2\right]\right\}e_m(k_z)+\left\{\frac{1}{k^{(l)}}k_r^{(l)2}N_m\left[k_r^{(l)}r_2\right]\right\}g_m(k_z)\\&-\left\{\frac{1}{k^{(s)}}k_r^{(s)2}H_m^{(1)}\left[k_r^{(s)}r_2\right]\right\}a_m(k_z)=A_m(k_z)\end{aligned} \qquad \text{A- 33}$$

$$\begin{aligned}&-\left\{\frac{1}{k^{(l)}}mk_zJ_m\left[k_r^{(l)}r_2\right]\right\}e_m(k_z)-\left\{\frac{1}{k^{(l)}r_2}mk_zN_m\left[k_r^{(l)}r_2\right]\right\}g_m(k_z)\\&-\left\{k_r^{(l)}J_m{}'\left[k_r^{(l)}r_2\right]\right\}f_m(k_z)\qquad-\left\{k_r^{(l)}N_m{}'\left[k_r^{(l)}r_2\right]\right\}h_m(k_z)\\&+\left\{\frac{1}{k^{(s)}r_2}mk_zH_m^{(1)}\left[k_r^{(s)}r_2\right]\right\}a_m(k_z)+\left\{k_r^{(s)}H_m^{(1)}{}'\left[k_r^{(s)}r_2\right]\right\}b_m(k_z)=B_m(k_z)\end{aligned} \qquad \text{A- 34}$$

$$\begin{aligned}&-\left\{\frac{\overline{n_2}}{k^{(l)}}k_r^{(l)2}J_m\left[k_r^{(l)}r_2\right]\right\}f_m(k_z)-\left\{\frac{\overline{n_2}}{k^{(l)}}k_r^{(l)2}N_m\left[k_r^{(l)}r_2\right]\right\}h_m(k_z)\\&+\left\{\frac{1}{k^{(s)}}k_r^{(s)2}H_m^{(1)}\left[k_r^{(s)}r_2\right]\right\}b_m(k_z)=C_m(k_z)/\left(i\sqrt{\varepsilon_{ext}}\right)\end{aligned} \qquad \text{A- 35}$$

$$+\left\{\overline{n_2}k_r^{(l)}J_m'\left[k_r^{(l)}r_2\right]\right\}e_m(k_z)\quad+\left\{\overline{n_2}k_r^{(l)}N_m'\left[k_r^{(l)}r_2\right]\right\}g_m(k_z)$$
$$+\left\{\frac{\overline{n_2}}{k^{(l)}r_2}mk_zJ_m\left[k_r^{(l)}r_2\right]\right\}f_m(k_z)+\left\{\frac{\overline{n_2}}{k^{(l)}r_2}mk_zN_m\left[k_r^{(l)}r_2\right]\right\}h_m(k_z)$$
$$-\left\{k_r^{(s)}H_m^{(1)}{}'\left[k_r^{(s)}r_2\right]\right\}a_m(k_z)-\left\{\frac{1}{k^{(s)}r_2}mk_zH_m^{(1)}\left[k_r^{(s)}r_2\right]\right\}b_m(k_z)=D_m(k_z)/\left(i\sqrt{\varepsilon_{ext}}\right)$$

A- 36

$$+\left\{\frac{1}{k^{(l)}}k_r^{(l)2}J_m\left[k_r^{(l)}r_1\right]\right\}e_m(k_z)+\left\{\frac{1}{k^{(l)}}k_r^{(l)2}N_m\left[k_r^{(l)}r_1\right]\right\}g_m(k_z)$$
$$-\left\{\frac{1}{k^{(w)}}k_r^{(w)2}J_m\left[k_r^{(w)}r_1\right]\right\}c_m(k_z)=0$$

A- 37

$$-\left\{\frac{1}{k^{(l)}r_1}mk_zJ_m\left[k_r^{(l)}r_1\right]\right\}e_m(k_z)-\left\{\frac{1}{k^{(l)}r_1}mk_zN_m\left[k_r^{(l)}r_1\right]\right\}g_m(k_z)$$
$$-\left\{k_r^{(l)}J_m'\left[k_r^{(l)}r_1\right]\right\}f_m(k_z)\quad-\left\{k_r^{(l)}N_m'\left[k_r^{(l)}r_1\right]\right\}h_m(k_z)$$
$$+\left\{\frac{1}{k^{(w)}r_1}mk_zJ_m\left[k_r^{(w)}r_1\right]\right\}c_m(k_z)+\left\{k_r^{(w)}J_m'\left[k_r^{(w)}r_1\right]\right\}d_m(k_z)=0$$

A- 38

$$-\left\{\frac{\overline{n_2}}{k^{(l)}}k_r^{(l)2}J_m\left[k_r^{(l)}r_1\right]\right\}f_m(k_z)-\left\{\frac{\overline{n_2}}{k^{(l)}}k_r^{(l)2}N_m\left[k_r^{(l)}r_1\right]\right\}h_m(k_z)$$
$$+\left\{\frac{1}{k^{(w)}}k_r^{(w)2}J_m\left[k_r^{(w)}r_1\right]\right\}d_m(k_z)=0$$

A- 39

$$+\left\{\overline{n_2}k_r^{(l)}J_m'\left[k_r^{(l)}r_1\right]\right\}e_m(k_z)\quad+\left\{\overline{n_2}k_r^{(l)}N_m'\left[k_r^{(l)}r_1\right]\right\}g_m(k_z)$$
$$+\left\{\frac{\overline{n_2}}{k^{(l)}r_1}mk_zJ_m\left[k_r^{(l)}r_1\right]\right\}f_m(k_z)+\left\{\frac{\overline{n_2}}{k^{(l)}r_1}mk_zN_m\left[k_r^{(l)}r_1\right]\right\}h_m(k_z)$$
$$-\left\{k_r^{(w)}J_m'\left[k_r^{(w)}r_1\right]\right\}c_m(k_z)-\left\{\frac{1}{k^{(w)}r_1}mk_zJ_m\left[k_r^{(w)}r_1\right]\right\}d_m(k_z)=0$$

A- 40

where

$$A_m(k_z)=\frac{1}{(2\pi)^2}\int_0^{2\pi}\left[\int_{-\infty}^{\infty}E_z^i(r_2,\theta,z)e^{-ik_z z}dz\right]e^{-im\theta}d\theta, \qquad \text{A- 41}$$

$$B_m(k_z)=\frac{1}{(2\pi)^2}\int_0^{2\pi}\left[\int_{-\infty}^{\infty}E_\theta^i(r_2,\theta,z)e^{-ik_z z}dz\right]e^{-im\theta}d\theta, \qquad \text{A- 42}$$

$$C_m(k_z)=\frac{1}{(2\pi)^2}\int_0^{2\pi}\left[\int_{-\infty}^{\infty}H_z^i(r_2,\theta,z)e^{-ik_z z}dz\right]e^{-im\theta}d\theta, \qquad \text{A- 43}$$

$$D_m(k_z)=\frac{1}{(2\pi)^2}\int_0^{2\pi}\left[\int_{-\infty}^{\infty}H_\theta^i(r_2,\theta,z)e^{-ik_z z}dz\right]e^{-im\theta}d\theta, \qquad \text{A- 44}$$

(c) Laser Beam TEM_{00}^{z} Mode

For a linearly polarized, fundamental Gaussian beam (i.e., a $TEM00^{z}$ mode beam), the incident electromagnetic field components required in equations (A-40 – A-44) can be determined from the fifth-order algebraic expressions given by [15]

$$\begin{aligned}E_z^{\bullet}=E_0\{&1+s^2(-\rho^2Q^2+i\rho^4Q^3-2\xi^2Q^2)\\&+s^4[+2\rho^4Q^4-3i\rho^6Q^5-0.5\rho^8Q^6\\&+(8\rho^2Q^4-2i\rho^4Q^5)\xi^2]\}\psi_0e^{-i\zeta/s^2}\end{aligned} \qquad \text{A- 45}$$

$$E_y^{\bullet}=-E_0\{s^2(-2Q^2\xi\eta)+s^4[(8\rho^2Q^4-2i\rho^4Q^5)\xi\eta]\}\psi_0e^{-i\zeta/s^2} \qquad \text{A- 46}$$

$$E_x^* = E_0\{s(-2Q\xi) + s^3[(+6\rho^2Q^3 - 2i\rho^4Q^4)\xi] + s^5[(-20\rho^4Q^5 + 10i\rho^6Q^6 + \rho^8Q^7)\xi]\}\psi_0 e^{-i\zeta/s^2} \quad \text{A- 47}$$

$$H_z^* = \sqrt{\varepsilon}E_0\{s^2(-2Q^2\xi\eta) + s^4[(8\rho^2Q^4 - 2i\rho^4Q^5)\xi\eta]\}\psi_0 e^{-i\zeta/s^2} \quad \text{A- 48}$$

$$H_y^* = -\sqrt{\varepsilon}E_0\{1 + s^2(-\rho^2Q^2 + i\rho^4Q^3 - 2\eta^2Q^2) + s^4[+2\rho^4Q^4 - 3i\rho^6Q^5 - 0.5\rho^8Q^6 + (8\rho^2Q^4 - 2i\rho^4Q^5)\eta^2]\}\psi_0 e^{-i\zeta/s^2} \quad \text{A- 49}$$

$$H_x^* = \sqrt{\varepsilon}E_0\{s(-2Q\eta) + s^3[(+6\rho^2Q^3 - 2i\rho^4Q^4)\eta] + s^5[(-20\rho^4Q^5 + 10i\rho^6Q^6 + \rho^8Q^7)\eta]\}\psi_0 e^{-i\zeta/s^2} \quad \text{A- 50}$$

where

$$s = \frac{1}{2\pi}\left(\frac{\lambda_{ext}}{\omega_0}\right), \xi = \frac{z}{\omega_0}, \eta = \frac{-y}{\omega_0},$$
$$\zeta = \frac{x}{\left(k\omega_0^2\right)}, \rho = \sqrt{\xi^2 + \eta^2}, Q = \frac{1}{i + 2\zeta} \quad \text{A- 51}$$
$$E_0^2 = \frac{16\mu_0 P}{\sqrt{\varepsilon_r}\omega_0^2\left(1 + s^2 + 1.5s^4\right)}$$

(d) TEM_{00}^{y} Mode

For a linearly polarized, fundamental Gaussian beam (i.e., a TEM00 mode beam), the incident electromagnetic field components required in equations (A-41-A-44) can be determined from the fifth-order algebraic expressions given by [15]

$$E_y^* = -E_0\{1 + s^2(-\rho^2 Q^2 + i\rho^4 Q^3 - 2\xi^2 Q^2) + s^4[+2\rho^4 Q^4 - 3i\rho^6 Q^5 - 0.5\rho^8 Q^6 + (8\rho^2 Q^4 - 2i\rho^4 Q^5)\xi^2]\}\psi_0 e^{-i\zeta/s^2} \quad \text{A- 52}$$

$$E_z^* = E_0\{s^2(-2Q^2\xi\eta) + s^4[(8\rho^2 Q^4 - 2i\rho^4 Q^5)\xi\eta]\}\psi_0 e^{-i\zeta/s^2} \quad \text{A- 53}$$

$$E_x^* = E_0\{s(-2Q\eta) + s^3[(+6\rho^2 Q^3 - 2i\rho^4 Q^4)\eta] + s^5[(-20\rho^4 Q^5 + 10i\rho^6 Q^6 + \rho^8 Q^7)\eta]\}\psi_0 e^{-i\zeta/s^2} \quad \text{A- 54}$$

$$H_y^* = \sqrt{\varepsilon}E_0\{s^2(-2Q^2\xi\eta) + s^4[(8\rho^2 Q^4 - 2i\rho^4 Q^5)\xi\eta]\}\psi_0 e^{-i\zeta/s^2} \quad \text{A- 55}$$

$$H_z^* = -\sqrt{\varepsilon}E_0\{1 + s^2(-\rho^2 Q^2 + i\rho^4 Q^3 - 2\xi^2 Q^2) + s^4[+2\rho^4 Q^4 - 3i\rho^6 Q^5 - 0.5\rho^8 Q^6 + (8\rho^2 Q^4 - 2i\rho^4 Q^5)\xi^2]\}\psi_0 e^{-i\zeta/s^2} \quad \text{A- 56}$$

$$H_x^* = -\sqrt{\varepsilon}E_0\{s(-2Q\xi) + s^3[(+6\rho^2 Q^3 - 2i\rho^4 Q^4)\xi] + s^5[(-20\rho^4 Q^5 + 10i\rho^6 Q^6 + \rho^8 Q^7)\xi]\}\psi_0 e^{-i\zeta/s^2} \quad \text{A- 57}$$

where

$$s = \frac{1}{2\pi}\left(\frac{\lambda_{ext}}{\omega_0}\right), \xi = \frac{z}{\omega_0}, \eta = \frac{-y}{\omega_0},$$
$$\zeta = \frac{x}{\left(k\omega_0^2\right)}, \rho = \sqrt{\xi^2 + \eta^2}, Q = \frac{1}{i + 2\zeta} \quad \text{A- 58}$$
$$E_0^2 = \frac{16\mu_0 P}{\sqrt{\varepsilon_r}\omega_0^2\left(1 + s^2 + 1.5s^4\right)}$$

Numerical Manipulation

Even though the methods proposed by J.P. Barton to calculate the internal field in the single cylinder is simple and elegant, in practice the calculation is very tedious. Even more tedious is our model because there are two layered cylinder.

In our model described above, there are 4 double integrations to calculate the value of Am (kz), Bm (kz), Cm (kz), and Dm (kz). There are 8 simultaneous linear equations involving Bessel functions to be solved to find $a_m(kz)$ and $b_m(kz)$, the internal field, $c_m(kz)$ and $d_m(kz)$, and the layer field $e_m(kz)$, $f_m(kz)$, $g_m(kz)$, and $h_m(kz)$. Then, there 6 summation and integration to determine the final E^s, E^w, E^l and H^s, H^w, H^l. All of the integration can not be performed analytically because the Gaussian Beam that we are using is very complicated.

Using MATLAB, all of these steps could be accomplished within weeks. It takes so much time to calculate double integration as well as solving simultaneously 8 equations involving Bessel functions. To reduce the time taken, a new approach has been taken. This approach is a very good approximation and can be completed in a few minutes using MATLAB.

$$A_m(k_z,m)=\frac{1}{(2\pi)^2}\int_0^{2\pi}\left[\int_{-\infty}^{\infty}E_z^i(r_2,\theta,z)e^{-ik_z z}dz\right]e^{-im\theta}d\theta \qquad \text{A- 59}$$

$$\begin{aligned}A_m(k_z,m)&=\frac{1}{(2\pi)^2}\int_{-\pi}^{\pi}\left[\int_{-\infty}^{\infty}E_z^i(r_2,\theta,z)e^{-i2\pi\frac{k_z}{2\pi}z}dz\right]e^{-i2\pi\frac{m}{2\pi}\theta}d\theta,\\&=\frac{1}{(2\pi)^2}\Im\left(E_z^i(r_2,\theta,z)\right)=\frac{1}{(2\pi)^2}\mathbf{E}_z^i\left(\frac{k_z}{2\pi},\frac{m}{2\pi}\right)\end{aligned} \qquad \text{A- 60}$$

where $\mathbf{E}_z^i\left(\frac{k_z}{2\pi},\frac{m}{2\pi}\right)$ is the scaled Fourier transform.

In MATLAB, Fourier transform is evaluated using discrete Fast Fourier Transform Algorithm which takes only a few second to accomplish. Similarly, we can find Bm (kz), Cm (kz), and Dm (kz) is similar manner.

Using the same approach, the following summation and integration can be evaluated using inverse Fourier transform.

$$\begin{aligned} E^s(r,\theta,z) &= \sum_{m=-\infty}^{\infty}\int_{-\infty}^{\infty}\left[a_m(k_z)N_m^{(s)}(k_z,r)+b_m(k_z)M_m^{(s)}(k_z,r)\times e^{ik_z z}dz\right]e^{im\theta} \\ &= \sum_{m=-\infty}^{\infty}\int_{-\infty}^{\infty}\left[a_m(k_z)N_m^{(s)}(k_z,r)+b_m(k_z)M_m^{(s)}(k_z,r)\times e^{i2\pi k_z\frac{z}{2\pi}}\right]e^{i2\pi\theta\frac{m}{2\pi}} \\ &= \Im^{-1}\left[a_m(k_z)N_m^{(s)}(k_z,r)+b_m(k_z)M_m^{(s)}(k_z,r)\right] \end{aligned}$$

A- 61

Inverse Fourier Transform too can be evaluated in MATLAB using fast Fourier transform algorithm.

Appendix A- 5: Axial Offset between LMA-PCF and SMF

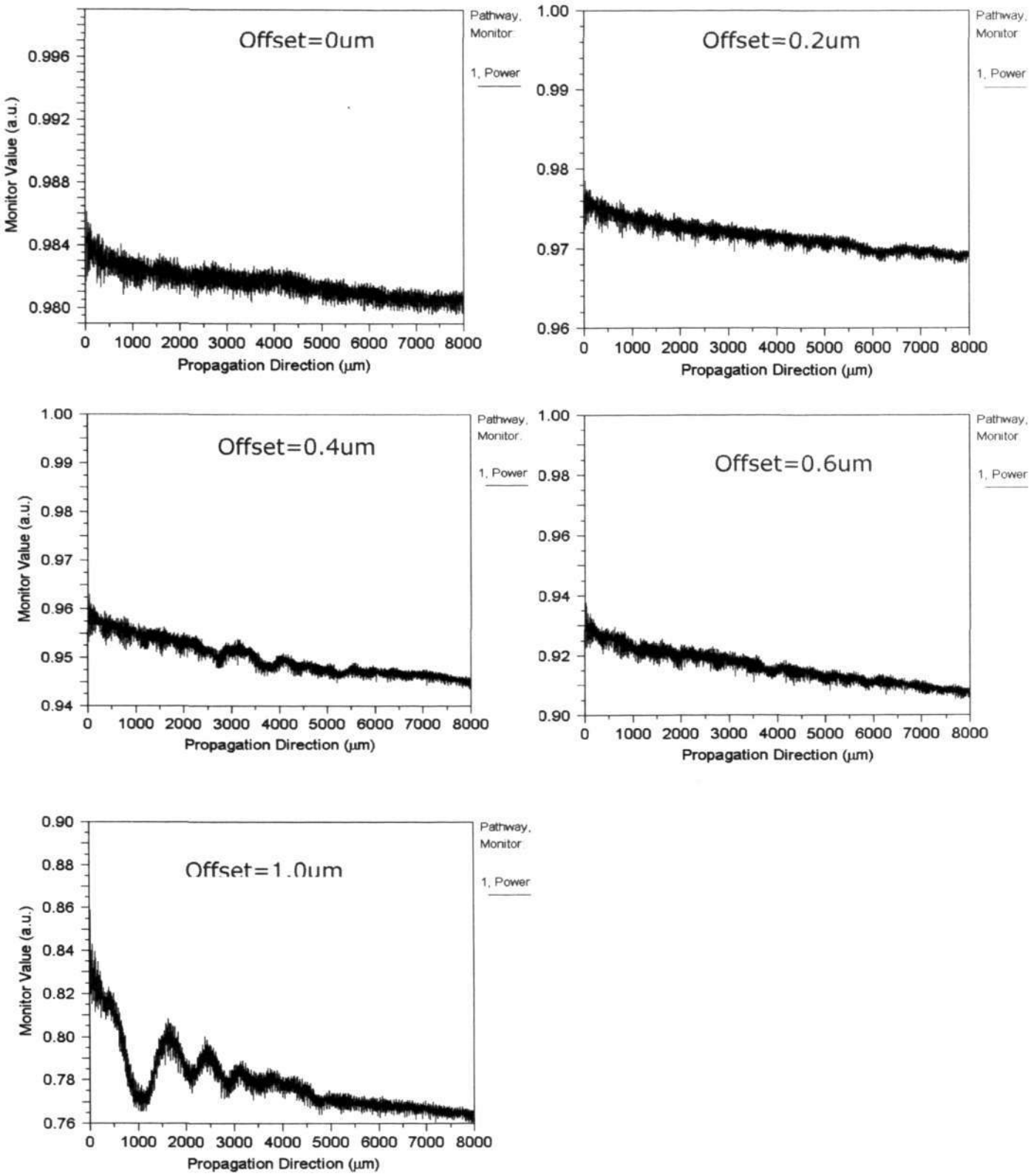

Appendix A- 6: Tilt Offset between LMA-PCF and SMF